

Faculty of Science and Engineering

Synthesis and Characterisation of Metal Oxide-Based Nano-Photosensitisers for Effective Photodynamic Therapy

Xiaohui Feng

**This thesis is presented for the Degree of
Doctor of Philosophy
of
Curtin University**

August 2014

DECLARATION

To the best my knowledge and belief this thesis contains no material previously published by any other person except where due acknowledgement has been made. This thesis contains no material which has been accepted for the award of any other degree or diploma in any university.

Signature of Student: _____

Date: _____

ABSTRACT

Photosensitisers are essential components in photodynamic therapy (PDT) that uses a photosensitiser, together with light of a specific wavelength, to kill diseased cells and tissues. Upon exposure to light, the photoexcited photosensitiser stimulates a series of photochemical reactions to form reactive oxygen species (ROS) that are able to destroy cell membrane, damage the blood stream and initiate an immune response. Classic photosensitisers are phosphrin- and non phosphrin-based materials, which are generally low in photoefficiency and lack of tumour-targeting ability. Semiconductor metal oxide-based nanomaterials are known for their high efficiency in generating strong oxidising ROS and, therefore, have been widely studied and used in water treatment to remove organic pollutants and/or bacteria through ROS-facilitated oxidation. They also have been considered as a new generation of photosensitiser and have gained increasing attention in cancer-targeting.

This thesis aimed to develop a high performance, targeted photosensitiser for cancer treatment that utilises PDT. Two types of nanosemiconductors, titanium dioxide (TiO_2) and zinc oxide (ZnO), were used in the development and investigation. Initially, silica coated TiO_2 nanoparticles ($\text{TiO}_2\text{-SiO}_2$), with a core-shell structure, of varying shell thicknesses were fabricated and characterised using various analytical instruments, including a field emission scanning electron microscope (FESEM), a transmission electron microscope (TEM) equipped with an energy dispersive spectroscope (EDS) and a Fourier transform infrared (FTIR) spectroscope. The influence of the silica coating on the photoreactivity, cytotoxicity and photokilling effect of the core TiO_2 was investigated through examining the resultant photodynamic activity and cell viability, both in the dark and under UV-irradiation, using mouse fibroblast cells (L929). Subsequently, folic acid, as a targeting ligand, was conjugated to the core-shell structured nanoparticles to form $\text{TiO}_2\text{-SiO}_2$ folate (TS-FA). The effects of the targeting ligand on the cellular-toxicity and phototoxicity, and the cell internalisation, were investigated. The results indicated that an optimal silica shell thickness (5.5 nm) could improve the stability and dispersity of the nanoparticles whilst promoting a high level of photodynamic activity of the produced photosensitiser. Conjugating folic acid to the $\text{TiO}_2\text{-SiO}_2$ nanoparticles with optimal shell thickness significantly improved the biocompatibility of the

nanoparticles to both mouse fibroblast cells (L929) and human nasopharyngeal epidermoid cancer (KB) cells, in the dark. Enhanced internalisation of $\text{TiO}_2\text{-SiO}_2$ was well demonstrated after folic acid conjugation, which also led to increased photokilling of the cancerous cells.

Secondly a high performance photosensitiser based on $\text{Fe}_3\text{O}_4\text{-ZnO}$ hybrid nanoparticles was developed and characterised. The hybrid nanoparticles were produced using magnetite (Fe_3O_4) nanoparticles that were treated with tetramethylammonium hydroxide and citric acid to form surfaces that were positively charged and negatively charged, respectively. Investigation of the photoreactivity of the two different types of hybrid nanoparticle indicated that the positively charged Fe_3O_4 nanoparticles led to the formation of $\text{Fe}_3\text{O}_4\text{-ZnO}$ hybrid nanoparticles that were smaller, denser and with higher ZnO content, which in turn resulted in much higher photocatalytic activity. In comparison to plain ZnO, both types of hybrid nanoparticles showed enhanced photocatalytic activity. The decreased photoluminescent intensity indicated the suppression effect of the hybrid nanoparticles on the fast recombination of the photogenerated charge carriers. A hypothesised mechanism was presented, showing that free iron ions act as electron-trapping sites to capture the photoexcited electrons, leading to the improved photocatalytic activity. This hypothesis was further confirmed by the results obtained from photocatalytic reactions that were performed under acidic conditions. At $\text{pH}=4$, the hybrid nanoparticles exhibited similar photocatalytic activity to the TiO_2 nanoparticles that are generally accepted as the best semiconductor photocatalyst materials.

In summary, both folic acid-conjugated $\text{TiO}_2\text{-SiO}_2$ nanoparticles and $\text{Fe}_3\text{O}_4\text{-ZnO}$ hybrid nanoparticles are effective in producing high efficiency ROS groups. Whilst the cytotoxicity and phototoxicity of the latter are still under investigation, the targeted photokilling of KB cancer cells by the former has been well demonstrated. It provides a dually targeted nanosystem that promises great potential to be used as a photosensitiser in effective PDT. In addition, this work has made a contribution to general understanding of the effects of electron transfer between components in the hybrid $\text{Fe}_3\text{O}_4\text{-ZnO}$ nanoparticles and how this affects their photoeffectiveness. This understanding will lead to further improvements in the design and development of novel semiconductor-based photosensitisers.

ACKNOWLEDGEMENT

First and foremost, I would like to express my sincerest gratitude to my supervisor, Associate Professor Dr. Xia Lou, for her great support, help and guidance. It is a privilege to work under her supervision. Throughout the course of my research project, her guidance and passion for research has continuously encouraged me to devote to pursuing research excellence, without which, I would not be able to complete the project and thesis writing.

My sincere gratitude also goes to Professor Shaokun Zhang of the Department of Orthopedics at The First Hospital of JinLin China for the assistance in carrying out the cell culture work.

Thanks are also extended to my friends, Kunal Patel and Pei Wen Lau, for their friendship as well as their help in instrument operation and software support.

Appreciation also goes to Curtin University and Department of Chemical Engineering for their financial support.

Finally, I would like to thank my parents for their deepest love, support and encouragements throughout my life.

PUBLICATION

Published Journal Paper:

Feng, X., Zhang, S. and Lou, X.. 2013. Controlling silica coating thickness on TiO₂ nanoparticles for effective photodynamic therapy. *Colloids and Surfaces B: Biointerfaces*, 107: 220-226.

Feng, X., Guo, H., Patel, K., Zhou, H. and Lou, X.. 2014. High performance, recoverable Fe₃O₄-ZnO nanoparticles for enhanced photocatalytic degradation of phenol. *Chemical Engineering Journal*, 244: 327-334.

Published Conference Paper:

Feng, X. and Lou, X.. 2012. The effect of shell thickness on photoactivity of TiO₂-SiO₂ nanoparticles of core-shell structure. *Chemeca 2012: Quality of Life Through Chemical Engineering*, Wellington, New Zealand, 23-26 September 2012, 139-149. Barton, A.C.T.: Engineers Australia.

Manuscripts in preparation:

Feng, X., Zhang, S., Wu H. and Lou, X.. A novel folic acid-conjugated TiO₂-SiO₂ photosensitizer for cancer targeting in photodynamic therapy (Submitted to *Colloids and Surfaces B: Biointerfaces*).

Feng, X. and Lou, X.. A systematic investigation on the effect of the nanostructure, the surface charges and other parameters on the photodynamic reactivity of Fe₃O₄-ZnO hybrid nanoparticles.

Feng, X., Lou, X. et al. A new generation photosensitizers for effective photodynamic therapy: A Review.

TABLE of CONTENTS

DECLARATION	ii
ABSTRACT	iii
ACKNOWLEDGEMENT	v
PUBLICATION	vi
TABLE of CONTENTS	vii
LIST of FIGURES	xi
LIST of TABLES	xvi
CHAPTER 1 INTRODUCTION	1
1.1 Aims and Objectives	1
1.2 Background	1
1.2.1 Conventional cancer therapy	2
1.2.2. Photo-triggered therapy	4
1.2.2.1 <i>Photothermal therapy</i>	4
1.2.2.2 <i>Photodynamic therapy</i>	5
1.3 New Generation Nanoparticles for Photodynamic Therapy	11
1.2.1 Quantum dots	12
1.2.2 Titanium dioxide	13
1.2.3 Zinc oxide	17
1.4 Design Parameters that Affect the Effectiveness of Delivery and Targeting	22
1.5 Proposed Research and Methodology	25
1.5.1 Synthetic pathway	26
1.5.2 Physicochemical characterisation	27
1.5.3 Evaluation of photocatalytic properties	27
1.5.4 Cytotoxicity, haemolysis and cell internalisation study	28
1.5.5 Photo-killing effect	28
1.6 Thesis Overview	29
CHAPTER 2 SILICA COATING AND ITS INFLUENCE ON PHYSICOCHEMICAL, PHOTODYNAMIC AND CELLULAR ACTIVITIES OF TiO ₂ NANOPARTICLES	31
2.1 Introduction	31
2.1.1 Background	32

2.2 Experiment	34
2.2.1 Materials and chemicals	34
2.2.2 Synthesis of TiO ₂ -SiO ₂ (TS1-4) core-shell nanoparticles	35
2.2.3 Characterisation of TS1-4	35
2.2.4 Photoreactivity study	36
2.2.5 Cell culture and nanoparticle preparation	37
2.2.6 Cytotoxicity study	38
2.2.7 Haemolysis assay	38
2.2.8 Photo-killing effect	39
2.2.9 Statistical analysis	39
2.3 Results and Discussion	40
2.3.1 Characterisation of P25 and TS1-4	40
2.3.2 Photocatalytic reactivity of P25 and TS1-4	44
2.3.3 Cytotoxicity and haemocompatibility of P25, TS1 and TS4	48
2.3.4 Photo-killing effect of P25 and TS1	51
2.4 Conclusions	53
CHAPTER 3 INVESTIGATION OF CELL COMPATIBILITY, PHOTOTOXICITY AND CELL INTERNALISATION OF FOLIC ACID CONJUGATED TiO ₂ NANOPARTICLES	54
3.1 Introduction	54
3.1.1. Background	54
3.2 Experimental	61
3.2.1 Materials	61
3.2.2 Synthesis of amine-functionalised TS hybrid nanoparticles (TS-NH ₂)	61
3.2.3 Preparation of FA-conjugated TS hybrid nanoparticles (TS-FA)	62
3.2.4 Physicochemical characterisations	63
3.2.5 Photoreactivity study	64
3.2.6 Cell culture and nanoparticle preparation	65
3.2.7 MTS assay	65
3.2.8 Haemolysis assay	66
3.2.9 Photo-killing effect	66
3.2.10 Cell internalisation	66
3.2.11 Statistical analysis	67
3.3 Results and Discussion	67

3.3.1 Synthesis and characterisation of NHS-FA	67
3.3.2 Characterisation of TS-NH ₂ and TS-FA nanoparticles	71
3.3.3 Photocatalytic reactivity	77
3.3.4 Cytotoxicity and haemocompatibility study	79
3.3.5 Photo-killing effect	86
3.3.6 Cell internalisation	88
3.4 Conclusion	89
CHAPTER 4 SYNTHESIS AND CHARACTERISATION OF Fe ₃ O ₄ -ZnO NANOPARTICLES FOR ENHANCED PHOTOCATALYTIC PROPERTIES	91
4.1 Introduction	91
4.1.1. Background	92
4.2 Experimental	94
4.2.1 Materials and chemicals	94
4.2.2 Synthesis of Fe ₃ O ₄ nanoparticles	94
4.2.3 Synthesis of Fe ₃ O ₄ -ZnO hybrid nanoparticles	95
4.2.4 Characterisation of Fe ₃ O ₄ , Fe ₃ O ₄ -ZnO and ZnO nanoparticles	96
4.2.5 Adsorption and photoreactivity study	99
4.2.6 Reusability and stability study of Fe ₃ O ₄ -ZnO hybrid nanoparticles	99
4.3 Results and Discussion	100
4.3.1 Characterisation of the Fe ₃ O ₄ , Fe ₃ O ₄ -ZnO and ZnO nanoparticles	100
4.3.2 Photocatalytic properties of Fe ₃ O ₄ -ZnO hybrid nanoparticles	104
4.3.3 Reusability and stability of the catalyst	109
4.5 Conclusions	110
CHAPTER 5 INVESTIGATION OF THE PHOTOCATALYSIS MECHANISM OF Fe ₃ O ₄ -ZnO HYBRID NANOPARTICLES	113
5.1 Introduction	113
5.1.1 Background	114
5.2 Experimental	116
5.2.1 Materials	116
5.2.2 Synthesis of Fe ₃ O ₄ (TMAH) and Fe ₃ O ₄ (CA) nanoparticles	116
5.2.3 Preparation of Fe ₃ O ₄ -ZnO hybrid nanoparticles	117
5.2.4 Physicochemical characterisations	117
5.2.5 Photoreactivity study	121
5.3 Results and Discussion	123

5.3.1 Characterisation of Fe ₃ O ₄ , Fe ₃ O ₄ (TMAH) and Fe ₃ O ₄ (CA)	123
5.3.2 Characterisation of Fe ₃ O ₄ (TMAH)-ZnO and Fe ₃ O ₄ (CA)-ZnO hybrid nanoparticles	130
5.3.3 Photocatalytic properties of Fe ₃ O ₄ -ZnO hybrid nanoparticles	134
5.3.4 Comparison of photocatalytic properties of different nanoparticles	144
5.4 Conclusion	145
CHAPTER 6 CONCLUSION AND RECOMMENDATIONS	147
6.1 Conclusion	147
6.2 Limitation of the Work and Future Direction	149
REFERENCES	150

LIST of FIGURES

Fig.1.1	The milestones in the development of PDT	7
Fig.1.2	Graphical illustration of the photodynamic reaction in PDT	9
Fig.1.3	Basic chemical structure of some PSs	10
Fig.1.4	A schematic illustration of the TiO ₂ photocatalytic reaction and its photodynamic effect on cancer cells	17
Fig.1.5	A schematic illustration of FA-conjugated silica-coated nanoparticles as a photodynamic therapeutic agent	27
Fig.2.1	A schematic representation of TiO ₂ to silica-coated TiO ₂ via the TEOS hydrolysis and condensation reaction. The theoretical molar ratios of Si/Ti in TS1-4 were 0.14, 0.29, 0.43 and 0.57, respectively	32
Fig.2.2	Photocatalytic reaction set-up	37
Fig.2.3	FESEM micrographs of non-coated TiO ₂ (P25) and silica-coated TiO ₂ (TS1-4) nanoparticles	41
Fig.2.4	TEM images of P25 and TS1 (top), showing the core-shell structure of TS1. EDS of TS1 (bottom), showing the presence of elemental Ti, Si and O. Cu is from the copper grid and C is from both TS1 and the carbon film coated on the copper grid	42
Fig.2.5	FTIR spectra for P25 and TS1-4	43
Fig.2.6	UV-Vis spectra of P25 and TS1-4	44
Fig.2.7	Phenol concentration change with time (Insert: degradation rate change with shell thickness)	45
Fig.2.8	Effect of catalyst dosage on (a) phenol degradation efficiency and (b) apparent reaction rate of phenol	48
Fig.2.9	Cell viability after treatment with P25, TS1 and TS4 for (a) 6 h and (b) 24 h. *p<0.05 as compared to control (untreated) cells. **p<0.05 as compared to the P25 treated cells. All data are expressed as the mean±SD and n=3	49
Fig.2.10	Light micrographs of L929 cells treated with (a) no nanoparticles, (b) P25, (c) TS1, and (d) TS4. Incubation time = 24 h. Nanoparticle concentration = 200 µg ml ⁻¹	50

Fig.2.11	Haemolysis assays of P25, TS1 and TS4 nanoparticles. All data are expressed as the mean±SD and n=3	51
Fig.2.12	Effect of UV irradiation period on viability of L929 cells. *p<0.05 as compared to cells without UV irradiation. All data are expressed as the mean±SD and n=4	52
Fig.2.13	Effect of photoexcited TiO ₂ and TiO ₂ -SiO ₂ nanoparticles on cell viability. Irradiated time was 20 min. *p<0.05 as compared to control. All data are expressed as the mean±SD and n=4	52
Fig.3.1	The amide formation process using DCC coupling chemistry	58
Fig.3.2	A schematic illustration of the FA-conjugated silica-coated TiO ₂ . (A) Amine-functionalised TiO ₂ -SiO ₂ nanoparticles were fabricated (B) NHS-FA was produced by mixing FA with NHS in the presence of a DCC coupling agent, using triethylamine as the catalyst. (C) The obtained NHS-FA was reacted with TS-NH ₂ to generate TS-FA	60
Fig.3.3	FTIR spectra for FA and NHS-FA	68
Fig.3.4	¹ H NMR spectrum of NHS-FA	70
Fig.3.5	FESEM micrographs of, (a) non-coated TiO ₂ (P25), (b) silica-coated TiO ₂ (TS), (c) amine-terminated TiO ₂ -SiO ₂ (TS-NH ₂) and (d) folic acid-conjugated TiO ₂ -SiO ₂ (TS-FA)	71
Fig.3.6	High resolution TEM images of (a) TS-NH ₂ and (b) TS-FA	73
Fig.3.7	(a) FTIR spectra of P25, TS, TS-NH ₂ and TS-FA in the range of 100-4000 cm ⁻¹ and (b) FTIR spectra of TS-NH ₂ and TS-FA in the 1300-1700 cm ⁻¹ region	75
Fig.3.8	TGA curves of P25, TS, TS-NH ₂ and TS-FA nanoparticles	76
Fig.3.9	UV-Vis spectra of P25, TS, TS-NH ₂ and TS-FA nanoparticles	77
Fig.3.10	Phenol concentration changes with time	79
Fig.3.11	Cell Viability after treatment with P25, TS, TS-NH ₂ and TS-FA nanoparticles for (a) 6h and (b) 24 h. *p<0.5 as compared with control. All the data were displayed as mean ± SD and n=3. The error bar was based on the standard deviation	81

- Fig.3.12 Light microscope micrographs of L929 cells treated with (a) no nanoparticles, (b) P25, (c) TS, (d) TS-NH₂ and (e) TS-FA. Incubation time=6 h. The nanoparticle concentration was 200 µg ml⁻¹. Magnification bar was 5× for all samples 82
- Fig.3.13 KB cell viability after treatment with P25, TS and TS-FA at various concentrations for (a) 6 h and (b) 24 h. *p<0.5 as compared with control cells. All data are expressed as the mean±SD and n=3. The error bar was based on the standard deviation. 84
- Fig.3.14 Haemolysis assays of P25, TS, TS-NH₂ and TS-FA nanoparticles. *p<0.05 as compared with the particles' concentration at 12.5 µg ml⁻¹. All data are expressed as mean±STD and n=3. The error bar was based on the standard deviation 85
- Fig.3.15 The surviving fraction of KB cells treated with P25, TS and TS-FA nanoparticles in the dark and after 30 min of irradiation. The particle concentration was 100 µg ml⁻¹. *p<0.05 as compared to the viability in the dark. **p<0.05 as compared to control cells at t=30 min. All data are expressed as mean±SD and n=3 87
- Fig.3.16 Effect of photoexcited P25, TS and TS-FA nanoparticles on cell viability. Irradiation time is 60 min. *p<0.05 as compared to control. All the data were expressed as mean ± SD and n=3 88
- Fig.3.17 Fluorescence confocal micrographs of KB cells (a) internalised with 100 µg ml⁻¹ suspension of TS and TS-FA. All images were recorded after 6 h of incubation at 37 °C 89
- Fig.4.1 A schematic illustration of the Fe₃O₄-mediated growth process. Nanoparticulate Fe₃O₄ seeds were added to the reaction mixture of Zn(Ac)₂·2H₂O and DEG. Fe₃O₄-ZnO was produced via the dehydration of Zn(Ac)₂·2H₂O in the presence of DEG at a high temperature 92

Fig.4.2	A schematic illustration of the ZnO photocatalytic reaction mechanism	93
Fig.4.3	FESEM image of (a) Fe ₃ O ₄ ; TEM images of (b) ZnO, (c) Fe ₃ O ₄ -ZnO(2), (d) Fe ₃ O ₄ -ZnO(4) and (e) Fe ₃ O ₄ -ZnO(8); and EDS spectrum of (f) Fe ₃ O ₄ -ZnO(8), showing the morphology, the size and the presence of elemental Fe, Zn and O in the relevant nanoparticles. In (f), Cu is from the copper grid and C is from the carbon film on the copper grid	101
Fig.4.4	XRD patterns of (a) Fe ₃ O ₄ , (b) Fe ₃ O ₄ -ZnO(2), (c) Fe ₃ O ₄ -ZnO(4), (d) Fe ₃ O ₄ -ZnO(8) and (e) ZnO	102
Fig.4.5	FTIR spectra of (a) Fe ₃ O ₄ , (b) Fe ₃ O ₄ -ZnO(2), (c) Fe ₃ O ₄ -ZnO(4), (d) Fe ₃ O ₄ -ZnO(8) and (e) ZnO	103
Fig.4.6	UV-Vis spectra of (a) Fe ₃ O ₄ , (b) Fe ₃ O ₄ -ZnO(2), (c) Fe ₃ O ₄ -ZnO(4), (d) Fe ₃ O ₄ -ZnO(8) and (e) ZnO	104
Fig.4.7	Phenol concentration changes with time	106
Fig.4.8	Photoluminescence spectra of (a) ZnO and (b) Fe ₃ O ₄ -ZnO(4) hybrid nanoparticles	108
Fig.4.9	A hypothesised photocatalytic reaction mechanism of the Fe ₃ O ₄ -ZnO hybrid nanoparticles	108
Fig.4.10	Photographs of a Fe ₃ O ₄ -ZnO(4) suspension (a) before, and (b) after, an external magnetic field was applied	109
Fig.5.1	TEM images of (a) pure Fe ₃ O ₄ , (b) Fe ₃ O ₄ (CA) and (c) Fe ₃ O ₄ (TMAH)	124
Fig.5.2	The DLS spectra of (a, b) Fe ₃ O ₄ , (c, d) Fe ₃ O ₄ (CA) and (e,f) Fe ₃ O ₄ (TMAH). The left panel is nanoparticles suspended in deionised water and the right panel is nanoparticles suspended in DEG	126
Fig.5.3	Zeta potential of Fe ₃ O ₄ , Fe ₃ O ₄ (TMAH) and Fe ₃ O ₄ (CA) nanoparticles versus pH values	127
Fig.5.4	FTIR spectra of Fe ₃ O ₄ , Fe ₃ O ₄ (CA) and Fe ₃ O ₄ (TMAH)	129
Fig.5.5	Schematic presentation of (a) Fe ₃ O ₄ (CA) and Fe ₃ O ₄ (TMAH) nanoparticles	129

Fig.5.6	TEM images of (a) Fe ₃ O ₄ (TMAH)-ZnO and (b) Fe ₃ O ₄ (CA)-ZnO; FESEM image of (c) ZnO nanoparticles	131
Fig.5.7	FTIR spectra of (a) ZnO, (b) Fe ₃ O ₄ (TMAH)-ZnO, (c) Fe ₃ O ₄ (CA)-ZnO and (d) Fe ₃ O ₄	132
Fig.5.8	(a) Nitrogen adsorption-desorption isotherms and (b) BJH pore-size distribution curves for TiO ₂ , Fe ₃ O ₄ (TMAH)-ZnO and Fe ₃ O ₄ (CA)-ZnO hybrid nanoparticles	133
Fig.5.9	UV-Vis spectra of (a) ZnO, (b) TiO ₂ , (c) Fe ₃ O ₄ (TMAH)-ZnO, (d) Fe ₃ O ₄ (CA)-ZnO and (e) Fe ₃ O ₄	134
Fig.5.10	Phenol concentration changes with time	135
Fig.5.11	PL emission spectra of (a) TiO ₂ , (b) Fe ₃ O ₄ (TMAH)-ZnO, (c) Fe ₃ O ₄ (CA)-ZnO (d) ZnO and (e) Fe ₃ O ₄	137
Fig.5.12	Phenol concentration changes as a function of catalyst loading	139
Fig.5.13	Effect of initial phenol concentration on performance of Fe ₃ O ₄ (TMAH)-ZnO	140
Fig.5.14	Effect of pH value on performance of Fe ₃ O ₄ (TMAH)-ZnO regarding phenol degradation	142
Fig.5.15	Effect of catalyst dosage on the performance of Fe ₃ O ₄ (CA)-ZnO in regard to phenol degradation	143
Fig.5.16	Effect of pH on the performance of Fe ₃ O ₄ (CA)-ZnO regarding phenol degradation	144
Fug.5.17	Phenol removal as a function of pH in the presence of various materials. The catalyst concentration was 0.325 g L ⁻¹ . The initial phenol concentration was 20 mg L ⁻¹	145

LIST of TABLES

Table 4.1	Chemical and physical properties of the synthesised nanoparticles	98
Table 5.1	Chemical and physical properties of the synthesised nanoparticles	120
Table 5.2	Kinetic parameters, phenol degradation efficiency, and the dissolved content of iron and zinc obtained using various reaction parameters	122

CHAPTER 1 INTRODUCTION

1.1 Aims and Objectives

The purpose of this thesis was to use titanium dioxide (TiO_2) and zinc oxide (ZnO) based nano-photosensitisers for cancer treatment that utilises effective photodynamic therapy (PDT). The objectives of the project were to:

1. Synthesise folic acid-conjugated TiO_2 - SiO_2 nanoparticles;
2. Investigate the effect of silica coating on photoreactivity, cytotoxicity and photo-killing ability of TiO_2 nanoparticles;
3. Study the effect of folic acid, as the targeting ligand, on the effectiveness and cancer specificity of TiO_2 nanoparticles;
4. Fabricate Fe_3O_4 - ZnO hybrid nanoparticles of varying surface characteristics;
5. Optimise the fabrication parameters for production of high photocatalytic performance of the hybrid nanoparticles;
6. Investigate the effect of the catalyst dosage, phenol concentration and pH value on the photoreactivity of the hybrid nanoparticles, and the dissolution kinetics of iron ions and zinc ions.

1.2 Background

Cancer, which is also known as malignant tumours and neoplasms, is a genetic disease in which tumour cells proliferate in an uncontrollable manner and then can be transferred to other tissues through the blood stream (Peer et al. 2007). The rapid division and growth of cancerous cells is due to the mutation of DNA in cells that can occur due to factors such as tobacco, chemicals, radiation, inherited mutations and hormones (American Cancer Society 2011). It has become one of the leading causes of human death on the global level. According to the World Health Organization, in the year 2012 alone, cancer deaths were around 8.2 million, which was approximately thirteen percent of all deaths worldwide. Over the same period, there were estimated to be around 14.1 million new cases of cancer all over the world (International Agency for Research on Cancer 2012). In the United States, there were around 1.7 million estimated new cases and over 577,190 American deaths from

cancer in the same year (Siegel et al. 2012). In 2012, an estimated 120,000 Australians were treated for cancer and the total economic burden of cancer was about \$4.7 billion. In the same year, there were more than 42,961 Australian deaths from cancer, accounting for around three out of every ten deaths (Australia Institute of Health and Welfare 2013). In view of these statistics, the design and development of novel materials and technology has become a significant part of cancer therapy.

1.2.1 Conventional cancer therapy

Conventional methods for cancer treatment involve surgery, radiotherapy, chemotherapy, immunotherapy and other small molecule-based therapies. The selection of cancer treatment methods largely depends on cancer categories, cancer staging and personal condition of patients (Brizel et al. 1998). For example, at the early stage of melanoma, surgical removal of the tumour is the optimal method and for metastatic melanoma, surgical removal of the primary tumour is followed by chemotherapy and radiotherapy (Martinez and Young 2008).

Surgery, as the first option for cancer treatment, is intended to remove the tumour diagnosed at an early stage. This type of cancer treatment also is applicable when tumours are resistant to other cancer treatments (Kristjansson et al. 2010). With the rapid developments in cancer therapy, surgery has been widely applied in the screening, prevention, diagnosis and staging, reconstruction and palliation of cancer (Lefemine and Sweetland 2012). It should be noted that, after surgery, a high risk of recurrence of tumours in the same organ need to be considered.

Radiotherapy (RT) was first reported for medical application in 1896 (Juzenas et al. 2008). The role of RT is to utilise ionising radiation to destruct one or both chains of the deoxyribonucleic (DNA) in tumour cells and inhibit the rapid proliferation of the cancer cells, subsequently leading to shrinkage of the tumour. Electromagnetic radiation and particulate radiation are two major types of radiotherapy. Electromagnetic radiation involves X-rays from a linear accelerator and Gamma-rays from a radiation material (such as cobalt-60, cesium-137 or iridium-192), whereas particulate radiation refers to the use of particles such as α - or β -particles, electrons, neutrons or photons (Hogle 2006). The selection of ionising RT largely depends on

tumour categories and the location of the tumour. The ionising radiation may interact with target tissue or react with water in the biological system to produce reactive oxygen species (ROS) that are toxic to the target tissue. Since approximately 75-90% of the human body is water, the radiolysis of water causes major damage to a number of intracellular components, especially DNA. Ionisation of water in biological systems, using high-energy radiation, destructs the chemical bonds of H-O and subsequently produce a series of free radicals such as $\text{OH}\bullet$ and O_2^+ (Halliwell and Aruoma 1991). Among these free radicals, hydroxyl $\text{OH}\bullet$ is the most active one, resulting in the peroxidation of lipid (Juzenas et al. 2008). The side effects of radiotherapy involve unwanted damage to normal cells and surrounding tissues, the generation of scars and reduced efficiency of the body's immune system (Chaplin et al. 1998).

Surgery and radiotherapy are principle treatment methods for primary solid tumours. However, many cancer patients suffer solid tumours at the advanced stages. In these cases, systemic therapies which utilise the injection of anticancer agents into blood vessels are required (Hajjaji and Bougnoux 2013). Chemotherapy, as one type of systemic therapy, was first introduced in the 1950s. The mechanism of how anticancer drugs work involves targeting DNA or attacking the proteins that are essential for cell division. They can be applied either before attempting surgery (neoadjuvant chemotherapy) or after surgery (adjuvant chemotherapy) (Caley and Jones 2012). They target the cells which proliferate at a higher rate, such as cancer cells. However, cells in the bone marrow, digestive tract or hair follicles that also grow at a rapid rate can be attacked by chemotherapeutic drugs. Hence, the adverse effects of chemotherapeutic agents involve an abnormally low amount of platelets and red blood cells, mouth ulcers and hair loss (Corrie 2011, Kievit and Zhang 2011). To minimise these side effects, ligand-conjugated anticancer drugs such as immunotoxins (toxins conjugated with antibodies) are being developed (Orive et al. 2003, Misra et al. 2010).

Immunotherapy, also called biological therapy or biotherapy, is regarded as the fourth cancer therapeutic modality and was first introduced by William Coley in the 1890s (Coley 1991). The role of immunotherapy regarding cancer treatment is to stimulate the host's immune system to attack the cancer cells, disrupt their cycle and enhance the body's self-repair ability for the cells damaged by chemotherapy or

radiotherapy. It can be classified into three major groups: passive, active and combination immunotherapy. For passive immunotherapy, antibodies provide immunity to resist tumour cells while for active immunotherapy, antibodies stimulate the patient's own immune system to kill cancer cells. Combination immunotherapy refers to a drug that has the biological capabilities presented by both active and passive immunotherapy. Although immunotherapy has achieved great success in clinical trials, its industrial application has been postponed because the immunotherapeutic agent is an autologous drug derived from the patient's own tumour cells and can be used only to kill the cancer cells of the same patient.

1.2.2. Photo-triggered therapy

Although improvements of various established cancer therapies mentioned in the previous section are an important issue, researches also have been widely undertaken to develop a new cancer treatment modality that may be safer. Phototherapy is a relatively new type of cancer treatment method in which light is utilised to treat cancer or other diseases. There are two types of phototherapy: photodynamic therapy (PDT) and photothermal therapy (PTT). For PDT, photosensitive materials are photoexcited under light with a certain wavelength to generate cytotoxic reactive oxygen species via a sequence of photochemical reactions while, for PTT, photothermal agents are initiated by light, leading to a temperature increase in the localised tumour site.

1.2.2.1 Photothermal therapy

Since 1700 BC, heat was used as a cancer therapy to treat breast cancer (Huang et al. 2008). When heat interacts with tumour tissues, the temperature of a region of the body influenced by cancer is increased to 41-43 °C in a short time. This therapeutic procedure is termed as hyperthermia (Svaasand et al. 1990). Since thermal-tolerance of tumour cells is relatively lower than that of normal cells, tumour cells are selectively damaged in this temperature range via disruption of cell membranes or denaturing of proteins. Hyperthermia can be used as an adjunctive method to treatment by surgery or radiotherapy. However, it also causes irreversible damage to

normal tissues at the same time. (Sultan 1990). To overcome this problem, photothermal therapy (PTT) is applied, in which photothermal therapeutic agents are used to selectively heat the tumour-loaded tissue. Under laser light irradiation, photothermal therapeutic agents absorb photons and are photo-excited from the ground state to the excited state. Then the absorbed energy is released in the form of heat (in a non-radiative way), leading to cell apoptosis. The requirements for an ideal photothermal therapeutic agent include biocompatibility, a large absorption coefficient in near infrared light and high ability to convert energy to heat (Chen et al. 2010a). Nowadays, the most widely investigated photothermal therapeutic agents are magnetic iron oxide and noble metals like gold (Huang et al. 2010, Qin and Bischof 2012).

1.2.2.2 Photodynamic therapy

Photodynamic therapy (PDT) is a promising cancer treatment method. It involves the use of PDT drugs, also called photosensitisers (PS), combined with non-thermal light of a suitable wavelength, which stimulates a series of photochemical reactions to produce singlet oxygen. The derived singlet oxygen has a short lifetime and is able to kill diseased cells and tissues and also to damage tumour blood vessels. In addition, it might initiate the immune system to fight against cancer cells. It should be noted that the application of either the PS or the non-thermal light alone is non-toxic to cells (Weishaupt et al. 1976).

The application of light as a therapeutic agent can be dated from 1400 BC when the Egyptians, Indians and Chinese used sunlight to treat skin illnesses (Epstein 1990). However, it was not until 1901 that the application of light as a therapeutic agent, termed “phototherapy”, was further developed by Niels Finsen. He was granted the Nobel Prize because of his successful treatment of smallpox using light (Finsen Edward Arnold 1901). During the same period, Oscar Raab, who was supervised by Tappeiner and Jodlbauer, first reported that the combination of light with chemicals can lead to cell apoptosis (Raab 1900, Von Tappeiner and Jodlbauer 1904, Dolans et al. 2003). In 1913, the first experimental use of porphyrins as phototherapeutic agents in humans was carried out by Friedrich Meyer-Betz on his own skin (Meyer-Betz 1913). Sixty years later, Diamond et al. have successfully

treated glioma, both *in vivo* and *in vitro*, with haematoporphyrin (Diamond et al. 1972). A significant breakthrough in the development of PDT took place in 1975 when Dougherty et al. successfully killed tumour cells using HpD under red light (Dougherty et al. 1975). Another milestone occurred in 1976, when the first human investigation using HpD to completely cure bladder cancer was preceded by Kelly and Snell (Kelly et al. 1975, Kelly and Snell 1976). It was in 1999 that the first PDT drug, verteporfin, was approved in Canada (Ackroyd et al. 2001). The milestones of development of PDT are shown in Fig. 1.1.

PDT has developed over the last century and has emerged as one of the important therapeutic options in the management of cancer and non-cancer diseases. In comparison with conventional cancer therapy, PDT has minor systemic toxicity to normal tissue, since the PDT drug exhibits minor toxicity in the absence of light (Awan and Tarin 2006, Buggiani et al. 2008). Additionally, PDT requires a shorter treatment period than radiotherapy and chemotherapy, which take more than two months (Chatterjee et al. 2008, Nyst et al. 2009). PDT can be applied either alone or as an adjunctive therapy to conventional cancer therapy. However, the clinical application of this therapeutic method has been hindered due to the lack of tumour specific targeting and the side-effect of skin hyper-photosensitivity. To solve these problems related to the use of PDT, better understanding of the mechanisms of the actions of PDT will be necessary.

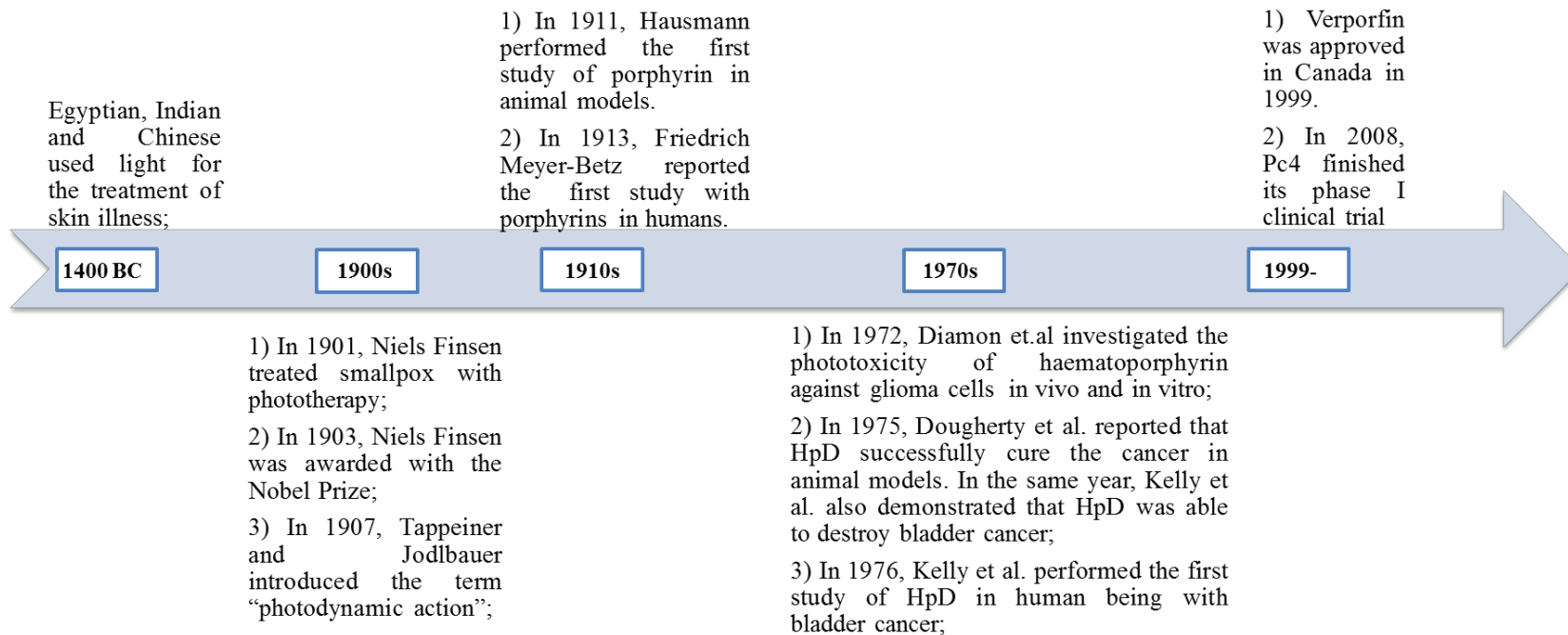


Fig.1.1 The milestones in the development of PDT

The processes of light absorption and energy transfer are the keys for the action of PDT, displayed in Fig. 1.2. Upon exposure to light, the PS is photoexcited from the ground state (S_0) to a high-energy single state (S_1). This excited single state PS has a short lifetime, which is approximately nanoseconds, so that it does not have enough time to interact with the molecules within the biological environment. It may release its energy in the form of fluorescence or heat (Castano et al. 2004). It may also go through a process, called intersystem crossing, to yield an excited triplet-state (T_1) PS that has a relatively long lifetime, in the range of micro- to milliseconds. The photodynamic effects are mainly caused by two types of reaction. In the Type I reaction, the absorbed energy can be transferred from the T_1 species to the biomolecule or cell membrane to generate radical ions. Then, these radical ions react with oxygen to produce reactive oxygen intermediates (ROIs) such as hydrogen peroxide (H_2O_2) and superoxide (O_2^-) (Ma and Jiang 2001). Among these ROIs, a superoxide will act as a reducing agent, giving an electron to a metal ion to yield a reduced metal ion which can break the oxygen-oxygen bond in H_2O_2 to form a hydroxyl radical ($\bullet OH$). The superoxide and hydroxyl radical ($\bullet OH$) derived from the Fenton reaction are toxic to diseased cells and tissues. In the Type II reaction, the energy absorbed by the excited triplet-state (T_1) PS can be directly transferred to oxygen to yield an excited-state singlet oxygen. The produced singlet oxygen molecules are highly reactive oxidizing agents and can lead to DNA damage at both nucleic base and sugars linkage (Buchko et al. 1995). Both Type I and Type II reactions take place at the same time and the ratio of the two reactions relies on the properties of the PS and the amount of oxygen involved in the biological system. Since the half-life of an ROI is less than forty nanoseconds, its action is close to the area of PS concentration (e.g. for 1O_2 , the diameter for ROI action is smaller than 100 nm) (Allison and Sibata 2010, Shibu et al. 2013).

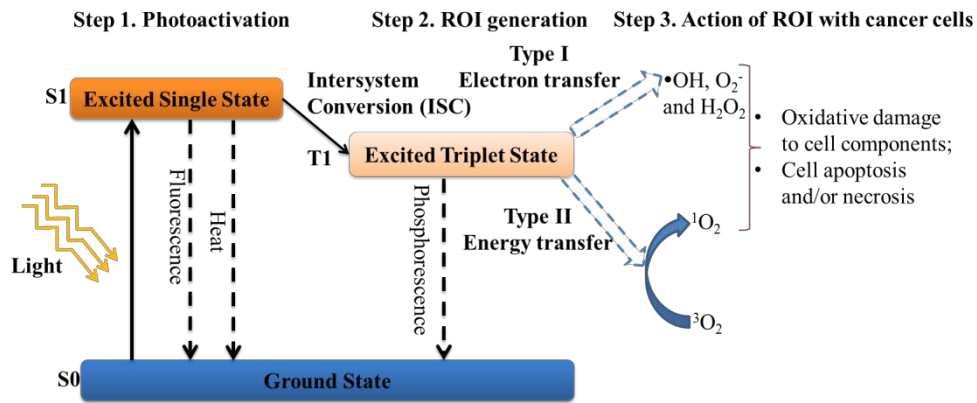


Fig.1.2 Graphical illustration of the photodynamic reaction in PDT

Based on the mechanism of action, there are three essential elements that affect the efficiency of PDT: a PS drug, light with a specific wavelength to activate the PS drug and, thirdly, oxygen. Efficiency also largely depends on the composition of the PS, the concentration of PS at the treated sites and the irradiation time and dosage at the tumour sites (Roberts and Cairnduff 1995, Juarranz et al. 2008).

Photo-activating light is one of the most important elements involved in PDT. Since the biological system is heterogeneous, light can either be absorbed by haemoglobin and cytochromes or be scattered by the turbid medium, leading to a decrease in the light dose that is delivered to the target tissue. Spectral wavelength, closely related to the penetration depth of light, also influences the effectiveness of PDT. For example, when the light is in the region of 400-450 nm, the penetration depth is less than 1 mm, while the penetration depth is around 1.5 mm when the wavelength ranges from 590 nm to 620 nm (Juzeniene and Moan 2007, Barolet 2008).

To improve the effectiveness of PDT, various PSs with high extinction coefficients and high quantum yields of ROS have been extensively investigated. Classic PS drugs involve porphyrins, porphines, phthalocyanines (PC) and protoporphyrin IX. Most of them have large π -conjugation domains, as presented in Fig.1.3 (Juzeniene et al. 2007).

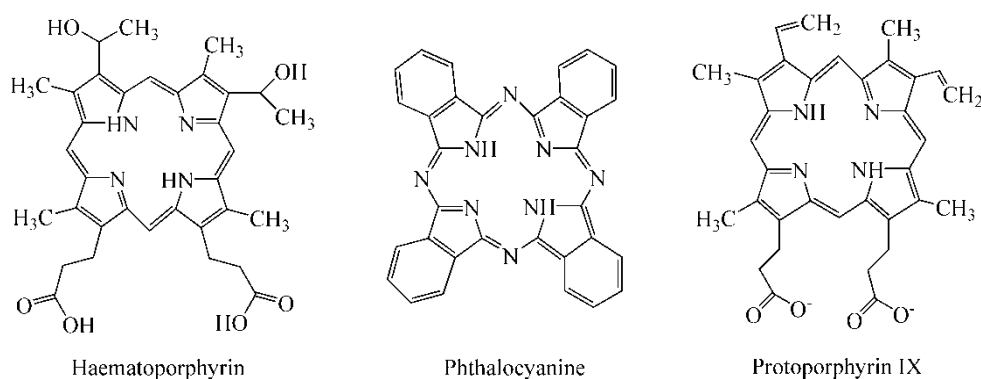


Fig.1.3 Basic chemical structure of some PSs (Kessel et al. 1987b, a).

The most widely clinically-investigated types of PS are the porphyrin-based sensitising agents: haematoporphyrin (Hp) and its derivative (HpD). Initially, it was believed that these materials could selectively accumulate at the tumour site and exhibit minimal side effects on normal tissues. Recently, a few researchers have reported that the uptake of HpD by normal tissues is much higher than that by cancerous lesions. Additionally, the chemical structure, individual components and ratio of these components in these PSs were difficult to identify. To overcome these problems, Photofrin®, which was purified from the HpD, was introduced and became the first approved PS in the development of PDT. It has been widely used in the treatment of bladder, lung and cervical cancer. Although this PS drug has achieved success, to some extent, patients have suffered serious skin photosensitivity post-treatment due to difficulties in eliminating it from their skin (Kessel et al. 1987b, a). This promoted the development of second generation PSs such as porphines, phthalocyanines (PCs) and protoporphyrin IX.

As the second generation of PSs, porphines, which are synthetic porphyrins, can specifically accumulate at the stroma of tumours (Pass 1993). Under the illumination of light at 630 nm, they are photoexcited to form ROS that are toxic to the proteins involved in cell division (Kreimeier-Birnbaum 1989). They have been widely applied in the treatment of skin cancer. The major drawback of porphine use is the unwanted damage to the nervous system (Winkelman and Collins 1987). PCs have a similar chemical structure to porphyrins, with a central metal atom such as zinc, silicon or aluminium. The PCs exhibit unique properties, including significant absorption of photo-activating light at 630 nm, high quantum yield of ROS and minimal toxicity in

the absence of light (Allison and Sibata 2010). Examples include photosens® and silicon-based phthalocyanine photosensitisers Pc 4. They have been extensively investigated in the treatment of non-melanoma skin cancer and lung cancer (Lukyanets 1999).

Another PS, 5-aminolevulinic acid (5-ALA), is used as a prodrug in the endogenous synthesis of protoporphyrin IX (PpIX). Its production is closely related to the biosynthesis pathway of haem. This pathway involves the synthesis of 5-ALA from glycine and succinyl-CoA, followed by the formation and conversion of porphobilinogen (PBG) to PpIX. After that, the produced PpIX combines with ferrous to generate haem (Berg et al. 2005). The addition of exogenous 5-ALA to the haem biosynthesis pathway can lead to an increase in the intracellular dosage of PpIX at tumour sites. Upon exposure to UV light, the ROS formed by PpIX kill cancer cells and destruct tumour tissues (Berlin et al. 1956b, a). As a precursor for PS drugs, 5-ALA has advantages such as being naturally produced by the body, having low cytotoxicity in the dark, requiring a short time interval between the administration and UV light application and rapid elimination from the human body (Peng et al. 1997).

Great effort is being made to improve the photoefficiency of classic PSs, but they are far from ideal. There are still some problems that hamper the clinical application of the classic PSs. Firstly, most of the PSs are hydrophobic, which makes them easily aggregate in the biological fluids and subsequently results in their low quantum yield. Secondly, they have short circulation and retention times. Last but not foremost, they exhibit limited tumour specificity (Lopez et al. 2004).

1.3 New Generation Nanoparticles for Photodynamic Therapy

An ideal PS should show low dark toxicity and selective accumulation within tumour tissues. After PDT treatment, the pharmacokinetic elimination of these PSs should be fast to avoid the skin's post-photosensitivity (D'Angelo et al. 2014). In this sense, the semiconductors TiO₂, ZnO and quantum dots (QDs), can be considered to be ideal PSs for PDT (Allison et al. 2004, Detty et al. 2004, Paszko et al. 2011). Each

of these three types of nanomaterial has been reviewed by investigating the three aspects of synthesis methods, properties and applications, as presented in the following sections.

1.2.1 Quantum dots

Quantum dots (QDs) which are sized in the range of 2-10 nm are semiconductor nanoparticles with high fluorescence (Walther et al. 2008). They are made from atoms from group II-VI (eg. CdSe, CdS and CdTe), group IV-VI (eg. PbS, PbSe, PbTe and CdTe) or group III-V (eg. InAs and InP) in the periodic table (Walling et al. 2009). They have been widely used in the fields of photovoltaics, optoelectronics, electro-optics and biomedicine (Biju 2014). To activate semiconductor nanoparticles, the external stimuli are able to provide the energy that exceeds their own band gap energy. Upon exposure to the external stimulus, the electrons in the valence band can be promoted to the conduction band. Then the energy absorbed by the photoexcited electrons can be released in the form of light (fluorescence) (Slivisatos 1996). Compared with conventional fluorophores, QDs possess the unique property of size-dependent emission. For example, when the particle size is around 2 nm, the emission spectra of QDs is in the range of 380 to 440 nm, while that of QDs with size of approximately 5 nm is between 605 and 630 nm (Murray et al. 1993). They also have higher extinction coefficients and improved brightness, with high photostability against photo-bleaching and degradation (Zrazhevskiy et al. 2010). Moreover, QDs with large surface area can combine with multiple imaging molecules and therapeutic agents (Barreto et al. 2011). Although the investigations of QDs have achieved promising outcomes, the clinical application of QDs has been hampered due to their water insolubility and easy aggregation (Wang and Chen 2011). These QDs can be oxidized, and the derived cadmium or selenium ions may be toxic to cancer cells (Tsay and Michalet 2005). Additionally, QDs made from atoms such as elemental cadmium and selenium can induce oxidant stress to normal cells, leading to cell death. To circumvent these problems, amphiphilic polymer and silica can be applied to modify QDs to form nanoparticles with a core-shell structure. The core-shell structure may improve the solubility and stability of QDs, increase the overall size of nanoparticles and exhibit low cytotoxicity (Wang and Chen 2011).

Apart from *in vivo* imaging, QDs also can be used as phototherapeutic agents. QDs alone as PSs show low yields of singlet oxygen. However, after conjugation with other PSs, such as Chlorin E6, the QD-PS complex had a higher production yield of singlet oxygen compared with QDs alone (Chatterjee et al. 2008).

1.2.2 Titanium dioxide

Titanium dioxide (TiO_2), also called titania, is one of the more well-known semiconductors. It exists as three different crystalline structures: anatase, rutile and brookite (Nolan et al. 2009). Among these polymorphs, rutile is the most thermodynamically stable structure. Anatase and brookite will convert to rutile when the calcination temperature is over 600 °C (Hu et al. 2003). Among these three polymorphs, anatase, with a band gap energy of 3.2 eV, is considered to be the most photoactive TiO_2 (Aguado et al. 2002). As an n-type semiconductor, TiO_2 has been widely investigated due to its high photoactivity, environmental friendliness, and high thermal and chemical stability (Linsebigler et al. 1995). Utilisation of TiO_2 as an anode to photoelectrochemically split water was first introduced by Fujishima's group in 1972 (Fujishima and Honda 1972). Commonly used methods for the preparation of TiO_2 are the sol-gel method and the hydrothermal method.

The sol-gel method begins with the hydrolysis of a titanium precursor to form titanium (IV) alkoxide, involving the condensation of titanium (IV) alkoxide to remove water and form TiO_2 . The size and morphology of the produced TiO_2 nanoparticles can be altered by changing the pH value of the reaction solution and/or the reaction temperature (Sugimoto and Zhou 2002, Sugimoto et al. 2002, 2003a, b). The prepared TiO_2 nanoparticles have high purity but require high manufacturing costs. In the case of the hydrothermal method, critical reaction conditions such as high reaction temperature and pressure are required. The size and morphology of the prepared TiO_2 nanoparticles are determined by the initial concentration of Ti precursors, the solvent chosen, reaction conditions and pH value (Chae et al. 2003). Nanoparticles of TiO_2 obtained from this method have some advantages such as high crystallization, narrow size distribution, ease of controlling morphology and long-term stability. However, the high energy requirement and unavoidable impurity of

final products are major challenges to be overcome for their use in practical applications (Chen and Mao 2007).

TiO₂, as a semiconductor material, has a wide range of applications, from paint to sunscreen to food colouring. The wide applications of TiO₂ are mostly due to its unique photocatalytic properties, chemical stability and low cost. In recent years, nanoparticles of TiO₂ have attracted increasing attention in environmental science and engineering (air and water treatment), as well as in nanomedicine to which the photoactivity of the TiO₂ nanoparticles is very critical. Upon exposure to UV light, electrons in the valence band absorb the photons and are activated to the conduction band (e_{CB}^-), leaving a positive hole in the valence band (h_{VB}^+) (Eq. 1.1). These charge carriers can either recombine to release energy (Eq. 1.2) or react with oxygen or water in the aqueous solution. The produced electron can reduce oxygen molecules to form superoxide radicals ($\bullet O_2^-$), which subsequently react with superoxide radical anions to yield hydroperoxide radicals ($\bullet O_2H$) and hydrogen peroxide (H₂O₂) (Eqs. 1.3-1.5) (Pelaez et al. 2012). The positive hole in the valence band can react with water molecules to produce hydroxyl radicals ($\bullet OH$) (Eq. 1.6) (Hoffman et al. 1994). The produced superoxide radicals ($\bullet O_2^-$), hydroperoxide radicals ($\bullet O_2H$), hydrogen peroxide (H₂O₂) and hydroxyl radicals ($\bullet OH$) are called reactive oxygen species (ROS) which are strong oxidizers and can be utilized to destroy various organic molecules and biological species.



Since the photocatalytic activities of ROS occur on the surface of catalysts, nanoparticles of TiO₂, with their large surface area, are more active than bulk

materials. However, the photocatalytic effectiveness of TiO₂ is compromised by the fast recombination of photogenerated charge carriers, presented in Eq. (1.2) (Choi et al. 1994). It has been reported that the recombination reaction between photoexcited electrons and holes occurs in 10 ns (Serpone et al. 1995). Another drawback is that the pure TiO₂ can be activated by the photons of UV light which make up 4-5% of solar light. To overcome these problems, doping TiO₂ with metal or non-metal ions and hetero-conjunction coupling are the two major solutions.

Doping TiO₂ nanoparticles with metal (Ag) or metal ions (Fe³⁺) can improve their photocatalytic activity and extend the optical spectrum from UV-light to visible light. Doped metal acts as an electron acceptor and stimulates interfacial charge transfer, resulting in an increase in the quantum efficiency. In the case of nano Ag-doped TiO₂, the optical spectra of Ag-TiO₂ has been extended to visible light. In the presence of UV light (300 nm < λ < 400 nm), electrons on the valence band of TiO₂ were excited to the conduction band and migrated to the surface of Ag. On the other hand, under visible light (λ > 450 nm), the photons were absorbed by Ag and electrons transferred from Ag to the conduction band of TiO₂ (Guanawa et al. 2009). Deposition of metal on the surface of TiO₂ nanoparticles may improve the photocatalytic activity; however, metal-doped TiO₂ suffers from thermal instability and may produce secondary impurities such as metal oxide.

Non-metal doped TiO₂, especially nitrogen-doped TiO₂, has achieved promising results in heterogeneous photocatalysis. It was firstly introduced by Sato's group in 1986 (Sato et al. 2005). After that, a significant number of works with respect to N-doped TiO₂ nanoparticles have been undertaken. Etacheri reported that the photocatalytic efficiency of N-doped TiO₂ was nine times higher than that of pure TiO₂ (Etacheri et al. 2010). The enhanced photocatalytic activity of N-doped TiO₂ nanoparticles may be due to the induction of a mid-band gap between the pre-existing conduction band and valence band of TiO₂ (Irie et al. 2003, Zhang et al. 2010).

Another method to improve the photocatalytic performance of TiO₂ is to couple TiO₂ with other semiconductors, such as CdS, WO₃ and Cu₂O, to form hetero-conjunction coupling (Georgieva et al. 2012, Liu et al. 2012, Pan et al. 2013). The produced materials also exhibit enhanced photocatalytic properties due to the

reduced recombination rate of photogenerated charge carriers. They also can induce the synergistic effect to overcome the limitations of single components. For instance, Li et al demonstrated that the coupling of TiO₂ with ZnFe₂O₄ exhibited better photocatalytic performance than either TiO₂ or ZnFe₂O₄ alone, and the recombination rate of charge carriers was restrained (Li et al. 2011a).

Increasing research activities have been focused on the application of TiO₂ nanoparticles to life science. As potential PS for PDT, TiO₂ nanoparticles can be photoexcited under the UV light to generate charge carriers, which subsequently react with surrounding molecules to produce powerful oxidative radicals. These strong oxidizers are able to destroy the structure of diseased cells, leading to cancer cell apoptosis or necrosis (Lee et al. 2010). The generation of the ROS and their further reaction with cancer cells are schematically displayed in Fig. 1.4. Fujishima's group firstly reported that under UV irradiation, the photo-excited TiO₂ were able to damage the membrane of HeLa cells, leading to the death of cancer cells (Fujishima et al. 1986). Later, the same group also proved the anticancer effect of TiO₂ in animal tumor model. For *in vivo* experiment, it showed that upon exposure to UVA, the illuminated TiO₂ particles can effectively suppress the growth of tumor (Cai et al. 1992). It is noted that all these studies were performed using Degussa P25 that contained anatase and rutile phases in a ratio of 3:1 (Lee et al. 2010, Harada et al. 2011). Similar researches have also carried out on the TiO₂ doping with other element such as non-metal such as nitrogen or metal element such as Ag. For example, Matsunaga et al. reported that microbial cells were photoelectrochemically oxidised by platinum-loaded TiO₂ in the presence of UV light (Matsunaga et al. 1985). Even though TiO₂ nanoparticles have the potential to cause phototoxicity to tumour cells, the application of TiO₂ nanoparticles within the biomedical system has been delayed because UV light could only penetrate to the superficial tissues (Cai et al. 1992, Maness et al. 1999). However, the problem might be solved through use of an external stimulus such as ultrasound (Harada et al. 2011). Detail information regarding the cancer therapy of TiO₂ will be reviewed in Section 2.1.1 and Section 3.1.1.

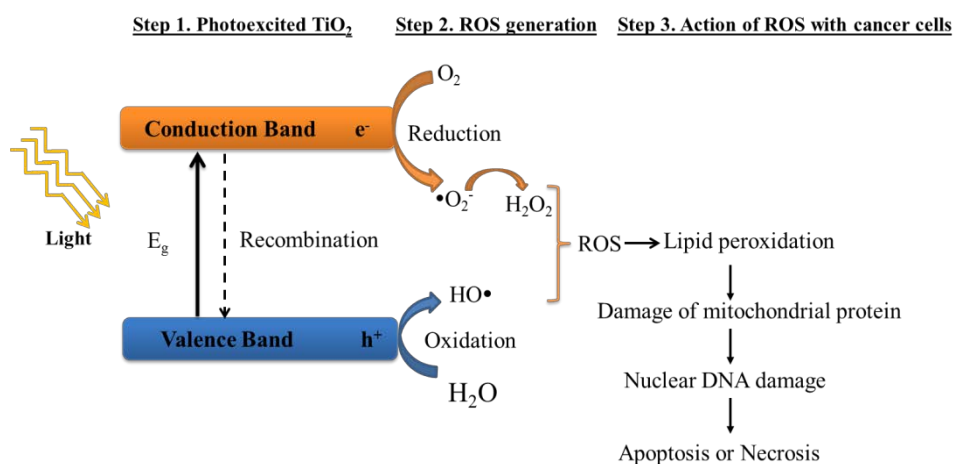


Fig. 1.4 A schematic illustration of the TiO_2 photocatalytic reaction and its photodynamic effect on cancer cells.

1.2.3 Zinc oxide

Zinc oxide (ZnO) has a hexagonal wurtzite structure with a wide band gap of 3.20 eV (390nm). Due to its high photocatalytic activity and high quantum efficiency, ZnO has been extensively applied in solar cells, gas sensors, fluorescent devices and devices that emit or detect ultraviolet light (Dutta et al. 2010). ZnO, similar to TiO_2 , has received increasing attention for possible applications in the biomedical field due to its low dark toxicity both *in vivo* and *in vitro* (Ansari et al. 2011). In addition, it is biodegradable and can be degraded to zinc ions which could be completely utilised in the body as nutrients (Zhou et al. 2006). According to the data obtained from the National Health and Medical Research Council, 14.0 mg and 8.0 mg of zinc ions per day are recommended for adult men and women, respectively (The Australian National Health and Medical Research Council).

Researchers have found that nano-sized ZnO exhibits size-dependent toxicity towards some types of cancer cells in the dark because it can induce reactive oxygen species (ROS) due to the Fenton reaction, which can cause oxidant stress to cells. Generally, the smaller is the particle size, the greater its toxicity towards cancer cells will be (Brunner et al. 2006). In addition, ZnO nanoparticles could overcome multidrug resistance (MDR) that was a major problem faced by anticancer drug developers (Hamada and Tsuruo 1988). As a potential photosensitiser, ZnO nanoparticles also can be photoexcited by light of a specific wavelength to yield the

photoinduced charge carriers that subsequently react with surrounding molecules such as water and oxygen to form reactive oxygen species (ROS) such as the hydroxyl radical ($\bullet\text{OH}$) and superoxide radical anion ($\bullet\text{O}_2^-$). The produced ROS and photoinduced holes can destroy cell membranes, leading to the efflux of the intercellular components from cancer cells (Guo et al. 2008, Manthe et al. 2010). The photo-killing effect of ZnO nanoparticles on cancer cells in the presence of UV irradiation is time-dependent and dose-dependent (Li et al. 2010). In addition, they can stimulate the immune system to fight against cancer cells. However, the clinical application of ZnO nanoparticles has been hampered due to lack of tumour specificity. Also the fast recombination of photogenerated carriers result in decreased photocatalytic activity. It is noted that around 90% of charge carriers from ZnO recombine without being utilised in photochemical reactions (Rothenberger et al. 1985). Detail information regarding the cancer therapy of ZnO will be reviewed in Section 5.1.1.

To improve the photoreactivity of ZnO, increasing research interests have been attracted to incorporate metal or metal ions with ZnO. The metal-doped ZnO may increase the surface defects and shift the optical absorption from ultraviolet to the visible region (Ullah and Dutta 2008). Another method is to couple ZnO with other semiconductors such as SnO_2 and CdS. The coupled ZnO nanoparticles may decelerate the fast recombination of photoinduced charge carriers. Most recent investigations have been focused on the deposition of ZnO onto carbon-based materials such as graphene oxide (GO) (Chen et al. 2010b), graphite-like C_3N_4 (g- C_3N_4) (Wang et al. 2011) and fullerene (C_{60}) (Fu et al. 2008). The carbon-based ZnO materials exhibit strong visible light absorption ability accompanied by deceleration of the charge recombination rate (Yu et al. 1995).

Although promising results have been achieved, the delivery of doped ZnO to cancer sites is still a problem. A possible solution to improve photoreactivity and site specific delivery of ZnO is to combine ZnO with Fe_3O_4 nanoparticles to form Fe_3O_4 -ZnO hybrid nanoparticles. In our research groups, novel magnetic ZnO nanoparticles were successfully synthesised and the derived hybrid nanoparticles exhibited higher photocatalytic activity than pure ZnO. Additionally, these magnetic nanoparticles were able to be recycled using an external magnetic field and were reused three times,

with well-maintained high photocatalytic activity (Feng et al. 2014). Hence, Fe₃O₄ nanoparticles, as magnetic targeting agents, also are reviewed below.

Magnetite nanoparticles (Fe₃O₄) which possess unique magnetic properties have been extensively applied in the fields of catalysis, data storage, bioseperation and magnetic resonance imaging (MRI) (Barreto et al. 2011). They have been widely investigated in the biomedical field owing to their biocompatibility (Cornelis and Hurlburt Wiley 1977). Additionally, they are biodegradable and the derived iron ions act as oxygen carriers from the lungs to other tissues in the body. According to daily nutrient requirement values, 8.0 mg and 18.0 mg of iron ions per day are recommended for adult men and women in Australia, respectively (Nel et al. 2006). Due to their biocompatibility and biodegradability, magnetite nanoparticles can be widely utilised as MRI contrast agents, drug delivery vehicles and hypothermal therapeutic agents (Gupta and Gupta 2005) .

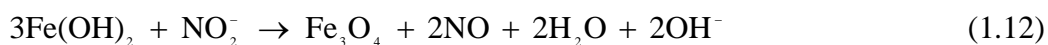
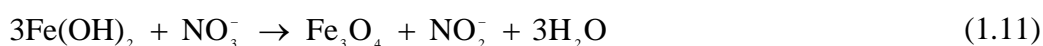
Magnetite nanoparticles can be prepared using various methods. The chemical co-precipitation method is the simplest one, which was firstly reported by Massart in 1981. In this method, ferric and ferrous salts at a molar ratio of 2:1 are precipitated by adding base solution under nitrogen protection (Massart 1981). The relative chemical reactions are shown below.



The size, shape and composition of the magnetic nanoparticles are determined by the types of anions involved in the salts (chlorides, sulphates, nitrates and so on), the ratio of ferrous and ferric ions (ideally 0.4-0.6), pH value (pH=9-14), ionic strength and reaction temperature (Sjogren et al. 1994).

Another well-established co-precipitation method is to add potassium nitrate and potassium hydroxide into the aqueous solution of ferrous salts (Sugimoto and Matijevic 1980). The relative chemical reactions are presented in Eqs. (1.10-1.13).





The size and morphology of produced nanoparticles can be governed by adjusting the molar ratio of ferrous ions and hydroxide ions. The size of prepared magnetite nanoparticles, using Massart's method, is smaller than 20 nm, while that produced by Sugimoto's method varies between 30 and 200 nm (Sen et al. 2006). The coprecipitation method has advantages such as being simple, having a high yield and greater productivity. However, the produced magnetite nanoparticles have a broad size distribution, poor crystallization and aggregate easily (Flensch et al. 2005).

Fe_3O_4 nanoparticles with smaller size have a larger surface area-to-volume ratio and high surface energy, hence, these nanoparticles turn into an aggregate. In addition, due to the inherent magnetic dipolar force, these nanoparticles attract each other to form large clusters (Hamley 2003). To improve the dispersion of Fe_3O_4 nanoparticles, surface coating is an alternative method. The commonly used stabilisers can be organic (e.g. surfactants) or inorganic (e.g. silica). In the case of an organic stabiliser, surfactants can be either absorbed or chemically attached to the surfaces of nanoparticles to generate a double-layer protection (Sousa and Tourinho 2001). The produced steric forces between nanoparticles are able to balance the magnetic dipolar forces and electrostatic forces. The commonly used surfactants contain tetramethylammonium (TMAH) and citric acid (CA). (Sahoo et al. 2005b). Silica also can be used to protect the magnetite core from magnetic dipole interaction, to counter aggregation. After being coated with silica shells, both thermal stability and biocompatibility of the core nanoparticles are improved (Lesnikovich et al. 1990, Sun et al. 2005).

Due to their unique magnetic property, these nanoparticles have been widely applied in the fields of wastewater treatment and biomedicine (Lu et al. 2007). In the case of wastewater treatment, after being coated with organic functional groups such as thiol groups or amine groups, the functionalised magnetite nanoparticles can be used to remove heavy metal ions (Chung et al. 2012, Hakami et al. 2012, Xin et al. 2012, Zhang et al. 2012a, Tang and Lo 2013). The produced functionalised

nanoparticles can react with metal ions to form metal complexes and these metal complexes are removed from water by applying an external magnetic field (Liu et al. 2011). In addition, the combination of magnetite nanoparticles and photocatalysts can form magnetic photocatalysts, which exhibit the dual properties of high photocatalytic performance and easy separation.

In the biomedical field, the applications of magnetite nanoparticles can be classified into three groups: photothermal therapeutic agents, drug carriers for site-specifically delivery of anticancer agents and contrast agents in magnetic resonance imaging (MRI).

Magnetite nanoparticles can be utilised as therapeutic agents via hyperthermia. In the presence of an alternating magnetic field (AMF), magnetite nanoparticles are able to convert the energy of an oscillating magnetic field to heat, leading to irreversible damage of cancer cells that are more sensitive to heat than normal cells (Moroz et al. 2002, Laurent et al. 2008). For example, it has been reported that the magnetite nanoparticle-loaded anti-HER2 immunoliposome, in which magnetite nanoparticles act as hyperthermia therapeutic agents, can cause severe damage to tumour tissues (Ito et al. 2004). The heat generated via hyperthermia largely depends on the strength of the AMF, as well as the concentration, size and shape of the magnetite nanoparticles (Lu et al. 2007). Recent investigation also has found that near-infrared (NIR) light also can be used to excite the magnetite nanoparticles to release heat into cancer cells (Chu et al. 2013).

They also can be used as drug carriers which involve the following process: anticancer agents are bound to magnetite nanoparticles to form the complex, followed by injection of this complex into the blood stream, directing it to the cancerous lesions upon exposure to an external magnetic field and release of the anticancer agents from the complex caused by the temperature change (Mahmoudi et al. 2011). The major problem faced by magnetic drug delivery is the reduced magnetic strength caused by the fast flow rate of blood (Arruebo et al. 2007). Another application of magnetite nanoparticles is to exploit them as MRI contrast agents to visualise tumour sites, inflammation areas and angiogenesis (Singh and Sahoo 2014). They are able to distinguish the cancerous tissue from healthy tissue. Magnetite nanoparticles in a size that is smaller than 60 nm have a long blood

circulation time, hence, they possess high sensitivity and selectivity to cancerous lesions (Qiao et al. 2009) When the size of magnetite nanoparticles is larger than 60 nm, they can be captured by liver and spleen, resulting in the identification of any cancerous lesions in the liver (Lin et al. 2008). It has been reported that magnetite nanoparticles, as contrast agents, have the capability of detecting tumours sized as small as 2-3 mm present in the liver (Semelka and Helmberger 2001).

1.4 Design Parameters that Affect the Effectiveness of Delivery and Targeting

Nanoparticles should satisfy certain criteria to ensure their effective and safe application as phototherapeutic agents in photo-triggered therapy. Biocompatibility is the most important criterion for nanomaterials applied in the biomedical field.

Prior to the application of nanoparticles to human beings, biocompatibility is the first parameter that should be considered. In the context of nanoparticles as therapeutic agents, the definition of biocompatibility is “*the ability of a material to perform with an appropriate host response in a specific situation*” (Kohane and Langer 2010). This is to say, the nanoparticles as a therapeutic agent should exhibit minimal toxicity to normal tissues and cells (Maeda et al. 2013). Nowadays, the scope of biocompatibility has been extended, including cytotoxicity, haemocompatibility, *in vivo* biodistribution, and clearance. As reported, biocompatibility of the nanoparticles is governed by the parameters involving particle size, shape and surface properties.

Particle size is one of most important physicochemical properties that affect the cell internalisation, biodistribution and clearance of the nanoparticles. Unlike the normal tight vascular wall, the tumour vascular wall is discontinuous and the gaps between the adjacent endothelial cells are in the region of 200-800 nm (Jain 1998). Through these gaps, nanoparticles could flow out from blood vessels and selectively accumulate in the tumour interstitial fluid. It has been reported that the nanoparticles with a size of below 200 nm could accumulate at the tumour sites via the form of non-specific targeting (Hughes 2005). In addition, particle size also influences cell internalisation. Generally, particles with smaller size are preferentially internalised

by the cells. It has been reported that nanoparticles sized around 50nm exhibited maximum cellular internalisation (Chithrani et al. 2006). Furthermore, to avoid fast elimination from the human body, the particle size should be larger than 10 nm (Banerjee et al. 2002, Choi et al. 2007).

Particle shape is another factor that influences the tumour cell internalisation process. Spherical-like nanoparticles are favoured to be internalised through a clathrin-mediated pathway, whereas the nanoparticles with a longer aspect ratio (AR) can be taken up via a caveolae-mediated pathway (Tang et al. 2012). Moreover, particle shape is related to the blood circulation time and excretion rate. As an example, the mesoporous silica nanoparticles (MSNs) with longer AR have longer circulation time and much slower clearance rate than MSNs with shorter AR (Huang et al. 2011c).

Surface properties also should be considered in the design of nanoparticles as therapeutic agents. It has been reported that the surface of the vascular endothelial cells has negatively charged sulphated groups and carboxyl groups (He et al. 2010). The nanoparticles with positive charges could selectively bind with the endothelial cells on the vascular wall, leading to a reduced concentration of nanoparticles accumulated at the cancerous site (Lee et al. 2011). The positively charged nanoparticles also induce immunological toxicity upon normal cells. (Li and Huang 2008). Based on previous findings, the weakly negatively charged and neutral nanoparticles are favoured for biomedical applications.

For nano-based cancer targeted therapy, one of the biggest challenges is to achieve sufficient drug concentration at the tumour site. Due to leaky blood vessels and a poor lymphatic system, nanoparticles selectively accumulate in the interstitium surrounding the cancerous lesions. The phenomenon, called the enhanced permeation and retention (EPR) effect, was first found by Mastumura and Maeda in 1986 (Maeda 2001, Fang et al. 2003, Maeda 2010). The EPR effect improves the accumulation of therapeutic nanoparticles to tumours, but not all types of tumour can be passively targeted. For example, the necrosis core of a metastatic cancer cannot be passively targeted due to limited access by the blood vessels (Maki et al. 1985, Wang et al. 2009, Fang et al. 2011).

One strategy to solve these problems is to modify nanoparticles with targeting ligands to form targeted nanoparticles. These nanoparticles can selectively bind to target receptors that are over-expressed on the surface of cancer cells, hence enhancing the cell internalisation via receptor-mediated endocytosis (Torchilin 2005). The most common used targeting moieties involve transferrin, folic acid and antibodies and their fragments.

Transferrin, a β -glycoprotein, is used to transport ferric ions into cancer cells through transferrin receptors (Pun et al. 2004). It has advantages such as high affinity to transferrin receptors and easy conjugation with nanoparticles through its amino groups (Daniels et al. 2006). Transferrin receptors are expressed at an elevated level in cancerous cells (Dowlati et al. 1997). However, they also are over-expressed in normal cells with rapid proliferation rates such as brain capillary endothelium cells.

Folic acid is an essential vitamin during the preparation of purines and pyrimidine (Kukowska-Latallo et al. 2005). It also has high affinity ($K_D = 10^{-9}$ M) and specificity for folate receptors that are over-expressed in a wide range of solid tumours such as ovarian, lung, brain, head and neck, renal cell, breast and melanoma skin cancers (Low and Antony 2004, Elnakat and Ratnam 2004). The level of FR expression is also unregulated at advanced stages of cancer (Shmeeda et al. 2006). There are still some drawbacks such as its hydrophobic nature. It was reported that the solubility of derived folic acid-conjugated nanoparticles in an aqueous solution decreases, compared with non-conjugated nanoparticles. They can dissolve in water only when basic or highly acidic (Maity et al. 2013). Detail information regarding cell internalisation and a general method to conjugate folic acid with nanoparticles will be reviewed in Chapter 3.

Antibodies which involve an $F(ab)_2$ fragment at the tip and an Fc fragment at the base could be used to target almost any type of tumour-associated antigen (TAA) (Carter 2001). They have some unique properties, such as high selectivity to cancer cells and stability when encountering biological fluid (Reiter 2001). Among these TAAs, vascular endothelial growth factor receptor (VEGFR) is considered to be the most important factor that influences tumour angiogenesis. When VEGFR or VEGFR-signalling is blocked, there will be insufficient oxygen and nutrients supplied to tumour cells, leading to necrosis of the tumour cells. The antibody-

conjugated nanoparticles enhance the intracellular uptake. However, they have short blood circulation time and are sensitive to changes in temperature, salt concentration and enzyme level (Bertrand et al. 2014, Simard and Leroux 2010).

Although targeting moieties significantly enhance the intracellular delivery of nanoparticles, they cannot increase the concentration of nanoparticles localised at the tumour site (Kirpotin et al. 2006). Hence, it is necessary to combine the passive and active approaches of targeting to improve the efficiency of intracellular delivery, which in turn increases the intracellular concentration of the nanoparticles (Wang et al. 2009). Besides passive and active forms of targeting, magnetic targeting also can be achieved via application of the external magnetic field to magnetic nanocarriers (Pankhurst et al. 2003, Dobson 2006). The limitations regarding magnetic targeting involve the possibility of blockage of the blood stream and the penetration limit of commercial magnets (Grief and Richardson 2005). All these findings provide essential information for the design of targeted photodynamic nanosystems.

1.5 Proposed Research and Methodology

This project aims to synthesise and characterise a novel multifunctional nanosystem to target cancer cells for possible applications as a photodynamic therapy. As mentioned above, nanoparticulate titanium dioxide and zinc oxide have been regarded as potential photosensitising agents for photodynamic therapy. Upon exposure to ultraviolet (UV) light, the electrons in the valence band of the photosensitising agents can be promoted to the conduction band, resulting in a negative electron in the conduction band and a positive hole in the valence band. In the biological environment, the photo-induced charge carriers can react with oxygen or water molecules to produce reactive oxygen species (ROS) that can attack cell membrane, leading to the necrosis of cells and destruction of tumour tissues. The clinical application of the photosensitising agents has been hampered by problems such as low efficiency and insufficient selectivity caused by lack of cell-specific accumulation at the cancerous lesions. In addition, TiO₂ or ZnO nanoparticles with

high surface area tend to aggregate in the biological environment, resulting in a decrease of their surface area and lower photoreactivity.

A possible solution to overcome these problems is to coat TiO₂ nanoparticles with a silica shell to generate core-shell structured nanoparticles. Silica coating can improve the dispersion of core nanoparticles and also protect the core nanoparticles from the biological environment. The nanoparticles can be further functionalised via a targeting ligand such as folic acid. The resulting folic acid-conjugated TiO₂ nanoparticles can initiate receptor-mediated endocytosis to enhance the intracellular delivery of ROS. Another method to increase cell-specific accumulation at the cancerous lesions is to combine magnetic nanoparticles with ZnO nanoparticles to form hybrid Fe₃O₄-ZnO nanoparticles. The hybrid nanoparticles can target the cancerous lesions by alternating the external magnetic field. In addition, the magnetic function in the hybrid nanoparticles can act as a photothermal therapeutic agent to delivery heat to the tumour site. In this study, the design parameters involving photoactivity, biocompatibility and photo-killing effects will be systematically investigated for possible application in the development of a targeted photodynamic nanosystem for cancer cells.

1.5.1 Synthetic pathway

The core nanoparticles are photosensitisers that can be photo-excited to generate ROS that can kill cancerous lesions. The surface of the core nanoparticles will be coated with a silica shell and further functionalised with amine groups. Folic acid (FA) as a targeting ligand will be conjugated to the silica shell for possible active targeting. The synthetic pathway for FA-conjugated silica-coated nanoparticles is schematically shown in Fig. 1.5. Also, active targeting can be achieved through the combination of photosensitisers with magnetic nanoparticles.

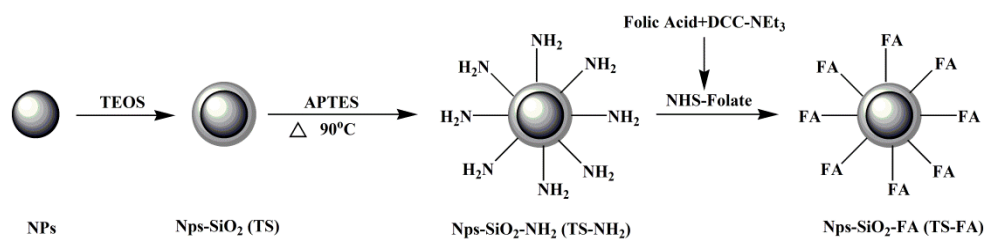


Fig.1.5 A schematic illustration of FA-conjugated silica-coated nanoparticles as a photodynamic therapeutic agent

1.5.2 Physicochemical characterisation

The chemical compositions of the produced nanoparticles at each stage will be analysed using X-ray diffraction (XRD) and atomic absorption spectroscopy (AAS) methods. The qualitative and quantitative analyses of functional groups presented on the surface of the derived nanoparticles will be characterised using Fourier transform infrared (FTIR) spectroscopy and thermo-gravimetric analysis (TGA). The size and morphology of the obtained nanoparticles will be examined via a transmission electron microscope (TEM) equipped with an energy dispersive spectrometer (EDS) and by a field emission scanning electron microscope (FESEM). The optical properties of the nanoparticles will be evaluated using an ultraviolet-visible diffuse reflectance spectroscope (UV-Vis DRS) and photoluminescence (PL) spectra.

1.5.3 Evaluation of photocatalytic properties

The photocatalytic performance of the obtained nanoparticles at each stage will be characterised using photodegradation of phenol in the presence of light illumination. Phenol is one of the most commonly used organic chemicals for evaluation of photocatalysts. The ultimate products for phenol degradation under UV light are carbon dioxide and water. In a typical procedure, a certain amount of the obtained catalyst will be mixed with phenol solution and the mixture will be maintained in the dark with constant stirring. After 30 min of stirring, the light will be switched on. At a given time interval, around 5 ml of the mixture will be withdrawn and the solid will be removed using filtration. The concentration of the resultant solution will be measured using high performance liquid chromatography

(HPLC). In the case of Fe₃O₄-ZnO nanoparticles, the loss of iron ions and zinc ions to phenol solution due to the photo-corrosion of Fe₃O₄ and ZnO will be evaluated using Atomic Absorption Spectroscopy (AAS) and Inductive coupled plasma atomic emission spectroscopy (ICP-AES).

1.5.4 Cytotoxicity, haemolysis and cell internalisation study

The cell cytotoxicity of the produced nanoparticles at each stage will be quantitatively analysed using MTS assay. In brief, normal or cancerous cells will be cultured in a 96-well plate and incubated at 37 °C in a humidified atmosphere involving 5% CO₂. After 24 h incubation, the culture medium will be replaced with cell medium involving various concentrations of the nanoparticles. After 6 h or 24 h incubation, the culture medium will be removed and the plate will be washed three times with PBS. The cell viability of the resultant samples will be measured using a microplate reader. The cytotoxicity study of the cells also will be visualised using live/dead assay. The haemocompatibility also will be assessed using blood cells.

The cell internalisation of ligand-conjugated nanoparticles will be tested using cancerous cells which over-express folate receptors. The sample used will be FA-conjugated TiO₂ nanoparticles. Control experiments will be conducted using silica-coated nanoparticles and non-coated nanoparticles. The incubation time will be 6 h. The qualitative analysis will be carried out using confocal laser scanning microscopy (CLSM).

1.5.5 Photo-killing effect

The photo-killing effect of the derived nanoparticles on cancer cells will be examined as follows. The experimental procedure is similar to that described in section 1.5.4. However, after 6 h incubation, the cells will be exposed to UV light. At the prescribed time interval, the cells will be removed from UV light and incubated in the dark, overnight. The viability of cells also will be examined using MTS assay.

1.6 Thesis Overview

Chapter 1 of this dissertation gave a comprehensive literature review on the application of nanometallic materials as therapeutic agents in the field of cancer treatment. A brief introduction to the conventional cancer therapy was followed by a more detailed description of photo-triggered therapy including its principle, the mechanism of action and commonly used phototherapeutic agents. After that, a review of new generation nanoparticles for photo-triggered therapy was presented. To ensure safety applications of these nanoparticles to human beings, the particular criteria that need to be considered were then summarised.

In Chapter 2, studies on silica coating and its influences on the physicochemical properties, photodynamic and cellular activities of TiO_2 nanoparticles will be presented. Core-shell structured titanium dioxide-silica ($\text{TiO}_2\text{-SiO}_2$) nanoparticles with varying shell thicknesses will be synthesised and confirmed using various analytical methods. The photocatalytic reactivity of the $\text{TiO}_2\text{-SiO}_2$ nanoparticles will be evaluated via the photodegradation of phenol. Cytotoxicity and haemocompatibility studies also will be assessed. The photo-killing effect of $\text{TiO}_2\text{-SiO}_2$ nanoparticles on cells will be evaluated.

Chapter 3 will present the experimental findings when silica-coated TiO_2 nanoparticles with optimal shell thickness, having retained good photoreactivity, were conjugated with folic acid, a targeting ligand that is over-expressed on various types of cancer cell. The characterisation, through various physical and chemical methods, of the physicochemical properties and photocatalytic activity of the obtained folic acid-conjugated silica-coated TiO_2 nanoparticles will be reported. Additionally, the cell compatibility and phototoxicity of the resulting folic acid-conjugated silica-coated TiO_2 nanoparticles exposure on primary adherent mouse fibroblast connective tissue (L929) cells and human nasopharyngeal epidermoid cancer (KB) cells, both in the dark and under UV irradiation, will be demonstrated.

Chapter 4 will focus on the synthesis and characterisation of novel magnetic $\text{Fe}_3\text{O}_4\text{-ZnO}$ hybrid nanoparticles that demonstrate enhanced photocatalytic activity in comparison with pure ZnO. The effect of the amount of Fe_3O_4 on the particle size and photodegradation efficiency of hybrid nanoparticles will be investigated. The mechanism in relation to the enhanced separation of photo-induced charge carriers

will be explored using photoluminescence (PL) spectra. The presence of iron ions in phenol solution will be proved.

Chapter 5 describes the synthesis of magnetic Fe₃O₄-ZnO hybrid nanoparticles using two surfactant-capped Fe₃O₄ nanoparticles as seeds. The effects of surfactants on the dispersity of Fe₃O₄ nanoparticles, and therefore the hybrid nanoparticles, will be discussed. Also, three parameters that influence the photocatalytic reactivity of the hybrid nanoparticles, regarding initial phenol concentration, catalyst dosage and pH value, will be investigated. The dissolution of elemental iron and zinc under UV irradiation also will be covered.

Finally, Chapter 6 summarises the main findings of each chapter.

CHAPTER 2 SILICA COATING AND ITS INFLUENCE ON PHYSICOCHEMICAL, PHOTODYNAMIC AND CELLULAR ACTIVITIES OF TiO₂ NANOPARTICLES

2.1 Introduction

This chapter focuses on the investigations regarding the influences of the silica coating on the photoreactivity, the cytotoxicity and the photo-killing ability of TiO₂ nanoparticles. The silica-coated TiO₂ nanoparticles were synthesised at room temperature via the Stöber method, using commercially available TiO₂ nanoparticles (Degussa P25) and tetraethoxysilane (TEOS) as reactants. Variation of the silica shell thickness was achieved through altering of the TiO₂-to-TEOS ratio in the reaction mixture. Four core-shell structured TiO₂-SiO₂ nanoparticles were synthesised and denoted as TSX (X=1-4). The schematic representation of the reaction is displayed in Fig. 2.1. The obtained core-shell structured nanoparticles were examined using a field emission scanning electron microscope (FESEM), a transmission electron microscope (TEM) equipped with an energy dispersive spectroscope (EDS), and a Fourier transform infrared (FTIR) spectroscope. The photoreactivity of the silica-coated nanoparticles was first examined through the photodegradation of phenol, a compound that can be degraded under UV light into carbon dioxide, water and corresponding mineral acids, in the presence of photocatalysts (Sun et al. 2011). The influence of various reaction parameters involving silica shell thickness, initial concentration of phenol and amount of photocatalysts on the photocatalytic activity of silica-coated TiO₂ was investigated. Control experiments were conducted using non-coated TiO₂ nanoparticles as photocatalysts under the same experimental conditions. Cytotoxicity and haemocompatibility were also assessed. Following these examinations, silica-coated TiO₂ nanoparticles with an optimal shell thickness, having retained good photoreactivity, were selected for the photo-killing effect investigation.

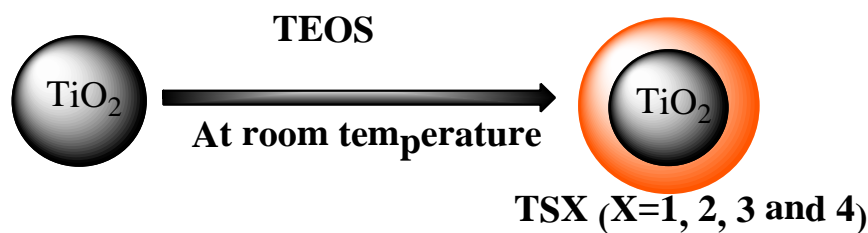


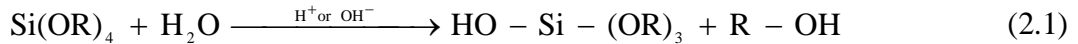
Fig. 2.1 A schematic representation of TiO_2 to silica-coated TiO_2 via the TEOS hydrolysis and condensation reaction. The theoretical molar ratios of Si/Ti in TS1-4 were 0.14, 0.29, 0.43 and 0.57, respectively.

2.1.1 Background

As mentioned in Chapter 1, nanoparticles of TiO_2 have attracted increasing attention in life sciences since the first report of photocatalytic disinfection by Matsunaga et al. in 1985 (Matsunaga et al. 1985). When being irradiated by ultraviolet (UV), the TiO_2 nanoparticles can be photoexcited to produce a negative electron (e_{CB}^-) in the conduction band and a positive hole (h_{VB}^+) in the valence band. In an aqueous environment, the photoinduced electron and hole pairs react with oxygen or water to generate reactive oxygen species (ROS) such as hydroxyl ($\text{HO}\cdot$) and superoxide radical ($\cdot\text{O}_2^-$). These reactive species are powerfully oxidative and can destroy the structure of various organic molecules and, therefore, have found extensive applications in the removal of infectious molecules and organic pollutants. TiO_2 nanoparticles also have been regarded as a potential photosensitizing agent for photodynamic therapy (PDT) (Fujishima et al. 2000, Fernández-Ibáñez et al. 2003, Zhu et al. 2004, Lopez et al. 2010). The ROS generated from the photoexcited TiO_2 nanoparticles can react with cell membranes and cell interiors, leading to toxic responses and/or death of cells (Manthe et al. 2010). Many investigations on photodecomposition of tumour cells have been undertaken recently. Cai et al. reported that TiO_2 nanoparticles completely killed HeLa cells when used with UV irradiation (Cai et al. 1992). Stefanous et al. also indicated that photoexcited TiO_2 nanoparticles efficiently inhibited the aggregation of platelets, which led to discontinuation of haematogenous metastasis (Stefanou et al. 2010). The photo-killing effect of nitrogen-doped TiO_2 nanoparticles in the visible region also has been reported (Li et al. 2011b). The research mostly has been limited to lab investigations. The clinical application of TiO_2 nanoparticles has been hampered by problems, such

as low efficiency and insufficient selectivity, resulting from the lack of cell-specific accumulation of TiO₂ on cancer cells (Xu et al. 2007). In addition, the metal ions exposed on the surfaces of nanoparticles can lead to metal toxicity for the cells (Yoon et al. 2006, Xu et al. 2007). The insolubility of TiO₂ in water is also a problem as the nanoparticles tend to aggregate in a physiological environment, leading to a reduction of surface area and reactivity of the particles (Pozzo et al. 1997, Pazokifard et al. 2012).

Coating nanoparticles with silica has been used widely to improve the dispersion, and the cell compatibility, of various nanoparticles in a physiological environment (Han et al. 2009, Teleki et al. 2009, Mbeh et al. 2012). A silica layer can be produced using the Stöber method, which is simple and can be operated at ambient temperature (Stöber et al. 1968). In this method, an alkoxy silane such as tetraethylorthosilicate (TEOS) is employed as the silica precursor, and an acid or base acts as the catalyst. It involves hydrolysis and, consequently, condensation of precursors. Firstly, the hydrolysis of the precursors takes place in the alcoholic solution in the presence of the acid or base, as presented in the following equations.



The derived products in the hydrolysis of alkoxy silane are HO-Si-(OR)₃, (HO)₂-Si-(OR)₂, (HO)₃-Si-OR and H₄SiO₄, which are suspended in the alcoholic medium (Vansant et al. 1995). After the concentration of silicic acid reaches more than the solubility limit, the condensation of silicic acid occurs to generate a siloxane polymer. The corresponding reactions are illustrated below.



The thickness of the produced silica layer can be controlled by varying the types of precursor used, concentration of reactants, reaction temperature and time. The surface charge is determined by changing the catalysts used. When a base is used as a catalyst, the derived silica layer has a negatively charged surface, while the silica

layer prepared using an acid as the catalyst has a positively charged surface (Rother et al. 2011).

As an important constituent of cell membrane, silica nanoparticles must be biocompatible and biodegradable so that they can eventually be eliminated from the body through the urine (Quintanar-Guerrero et al. 2009). It has been proven by long-term biocompatibility experiments that silica implants in animals have not presented any toxicity for around 42 days (Kortesuo et al. 2000). Silica, as the shell in the core-shell nanoparticles, can act as a protector to reduce the influence of the outer environment upon the core nanoparticles (Kenneth et al. 2005). Since the silica surface is electrostatically stable, it also improves the dispersion of the core nanoparticles (Carturan et al. 2004). Moreover, the outer surface of silica shell easily could be functionalized by different ligands that are useful for cancer targeting, therefore enhancing the cancer cells' internalization (Sun et al. 2008). Although the overall particle stability and dispersibility can be improved after silica coating, the properties of the core component, such as reactivity and thermal stability, also may be modified (El-Toni et al. 2010, Siddiquey et al. 2012).

In order to understand the effect of the silica layer on the TiO₂ nanoparticles, the core-shell structured TiO₂-SiO₂ nanoparticles with varying shell thicknesses were synthesised. The photoreactivity, cytotoxicity and photo-killing ability of the TiO₂-SiO₂ nanoparticles were systematically investigated.

2.2 Experiment

2.2.1 Materials and chemicals

Degussa P25 (TiO₂ nanoparticles consisting of 75% anatase and 25% rutile) was purchased from Degussa. The average size of the nanoparticles was 25 nm. Tetraethoxysilane (TEOS) (99.999%), ammonia aqueous solution (4.13%) and ethanol (99.5%) were purchased from Sigma-Aldrich. All chemicals were reagent grade and used without further purification. Deionised water was used in this investigation.

2.2.2 Synthesis of TiO₂-SiO₂ (TS1-4) core-shell nanoparticles

P25 (0.5g, 6.26 mmol) and ammonia solution (1.0 ml) were added to a mixture of deionized water (20 ml) and ethanol (60 ml). The mixture was dispersed using ultrasonic vibration for about 30 min. Twenty ml of ethanol, containing various amounts of TEOS, was added, dropwise, to the dispersion. This took about 30 min. The amounts of TEOS added into the dispersions were 200 μ l (0.90 mmol), 400 μ l (1.79 mmol), 600 μ l (2.69 mmol) and 800 μ l (3.58 mmol). These concentrations yielded theoretical Si/Ti molar ratios of 0.14, 0.29, 0.43 and 0.57 in the products, respectively. After stirring for 2 h, the reaction mixtures were centrifuged at 7500 rpm for 5 min. The liquid in the centrifuge tube was removed and the resultant silica-coated TiO₂ nanoparticles were washed with ethanol (three times), to remove any excess reactants, and then dried overnight at room temperature under vacuum.

2.2.3 Characterisation of TS1-4

FTIR analysis was conducted on a Perkin-Elmer Spectrum 100 using the KBr pellet technique at room temperature. The samples were mixed with dried KBr, using a mortar and pestle, and then the mixture was pelletized under vacuum. All the spectra were recorded in the range of 400-4000 cm⁻¹ at a resolution of 4 cm⁻¹.

UV-visible diffuse reflectance spectroscopy (UV-Vis DRS) was performed on a Jasco V-570 equipped with an integrating sphere, and BaSO₄ was used as a reference. The band-gap energy was estimated from the intercept of the UV-vis spectrum using the following equation, where λ is the threshold absorption wavelength of the nanoparticles (Irie et al. 2003):

$$E_g = \frac{1240}{\lambda} \quad (2.5)$$

A FESEM (Zeiss Neon 40EsB FIB-SEM) was used to examine the morphology of the P25 and the obtained TiO₂-SiO₂ nanoparticles. The samples were dispersed in deionised water using ultrasonic vibration and the solutions were deposited onto an aluminium stub where a platinum coating (2 nm) was applied as a conducting material. FESEM images of the nanoparticles were recorded at an accelerating

voltage of 5 kV. The size of the nanoparticles was measured using the in-built Zeiss operational software, SmartSEM that is linked to the magnification bar of the obtained images.

The detailed morphology and chemical composition of the nanoparticles were further examined using a TEM (JEOL JSM 2011) equipped with an energy dispersive spectroscope (EDS). Prior to the TEM examination, the nanoparticles were dispersed in ethanol using ultrasonic vibration with an approximate concentration of $10 \mu\text{g ml}^{-1}$. They were then distributed on carbon-coated copper grids for examination.

2.2.4 Photoreactivity study

Examination of the photoreactivity of the produced core-shell nanoparticles was conducted in a 1 L double-jacket reactor, as shown in Fig. 2.2. A water bath was connected to the reactor, through a pump, to maintain the reaction temperature at $25 \pm 0.5 \text{ }^\circ\text{C}$, and a magnetic stirrer was used for mixing. The UV irradiation was facilitated by a MSR 575/2 metal halide lamp (575 W, Philips) with its wavelength in the range of 315-1050 nm. In brief: a preferred amount of P25 and TSX (X=1-4) was added to 200 ml of aqueous phenol solution and stirred for 30 min in the dark to obtain a homogeneous solution. Then the light was immediately switched on. At set time intervals, 3 ml of solution was withdrawn via a syringe and filtered using a $0.45 \mu\text{m}$ Millipore filter. The concentration of phenol in the withdrawn samples was measured using a HPLC (Varian) with a UV-detector at the wavelength of 270 nm. The column was C-18 and the mobile phase was 30% acetonitrile and 70% deionised water. The amount of P25 used for the photocatalytic reaction was 0.2 g, resulting in a concentration of 1.0 g L^{-1} . To maintain the same concentration for TiO_2 , the added amounts of TS1-4 were 0.22 g, 0.24 g, 0.26 g and 0.28 g, respectively. Based on the results obtained, photoreactivity experiments were conducted with varying operational parameters using non-coated TiO_2 nanoparticles and silica-coated TiO_2 nanoparticles with an optimal shell thickness: two initial concentrations of phenol ($20 \mu\text{g ml}^{-1}$ and $50 \mu\text{g ml}^{-1}$) and four photocatalyst concentrations (0.125 , 0.25 , 0.50 and 1.0 g L^{-1}). The aforementioned photoreactivity experiments were performed once.

It is worthy to mention that the method employed in the work is well established and proven reproducible in our previous work (Sun et al. 2011).

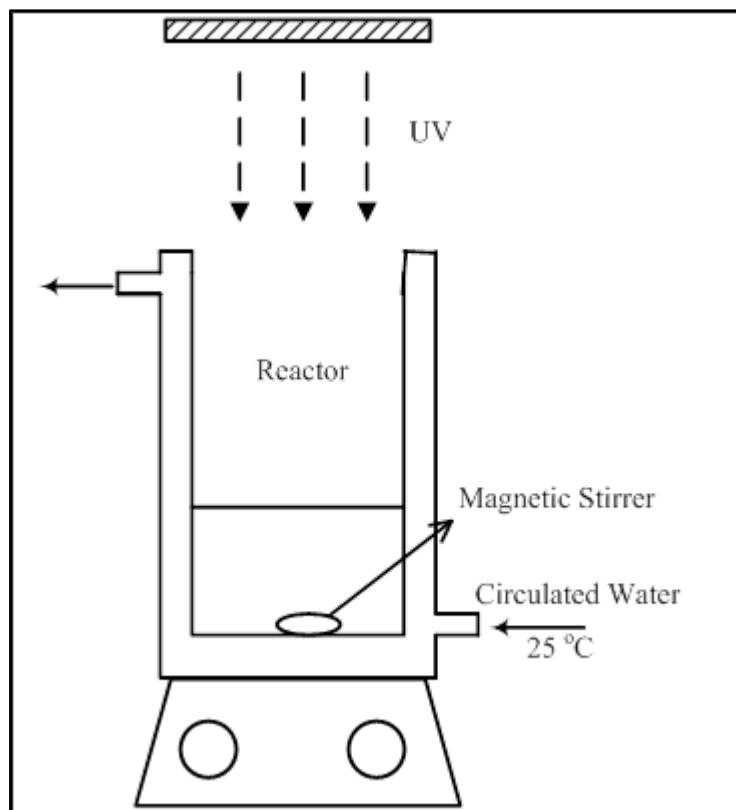


Fig.2.2 Photocatalytic reaction set-up.

2.2.5 Cell culture and nanoparticle preparation

Primary adherent mouse fibroblast connective tissue cells (L929) were purchased from ATCC (USA). The cells were cultured in Dulbecco's modified Eagle's medium (DMEM, Invitrogen, USA) supplemented with 10% fetal bovine serum (FBS, Sigma-Aldrich). The cells were maintained at 37 °C in a humidified incubator with 95% air and 5% CO₂. Nanoparticles of P25, TS1 and TS4 were suspended in growth medium, each at concentrations of 12.5, 25, 50, 100 and 200 µg ml⁻¹, for further investigation.

2.2.6 Cytotoxicity study

The cell cytotoxicity was measured using the 3-(4, 5-dimethylthiazol-2-yl)-5-(3-cayboxymethoxyphenyl)-2-(4-sulfophenyl)-2H-tetrazolium (MTS) assay (Erogbogbo et al. 2008). Briefly, L929 cells were plated at a density of 1×10^4 cells per well, in a 96-well plate, in 200 μl of medium and incubated at 37 °C in 5% CO_2 atmosphere. After overnight incubation, the medium in the wells was replaced with fresh medium, described previously, containing the nanoparticles at concentrations of 12.5, 25, 50, 100 and 200 $\mu\text{g ml}^{-1}$. A control experiment was conducted using cells treated with same growth medium containing no nanoparticles. After 6 h and 24 h of incubation at 37 °C under 5% CO_2 , the cell culture medium was removed and the plate was washed with PBS three times. Then, 200 μl of MTS reagent was added to each well, and the cells were incubated for 3 h under the same conditions. After the treatment, the absorbance of formed formazan at 490 nm was measured by a microplate reader. The cell viability was calculated using the following equation (Ahn et al. 2004):

$$\text{Cell viability} = \frac{\text{OD}_{490}(\text{sample})}{\text{OD}_{490}(\text{control})} \times 100\% \quad (2.6)$$

where $\text{OD}_{490}(\text{sample})$ is the optical density of cells treated with various concentrations of nanoparticles and $\text{OD}_{490}(\text{control})$ is the optical density of cells incubated with medium only.

All the experiments were performed in triplicate in the dark. Cell morphology was photographed at the two time intervals using an Olympus BX61 microscope. The magnification was set at 5 \times for all samples.

2.2.7 Haemolysis assay

Fresh blood was obtained from a rabbit. Red blood cells (RBCs) were isolated from plasma using a refrigerated centrifuge at 1500 rpm for 15 min at 4 °C. The RBCs were further washed three times with sterile PBS by centrifugation until the supernatant was clear. Then 100 μl of the obtained particle suspensions in PBS at concentrations of 12.5, 25, 50, 100 and 200 $\mu\text{g ml}^{-1}$ were added to 100 μl of the RBC suspension. The mixtures were incubated at 37 °C for 1 h under constant shaking,

and subsequently centrifuged at 1500 rpm for 15 min. After the treatment, 100 μ l of supernatant from each centrifuge tube was used to analyse haemoglobin release, using a microplate reader at the wavelength of 576 nm. Control experiments were performed under the same experimental conditions. 100 μ l of the RBC suspension was added to 100 μ l of PBS (as a negative control) and to 100 μ l of 0.5 % Triton X-100 (as a positive control). The percentage haemolysis was calculated using the following equation (He et al. 2012):

$$\text{Haemolysis(\%)} = \frac{\text{OD}_{576 \text{ sample}} - \text{OD}_{576 \text{ negative control}}}{\text{OD}_{576 \text{ positive control}} - \text{OD}_{576 \text{ negative control}}} \times 100\% \quad (2.7)$$

where $\text{OD}_{576 \text{ sample}}$, $\text{OD}_{576 \text{ negative control}}$ and $\text{OD}_{576 \text{ positive control}}$ are the optical densities of haemoglobin released from RBCs treated with, respectively, nanoparticles, PBS buffer and medium containing 0.5 % Triton X-100.

2.2.8 Photo-killing effect

The photo-killing effect of $\text{TiO}_2\text{-SiO}_2$ nanoparticles on L929 cells was examined as follows. L929 cells, at the density of 1×10^4 cells per well, were seeded in a 96-well plate in RPMI-1640 medium (Lonza) and incubated overnight, in the dark, with 5% CO_2 and a humidified atmosphere. Then, the medium was replaced with the medium containing P25 or TS1 nanoparticles, each at concentrations of 12.5 and 25 $\mu\text{g ml}^{-1}$. A control experiment was conducted using cells treated with the medium containing no particles. After 24 h, the cells were exposed to UV light (365nm, 50W) for 20 min. The cells were incubated for another 24 h in the dark and then the viability of the cells was tested using the MTS assay as described above. The cell viability was expressed as the ratio of the number of viable cells remaining after UV irradiation to those present in the samples without UV irradiation.

2.2.9 Statistical analysis

The experimental data of the aforementioned cellular work were analysed utilizing the Student's T-test and the results were presented as mean \pm standard

deviation. The standard deviation values were expressed as error bars. Statistical significance was considered at a probability of $p < 0.05$.

2.3 Results and Discussion

2.3.1 Characterisation of P25 and TS1-4

Four core-shell structured $\text{TiO}_2\text{-SiO}_2$ nanoparticles, TS1, TS2, TS3 and TS4, were synthesised via the Stöber method using varying ratios of P25 and tetraethoxysilane (TEOS). FESEM images showed that the resultant nanoparticles were sphere-like and slightly bigger than P25 (Fig. 2.3). The analysis of 30 particles from each of the FESEM images indicated that the non-coated TiO_2 (P25) had a mean diameter of 24 ± 1 nm, which is in agreement with the product specification provided by the supplier. The coated particles were about 35 ± 2 nm, 39 ± 1 nm, 42 ± 2 nm and 46 ± 2 nm for TS1, TS2, TS3 and TS4, respectively, indicating an increased shell thickness of 5.5 nm, 7.5 nm, 9 nm and 11 nm in TS1-4. The gradual increase in the particle size, and therefore the shell thickness, was due to the increase of TEOS concentration (Si/Ti ratio) in the reaction mixtures.

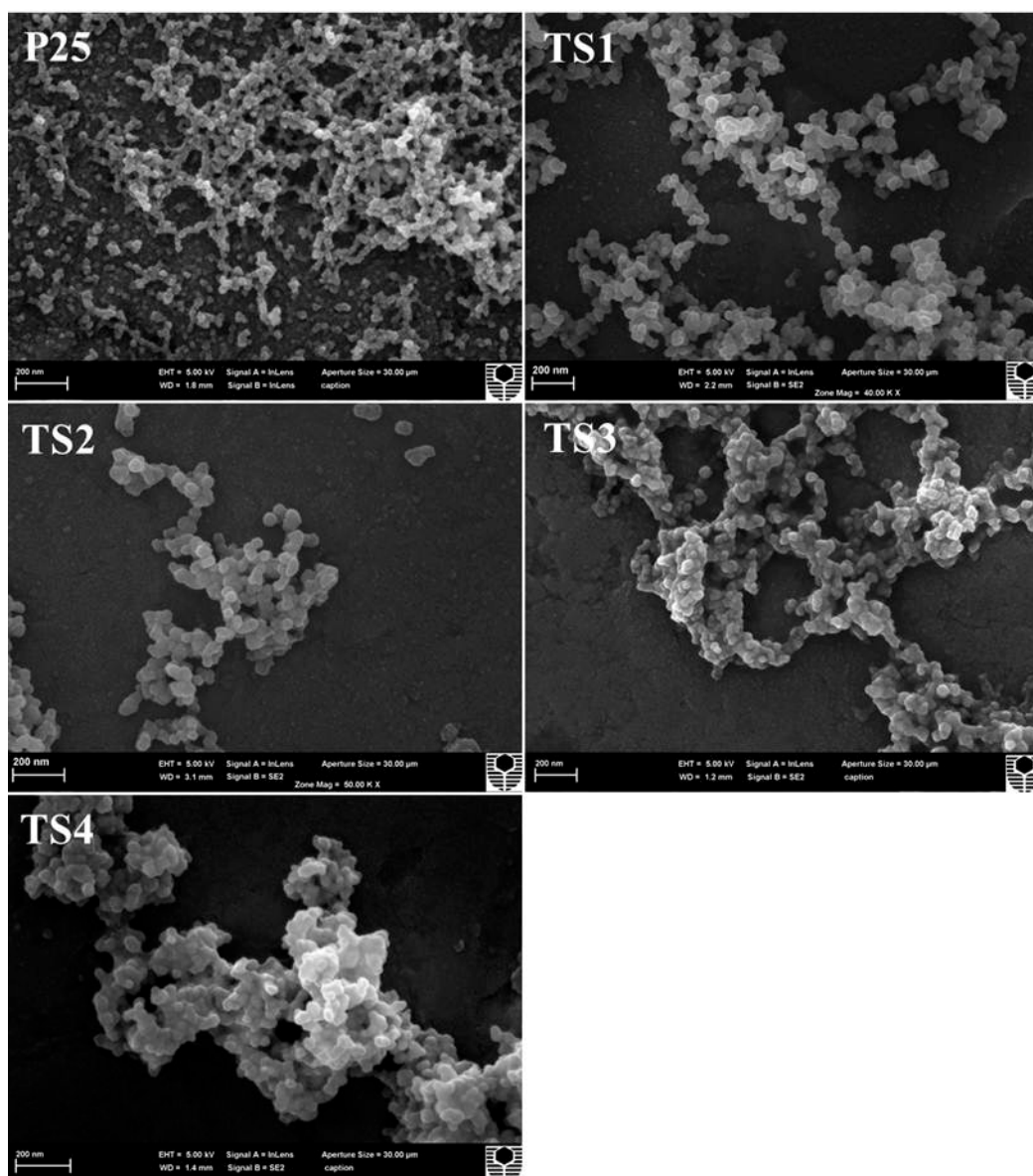


Fig. 2.3 FESEM micrographs of non-coated TiO_2 (P25) and silica-coated TiO_2 (TS1-4) nanoparticles.

The TEM micrographs in Fig. 2.4 (top) further demonstrate the core-shell structure of the TiO_2 - SiO_2 nanoparticles. EDS analysis of TS1 indicated the presence of silica on the surface of the TiO_2 nanoparticles (Fig. 2.4 bottom).

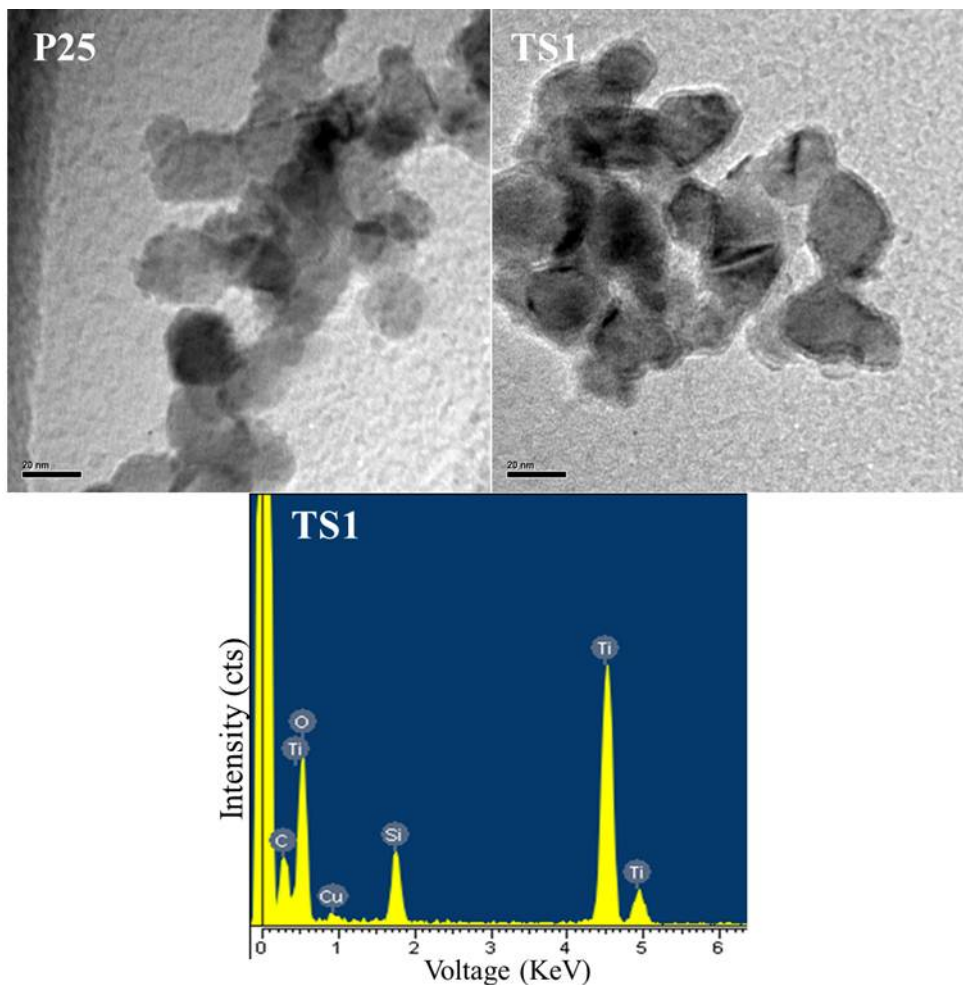


Fig. 2.4 TEM images of P25 and TS1 (top), showing the core-shell structure of TS1. EDS of TS1 (bottom), showing the presence of elemental Ti, Si and O. Cu is from the copper grid and C is from both TS1 and the carbon film coated on the copper grid.

Further analysis of these nanoparticles using FTIR, shown in Fig. 2.5, confirmed the formation of the silica network through the strong adsorption peaks at 1065 and 1180 cm^{-1} which correspond to the asymmetric Si-O-Si bending and stretching vibrations, respectively. The peak at 1625 cm^{-1} is attributed to O-H bending vibration of the surface silanol group of the silica gel (-Si-O-H groups). There is also a weak adsorption peak at 950 cm^{-1} , attributed to the flex vibrations of Si-O-Ti, indicating that the TiO_2 core is connected to the silica shell through a chemical bond (Ogura et al. 1999). The weak peaks at 2920 and 2853 cm^{-1} arise from the symmetric and asymmetric stretching vibrations of the $-\text{CH}_2$ and $-\text{CH}_3$ groups, which indicate the presence of the intermediate reaction product $(\text{OR})_3\text{Si}(\text{OH})$ ($\text{R} = -\text{CH}_2\text{CH}_3$) (Eqs. 2.7 and 2.8) (Hong et al. 2006, Crişan et al. 2008). As shown in Fig. 2.5, these peaks are

generally stronger in the coated TiO₂ containing the higher silica component. The strong signals at approximately 650 and 500 cm⁻¹ are due to the Ti-O stretching vibration, confirming the presence of TiO₂ in the nanoparticles (José Velasco et al. 1999, Siddiquey et al. 2008).

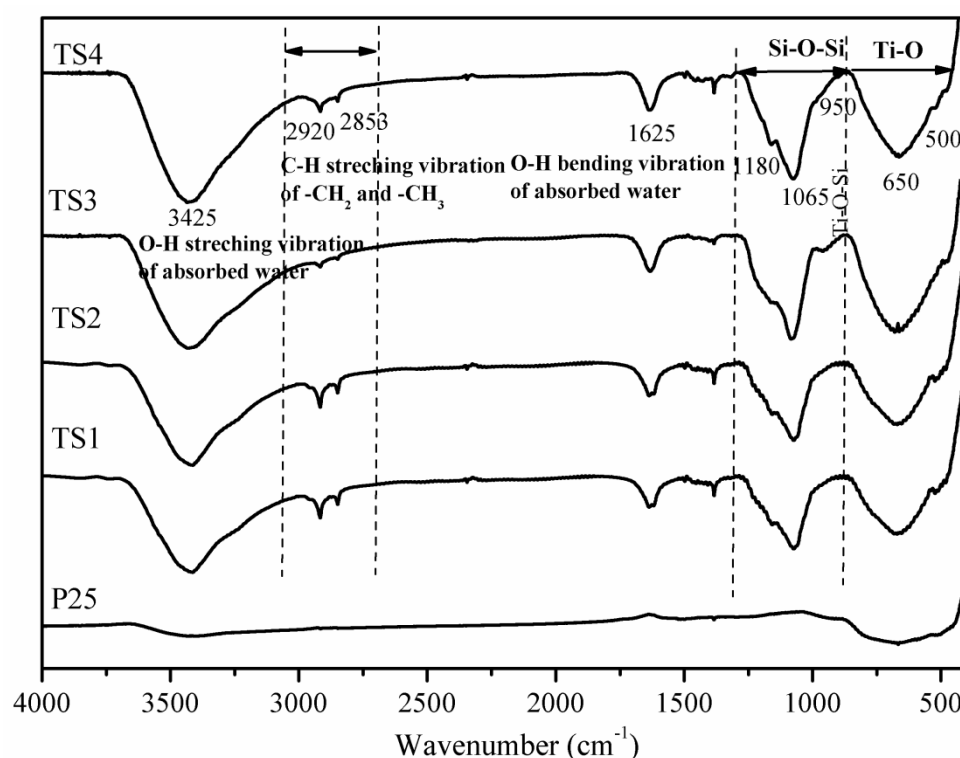


Fig. 2.5 FTIR spectra for P25 and TS1-4.

UV-Vis DRS analysis, presented in Fig. 2.6, showed that the absorption threshold of P25 is 410 nm. The corresponding band gap energy was 3.02 eV, which is in agreement with the reported value (Xu et al. 2008). After coating with silica, there was a slight red-shift. The adsorption thresholds of TS1-4 were shifted to 411, 411.2, 412.6 and 413.7 nm, respectively. There were only 2.7 nm differences between the TSX samples and 1-3.7 nm differences between the P25 and the TSX. Accordingly, the band gap energy was narrowed down to 2.99-3.01 eV. The changes

were due to the dielectric constant of the surrounding matrix upon encapsulation. A similar observation was reported by Liz-Marzán in their work on silica-coated gold nanoparticles (Liz-Marzán et al. 1996).

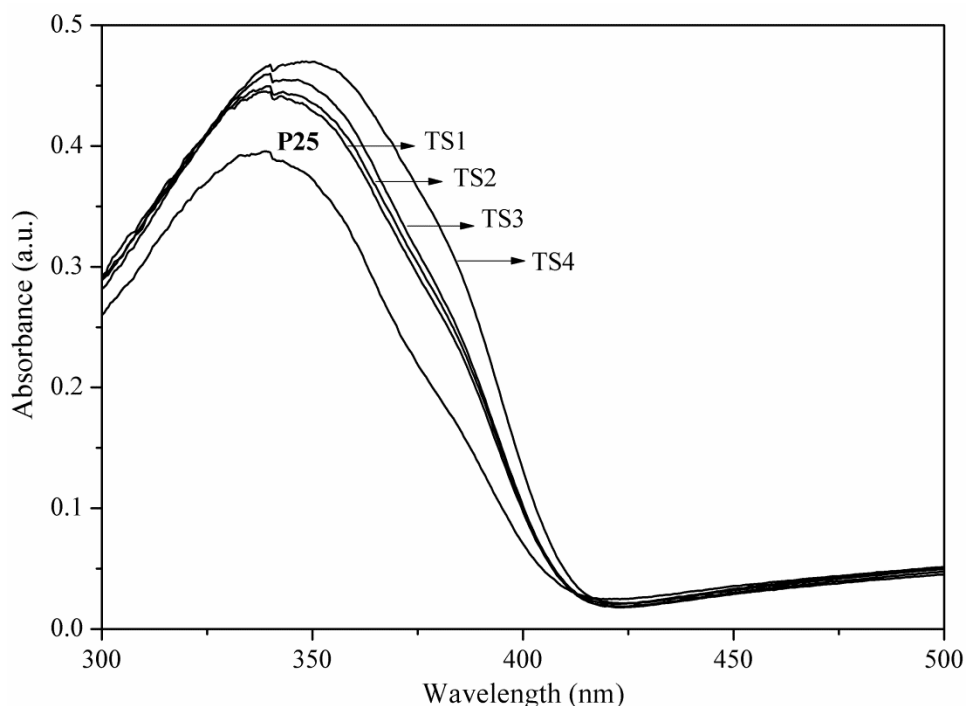


Fig. 2.6 UV-Vis spectra of P25 and TS1-4.

2.3.2 Photocatalytic reactivity of P25 and TS1-4

The photodegradation reaction of phenol was carried out in the presence of P25 and TS1-4, using a concentration that was equivalent to 1.0 g L^{-1} P25. As shown in Fig. 2.7, 94.5% of phenol was degraded after 60 min of irradiation when P25 was used. When TS1-4 were used, the phenol degradation yields were reduced to 86.6, 58.7, 50.5 and 36.7%, respectively, indicating a reduction in photocatalytic reactivity of the coated TiO_2 nanoparticles. The apparent degradation rate constant of these nanoparticles was estimated using the Langmuir-Hinshelwood equation (Sun et al. 2009):

$$\ln \frac{c}{c_0} = -\kappa t \quad (2.10)$$

where k is the apparent reaction rate constant in the unit of time^{-1} , C_0 is the initial concentration and C is the concentration at time t .

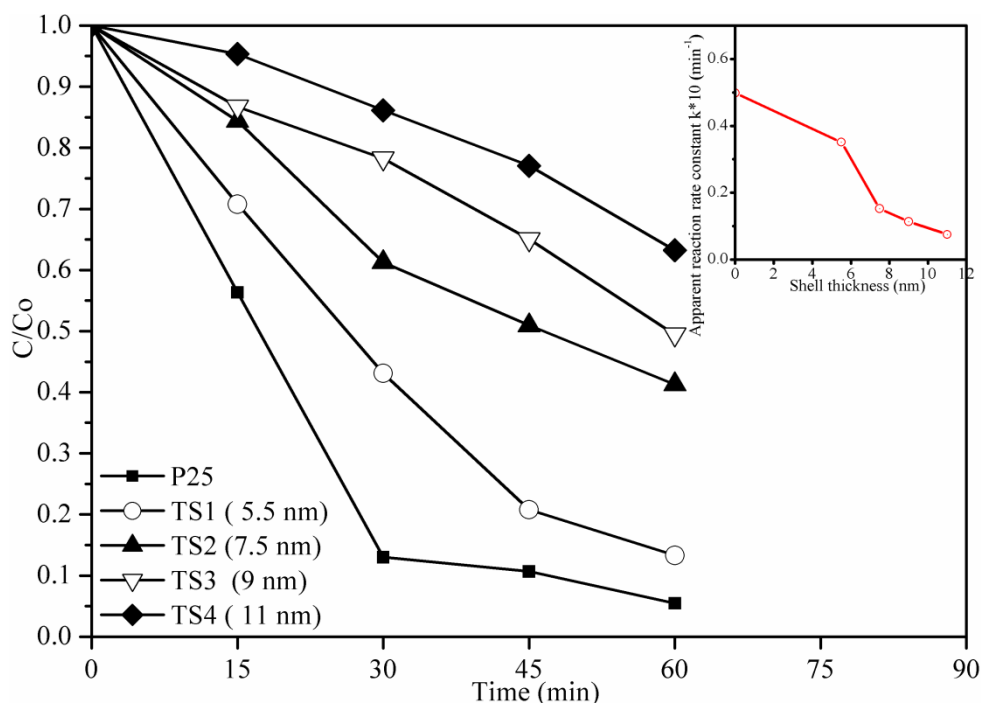


Fig. 2.7 Phenol concentration change with time (Insert: degradation rate change with shell thickness).

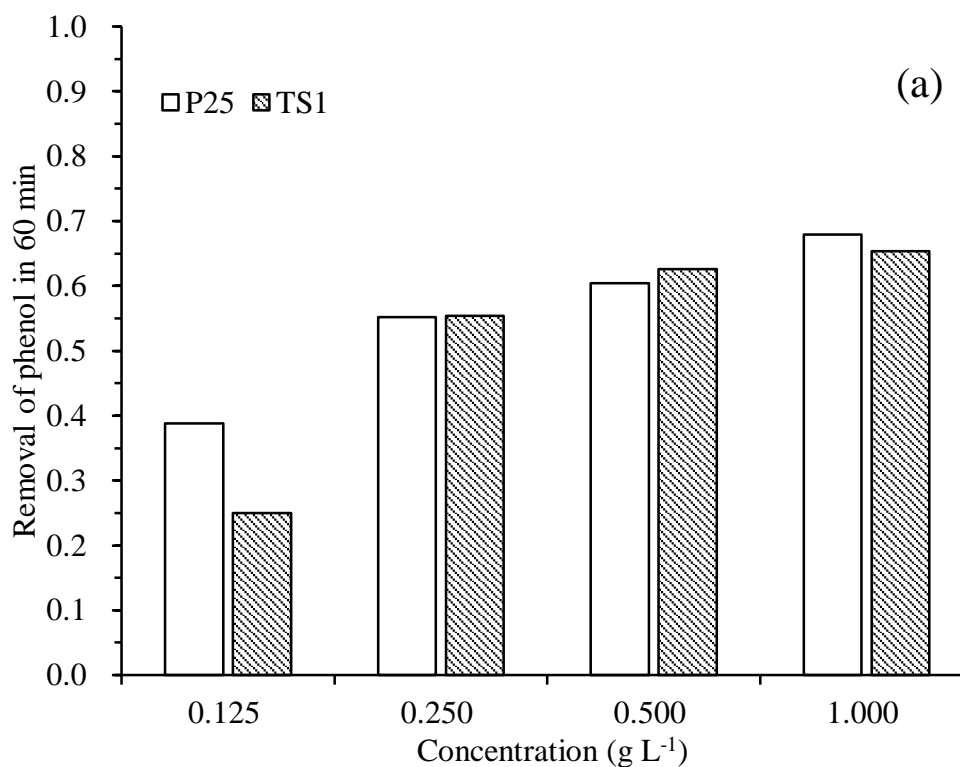
The computed k values for P25, TS1, TS2, TS3 and TS4 were 0.0498, 0.0351, 0.0152, 0.0113 and 0.0075 min^{-1} , respectively, indicating a rapid decrease in the photodegradation rate with increase in shell thickness (Fig. 2.7 insert). The reduced photocatalytic reactivity can be attributed to the shielding effect of the silica shell formed on the surface of TiO_2 nanoparticles. That is to say that the silica shell acted as a barrier to prevent the migration of reactive radicals to the surface of the nanoparticles, which led to a decrease of active radicals $\text{O}_2^{\bullet-}$ and $\text{OH} \bullet$ for the oxidation of phenol (Siddiquey et al. 2012). It should be noted that the calculation was carried out using the experimental data up to 60 min. The least squared R values for each fitting were 0.95, 0.99, 0.99, 0.97 and 0.96. When the reaction was extended to 90 min, phenol degradation results for P25, TS1, TS2, TS3 and TS4 were 99.9, 97.6, 87.5, 78.7 and 58.9%, respectively. This indicates that, with a slight increase in

reaction time, TS1 (with a shell thickness of 5.5 nm), is able to yield a complete photodegradation of phenol, similar to P25.

A similar reaction was conducted in the presence of TS1 and P25 with a fixed catalyst concentration (1.0 g L^{-1}) while phenol concentration was increased from $20 \text{ }\mu\text{g ml}^{-1}$ to $50 \text{ }\mu\text{g ml}^{-1}$. At 60 min, the removal of phenol was 68.0% for P25 and 65.4% for TS1, indicating a less than 5% reduction. The calculated apparent reaction rate constants for P25 and TS1 were $0.0195 \text{ (R}^2=0.94)$ and $0.0168 \text{ min}^{-1} \text{ (R}^2=0.97)$, a less than 14% reduction. This further demonstrated that the shell thickness can be controlled to the least so that the effect can be eliminated. In addition, it is noted that the phenol degradation rate depended on its initial concentration. As the phenol concentration increases, the degradation rate decreases. When phenol concentration was $20 \text{ }\mu\text{g ml}^{-1}$, 86.6% removal was achieved using TS1 as the catalyst. Only 65.4% was achieved when the initial concentration was $50 \text{ }\mu\text{g ml}^{-1}$. The decrease in the degradation yield with the increase of initial phenol concentration can be explained in the following two features. With the same amount of catalyst (1.0 g L^{-1}), the catalytic sites on the surface of TS1 are limited. A further increase in phenol concentration provides an excess amount of reaction intermediate to be degraded, which consequently competes with phenol molecules for the catalytic sites on the TS1 surface. Also the produced reaction intermediate can compete with OH⁻ absorbed onto the catalytic sites, leading to the reduced amount of •OH radicals involved in the photoreactivity experiments (Wei and Wan 1991). It is same for P25, the non-coated TiO₂, in which 94.5% phenol was degraded when the concentration was $20 \text{ }\mu\text{g ml}^{-1}$, whilst only 68.0% phenol degraded when the concentration was increased to $50 \text{ }\mu\text{g ml}^{-1}$.

To investigate the effect of catalyst concentration, the amount of catalyst was changed with the fixed concentration of phenol solution ($50 \text{ }\mu\text{g ml}^{-1}$). Fig. 2.8a shows the effect of varying catalyst concentration on phenol degradation during the photocatalytic reaction. When the catalyst concentration is at 0.125, 0.25, 0.50 and 1.0 g L^{-1} , the phenol degradation for TS1 is 25.0, 55.4, 62.6 and 65.4%, respectively, after 60 min of irradiation, while that for P25 is 38.8, 55.2, 60.4 and 68.0%. The variation in apparent rate constant of phenol against the catalyst concentration also was determined (Fig. 2.8b). It was found that the rate constant increases with

increasing concentration of TS1 and then approaches a limiting value. The increase in the degradation rate of phenol was due to the increase in the total number of catalytic sites available for photocatalytic reaction as the catalyst concentration increased. However, when catalyst concentration reaches saturation, the number of active sites is maintained at a constant value, which may be due to aggregation at higher concentrations of catalyst leading to a reduction of active sites on the catalyst's surface (Chen and Ray 1998, Vohra and Tanaka 2003). In addition, light penetration can be prevented due to the high concentration of catalysts (Bekkouche et al. 2004). A similar result was observed when P25 was used as the catalyst. In this study, the optimum concentration of TS1 and P25 is 1.0 g L^{-1} . Based on these observations, TS1, TS4 and P25 nanoparticles were selected for the cytotoxicity, haemocompatibility and photo-killing investigations.



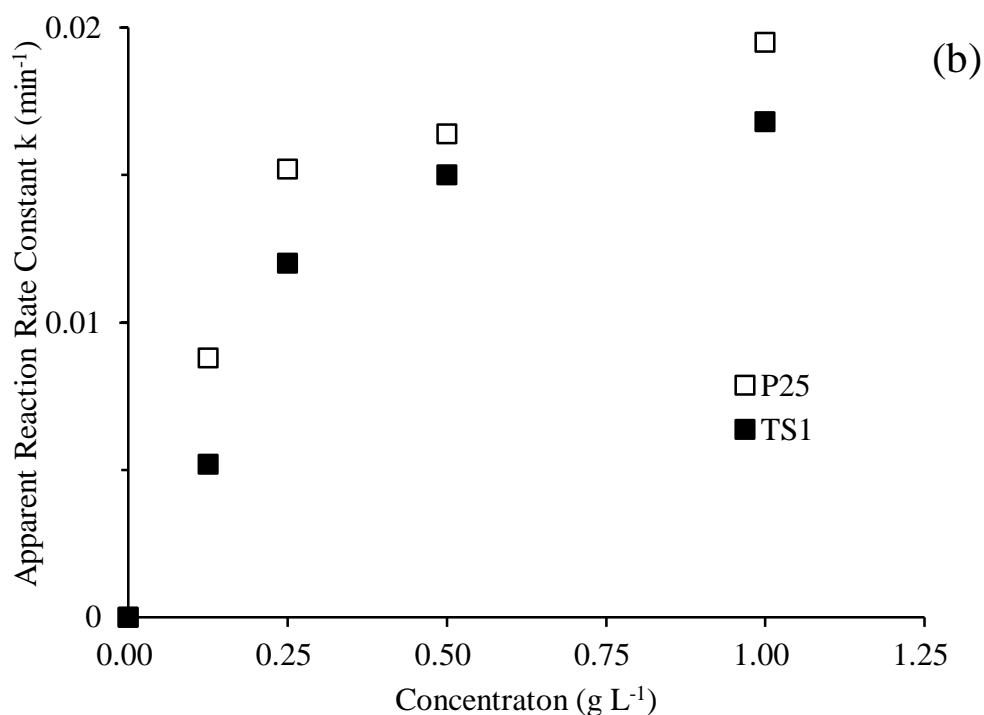


Fig. 2.8 Effect of catalyst dosage on (a) phenol degradation efficiency and (b) apparent reaction rate of phenol.

2.3.3 Cytotoxicity and haemocompatibility of P25, TS1 and TS4

The MTS assay was employed to determine the viability of L929 cells treated with P25 (the non-coated TiO₂ nanoparticles), TS1 and TS4 (the silica-coated TiO₂ nanoparticles) of varying concentrations (12.5, 25, 50, 100 and 200 µg ml⁻¹). The culture was carried out in the dark for various time intervals. Results are shown in Fig. 2.9. When the nanoparticle concentration was below 200 µg ml⁻¹, the viability was generally the same for both untreated cells and cells treated with P25, TS1 and TS4. Incubation for 6 h or 24 h did not make any difference. When the concentration of nanoparticles was increased to 200 µg ml⁻¹, no significant difference in cell viability was observed at 6 h. However, when the incubation time was extended to 24 h, the viability of P25-treated cells was reduced to 82.0% (relative to control) ($p < 0.05$), whilst the viabilities of TS1- and TS4-treated cells were 96.5% and 100%, suggesting a much lower cytotoxicity of the silica-coated nanoparticles. This can be attributed to the silica coating being cytocompatible.

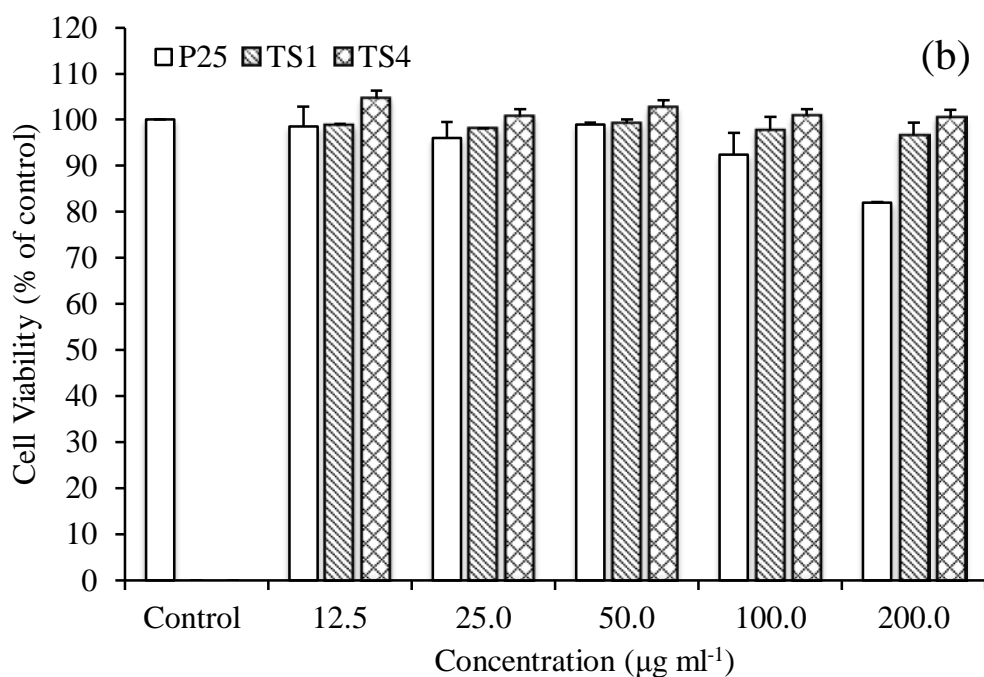
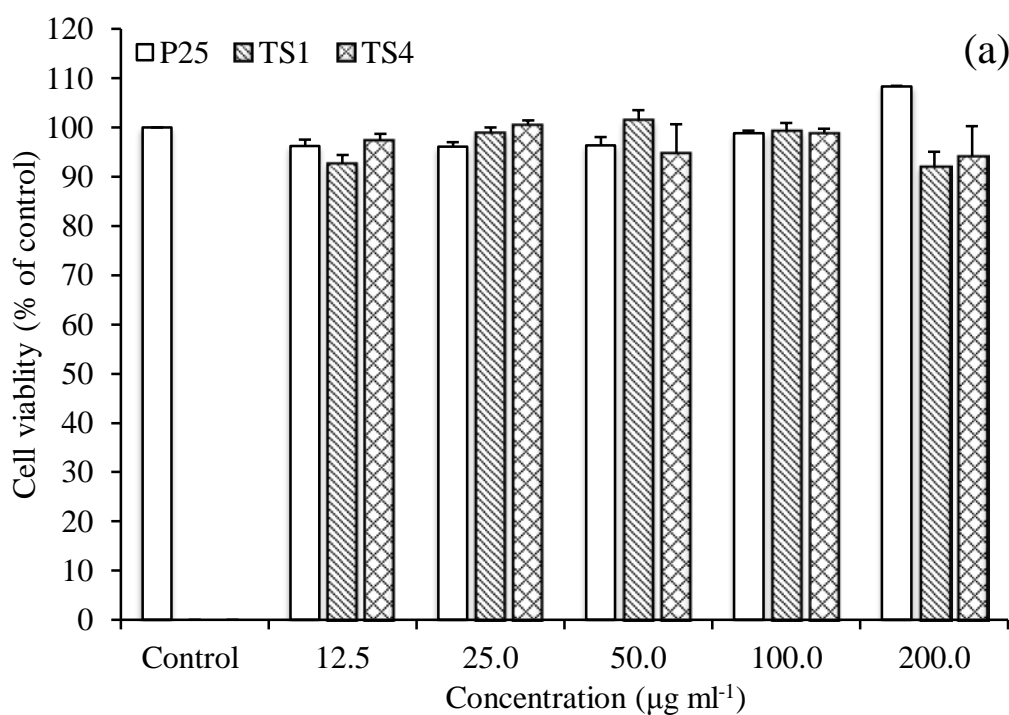


Fig. 2.9 Cell viability after treatment with P25, TS1 and TS4 for (a) 6 h and (b) 24 h. * $p < 0.05$ as compared to control (untreated) cells. ** $p < 0.05$ as compared to the P25 treated cells. All data are expressed as the mean \pm SD and $n = 3$.

The optical micrographs (Fig. 2.10) of the P25-treated cells, the TS1-treated cells and the TS4-treated cells at 24 h further confirm the results obtained from the MTS

assay. As shown in Fig. 2.10(b), there was a portion of red-stained nuclei in the cell culture, indicating that the cells had undergone apoptosis after exposure to P25 nanoparticles. However, under the same conditions, there were scarcely any red-stained nuclei in both control cells (Fig. 2.10(a)) and those treated with TS1 and TS4 nanoparticles (Fig. 2.10(c) and 2.10(d)). A similar result was reported by Mbeh et al. in a biocompatibility study of silica-coated magnetite nanoparticles. They have concluded that a silica shell significantly reduced the cellular toxicity of pure magnetite nanoparticles (Mbeh et al. 2012).

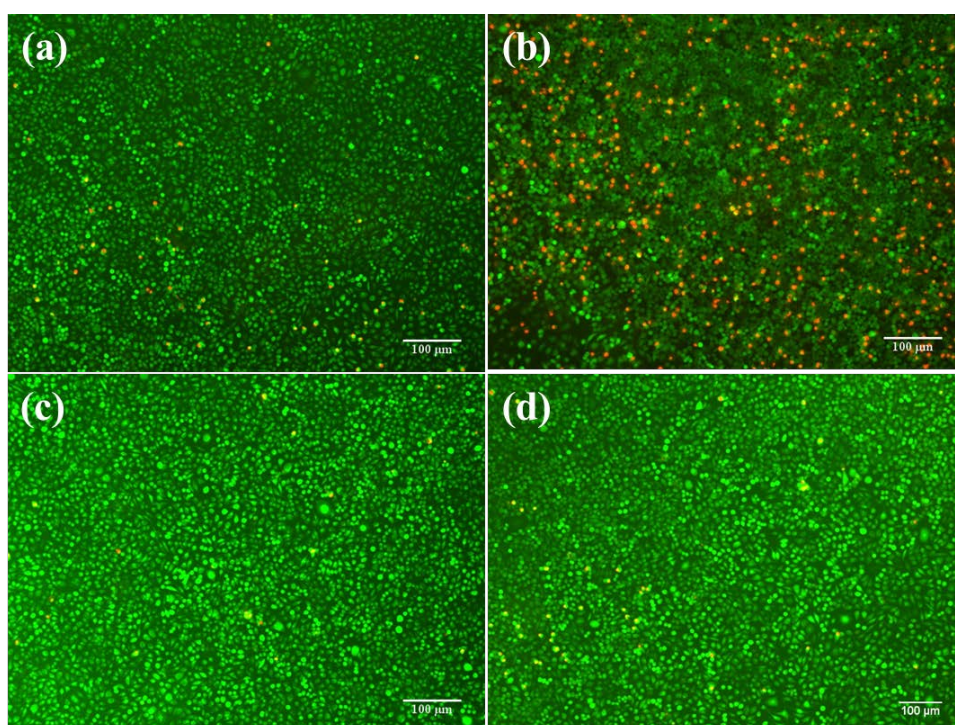


Fig. 2.10 Light micrographs of L929 cells treated with (a) no nanoparticles, (b) P25, (c) TS1, and (d) TS4. Incubation time = 24 h. Nanoparticle concentration = $200 \mu\text{g ml}^{-1}$.

In vitro haemolysis assays of P25 and TS1 were conducted at the same concentration range. A Triton X-100 was used to induce full haemoglobin release. As shown in Fig. 2.11, the haemolysis percentages were well below 5.0% across the range of investigated concentrations. This indicates that P25, TS1 and TS4 exhibit excellent haemocompatibility and can be further used *in vivo*.

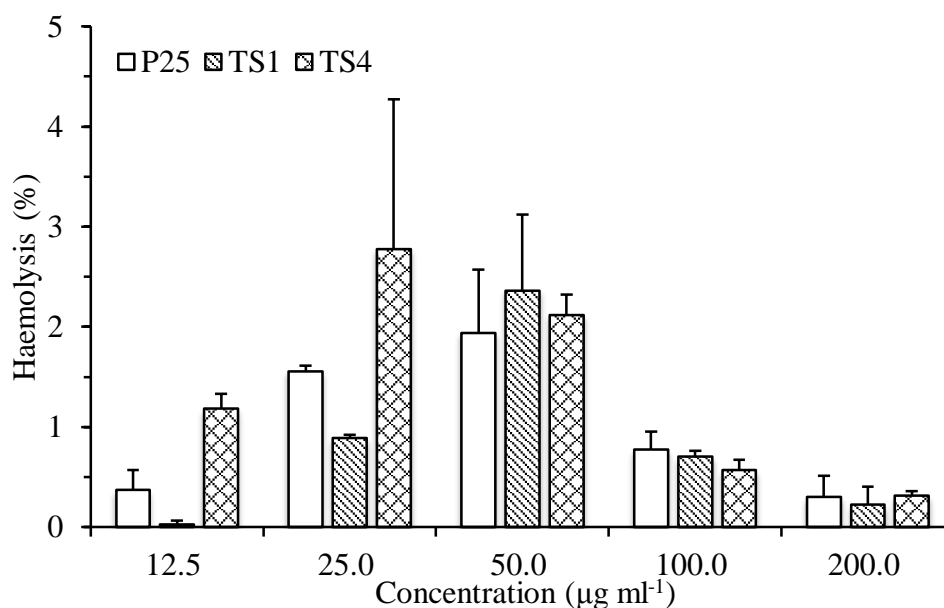


Fig. 2.11 Haemolysis assays of P25, TS1 and TS4 nanoparticles. All data are expressed as the mean \pm SD and n=3.

2.3.4 Photo-killing effect of P25 and TS1

In order to select an appropriate UV exposure time, the effect of UV irradiation on L929 cell viability was first tested. Fig. 2.12 shows that the surviving fraction of L929 cells generally decreased with increasing irradiation time. When the irradiation time was over 40 min, the surviving fraction of L929 cells was only 15.5%, suggesting UV irradiation is harmful to L929 cells. At 20 min, the surviving fraction of L929 cells was 90.2%, showing a small suppression in cell proliferation. Based on these results, the photo-killing effects of P25 and TS1 nanoparticles were evaluated through the comparison of the viability of non-treated cells, with those of cells treated with P25 or TS1, after UV irradiation for 20 min. As shown in Fig. 2.13, the viability of the L929 cells was 90.2% relative to that of cells without exposure to the UV light. However, the viability of L929 cells was reduced to 58.6% and 66.3% in the presence of 12.5 $\mu\text{g ml}^{-1}$ of P25 and TS1, respectively, and further, to 56.5% and 58.9%, when the concentration of the nanoparticles was increased to 25.0 $\mu\text{g ml}^{-1}$. In comparison to the untreated cells, a statistically significant ($p < 0.05$) photo-killing effect of both P25 and TS1 on L929 cells was demonstrated. P25 was slightly more powerful in killing the L929 cells at 12.5 $\mu\text{g ml}^{-1}$. However, the killing effect became almost the same ($p < 0.05$) when the nanoparticle concentration was increased to

25.0 $\mu\text{g ml}^{-1}$. It should be noted that the relative concentration of TiO_2 in TS1 is 90% of the apparent concentration in this experiment. These results further suggest that TS1 and P25 exhibit a similar photokilling effect on L929 cells under UV irradiation.

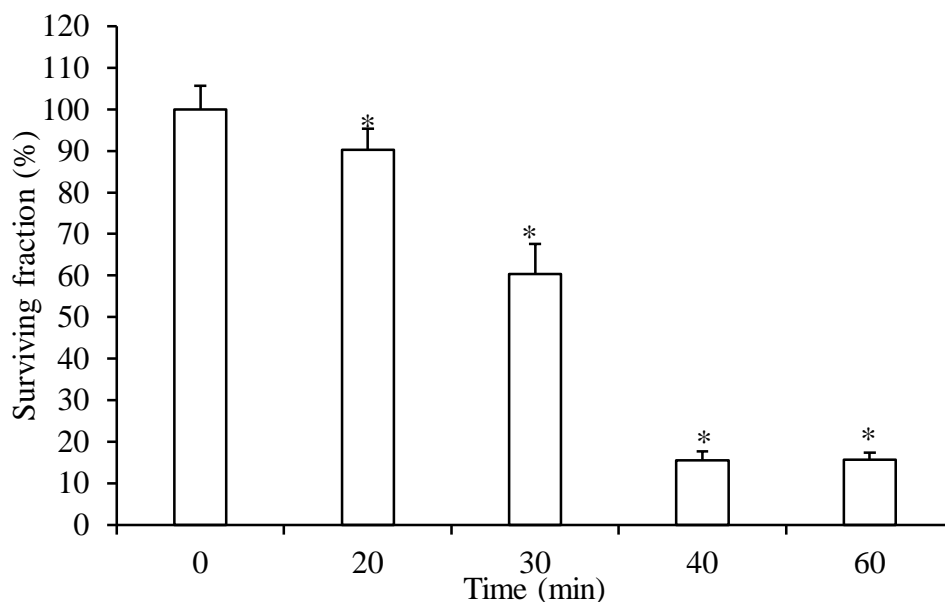


Fig. 2.12 Effect of UV irradiation time on viability of L929 cells. * $p < 0.05$ as compared to cells without UV irradiation. All data are expressed as the mean \pm SD and $n = 4$.

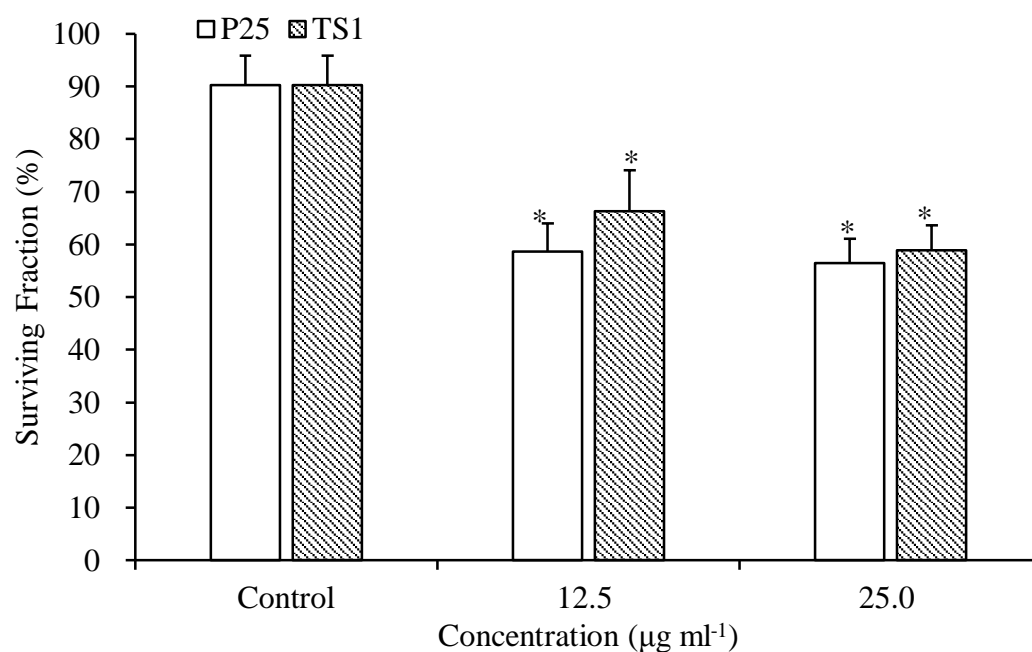


Fig. 2.13 Effect of photoexcited TiO_2 and $\text{TiO}_2\text{-SiO}_2$ nanoparticles on cell viability. Irradiated time was 20 min. * $p < 0.05$ as compared to control. All data are expressed as the mean \pm SD and $n = 4$.

2.4 Conclusions

In summary, core-shell structured $\text{TiO}_2\text{-SiO}_2$ nanoparticles of varying shell thicknesses were synthesised via the Stöber method using varying ratios of titanium dioxide and tetraethoxysilane (TEOS). FESEM images demonstrated that, with an increase in the concentration of TEOS in the reaction mixture, the particle size of $\text{TiO}_2\text{-SiO}_2$ nanoparticles, and therefore the silica shell thickness, increased. The core-shell structure of silica-coated TiO_2 nanoparticles was further confirmed using TEM/EDS examinations. FTIR analysis indicated the formation of Ti-O-Si chemical bonds on the surface of TiO_2 nanoparticles. A decrease in photocatalytic activity was evident after the TiO_2 nanoparticles were coated with silica. A series of reaction parameter studies, such as phenol concentration and catalyst dosage, have been performed to determine the optimum operating parameters of the phenol degradation process using non-coated (P25) and silica-coated TiO_2 (TS1) nanoparticles. The results showed that the optimal phenol concentration is $20 \mu\text{g ml}^{-1}$ and the optimal catalyst concentration is 1.0 g L^{-1} .

The influence of the silica-shell thickness on the cytotoxicity of the TiO_2 nanoparticles also was investigated. It was found that the presence of a silica shell improved the compatibility of TiO_2 nanoparticles with L929 cells. Both silica-coated TiO_2 nanoparticles and non-coated TiO_2 nanoparticles exhibited good haemocompatibility. When the silica thickness was about 5.5 nm, the coated TiO_2 nanoparticles retained a high level of photodynamic activity compared to the non-coated TiO_2 nanoparticles. The well-maintained photoreactivity of TiO_2 in $\text{TiO}_2\text{-SiO}_2$ nanoparticles was further demonstrated in cellular work, in which both P25 and TS1 were able to reduce the viability of L929 cells to below 60% after a 20 min UV irradiation. Based on the results, the silica-coated TiO_2 nanoparticles with optimal shell thickness have been further modified with folic acid as a targeting ligand for further investigation, and the details are outlined in Chapter 3.

CHAPTER 3 INVESTIGATION OF CELL COMPATIBILITY, PHOTOTOXICITY AND CELL INTERNALISATION OF FOLIC ACID CONJUGATED TiO₂ NANOPARTICLES

3.1 Introduction

This chapter reports the synthesis, the physicochemical characterisation, and the cellular toxicity and phototoxicity of folic acid-conjugated TiO₂ nanoparticles. The TiO₂-SiO₂ (TS) nanoparticles that had demonstrated optimal photocatalytic reactivity in the experiments outlined in Chapter 2 were chosen for this study.

3.1.1. Background

As discussed in Chapter 1, photodynamic therapy (PDT) offers better selectivity for cancerous cells and has been used for the treatment of various cancers and other diseases (Bae and Na 2010). It involves the administration of a photosensitiser (PS), either by systemic or topical application, and subsequent initiation of exposure to light to produce singlet oxygen that kills the cancer cells. There are three essential components that are involved in PDT: a PS drug, light with a specific wavelength and oxygen (Konan et al. 2002). Upon exposure to light, the PS is activated from a singlet ground state (S₀) to a singlet excited state (S₁). Due to a short lifetime (nanoseconds), the PS at S₁ can release energy, either via a non-radiative process in the form of heat or through a radiative process in the form of fluorescence. The PS at S₁ may be converted to the triplet state (T₁) via an intersystem crossing (ISC). The PS at T₁ that has a relatively long lifetime can react with molecular oxygen to form reactive oxygen species (ROS), such as singlet oxygen (¹O₂), that are chemically highly active oxidizers. The interactions between ROS and cell membranes lead to cancer cell death via the mechanisms of apoptosis or necrosis (Dolmans et al. 2003). In addition to directly killing tumour cells, ROS also could damage the blood vessels that supply the oxygen and nutrients to the tumour, leading to tumour shrinkage (Henderson and Dougherty 1992). It has been reported that the average lifetime of ROS is approximately 3 μs, which indicates that they can diffuse over a distance of

between 10 and 20 nm (Hatz et al. 2007). Thus, the effect of ROS on the diseased tissue is limited to the position where the PSs are concentrated. Compared to conventional cancer therapy, the major advantages of PDT are that the PS is of low toxicity to normal tissue or cells in the dark and activation by light alone permits minimal damage to cells (Davids and Kleemann 2011). Since the photodynamic effect of PDT is through the combination of light and PS, PDT can provide dual-selectivity through accumulation of PS in cancer cells only, via cell-specific targeting, and by selectively delivering light to tumour cells (Master et al. 2013).

Currently, the most commonly used PSs are porphyrinoid-based and non porphyrinoid-based (Yano et al. 2011). As the first generation of PSs, haematoporphyrin (Hp) and its derivative (HpD) accumulated at tumour cells have shown promising results in photo-killing tumour cells. However, they have some disadvantages, such as complicated chemical compositions which involve over sixty compounds, lack of tumour-targeting ability and long-lasting skin phototoxicity after treatment (Dougherty et al. 1998). For those reasons, the second generation of PSs involving porphines, phthalocyanines (PCs) and protoporphyrin IX have been developed and examined *in vivo* and *in vitro*. More details have been discussed in recent review papers (Allison and Sibata 2010, Yano et al. 2011). Although great efforts have been made, these organic PSs have some significant shortages including easy aggregation and shortness of stability in biological environments, resulting in a decrease in the yield of singlet oxygen (Lopez et al. 2010). In addition, they exhibit limited tumour specificity (Zhang et al. 2012b). To overcome these problems, a new generation of nano-semiconductor-based PSs, such as TiO₂, have attracted increasing attention.

Titanium dioxide (TiO₂), as a semiconductor nanomaterial, has been considered as a potential PS due to exhibiting its unique properties of no dark toxicity *in vitro* and *in vivo*, high stability in biological environments and strong oxidising ability (Cai et al. 1992). TiO₂ presents a band-gap energy of 3.0 eV. Upon the absorption of a photon with energy that is equal to or higher than this value, TiO₂ can be excited to produce negative electrons in the conduction band, leaving positive holes in the valence band. These charge carriers react with surrounding water or oxygen to yield cytotoxic reactive oxygen species (ROS) such as hydrogen peroxide and superoxide. Both the generated holes and ROS are strong oxidisers that can attack both cell

membranes and cellular components, leading to apoptosis of cancer cells (Feng et al. 2013). TiO₂ nanoparticles also have been proven to be effective in preventing drug efflux caused by multi-drug resistance (MDR), leading to selective accumulation of TiO₂ at the tumour site (Song et al. 2006, Li et al. 2009a). However, the clinical application of TiO₂ is rather challenging. This is because nano-sized TiO₂ particles, with a high surface area, aggregate easily in biological environments, leading to the decrease in photocatalytic reactivity (Zanella et al. 2002). Moreover, TiO₂ nanoparticles alone have difficulties in conjugating with targeting molecules due to the shortage of functional groups on the surface (Chen et al. 2011). A promising strategy to overcome these problems is to encapsulate TiO₂ within a silica matrix to form nanoparticles with a core-shell structure (Feng et al. 2013). The silica layer can improve dispersion of the core nanoparticles in aqueous solutions, due to its low Van der Waals force of attraction among particles (Kalele et al. 2006). Lee et al. demonstrated that a silica coating improved the dispersion of magnetic nanoparticles that were obtained from wet chemistry (Lee et al. 2008). Also it can act as a shield to protect the core particles from the outer environment. We have demonstrated that silica-coated TiO₂ nanoparticles exhibit improved cell compatibility when compared with pure TiO₂ nanoparticles (Feng et al. 2013). Moreover, silica shell easily can be functionalised using targeting molecules with a high affinity to the diseased tissues that can stimulate receptor-mediated endocytosis (Chaudhuri and Paria 2012).

It is known that the folate receptor (FR), glycosylphosphatidylinositol-anchored cell membrane protein, is expressed at elevated levels on the surface of many human carcinomas, such as in ovarian, uterine, brain, kidney and skin cancers, but it is distributed at a minimal level in most normal tissues (Sanchez-del-Campo et al. 2009, Davids and Kleemann 2011). The amount of FR expression at an advanced stage of cancer is much higher than that at earlier stages of cancer (Konan et al. 2002). For FR, folic acid (FA) with molecular weight of 441.4 g mol⁻¹ is considered to be an ideal targeting ligand. It has demonstrated advantages such as high binding affinity ($K_d \approx 10^{-10}$ mol/L) to FR, easy functionalisation, good stability and compatibility with a number of polar and non-polar solvents, and it is nonimmunogenic (Weitman et al. 1992). It also has been reported that, for FA-conjugated nanoparticles, the protein adsorption on the surface of nanoparticles is limited and the uptake of macrophages by the reticuloendothelial system (RES) is low, thereby rapid systemic filtration by

the biological system is avoided and the residence time of FA-conjugated nanoparticles is prolonged in the body (Huang et al. 2011a, Maity et al. 2013). In addition, these FA-conjugated nanoparticles can initiate specific cancer cell uptake via the form of receptor-mediated endocytosis (Sabharanjak and Mayor 2004). It has been reported that the folate-mediated uptake of FITC/PEI/FA-functionalised silica nanoparticles in HeLa cervical carcinoma cells was around five times higher than that in human embryonic kidney cells. In an FA competition experiment using free FA in culture medium, inhibition of the FA-conjugated nanoparticles' internalisation was observed, meaning that the FA-conjugated nanoparticles were internalised by FR-mediated endocytosis (Rosenholm et al. 2009).

In the chemical structure of FA, there are two types of carboxyl groups: α -carboxyl groups are used to bind with FR, while γ -carboxyl groups react with primary amine groups in the presence of coupling agents to form amide bonds (Guo et al. 1999). The most commonly used coupling agents are N, N'-dicyclohexylcarbodiimide (DCC) or 1-ethyl-3-(3-dimethylaminopropyl)carbodiimide (EDC). The mechanism for combining γ -carboxylic acid with the amine group is schematically illustrated in Fig. 3.1. In this reaction, carboxyl acid **1** reacts with DCC to yield the intermediate, o-acylurea **2**. This intermediate can directly react with a primary amine group to generate the amide **3**. At the same time, it can react with another carboxyl acid to produce carboxyl acid anhydride **5**, which subsequently reacts with a primary amine to form the desired amide **3**. The by-products involve dicyclohexyl urea **4** and N-acylurea **6**. It should be noted that the coupling agents used in this reaction have a short half-life in aqueous solution, resulting in low coupling efficiency, and the intermediate o-acylurea **2** can react with water to form carboxyl acid **1** (Erogbogbo et al. 2011). To improve the coupling yield, NHS-ester of folic acid, NHS-Folate (NHS-FA), is often used for the amide formation reaction. The NHS-FA can be produced from the reaction between N-hydroxysuccinimide (NHS) and folic acid, using DCC as the coupling agent in the presence of triethylamine. The as-prepared NHS-Folate can be decomposed through hydrolysis. The rate of hydrolysis increases in the base solution. Hence, the recommended pH range for the amide formation reaction is between 7.2 and 9 (Lee and Low 1994). The commonly used buffer solution for this reaction is a carbonate and bicarbonate solution.

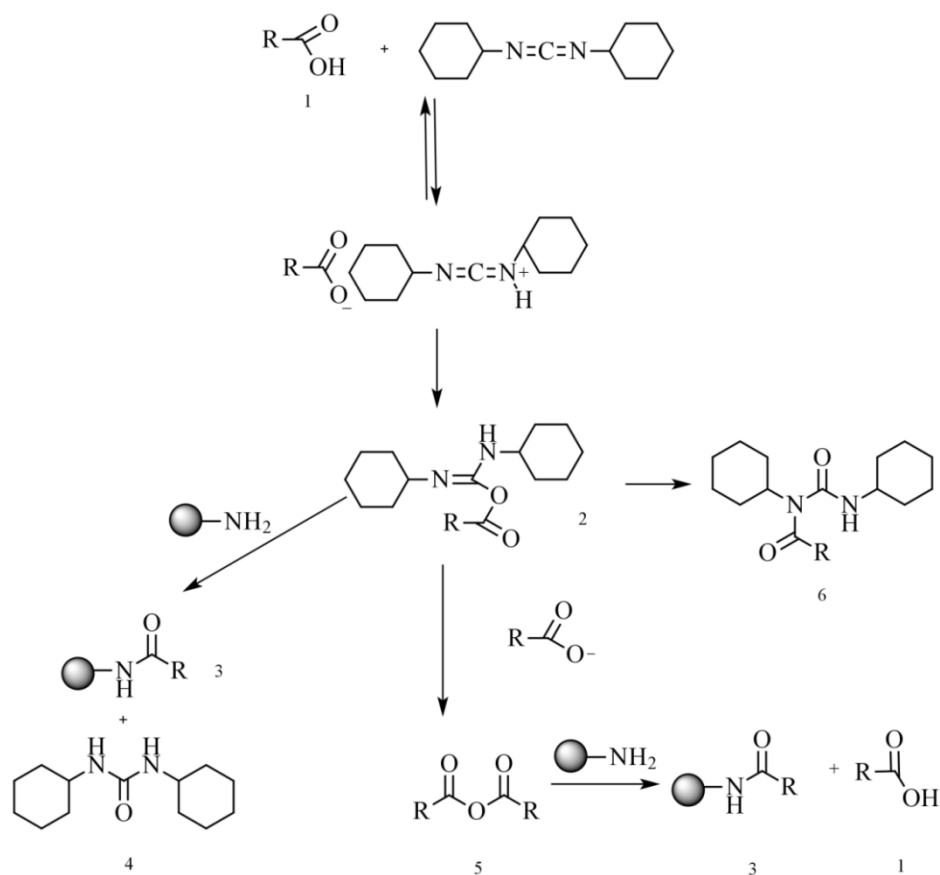


Fig. 3.1 The amide formation process using DCC coupling chemistry (Valeur and Bradley 2009).

In this study, FA-conjugated silica-coated TiO₂ (TS-FA) nanoparticles were prepared according to the reaction equation illustrated in Fig. 3.2. First, the amine-terminated silica-coated TiO₂ (TS-NH₂) nanoparticles were synthesised using a modified Stöber method (Fig. 3.2A). NHS-FA was prepared using the DCC-based coupling reaction (Fig. 3.2B). Then, NHS-Folate was reacted with TS-NH₂ nanoparticles in a buffer solution of carbonate and bicarbonate at pH 9.0 to produce TS-FA nanoparticles (Fig. 3.2C). The chemical and surface properties of the produced compounds were characterised using FTIR spectroscopy, TG/DTA and UV-Vis DRS spectroscopy. The size and morphology of the obtained nanoparticles were examined using a FESEM and an HRTEM. The photocatalytic properties of TS, TS-NH₂ and TS-FA nanoparticles were examined on the basis of photodecomposition of phenol, an organic pollutant that has been used as a model chemical to evaluate photocatalytic activity. For control purposes, the photocatalytic activity of TiO₂ also was evaluated under identical conditions. The cell cytotoxicity,

haemocompatibility and photo-killing effects were assessed according to the procedures described in Chapter 2. Following these experiments, the cell internalisation of TS-FA nanoparticles was evaluated using human nasopharyngeal epidermoid cancer (KB) cells as the positive folate receptor cells. All findings show that the TS-FA potentially can be applied as a photosensitising agent for active targeting of cancer cells.

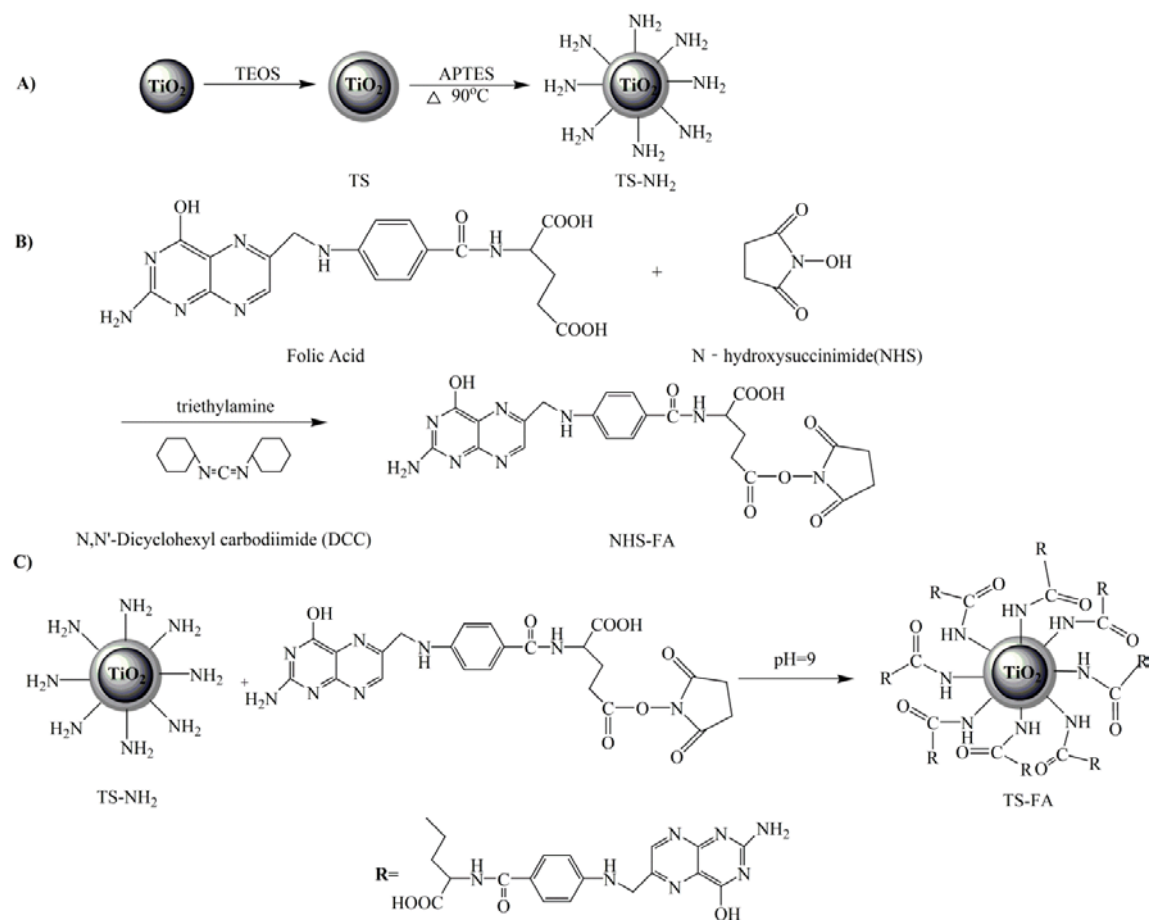


Fig. 3.2 A schematic illustration of the FA-conjugated silica-coated TiO_2 . (A) Amine-functionalised TiO_2 - SiO_2 nanoparticles were fabricated (B) NHS-FA was produced by mixing FA with NHS in the presence of a DCC coupling agent, using triethylamine as the catalyst. (C) The obtained NHS-FA was reacted with TS- NH_2 to generate TS-FA.

3.2 Experimental

3.2.1 Materials

Degussa P25 was purchased from Degussa. Tetraethyl orthosilicate (TEOS, 99.999%), (3-aminopropyl)triethoxysilane (APTES, $\geq 99\%$), absolute ethanol ($\geq 99.5\%$), N-Hydroxysuccinimide (NHS, 98%), N, N'-Dicyclohexylcarbodiimide (DCC, 99%), triethylamine ($\geq 99\%$), folic acid (FA, $\geq 97\%$), sodium carbonate (NaCO_3 , $\geq 99.5\%$) and sodium bicarbonate (NaHCO_3 , 99%) were purchased from Sigma-Aldrich. Diethyl ether anhydrous ($\geq 99.0\%$) and dimethyl sulfoxide (DMSO, 99.9%) were purchased from Alfa Aesar. Milli-Q water was used in all experiments.

3.2.2 Synthesis of amine-functionalised TS hybrid nanoparticles (TS-NH₂)

Amine-terminated $\text{TiO}_2\text{-SiO}_2$ (TS-NH₂) nanoparticles were prepared using the sol-gel method, schematically displayed in Fig. 3.2(A). TiO_2 nanoparticles (0.1 g, 1.3 mmol) were suspended in a solution containing 20 ml of ethanol, 60 ml of Milli-Q water and 1 ml of ammonia solution, using ultrasonic vibration for approximately 30 min. Then, 20 ml of ethanol containing TEOS (40 μl , 0.18 mmol) was added, dropwise, to the mixture under magnetic stirring. This provided a theoretical molar ratio for Si to Ti of 0.14. The reaction was maintained at room temperature for 2 h. TS-NH₂ nanoparticles were subsequently obtained by the addition of 20 ml ethanol solution containing APTES (81 μl , 0.36 mmol), resulting in the molar ratio of APTES to TEOS being 2:1. The reaction mixture was then heated up to 90 °C and kept for a further 2 h. Following this, the reaction mixture was allowed to cool down to room temperature and centrifuged at 7500 rpm for 10 min. The liquid was discarded and the TS-NH₂ nanoparticles were washed three times with 15 ml of ethanol (3 \times 15 ml), followed by three times with 15 ml of Milli-Q water (3 \times 15 ml) and dried overnight at room temperature under vacuum.

3.2.3 Preparation of FA-conjugated TS hybrid nanoparticles (TS-FA)

NHS-ester of folic acid (NHS-FA) was prepared using the DCC coupling reaction, schematically presented in Fig. 3.2(B). In brief, folic acid (5.0 g, 11.3 mmol) and triethylamine (1.8 g, 17.9 mmol) were added to 100 ml of freshly distilled dimethyl sulfoxide (DMSO) at room temperature under constant stirring. After stirring for 2 h, NHS (2.6 g, 22.6 mmol) and DCC (4.7 g, 22.8 mmol) were added to the mixture. The obtained reaction mixture had a molar ratio of 1.0 folic acid: 1.6 triethylamine: 2.0 NHS: 2.0 DCC. The reaction was allowed to proceed overnight in the dark. Then the by-product dicyclohexylurea was removed by filtration and the liquid was concentrated in the presence of reduced pressure and heating. The concentrated liquid (1.5 ml) was dispersed in THF (15 ml) with constant shaking to remove the excess amount of DMSO. Then anhydrous diethyl ether (5 ml) was added into the mixture and the characteristic yellow powder was formed, followed by collection via centrifugation at 7500 rpm for 10 min. The liquid was discarded. After that, the solid was dispersed into 15 ml of a mixture of THF/anhydrous diethyl ether (3:1) and the above procedure was repeated five times. The resultant NHS-FA was dried under vacuum overnight to remove any residual ether and THF, then stored at 4 °C in the dark.

The NHS groups of the obtained NHS-FA then reacted with the primary amine presented on the surface of TS-NH₂ to form amide bonds and release NHS. The corresponding chemical reaction is illustrated in Fig. 3.2(C). TS-NH₂ nanoparticles (100 mg) were suspended into 10 ml of sodium carbonate/bicarbonate buffer solution (0.01 M, pH=9.0) using ultrasonic vibration at room temperature. Then, NHS-FA (289 mg) was dissolved into dry DMSO (10 ml) under magnetic stirring. The solution of NHS-FA in DMSO was added, dropwise, to the obtained nanoparticle suspension and the reaction was maintained at room temperature with constant stirring. After stirring in the dark for 2 h, the derived TS-FA nanoparticles were collected using a centrifuge at 7500 rpm for 15 min. The product was washed with DMSO (3×15 ml), followed by ethanol (1×15 ml) and dried overnight under vacuum.

3.2.4 Physicochemical characterisations

Scanning electron micrographs of all nanoparticles produced were obtained using a FESEM (Zeiss Neon 40EsB FIB-SEM). Prior to FESEM examination, the sample suspension in Milli-Q water ($20 \mu\text{g ml}^{-1}$) was mounted on an aluminium stub. The aluminium stub was allowed to air-dry at ambient temperature overnight and then coated with platinum (2 nm) which was used as a conducting surface material. The operation condition for FESEM images recorded was at an accelerating voltage of 5 kV. The mean diameter of the particles was analysed using the SmartSEM software that was related to the scale bar for the recorded FESEM images. Sixty particles were randomly selected for size measurements.

The detailed morphology of the produced nanoparticles also were visualized using HRTEM (JEOL 3000F). The sample for HRTEM examination was performed by placing one drop of the sample dispersion in ethanol solution ($10 \mu\text{g ml}^{-1}$) on a copper grid with a substrate of carbon film and air-dried at room temperature overnight. HRTEM images of the nanoparticles were recorded at an accelerating voltage of 200 kV. The sizes of the nanoparticles were measured using the in-built JEOL operational software, DigitalMicrograph, which also was linked to the magnification scale bar of the obtained TEM images.

The surface chemistry of the produced TS, TS-NH₂ and TS-FA nanoparticles were characterised using a Thermo Scientific Nicolet iS50 FTIR spectrometer fitted with a diamond ATR sampling accessory. An FTIR spectrum of each sample was recorded between 200 and 4000 cm^{-1} .

The UV-Vis DRS of the nanoparticles was examined on a Jasco V670 spectrophotometer fitted with an integrating sphere, and BaSO₄ was used for the background scan. It was performed in the wavelength ranging from 250 to 750 nm with a band width of 2 nm.

The relative amount of the organic compounds presented on the surface of the samples was determined through burning the elements of carbon, nitrogen and hydrogen in air with a flow rate of 0.1 L min^{-1} , and calculated using the data obtained from TGA-DSC (Mettler-Toledo Star®). The obtained nanoparticles (10-15 mg) were heated from 35 °C to 900 °C in air with a heating rate of $10 \text{ }^\circ\text{C min}^{-1}$.

Nuclear magnetic resonance (NMR) spectroscopy was conducted on a Bruker Advance III NMR spectrometer (400 MHz), using dimethyl sulfoxide (DMSO)-d₆ as the solvent. In the ¹H NMR spectra, the signals at 2.50 and 3.30 belong to the DMSO-d₆ and water. To prepare the sample for ¹H NMR examination, NHS-FA (10 mg) was dissolved in DMSO-d₆ (1 ml) and the mixture was added into the dry NMR tube.

The amine groups on the surface of TS-NH₂ particles were qualified using a back titration method (Jung et al. 2012). In brief, TS-NH₂ nanoparticles (10 mg) and HCl aqueous solution (1.0 mM, 40 ml) were mixed with constant stirring for 2 h. Then, the mixture was separated using a centrifuge and the solid was discarded. The liquid was collected and titrated using 1.0 mM NaOH aqueous solution. In this reaction, phenolphthalein in ethanol solution was used as a pH indicator.

3.2.5 Photoreactivity study

The photocatalytic properties of TS-NH₂ and TS-FA nanoparticles were determined based on phenol degradation efficiency, using the procedure described in Chapter 2. P25 and TS also were assessed for comparison purposes. In brief, a preferred amount of catalyst was mixed with phenol solution (200 ml, 20 μg ml⁻¹) with constant stirring. The reaction was performed in a 1 L double-jacketed reactor that was connected to a water bath through a pump to maintain the reaction temperature at 25±1 °C. The light source was provided by an MSR 575/2 metal halide lamp (575 W, Philips) with a wavelength between 315 and 1050 nm. After the first 30 min, the reaction mixture was stirred in the dark to reach the adsorption-desorption equilibrium. After this, the reaction was carried out under light. At the prescribed time intervals, 5 ml of the catalyst suspension in phenol solution was withdrawn and the solid in the suspension was filtered using 0.45 μm Millipore filter. The liquid was reserved and sent for analysis using an HPLC (Varian) in which the UV detector was adjusted to 270 nm. The amount of P25 for phenol degradation was 0.05 g, leading to a catalyst concentration of 0.25 g L⁻¹. To maintain the same concentration of TiO₂ in phenol solution, the amounts of TS, TS-NH₂ and TS-FA added were 0.055 g, 0.056 g and 0.059 g, respectively. The aforementioned

photoreactivity experiments were performed once. It is worthy to mention that the method employed in the work is well established and proven reproducible in our previous work (Sun et al. 2011).

3.2.6 Cell culture and nanoparticle preparation

Human nasopharyngeal epidermoid cancer cell line (KB) and primary adherent mouse fibroblast connective tissue cell line (L929) were obtained from American Type Culture Collection (ATCC, USA). KB cells were applied as the positive folate receptor cells, while L929 cells were used as the negative folate receptor cells. KB cells were cultured in Roswell Park Memorial Institute (RPMI) 1640 folic acid-deficient medium supplemented with 10% fetal bovine serum (FBS, Sigma Aldrich) and 1% L-glutamate. L929 cells were cultured in Dulbecco's modified Eagle's medium (DMEM, Invitrogen, USA) with 10% FBS. The cells were grown into 96-well plates at a density of 10,000 cells per well and kept at 37 °C in a humidified atmosphere involving 5% CO₂ and 95% air. TiO₂, TS, TS-NH₂ and TS-FA nanoparticles were suspended into the growth medium, which led to concentrations of 12.5, 25, 50, 100 and 200 µg ml⁻¹, respectively.

3.2.7 MTS assay

A detailed description of the cytotoxicity study of the obtained P25, TS, TS-NH₂ and TS-FA nanoparticles using L929 cell line and KB cell line can be found in section 2.2.6 of Chapter 2. The particle concentrations involved in MTS analysis were 12.5, 25, 50, 100 and 200 µg ml⁻¹, respectively. A control experiment was performed using the cells treated with complete medium involving no particles, under identical conditions. After 6 h and 24 h of incubation, the cell medium was aspirated off and the plate was washed three times with PBS. The cells in each well were mixed with MTS reagent (200 µl) and the plate was returned to the incubator for another 3 h at 37 °C and 5% CO₂. The absorbance of the produced formazan at 490 nm was recorded using a microplate reader. The relative cell viability was estimated by $A_{\text{test}}/A_{\text{control}}$, where A_{test} and A_{control} are the absorbance of the samples

and controls, respectively. It should be noted that all the experiments were repeated three times in the dark. The cell morphology was recorded by an Olympus BX61 microscope with magnification bar 5× for all samples.

3.2.8 Haemolysis assay

Haemolysis studies of the samples were carried out using the procedure described in section 2.2.7 of Chapter 2. The sample concentrations were 12.5, 25, 50, 100 and 200 $\mu\text{g ml}^{-1}$, respectively. For control purposes, the mixture of the RBC suspension (100 μl) and PBS buffer (100 μl) was applied as a negative control while that of the RBC suspension (100 μl) and 0.5% Triton X-100 (100 μl) was used as a positive control. The percentage haemolysis was estimated using the Eq. 2.7, explained in Chapter 2. All the experiments were performed in triplicate.

3.2.9 Photo-killing effect

The procedure described in section 2.2.8 of Chapter 2 was applied to determine the photo-killing effect of P25, TS and TS-FA nanoparticles. The investigated concentrations of the nanoparticles were 100, 150 and 200 $\mu\text{g ml}^{-1}$, respectively. The experiments were carried out using KB cells.

3.2.10 Cell internalisation

Prior to the cell internalisation experiment, P25, TS and TS-FA particles were labelled with fluorescein isothiocyanate (FITC). FITC (1.0 mg) was dissolved in acetone (1.0 ml), resulting in the final concentration of 1.0 mg ml^{-1} . Then the sample (20 mg) was suspended into the resulting FITC solution (0.5 ml) and the suspension was continuously shaken overnight. Then, the particles were collected using a centrifuge at 7500 rpm and washed multiple times with Milli-Q water until the supernatant was clear. The resultant FITC-labelled nanoparticles were then re-suspended into culture medium for further investigation.

To determine the intracellular uptake of the derived particles, KB cells, at a density of 1×10^5 cells per well, were plated in a 12-well polystyrene dish and incubated at 37 °C and 5% CO₂. After incubation overnight, the culture medium was substituted with fresh medium containing the labelled nanoparticles, each at the concentration of 100 µg ml⁻¹. Then the polystyrene dish was returned to the incubator under 5% CO₂. After 6 h of incubation, the medium was removed and the cells were washed in triplet with PBS (pH 7.4) to clear the unattached particles away. Then the cells were fixed with 4% formaldehyde in PBS for 15 min and, subsequently, the fixed cells were visualised using a confocal laser scanning microscope with an FITC filter.

3.2.11 Statistical analysis

All the experimental data of the aforementioned cellular work were statically analysed using Student's T-test. The results were expressed as mean±standard error. Statistical significances were considered at $p < 0.05$.

3.3 Results and Discussion

The folic acid-conjugated TiO₂ (TS-FA) nanoparticles were fabricated, as shown in Fig. 3.1. TS was prepared using the method mentioned in Chapter 2 and, subsequently, was modified by the addition of APTES to form amine-terminated TS (TS-NH₂). To improve the coupling efficiency of folic acid with TS-NH₂, folic acid was firstly activated with NHS to form NHS-ester of folic acid (NHS-FA). Finally, the NHS-FA was reacted with TS-NH₂ to yield folic acid-conjugated TS (TS-FA).

3.3.1 Synthesis and characterisation of NHS-FA

FTIR was used to characterise NHS-FA in comparison with pure FA, as displayed in Fig. 3.3. For FA, the peaks in the 3600-2900 cm⁻¹ region are assigned to the -OH stretching vibrations of L-glutamic acid moiety and the -NH···H stretching vibrations of the pterin ring (He et al. 2009). The peak at 1694 cm⁻¹ belongs to the

C=O stretching vibration of the –COOH group while the peak at 1640 cm^{-1} relates to the C=O stretching vibration of the –CO-NH- (amide band II) group from the L-glutamic acid moiety (Zhang et al. 2008a). Also, the –NH stretching vibration of the –CO-NH (amide band II) groups appears at 1570 cm^{-1} (Muhammad et al. 2011a). The absorption peaks at 1485 and 1414 cm^{-1} are attributed to the phenyl ring and the –OH deformation band of the phenyl skeleton, respectively. After NHS was used to activate FA, the successful formation of NHS-FA was confirmed via two remarkable absorption peaks at 1201 and 1068 cm^{-1} , corresponding to the C-O and N-O stretching vibrations of the newly formed succinimidyl ester group, respectively (Wagner et al. 1996). Additionally, there is a strong peak at 1729 cm^{-1} which is due to splitting of the band associated to the C=O stretching vibration of the newly formed succinimidyl ester group. The absorption peaks at 1814 and 1782 cm^{-1} are related to the C=O stretching vibration of the succinimidyl carbonyl groups (Dordi et al. 2003). Other absorption peaks below 1400 cm^{-1} correspond to various vibration modes related to the ring structure of the pteridine moiety (Zhang et al. 2008a).

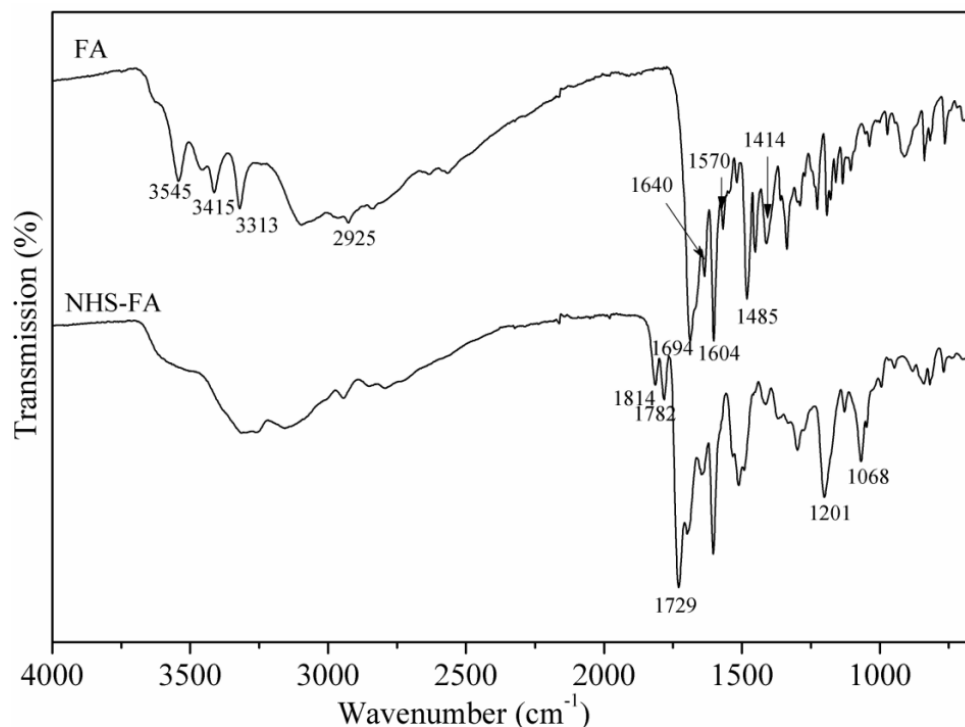
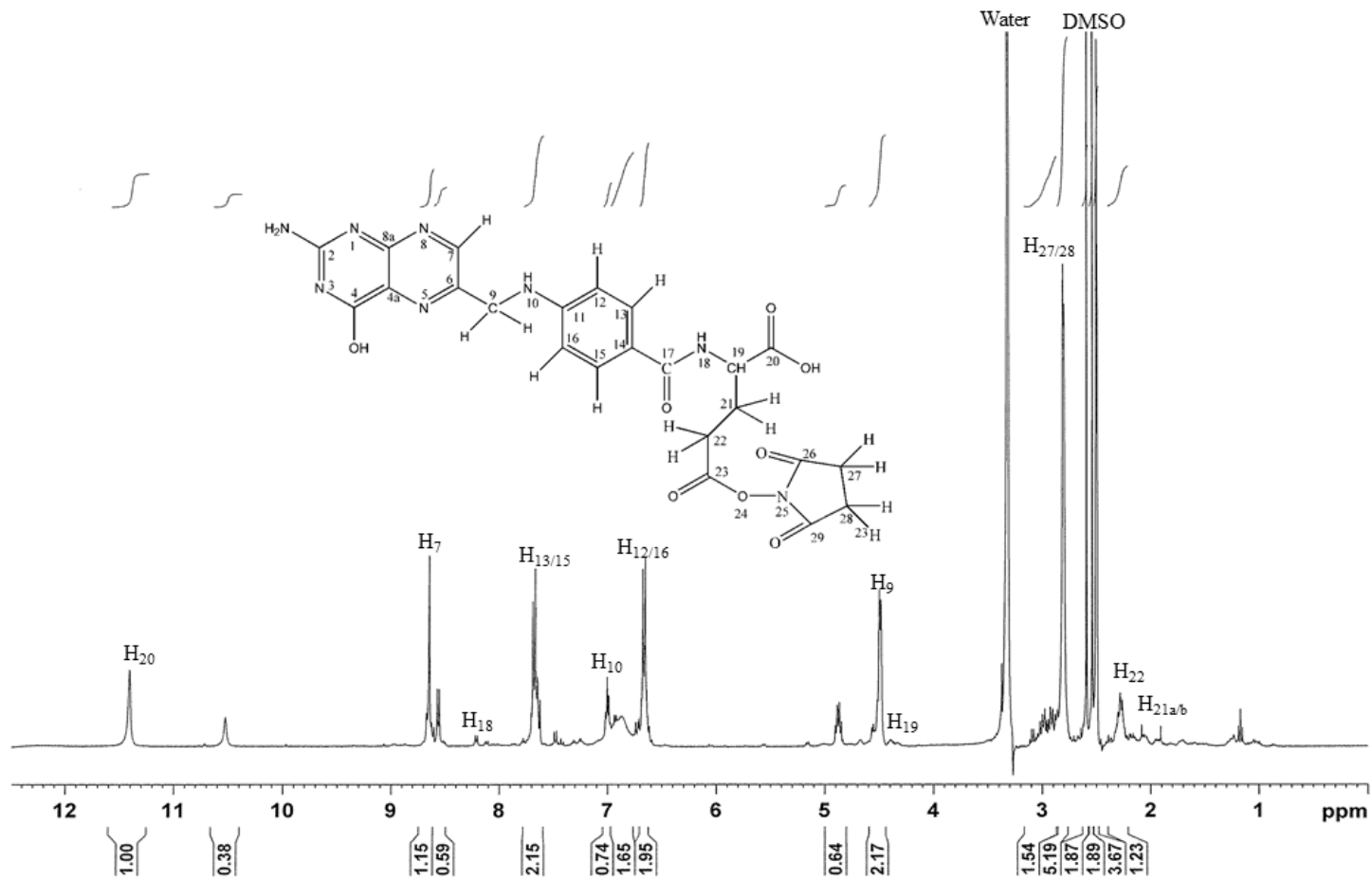


Fig. 3.3 FTIR spectra for FA and NHS-FA

^1H NMR was used to further confirm the successful synthesis of NHS-FA, shown in Fig. 3.4. In the ^1H NMR spectra of NHS-FA, the signal at 11.35 ppm is attributed to the $-\text{OH}$ proton in the carboxylic group of FA, while the signals at 8.65, 7.64 and 6.65 ppm are due to the aromatic proton of FA (Lu et al. 2009). The signals presenting at 7.00 and 8.13 ppm belong to the $-\text{NH}-$ protons in the p-amino benzoic acid moiety and the $-\text{CO}-\text{NH}-$ in the glutamate moiety of FA, respectively (Bonechis et al. 2004). The methylene protons in the pterin moiety and the glutamate moiety of FA appear at 4.48, 2.31 and 1.99-2.10 ppm, while the methylene protons of NHS can be observed at 2.8 ppm, indicating that FA has been successfully converted to NHS-ester of folic acid via DCC as a coupling agent (Alexander et al. 2014).

Fig. 3.4 ^1H NMR spectrum of NHS-FA

3.3.2 Characterisation of TS-NH₂ and TS-FA nanoparticles

FESEM images, presented in Fig. 3.5, indicate that the morphology of the P25, TS, TS-NH₂ and TS-FA were generally the same. The sizes of TS-NH₂ and TS-FA were 39±5 nm and 43±3 nm, respectively, indicating a slight increase of particle size in comparison with P25 (24±1 nm) and TS (35±2 nm). It was noted that TS-NH₂ nanoparticles terminated with amine groups tend to form agglomerates while TS-FA nanoparticles terminated with carboxyl acid were relatively well-dispersed. Similar phenomena were observed by Bagwe et al. (2006) in the silica nanoparticles modified with different functional groups. It was indicated that the pK_a value of amine-modified nanoparticles that were suspended in deionized water was 9.0. Under neutral conditions, the amine-modified nanoparticles have positively charged surfaces, which reduce the negativity of the silanolised surface of TS, resulting in low surface charge. Hence, the TS-NH₂ nanoparticles tend to aggregate more than TS. The further carboxylation of the primary amine groups brought back the negative charges, therefore leading to the improved dispersion of nanoparticles.

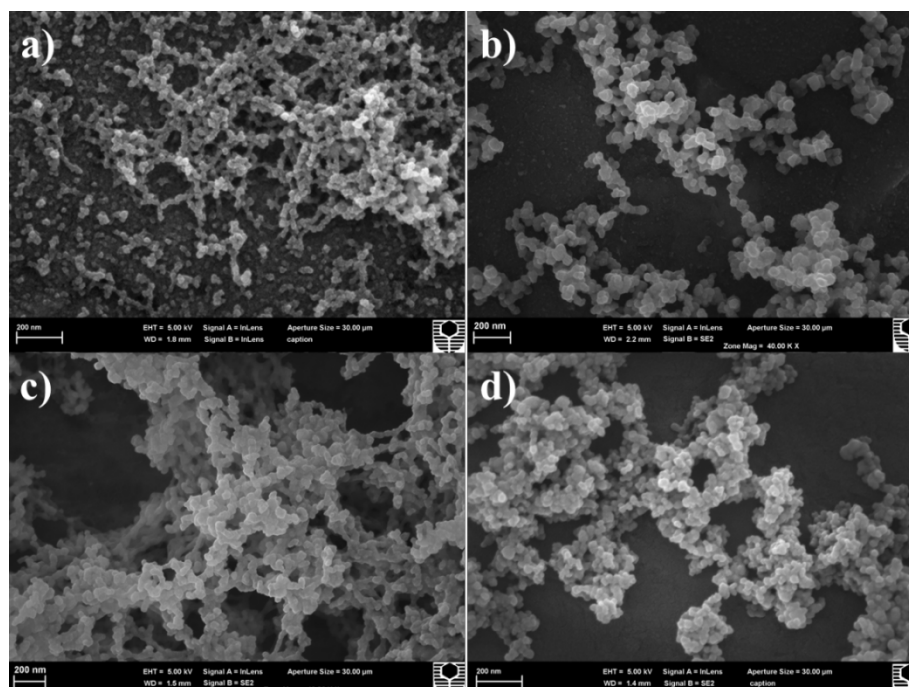


Fig. 3.5 FESEM micrographs of, (a) non-coated TiO₂ (P25), (b) silica-coated TiO₂ (TS), (c) amine-terminated TiO₂-SiO₂ (TS-NH₂) and (d) folic acid-conjugated TiO₂-SiO₂ (TS-FA).

The HRTEM images in Fig. 3.6 demonstrate the detailed morphology and crystallinity of TS-NH₂ and TS-FA nanoparticles. The core-shell structures in the TS-NH₂ and TS-FA nanoparticles were clearly demonstrated in these images due to the contrast difference between the TiO₂ cores and the silica shells. For TS-NH₂, presented in Fig. 3.6a, the core nanoparticles with well-defined crystal facets were evident via the obvious lattice fringes, which, at 0.35 nm, corresponds to the d spacing for (101) lattice planes of anatase TiO₂ nanoparticles. The coated silica layer is amorphous and the relative thickness is approximately 3 nm. After further conjugation with FA, the layer of the core-shell structured TS-FA nanoparticles increases up to approximately 5 nm. The lattice fringes of the core nanoparticles are at 0.32 nm and 0.35 nm, which agrees well with d spacings of the (110) plane in rutile TiO₂ nanoparticles and the (101) plane in anatase TiO₂ nanoparticles, respectively.

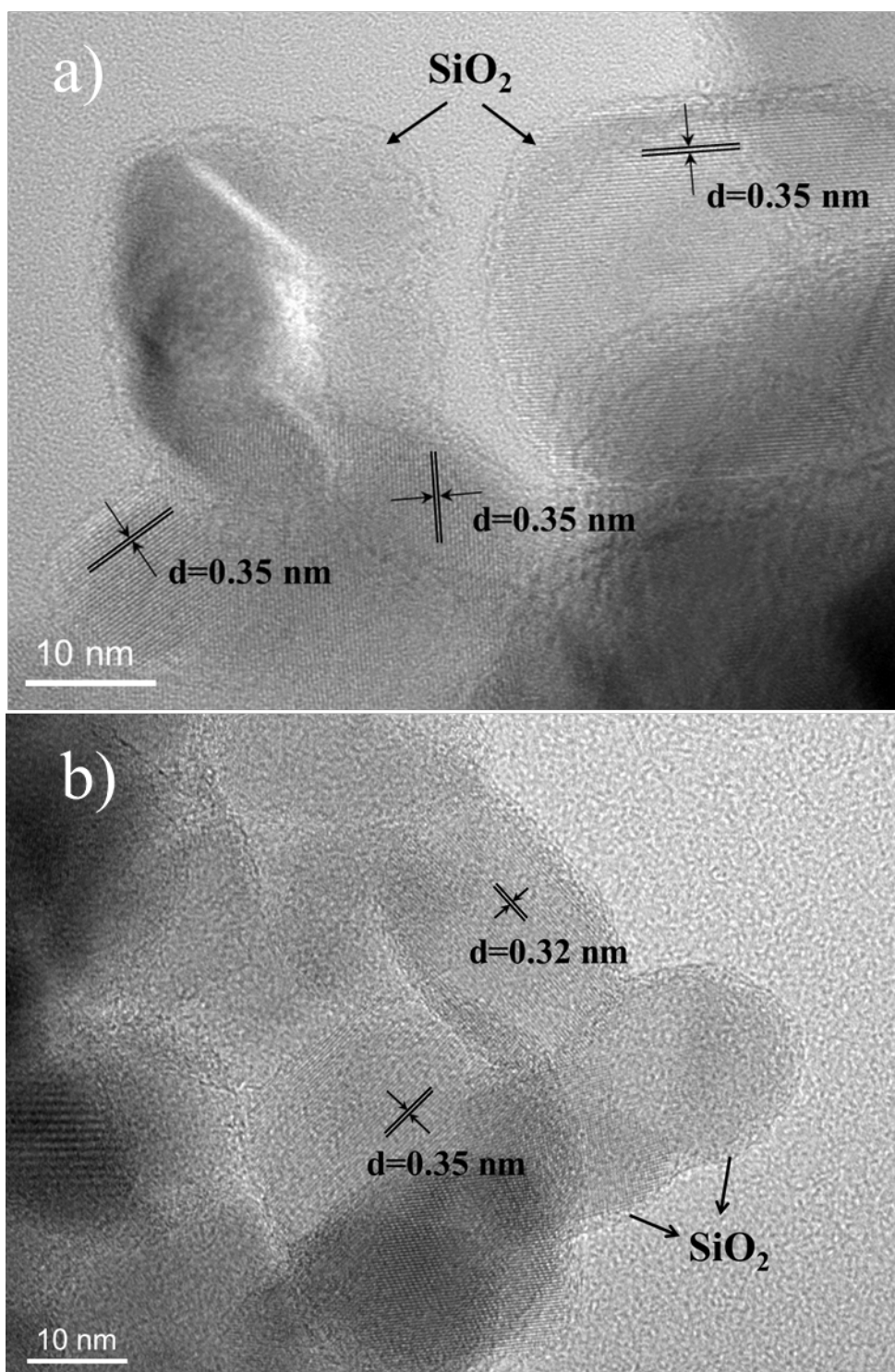


Fig. 3.6 High resolution TEM images of (a) TS-NH₂ and (b) TS-FA.

The FTIR of all samples in the region of 100-4000 cm⁻¹ is shown in Fig. 3.7a. The FTIR peaks located at 630 and 388 cm⁻¹ are attributed to the stretching vibration of Ti-O groups, confirming the presence of TiO₂ in all samples (Velasco et al. 1999).

After a silica layer was applied to the TiO₂ nanoparticles, the successful formation of the silica network was proven via the characteristic absorption peaks at 1065 cm⁻¹ and 1156 cm⁻¹, representing the bending and stretching vibrations of the Si-O-Si groups. Additionally, a weak peak at 950 cm⁻¹ is attributable to the formation of Ti-O-Si linkage between TiO₂ core nanoparticles and the silica layer via condensation (Ogura et al. 1999). The broad peak at 3350 cm⁻¹, presented in all samples' spectra, is assigned to the stretching vibration of O-H groups from the adsorbed water. And the absorption peak at around 2150 cm⁻¹ is from CO₂ in air.

To examine the formation of the amide bond in TS-FA nanoparticles, the representative FTIR spectra of TS-NH₂ and TS-FA in the region 1300-1700 cm⁻¹ are clearly shown in Fig. 3.7b. For TS-NH₂, an absorption peak at 1560 cm⁻¹, assigned to the -NH bending vibration, confirms the existence of primary amine groups on the surface of the TS-NH₂ nanoparticles (Ishida et al. 1982). This spectrum also displays the characteristic peak at 1491 cm⁻¹, associated with the symmetric deformation mode (bending vibration of -NH₂) of NH₃⁺ in the SiO⁻...H...NH₃⁺ structure (Okabayashi et al. 1997). The weak absorption peaks located at 1413, 1444 and 1472 cm⁻¹ are attributed to the bending vibration of -CH₂ groups in the n-propyl chain from APTES moieties (Rosenholm et al. 1976). After binding FA with the primary amine groups, the characteristic peak at 1560 cm⁻¹ disappeared and a new absorption peak at 1606 cm⁻¹, corresponding to -NH stretching vibration from the -CO-NH- (Amide II) groups, was observed (Sun et al. 2006). Meanwhile, the characteristic peak at 1628 cm⁻¹ is associated with the C=O stretching vibration of the -CO-NH- (Amide I) groups (Chen et al. 2011). Those observations indicated that FA was covalently linked to the surface of TS-NH₂ through the amide bond. The peak at 1400 cm⁻¹ is assigned to the stretching vibrations of -COO groups, and other absorption peaks at 1450 and 1512 cm⁻¹ are related to C=C in the backbone of the aromatic ring in the p-amino benzoic acid moieties (Sahu and Mallick 2010), which further reveals that FA has been successfully encapsulated on the surface of TS nanoparticles.

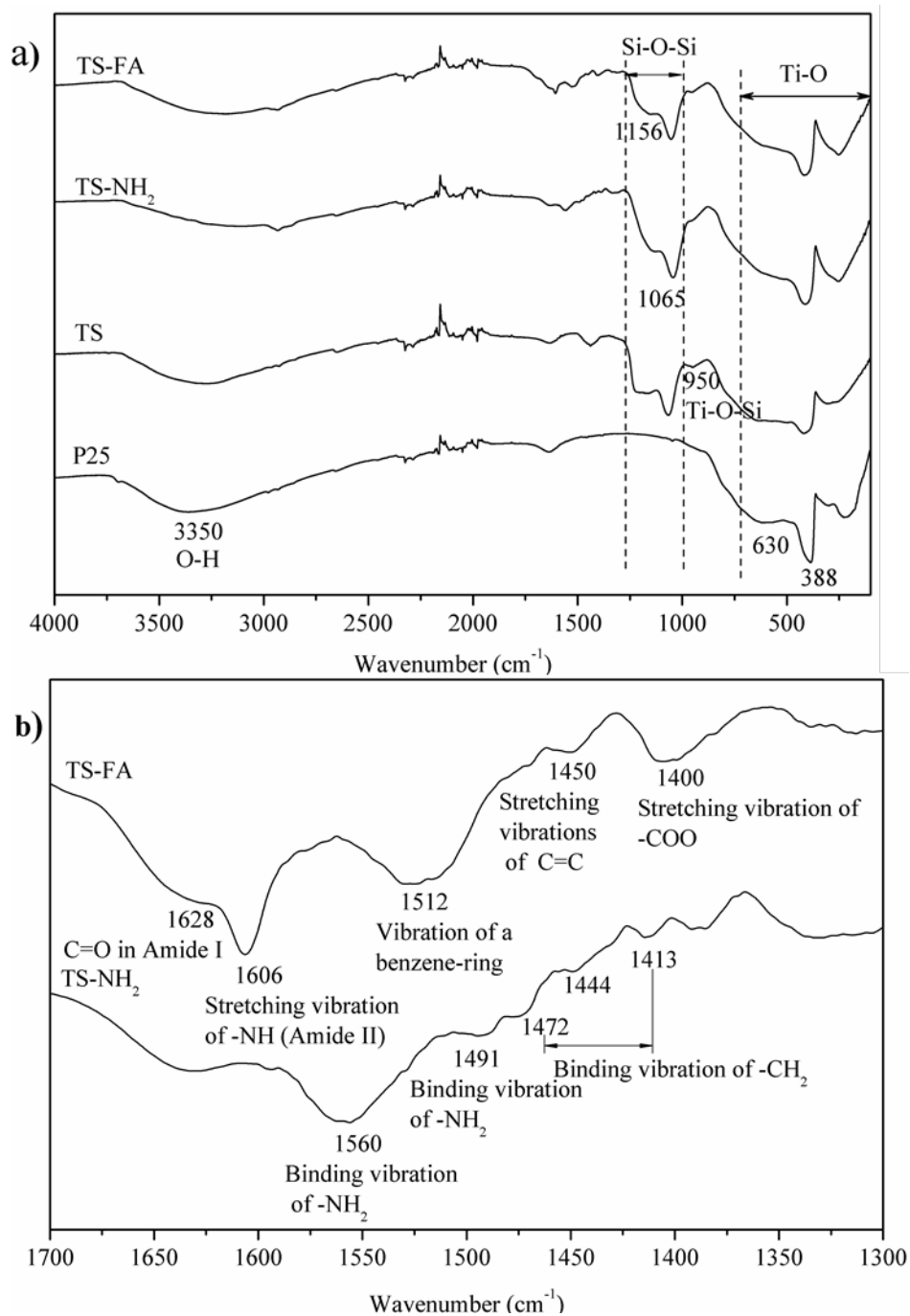


Fig. 3.7 (a) FTIR spectra of P25, TS, TS-NH₂ and TS-FA in the range of 100-4000 cm⁻¹ and (b) FTIR spectra of TS-NH₂ and TS-FA in the 1300-1700 cm⁻¹ region.

To verify the content of the -NH₂ groups and FA groups in TS-NH₂ and TS-FA nanoparticles, the TGA analysis was carried out in the presence of air. As shown in Fig. 3.8, a two-stage mass loss was observed in both compounds. When the temperature was in the region of 35-110 °C, a slight mass loss was observed due to the release of absorbed water molecules. There was a significant decrease in mass

when the temperature was between 110 and 850 °C. This can be assigned to the release of CO₂, CO, NO₂ or H₂O owing to the decomposition of organic groups grafted onto the surface of the particles (Vora et al. 2002, El-Wahed et al. 2008). The weight losses for P25, TS, TS-NH₂ and TS-FA nanoparticles in the region of 110-850 °C were 0.7, 1.8, 3.2 and 8.0 wt%, respectively. Assuming all the ethoxy groups were removed after the condensation of TEOS, thereby, the mass loss of TS-NH₂ must have been from the CH₂CH₂CH₂NH₂ of APTES. Hence, the surface density of -NH₂ was calculated to be 0.23 mmol g⁻¹.

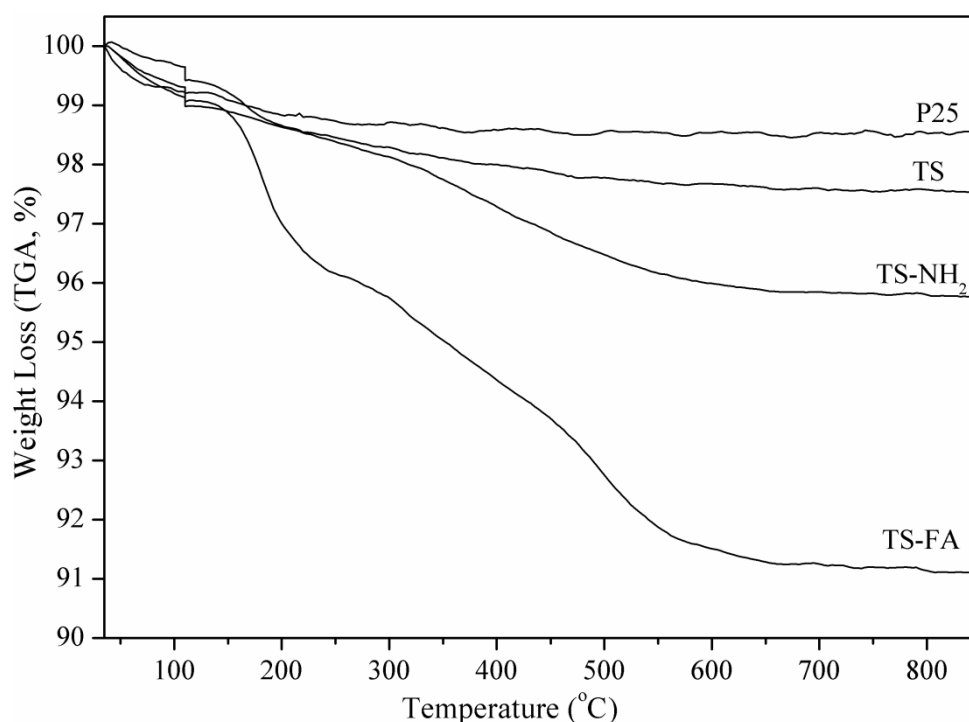


Fig. 3.8 TGA curves of P25, TS, TS-NH₂ and TS-FA nanoparticles

The quantitative analyses of amine groups on the surface of TS-NH₂ were carried out using a back titration method. The reactions were repeated three times. The obtained average surface density of amine groups on the TS-NH₂ nanoparticles was 0.20 mmol g⁻¹, which was comparable to the data obtained from TGA.

The UV-Vis spectra of P25, TS, TS-NH₂ and TS-FA are shown in Fig. 3.9. The absorption threshold of P25 and TS nanoparticles is at around 410 nm and 411 nm, respectively. There was 1 nm difference between non-coated and silica-coated TiO₂,

due to the increase in particle size (Huang et al. 2011b). For TS-FA nanoparticles, a further red shift of 20 nm in the absorption threshold of TS-FA, as compared to that of P25, was due to the dielectric constant of the medium surrounding the TiO₂ nanoparticles. A similar observation was reported by Bhattacharya et al (2007) for folic acid-conjugated gold nanoparticles. Additionally, there was a significant increase in the absorption intensity of TS-FA at 280, 370 and 530 nm, which are the characteristic absorption peaks of FA (Zhang et al. 2009). All these results suggest that folic acid was successfully covalently attached to the surface of TS nanoparticles.

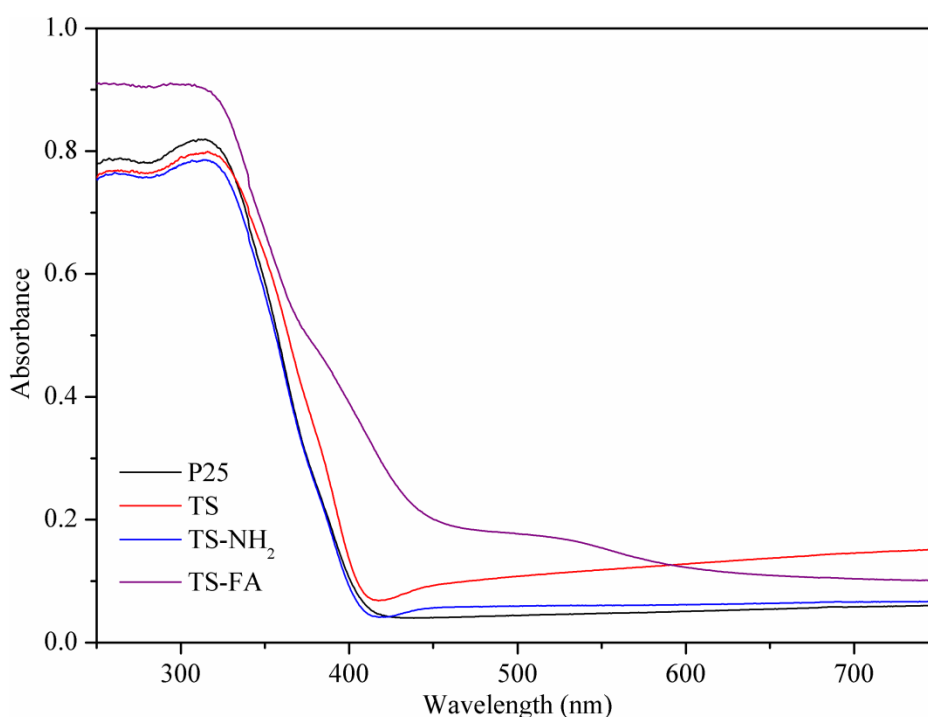


Fig. 3.9 UV-Vis spectra of P25, TS, TS-NH₂ and TS-FA nanoparticles.

3.3.3 Photocatalytic reactivity

The photoreactivity of the obtained nanoparticles was evaluated on the basis of phenol degradation in the presence of UV light. Fig. 3.10 shows the percentage degradation of phenol using P25, TS, TS-NH₂ and TS-FA at the given time intervals. Upon exposure to UV light for 150 min, complete removal of phenol with an initial concentration of 20 $\mu\text{g ml}^{-1}$ was obtained when 0.25 g L^{-1} non-coated TiO₂ was used. In the presence of TS, TS-NH₂ and TS-FA, the percentage degradation of phenol was

70%, 10% and 67%, respectively. The apparent rate constant of these nanoparticles was valued using the Langmuir-Hinshelwood equation where k represents the apparent reaction rate constant in the unit of min^{-1} , and C_0 and C are the phenol concentration at $t=0$ and $t=t$, respectively (Sun et al. 2009):

$$\ln \frac{C}{C_0} = -kt \quad (3.1)$$

The computed k values for P25, TS, TS-NH₂ and TS-FA were 0.0242, 0.0084, 0.0005 and 0.0066 min^{-1} , respectively. The irradiation time used was 120 min. The corresponding least squared R values for each sample were 0.9725, 0.9893, 0.9568 and 0.9688, respectively.

In comparison with non-coated TiO₂, a 2.9-fold decrease in the photodegradation rate was observed after the silica layer was applied, which is due to the shielding effect of the silica matrix encapsulated on the TiO₂ nanoparticles, as we have discussed before (Feng et al. 2013). For TS, TS-NH₂ and TS-FA, the silica layer (as a shielding barrier) blocks the pathway of the ROS such as O₂^{•-} and •OH, leading to a decrease in ROS yield and a reduction in the coated TiO₂ degradation rate. In addition, the increased particle size may lead to the reduced photoreactivity of the catalysts, as a consequence of reduced surface area. The TS-NH₂ nanoparticles displayed an even lower photodegradation rate than TS-FA, which is probably due to the competing photo-oxidation of primary amine groups on the surface of the TS-NH₂. A study has shown that, under UV illumination, the ROS generated from photoexcited TiO₂ nanoparticles can oxidize primary amine groups to yield NO₃⁻ ions, and the cleavage rate of the C-N bond from primary amine was faster than that of the C-C bond in the hydrocarbon molecules (Nohara et al. 1997). After the primary amine groups were combined with folic acid to form TS-FA, the photodegradation rate was enhanced to 0.0066 min^{-1} , a similar value to that of TS. As compared with TS-NH₂, the increased degradation rate was partly due to the presence of carboxyl groups on the surface of the TS-FA. Research has shown that the carboxyl groups react with photogenerated ROS to form reducing radicals (CO₂^{•-}) that are helpful for the reduction reaction (Colon et al. 2001). However, in comparison with TS, a slight decrease in degradation rate was evident. This might be because folic acid could

absorb light at wavelengths of 280 nm, 370 nm, and 530 nm, leading to reduced radiation intensity for TiO₂ excitation (Lai and Lee 2009).

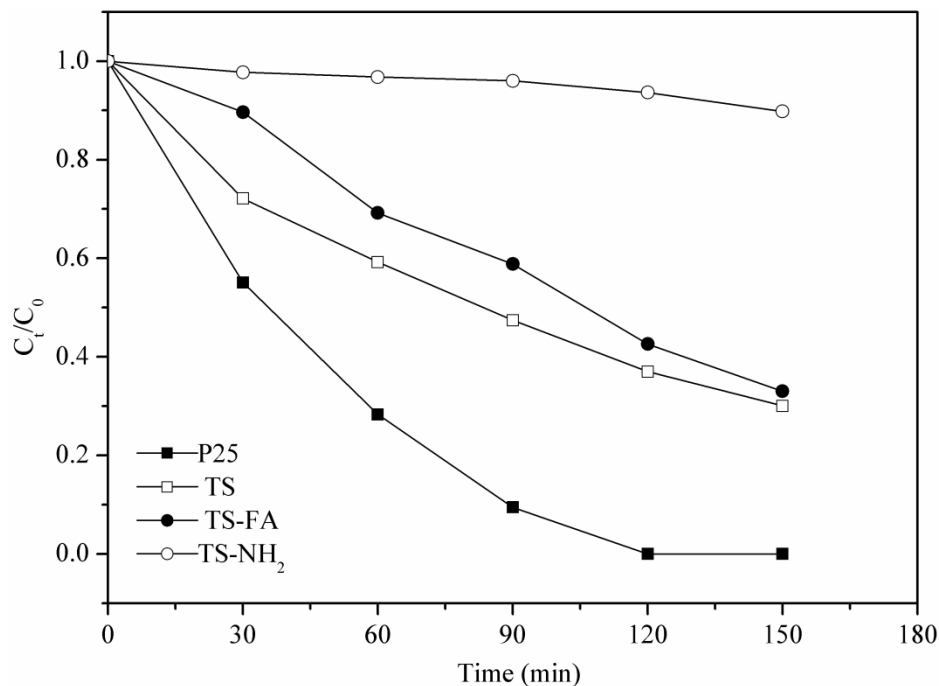


Fig. 3.10 Phenol concentration changes with time

3.3.4 Cytotoxicity and haemocompatibility study

Investigations on the cytotoxicity and haemocompatibility of the produced nanoparticles were undertaken using an MTS assay. P25, TS, TS-NH₂ and TS-FA particles of various concentrations were assessed using both normal mouse fibroblast cells (L929) and human nasopharyngeal cancer cells (KB) after 6 h and 24 h incubation time.

3.3.4.1 Toxicity of P25, TS, TS-NH₂ and TS-FA to L929

Fig. 3.11 displays the relative viability of L929 cells after 6h and 24 h incubation with P25, TS, TS-NH₂ and TS-FA of various concentrations (0, 12.5, 25, 50, 100 and 200 μg ml⁻¹). The culture was performed in the dark. When the incubation time was 6 h (Fig. 3.11a), there were no significant differences between the untreated cells and

cells treated with P25, TS, TS-NH₂ and TS-FA nanoparticles. The viability of L929 cells, in relation to the control, was well above 90% for all.

Upon prolonged incubation time to 24 h, a dramatic increase in cell viability was observed in the presence of TS-FA over the investigated concentration range. A decrease of cell viability to 82% was observed when P25 (200 µg ml⁻¹) was added into the cells. No significant change was observed in the viability of the cells treated with TS or TS-NH₂ nanoparticles. It is known that the silica coating improves the cytotoxicity of core nanoparticles (Feng et al. 2013). For TS-FA-treated cells, the viability was about two-fold greater than that of untreated cells or cells treated with other nanoparticles. The enhanced cell proliferation may be because folic acid, an essential vitamin B element for cell proliferation, promoted the cell growth. Similar observations have been reported by other researchers (Song et al. 2009). In the standard growth medium, the concentration of FA used to facilitate the cell proliferation is 1.01 µg ml⁻¹ (Miotti et al. 1995). In this study, the produced TS-FA contained 4.8% of FA, as demonstrated by TGA results. When the particle concentration values were 12.5, 25, 50, 100 and 200 µg ml⁻¹, the FA concentration involved in the cell culture was 0.6, 1.2, 2.4, 4.8 and 9.6 µg ml⁻¹, respectively, which is comparable to results using the standard culture medium.

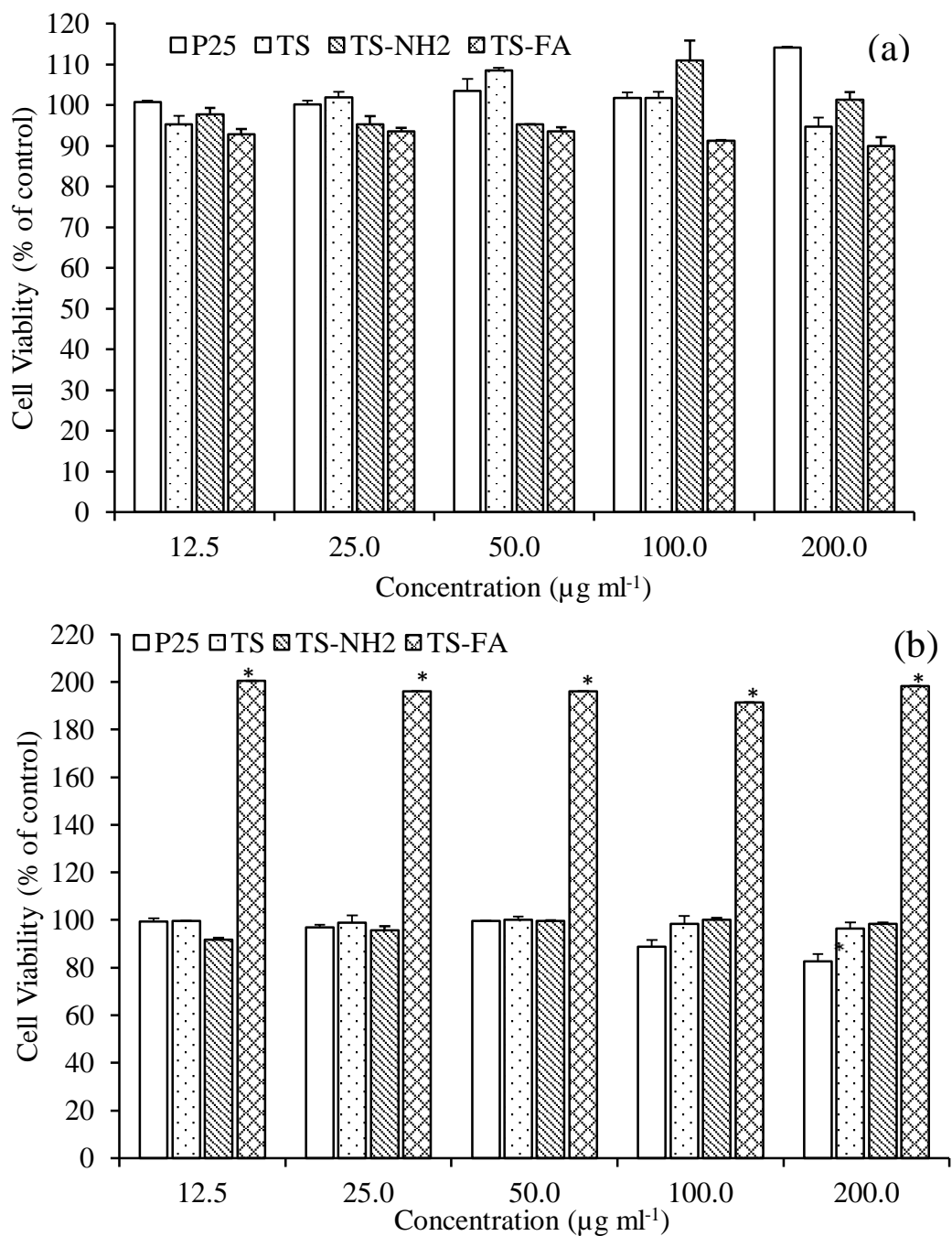


Fig. 3.11 Cell Viability after treatment with P25, TS, TS-NH₂ and TS-FA nanoparticles for (a) 6h and (b) 24 h. **p*<0.5 as compared with control. All the data were displayed as mean±SD and *n*=3. The error bar was based on the standard deviation.

The optical micrographs of L929 cells incubated with 200 µg ml⁻¹ of P25, TS, TS-NH₂ and TS-FA nanoparticles for 24 h are displayed in Fig. 3.12. There was a large portion of red-stained nuclei in the cell medium, after cells were exposed to P25, as shown in Fig. 3.12(b). Fewer or none red-stained dead cells were observed in

both untreated cells (Fig. 3.12(a)) and those treated with TS, TS-NH₂ and TS-FA (Fig.3.12(c-e)). These results further confirmed that, after coating with silica shell, the toxicity of TiO₂ particles on L929 cells was significantly reduced.

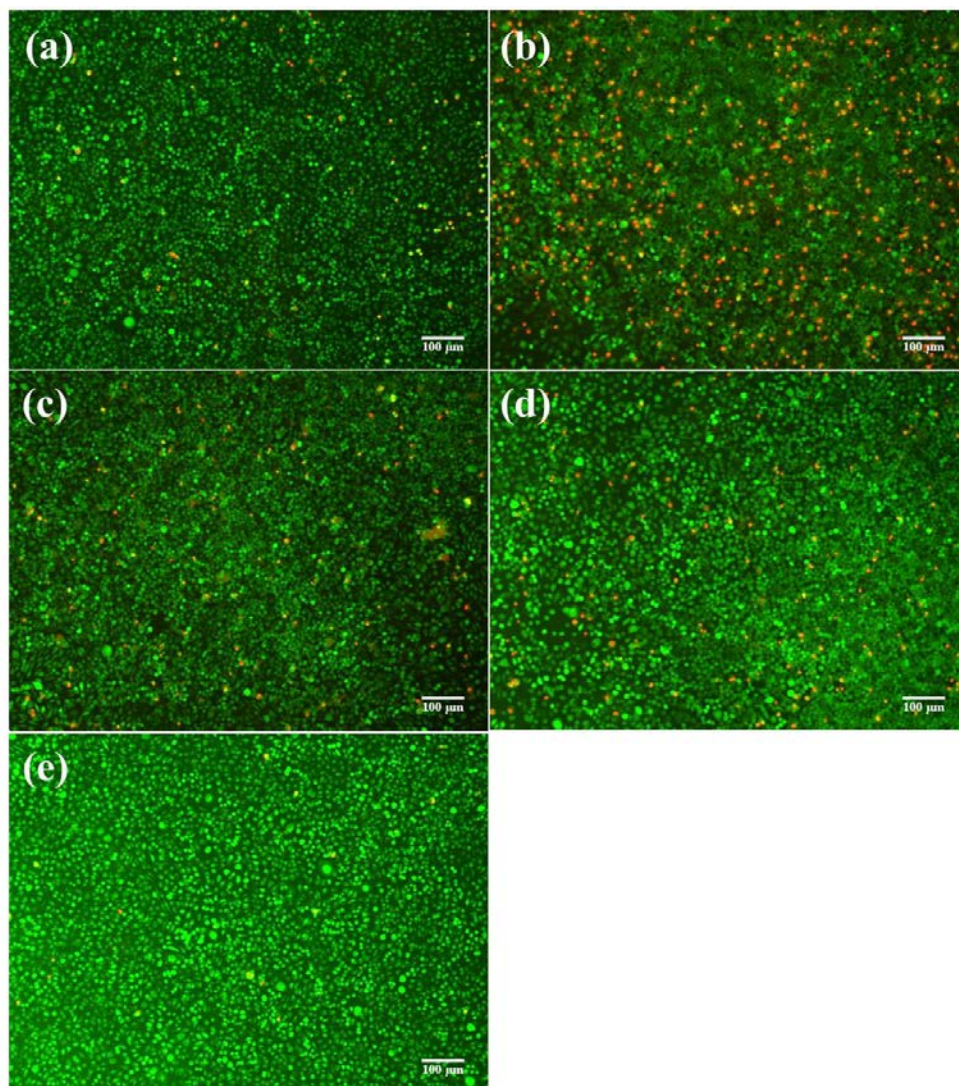


Fig. 3.12 Light microscope micrographs of L929 cells treated with (a) no nanoparticles, (b) P25, (c) TS, (d) TS-NH₂ and (e) TS-FA. Incubation time=6 h. The nanoparticle concentration was 200 $\mu\text{g ml}^{-1}$.

3.3.4.2 Toxicity of P25, TS and TS-FA to KB Cells

A toxicity study of P25, TS and TS-FA nanoparticles on KB cells also was conducted. The study was carried out by exposing the cells to the nanoparticles at the prescribed concentrations, shown in Fig. 3.13. Similar to the results for the L929 cells, after 6 h incubation, no apparent differences in cell viability ($p > 0.05$) were observed between control cells and cells treated with P25, TS and TS-FA over the investigated concentrations. When the incubation time was increased to 24 h, the viability of TS-treated cells was decreased to 73.3% and 79.7%, respectively, in the presence of 100 and 200 $\mu\text{g ml}^{-1}$ of TS nanoparticles. The toxic effect of TS nanoparticles on KB cells in the dark is possibly because silica increases the ROS level in KB cell, leading to cell apoptosis. In addition, the toxicity of silica is more apparent on cancerous cells (Chu et al. 2012). For TS-FA-treated KB cells, a concentration-dependent increase in viability was observed. When the particle concentration reached 200 $\mu\text{g ml}^{-1}$, the viability of TS-FA-treated cells was 2.6-fold greater than that of control cells, which is similar to the effects observed for the L929 cells.

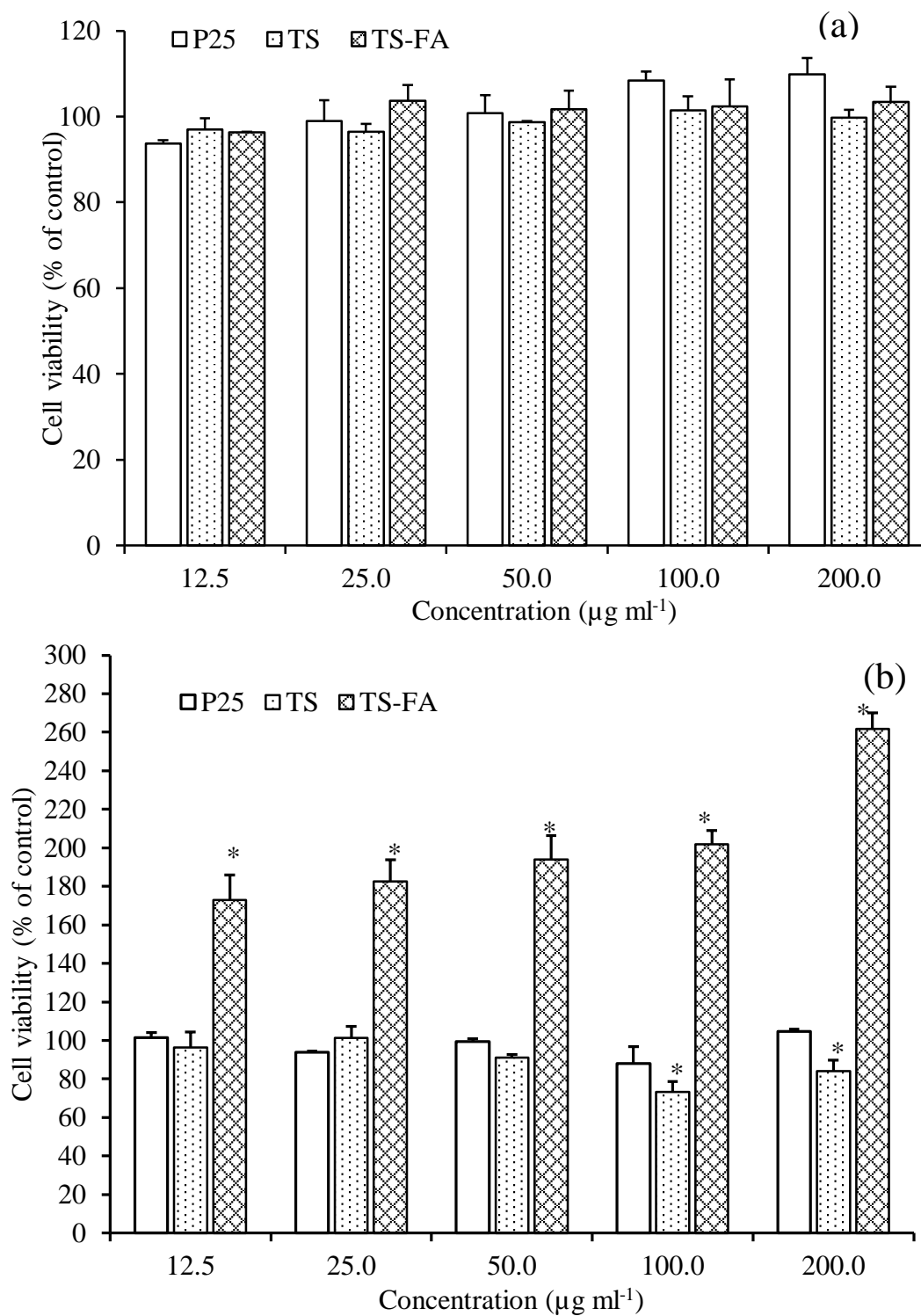


Fig. 3.13 KB cell viability after treatment with P25, TS and TS-FA at various concentrations for (a) 6 h and (b) 24 h. * $p < 0.5$ as compared with control cells. All data are expressed as the mean \pm SD and $n=3$. The error bar was based on the standard deviation.

3.3.4.3 Haemocompatibility study

Fig. 3.14 shows the *in vitro* haemolysis assays of P25, TS, TS-NH₂ and TS-FA at particle concentrations ranging from 12.5 to 200 µg ml⁻¹. The haemolysis percentage was estimated to be well below 5% in the investigated concentration range, indicating that all the samples showed low toxicity to blood cells. A two-fold greater haemolysis activity was observed for P25-treated RBCs while a five-fold increase in haemolysis activity was observed for RBCs treated with TS, TS-NH₂ and TS-FA at a particle concentration of 50 µg ml⁻¹ when compared with that at a particle concentration of 12.5 µg ml⁻¹. The increased particle concentration might have led to increased charges on the particle surfaces, resulting in RBC aggregation (Li et al. 2014). In addition, it was found that the silica-coated TiO₂ (TS, TS-NH₂ and TS-FA) exhibited higher haemolysis activity, which was caused by the hydrogen bonding between the silica shell and RBC's membrane components (Pandurangi et al. 1990). When the particle concentration was further increased to 200 µg ml⁻¹, the decreased haemolysis activity was observed due to the particle aggregation and thereby the decreased surface area interacting with the RBCs (Shi et al. 2012).

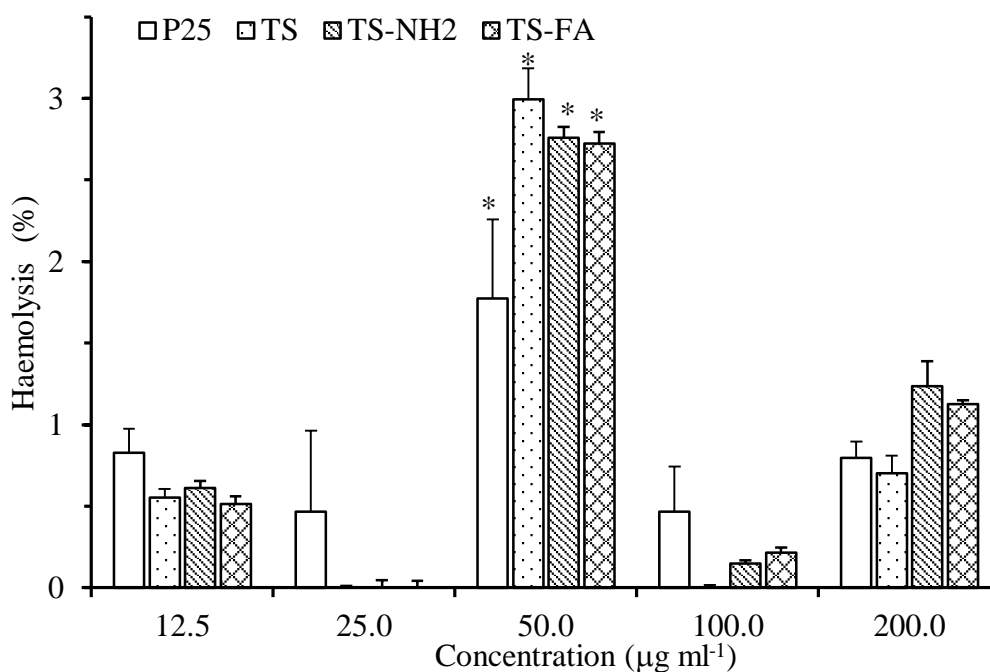


Fig. 3.14. Haemolysis assays of P25, TS, TS-NH₂ and TS-FA nanoparticles. *p<0.05 as compared with the particles' concentration at 12.5 µg ml⁻¹. All data are expressed as mean±STD and n=3. The error bar was based on the standard deviation.

3.3.5 Photo-killing effect

Based on the above observations, the photo-killing experiments were carried out on KB cells in the presence of P25, TS, TS-NH₂ and TS-FA nanoparticles after 6 h incubation. To investigate the influence of UV irradiation alone on KB cells, the viability of KB cells against irradiation time was assessed. The observed relative surviving fractions were 102.0%, 98.6% and 90.4% at 30 min, 45 min and 60 min, respectively. No significant differences relative to control were observed, even when the irradiation time was extended to 60 min. Both 30 min and 60 min were chosen, in this study, for the photo-killing investigations of the P25, TS and TS-FA nanoparticles.

Shown in Fig. 3.15 are the results after 30 min exposure for the cells treated with P25, TS and TS-FA. The surviving fraction of cells was reduced from 102.0% for the control to 88.8%, 94.2% and 88.5%, respectively. The reductions for both P25 and TS-FA were almost the same and were significant in comparison with the control cells (* $p < 0.05$). In addition, as compared with the cell viability in the dark, a significant decrease was observed. The surviving fraction was decreased to 82.0%, 86.9% and 81.6% for the cells treated with P25, TS and TS-FA nanoparticles,

respectively.

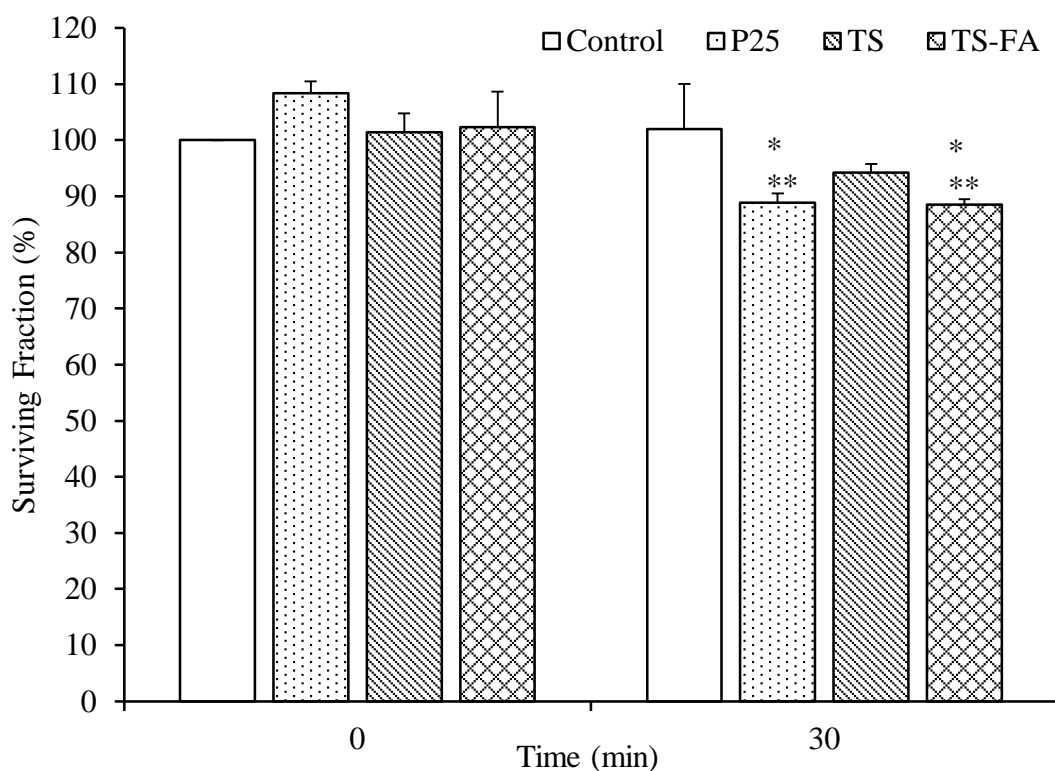


Fig. 3.15. The surviving fraction of KB cells treated with P25, TS and TS-FA nanoparticles in the dark and after 30 min of irradiation. The particle concentration was $100 \mu\text{g ml}^{-1}$. * $p < 0.05$ as compared to the viability in the dark. ** $p < 0.05$ as compared to control cells at $t = 30$ min. All data are expressed as mean \pm SD and $n = 3$.

When the exposure time was extended to 60 min, the viability of untreated cells (Fig.3.16) decreased to 90.4% relative to that of untreated cells in the dark. For P25-, TS- and TS-FA-treated cells, significantly reduced cell viability was observed. The relative cell viability became 10.4%, 14.9% and 68.6%, when $100 \mu\text{g ml}^{-1}$ of P25, TS and TS-FA was present in the cells. The killing effect was apparent for all samples investigated. In comparison with P25 and TS, TS-FA exhibited a relatively lower photo-killing effect. The photo-killing effect of TS-FA is obviously compromised by the higher FA content in the nanoparticles which has demonstrated the ability to enhance the growth of both KB cells and L929 cells in the dark. For KB cells, a 2.6-fold increase was seen in the dark, and a 0.68-fold reduction was observed under radiation. The photo-killing ability of TS-FA on KB cells was increased as the concentration of TS-FA rose. More systematic studies are required to optimise the

FA density of the nanoparticles. For P25 and TS nanoparticles, the photo-killing effect remained the same, which is consistent with our previous results (Feng et al. 2013).

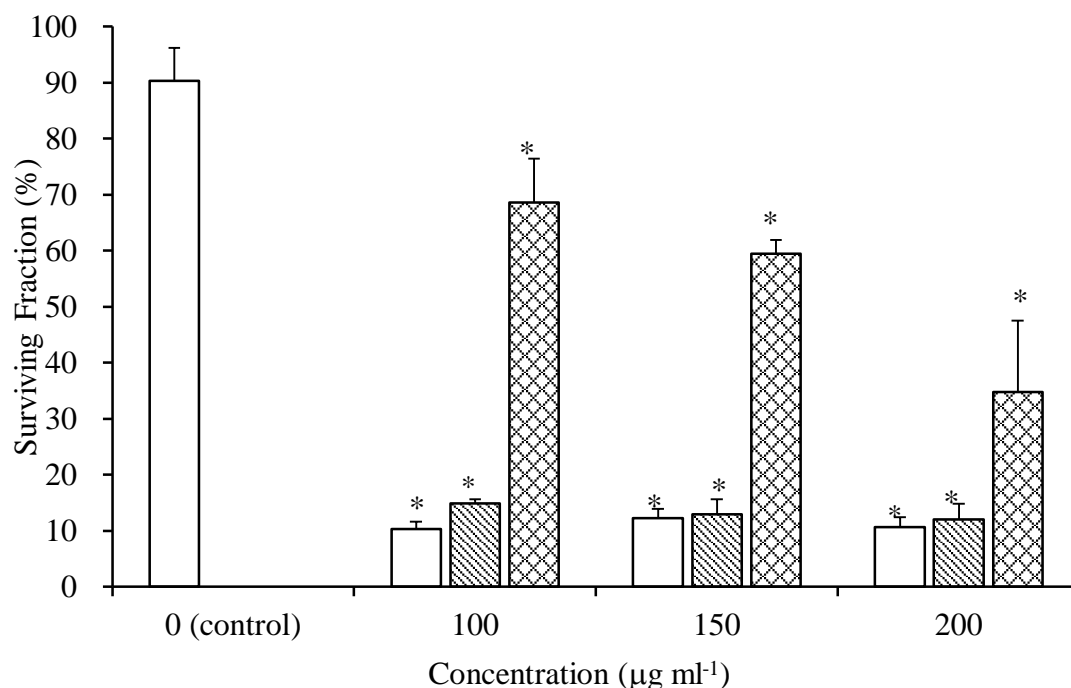


Fig.3.16 Effect of photoexcited P25 (□), TS (▨) and TS-FA (▩) nanoparticles on cell viability. Irradiation time is 60 min. * $p < 0.05$ as compared to control. All the data were expressed as mean \pm SD and $n=3$.

3.3.6 Cell internalisation

Results from cell internalisation experiments were shown in Fig. 3.17, and strong fluorescence was observed in both P25- and TS-FA-treated cells. However, there was little fluorescence observed in TS-treated cells. The strong fluorescence observed for the P25-treated cells may be because TiO_2 nanoparticles can incorporate with cell membrane proteins, resulting in preferential accumulation on cancer cells (Thevenot et al. 2008). Hence, the ROS generated from the photoexcited TiO_2 were concentrated at the cell membrane interface, leading to the destruction of the cell membrane and, thereby, cell death in the form of necrosis or apoptosis. A higher photo-killing effect by P25 was well demonstrated in the previous section. For TS-

treated KB cells, there was a slight fluorescence observed, suggesting that TS nanoparticles were randomly bound to KB cells. The TS-FA-treated cells showed strong fluorescence, indicating that the folic acid presented on the surface of TS-FA nanoparticles had been specifically bound with the folate receptors on the KB cells (folate-receptor positive cells). This is the reason that the photo-killing effect of the TS-FA nanoparticles was comparable to that of the TiO₂ nanoparticles, as discussed in the previous section.

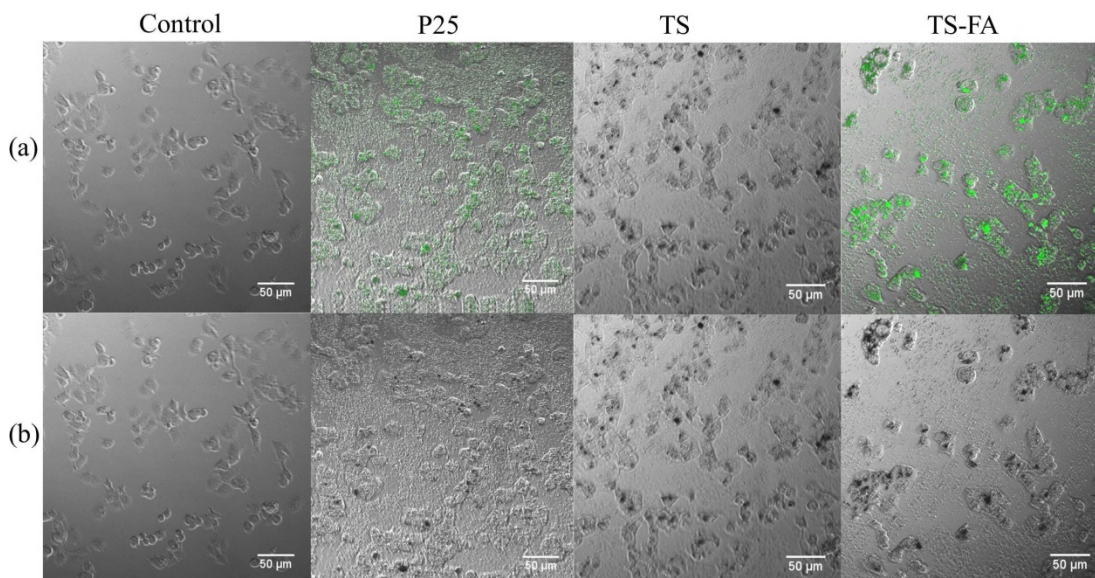


Fig. 3.17. Fluorescence confocal micrographs of KB cells internalized with P25, TS, and TS-FA. All images were recorded after 6 h of incubation with 100 µg ml⁻¹ nanoparticles at 37 °C. Upper panel (a): fluorescence images. Lower panel (b): the corresponding differential interference contrast (DIC) micrographs.

3.4 Conclusion

In summary, a novel folic acid-conjugated TiO₂-SiO₂ core-shell hybrid nanoparticulate system, TS-FA, was fabricated using the commercially available semiconductor catalyst, P25, and confirmed by various chemical and physical characterisation methods. The results have shown that the produced TS-FA nanoparticles are nontoxic to both L929 cells and KB cells in the dark, and are well tolerated by human red blood cells. A strong increase in viability of both L929 and KB cells was demonstrated after cells were incubated with TS-FA in the range between 12.5 and 200 µg ml⁻¹, showing that the presence of the folate element acts as

a nutrient for the cells. Upon exposure to UV light for 30 min, both P25 and TS-FA were toxic to KB cells due to their high photocatalytic activities. The cell internalisation experiments proved that folic acid-conjugated nanoparticles were bound to KB cells (folate receptor-positive cells), indicating a high ability to target cancerous cells. The dual targeting capabilities, through both the folic acid conjugation and high photoexcitation efficiency of the TS-FA system, promises great potential in the treatment of cancer, and possibly other diseases. It is worth noting the very strong concentration and exposure time dependence of the photo-killing effects that were observed in the cells exposed to TS-FA. This is an observation different from that of the cells exposed to other nanoparticles, and has never been reported before. It is understood that the reason is most likely due to the nutrimental function of the folate elements, but a more systematic study is under way to optimise the photo-killing power of the TS-FA system for a greater variety of cancerous cells.

CHAPTER 4 SYNTHESIS AND CHARACTERISATION OF Fe₃O₄-ZnO NANOPARTICLES FOR ENHANCED PHOTOCATALYTIC PROPERTIES

4.1 Introduction

This chapter aims to develop highly photocatalytic ZnO nanoparticles through their hybridisation with Fe₃O₄. Magnetic iron oxide (Fe₃O₄) nanoparticles with an average size of 21±5 nm were first prepared using a chemical co-precipitation method and, subsequently, suspended in tetramethylammonium hydroxide (TMAH) solution. The iron oxide-zinc oxide (Fe₃O₄-ZnO) hybrid nanoparticles were prepared through the dehydration of zinc acetate dihydrate using magnetite nanoparticles as the seeding template. Varying amounts of Fe₃O₄ nanoparticles were used to adjust the theoretical mass ratio of ZnO and Fe₃O₄ in the hybrid nanoparticles, with the corresponding reactions schematically presented in Fig. 4.1. The produced Fe₃O₄ nanoparticles and Fe₃O₄-ZnO hybrid nanoparticles were examined using various instruments including a field emission scanning electron microscope (FESEM), a transmission electron microscope (TEM) equipped with an energy dispersive spectroscope (EDS), an X-ray Diffractometer (XRD), a Fourier transform infrared (FTIR) spectroscope, an atomic absorption spectrometer (AAS) and an ultraviolet-visible diffuse reflectance spectroscope (UV-Vis DRS). The photocatalytic performance of the produced nanoparticles was examined using phenol as a target organic molecule. During the photocatalytic reaction, the loss of Fe²⁺/Fe³⁺ and Zn²⁺ due to the photocorrosion of the hybrid nanoparticles also was investigated. The recoverability and stability studies of the hybrid nanoparticles also were carried out.

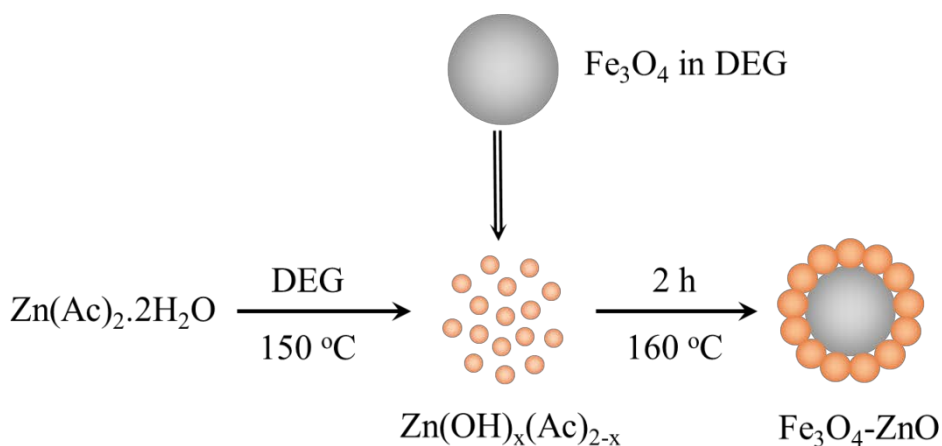


Fig.

4.1 A schematic illustration of the Fe_3O_4 -mediated growth process. Nanoparticulate Fe_3O_4 seeds were added to the reaction mixture of $\text{Zn}(\text{Ac})_2 \cdot 2\text{H}_2\text{O}$ and DEG. Fe_3O_4 -ZnO was produced via the dehydration of $\text{Zn}(\text{Ac})_2 \cdot 2\text{H}_2\text{O}$ in the presence of DEG at a high temperature.

4.1.1. Background

Heterogeneous photocatalysis in the presence of semiconductors has been investigated increasingly in the past two decades due to a wide variety of applications, particularly in the degradation of organic pollutants discharged into water (Kubacka et al. 2011). Among those semiconductors, zinc oxide (ZnO) is widely recognised as an excellent material for photocatalytic processes, owing to its high photosensitivity, environmentally friendly nature and relatively low cost (Hoffmann et al. 1995, Yu and Yu 2008). Zinc oxide is an n-type semiconductor with a wide band-gap of 3.2 eV. Upon exposure to ultraviolet (UV) radiation, ZnO can be photoexcited to generate negative electrons (e_{CB}^-) in the conduction band and positive holes (h_{VB}^+) in the valence band. The photoinduced electron-hole pairs are able to either recombine or be captured by other molecules, such as water or oxygen, forming reactive oxygen species (ROS) such as the hydroxyl radical ($\bullet\text{OH}$) and superoxide radical anion ($\bullet\text{O}_2^-$). The mechanism of formation of the electrons and holes, and their further chemical reactions with water and oxygen, is schematically illustrated in Fig. 4.2, in which the h_{VB}^+ reacts with water to produce hydroxyl radicals ($\bullet\text{OH}$), whilst the e_{CB}^- reacts with O_2 to form superoxide radical anions ($\bullet\text{O}_2^-$) and hydrogen peroxide (H_2O_2). The latter also can generate hydroxyl radicals ($\bullet\text{OH}$). These ROS can destroy the structure of various organic pollutants, leading to the

formation of non-toxic carbon dioxide and water (Pirkanniemi and Sillanpää 2002, Rajeshwar et al. 2008).

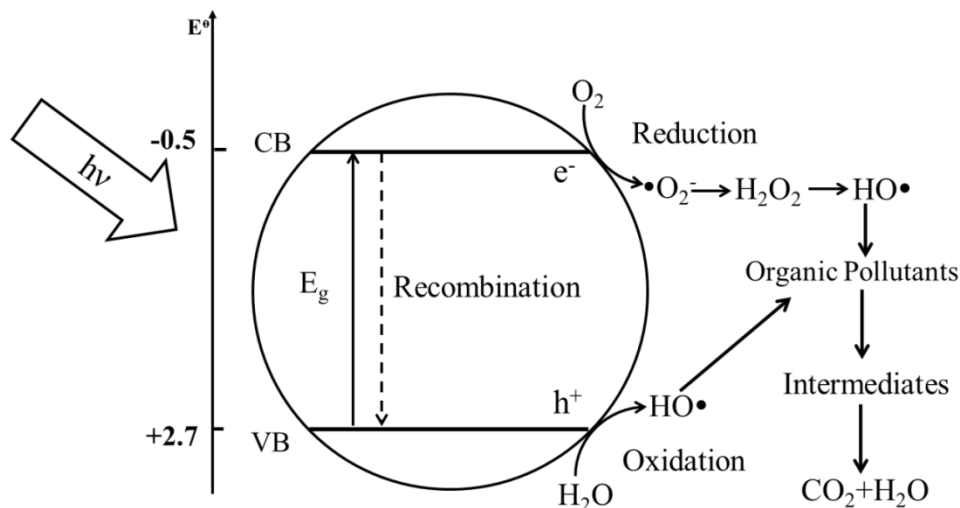


Fig. 4.2. A schematic illustration of the ZnO photocatalytic reaction mechanism.

Since the catalytic activities of ROS take place on the surface of the catalysts, nanoparticulate ZnO is generally more active than conventional bulk material (Hoffmann et al. 1995). However, the photocatalytic effectiveness of ZnO nanoparticles often is compromised by the fast recombination of the photoinduced electron-hole pairs, which has led to increasing developmental research on novel strategies that can suppress the charge recombination (Jiang et al. 2010). Enhanced photocatalytic activity has been seen in $\text{Fe}_3\text{O}_4/\text{TiO}_2$ nanocomposites, reportedly due to the decelerated electron-hole recombination in the presence of iron ions (Jing et al. 2013). The presence of iron ions also have been said to be electron or hole traps in a TiO_2 lattice. In this work we intend to add Fe_3O_4 into ZnO in order to retain the fast recombination of the photo-induced charge carriers, thereby enhancing photocatalytic activity of the resultant nanoparticles.

In addition, the industrial applications of such nanoparticles as TiO_2 and ZnO require efficient recovery and removal of these particles after usage. This is particularly important for wastewater treatment. Filtration, or centrifugation, is often required to prevent the possible large scale loss and the potential secondary pollution

caused by the loss of ultrafine nanoparticles (Guo et al. 2011). Magnetic nanoparticles (Fe_3O_4 or $\gamma\text{-Fe}_2\text{O}_3$ or ferrite) as the employed nanoparticles have provided a solution to these problems. For instance, the core-shell structured $\text{Fe}_3\text{O}_4/\text{SiO}_2/\text{TiO}_2$ particles can be recovered using an external magnetic field, and their photocatalytic activity is maintained, even after eighteen cycles of use (Ye et al. 2010). Hence, these materials have been proved to be effective in both separation and reuse (Shylesh et al. 2010).

In this work, it was attempted to develop a novel type of magnetic ZnO hybrid nanoparticle with enhanced photocatalytic activities and recoverability. $\text{Fe}_3\text{O}_4\text{-ZnO}$ hybrid nanoparticles were synthesised, with varying mass ratios of Fe_3O_4 and ZnO, and the physicochemical properties, photocatalytic properties and recoverability of the produced hybrid nanoparticles were investigated. This is the first work demonstrating an enhanced photocatalytic activity of magnetic ZnO nanoparticles due to the presence of iron ions.

4.2 Experimental

4.2.1 Materials and chemicals

Ferric chloride hexahydrate ($\text{FeCl}_3\cdot 6\text{H}_2\text{O}$, 99.99%), ferrous chloride tetrahydrate ($\text{FeCl}_2\cdot 4\text{H}_2\text{O}$, 99.99%), zinc acetate dihydrate ($\text{Zn}(\text{Ac})_2\cdot 2\text{H}_2\text{O}$, $\text{Ac}=\text{CH}_3\text{COO}$, $\geq 98\%$), hydrochloric acid solution (HCl, 7.3%), diethylene glycol (DEG, 99%) and ethanol anhydrous ($\geq 99.5\%$) were obtained from Sigma-Aldrich. Ammonia solution ($\text{NH}_3\cdot \text{H}_2\text{O}$, 25%) and tetramethylammonium hydroxide (TMAH, 25%) were obtained from Fluka. Deionised water was used in all experiments.

4.2.2 Synthesis of Fe_3O_4 nanoparticles

Magnetite (Fe_3O_4) nanoparticles were synthesised using the chemical co-precipitation method reported by Massart (Massart 1981). The chemical reaction is illustrated as follows:



In brief, a 2 M FeCl₂ solution and a 1 M FeCl₃ solution were prepared by dissolving iron salts in 2 M HCl solution. One ml of FeCl₂ solution was mixed with 4 ml of FeCl₃ solution under nitrogen atmosphere with vigorous stirring, and then 50 ml of ammonia solution was added, dropwise, to the Fe²⁺ /Fe³⁺ mixture. After allowing the reaction to proceed for 15 min, the black precipitate was washed three times with deionised water (15 ml) to remove any excess reactants. The obtained Fe₃O₄ nanoparticles were dispersed in TMAH solution to prevent aggregation. In general, Fe₃O₄ (0.4 g) was dispersed in TMAH solution (0.5 ml) and then further diluted with deionised water to a total volume of 4.0 ml.

4.2.3 Synthesis of Fe₃O₄-ZnO hybrid nanoparticles

Fe₃O₄-ZnO hybrid nanoparticles were prepared by dehydrating Zn(Ac)₂·2H₂O in the presence of various amounts of Fe₃O₄ nanoparticles in DEG. In a typical procedure, Zn(Ac)₂·2H₂O (2.24 g, 0.01 mol) was added to DEG (100 ml) and the reaction mixture was heated to 150 °C under nitrogen protection. Thirty ml of DEG, containing Fe₃O₄ nanoparticles (0.1 g, 0.43 mmol), was added, dropwise, to the reaction mixture. The temperature of the reaction mixture then was heated up to 160 °C and maintained for 2 h. The reaction mixture was allowed to cool to room temperature. The resultant Fe₃O₄-ZnO particles were collected using a centrifuge. The particles were washed three times with DEG (3×15 ml) then three times with deionised water (3×15 ml) and dried overnight at room temperature, under vacuum. The product was named Fe₃O₄-ZnO(8) since the theoretical mass ratio of Fe₃O₄ and ZnO in the compound is 1:8.

By varying the amounts of Fe₃O₄ nanoparticles added in the reaction mixture, using 0.2 g (0.86 mmol) and 0.4 g (1.72 mmol), respectively, Fe₃O₄-ZnO(4) and Fe₃O₄-ZnO(2) also were produced. The chemical reaction is schematically illustrated in Fig. 4.1. The chemical compositions of these nanoparticles are listed in Table 4.1.

As a control, pure ZnO nanoparticles were synthesised using a similar procedure to that described above. However, Fe₃O₄ nanoparticles were replaced with colloidal

ZnO, produced in a primary reaction in which dehydration of $\text{Zn}(\text{Ac})_2 \cdot 2\text{H}_2\text{O}$ took place. The details of this reaction procedure were reported previously by Seeling et al. (Seeling et al. 2003).

4.2.4 Characterisation of Fe_3O_4 , Fe_3O_4 -ZnO and ZnO nanoparticles

A FESEM (Zeiss Neon 40EsB) was used to examine the morphology of Fe_3O_4 nanoparticles. The sample, suspended in deionised water, was deposited onto an aluminium stub, where a platinum coating (2 nm) was used as a conducting surface material. The FESEM images were recorded at an accelerating voltage of 5 kV. The sizes of the particles were measured using the SmartSEM software installed on the Zeiss Neon 40EsB operating system. This software is linked to the magnification scale bar of the obtained image. Thirty particles were randomly selected for the size measurements. For morphological examination of ZnO and Fe_3O_4 -ZnO nanoparticles, an ethanol suspension of nanoparticles was distributed on a copper grid with a carbon substrate and examined using a TEM (JEOL JSM 2011) equipped with a Gatan Digital Camera. The TEM images were recorded at an accelerating voltage of 200 kV. The size was analysed using the in-built JEOL operational software, DigitalMicrograph, which also is related to the magnification scale bar of the obtained TEM images. The average value of thirty measurements was taken as the representative size of each type of particle.

X-ray diffraction (XRD) analysis was conducted on all samples using a Bruker D8-Advance X-ray Diffractometer with $\text{Cu K}\alpha$ radiation ($\lambda = 1.54178 \text{ \AA}$). A scan rate of $0.015^\circ \text{ s}^{-1}$ was used to record the patterns in a 2θ range of $20\text{--}80^\circ$, and the accelerating voltage and current were 40 kV and 40 mA, respectively. FTIR spectroscopy was performed on a Thermo Scientific Nicolet iS50 fitted with an Automated Beamsplitter Exchanger (ABX), affording both mid-IR and far-IR capabilities. All spectra were recorded in the range of $200\text{--}4000 \text{ cm}^{-1}$ at a resolution of 4 cm^{-1} with 64 co-added scans. UV-Vis diffuse reflectance spectra (DRS) of samples were obtained on a Jasco V670 spectrophotometer equipped with an integrating sphere, and BaSO_4 was used as a reference material. UV-Vis DRS scans were recorded in the wavelength range from 300 to 750 nm with a band width of 2 nm.

To determine the ratio of elemental Fe and Zn in the hybrid nanoparticles, an AAS (Shimadzu AA-7000) equipped with a hollow cathode lamp using an air-acetylene flame was used. The analysis of iron was performed at a wavelength of 248.3 nm with a slit width of 0.2 nm, while that of zinc was obtained at a wavelength of 213.9 nm with a slit width of 0.7 nm. Two calibration curves were obtained by working with a standard iron solution ($0.06\text{--}15\ \mu\text{g ml}^{-1}$) and a standard zinc solution ($0.01\text{--}2\ \mu\text{g ml}^{-1}$), respectively. For sample analysis, around 1 mg of each sample was dissolved in 25 ml of 2 M HNO_3 and the mixture was heated at 80 °C for 60 min in a water bath. After allowing the mixture to cool to room temperature, the sample was diluted with deionised water to a concentration within the range of the prepared standard concentrations.

Table 4.1 Chemical and physical properties of the synthesised nanoparticles.

Sample ID	Reactants' Fe ₃ O ₄ : Zn(Ac) ₂ ·2H ₂ O	Ratio (g:g)	Fe ₃ O ₄ :ZnO (theoretical)	Particle size (nm)	Metal Content by AAS (wt%)		Phenol Removal (%)
					Fe	Zn	
Fe ₃ O ₄	-	-	1:0	21±5	72.4	0	0
ZnO	0 : 2.24	-	0:1	49±7	0	80.3	52
Fe ₃ O ₄ -ZnO(2)	0.1 : 2.24	-	1:2	43±8	18.2±1.0	60.2±1.0	65.5
Fe ₃ O ₄ -ZnO(4) (C1)	0.2 : 2.24	-	1:4	45±8	11.8±0.2	67.2±0.8	82.8
Fe ₃ O ₄ -ZnO(4) (C2)	-	-	-	-	14.6±0.4	64.1±0.4	72.4
Fe ₃ O ₄ -ZnO(4) (C3)	-	-	-	-	20.1±1.5	60.6±0.2	65.1
Fe ₃ O ₄ -ZnO(8)	0.4 : 2.24	-	1:8	142±19	8.6±1.0	70.8±0.8	38

C1, C2 and C3 denote the phenol degradation cycles.

4.2.5 Adsorption and photoreactivity study

The photocatalytic performances of the produced Fe₃O₄ nanoparticles, Fe₃O₄-ZnO hybrid nanoparticles and ZnO nanoparticles were evaluated by measuring the degradation efficiency of phenol solution under light irradiation, using a procedure and experimental set-up reported previously. The adsorption of phenol on the investigated nanoparticles also was studied using the same experimental set-up and procedure. However, the reaction mixtures were kept in the dark. In a typical procedure, the photocatalyst (65 mg) was suspended in aqueous phenol solution (200 ml), which resulted in a catalyst concentration of 0.325 g L⁻¹. This reaction mixture was put into a 1 L double-jacket reactor with cycled cooling water (25±1 °C). The light irradiation was facilitated by an MSR 575/2 metal halide lamp (575 W, Philips) with a wavelength in the range of 315–1050 nm. The reaction mixture firstly was stirred for 30 min, in the dark, then the light was immediately switched on. At set time intervals, 3 ml of solution was withdrawn via a syringe and filtered using a 0.45 µm Millipore filter. The concentration of phenol was determined by an HPLC (Varian) with a UV detector adjusted to 270 nm. The mobile phase was a mixture of acetonitrile and ultrapure water (30:70, v/v) with a flow rate of 1.0 ml min⁻¹. The aforementioned photoreactivity experiments were performed once. It is worthy to mention that the method employed in the work is well established and proven reproducible in our previous work (Sun et al. 2011).

4.2.6 Reusability and stability study of Fe₃O₄-ZnO hybrid nanoparticles

For the catalyst reuse studies, only Fe₃O₄-ZnO(4) nanoparticles were used in the photodegradation of phenol experiment. After the first photodegradation cycle, these nanoparticles were collected by applying a magnet to the reaction solution, and then washing them three times with deionised water (3×15 ml), followed by three times with ethanol (3×15 ml). Then they were dried them overnight at room temperature under vacuum. Fresh phenol solution was mixed with the used nanoparticles and subjected to the cyclic experiment. The third photodegradation cycle experiment was performed in the same manner as the first and second cycles. Each photodegradation

cycle was carried out using the same quantities: phenol solution (200 ml, 20 $\mu\text{g ml}^{-1}$) and catalyst (0.325 g L^{-1}). The same amounts of catalyst were used in each cycle because the lost portion was made up with recovered nanoparticles from each previous cycle. In order to maintain the amount of $\text{Fe}_3\text{O}_4\text{-ZnO}(4)$ used in each reaction cycle, extra sets of photodegradation experiments were carried out in cycles one and two.

4.3 Results and Discussion

4.3.1 Characterisation of the Fe_3O_4 , $\text{Fe}_3\text{O}_4\text{-ZnO}$ and ZnO nanoparticles

Fe_3O_4 nanoparticles were obtained from the co-precipitation reaction of FeCl_2 and FeCl_3 , with an average size of 21 ± 5 nm (Fig.4.3a). Dehydration of $\text{Zn}(\text{Ac})_2 \cdot 2\text{H}_2\text{O}$ at 160 $^\circ\text{C}$, in the presence of various amounts of Fe_3O_4 nanoparticles, resulted in the formation of three hybrid nanoparticles: $\text{Fe}_3\text{O}_4\text{-ZnO}(8)$, $\text{Fe}_3\text{O}_4\text{-ZnO}(4)$ and $\text{Fe}_3\text{O}_4\text{-ZnO}(2)$. The Fe_3O_4 nanoparticles have been shown to act as seeds to facilitate the precipitation and growth of ZnO, which clearly can be seen in the TEM images displayed in Fig. 4.3(c-e). The presence of ZnO on the surface of Fe_3O_4 nanoparticles was clearly demonstrated in the EDS spectrum of $\text{Fe}_3\text{O}_4\text{-ZnO}(8)$ (Fig. 4.3f).

The morphology of each hybrid nanoparticle was generally the same, however the particle sizes increased with the decreasing amounts of Fe_3O_4 added into the reaction. This is particularly significant when the theoretical mass content of Fe_3O_4 was reduced to 1 in 8 parts of ZnO. The measured average sizes of the hybrid nanoparticles were 43 ± 8 nm, 45 ± 8 nm and 142 ± 19 nm for $\text{Fe}_3\text{O}_4\text{-ZnO}(2)$, $\text{Fe}_3\text{O}_4\text{-ZnO}(4)$ and $\text{Fe}_3\text{O}_4\text{-ZnO}(8)$, respectively. A similar effect was observed by Seeling et al. in the synthesis of ZnO nanospheres (Seeling et al. 2003). They concluded that the size of the obtained nanospheres varies inversely with the amount of colloidal seeds added into the reaction mixture. Using a similar method, pure ZnO nanoparticles were synthesised as a control. The measured average size of ZnO nanoparticles was 49 ± 7 nm (Fig. 4.3b).

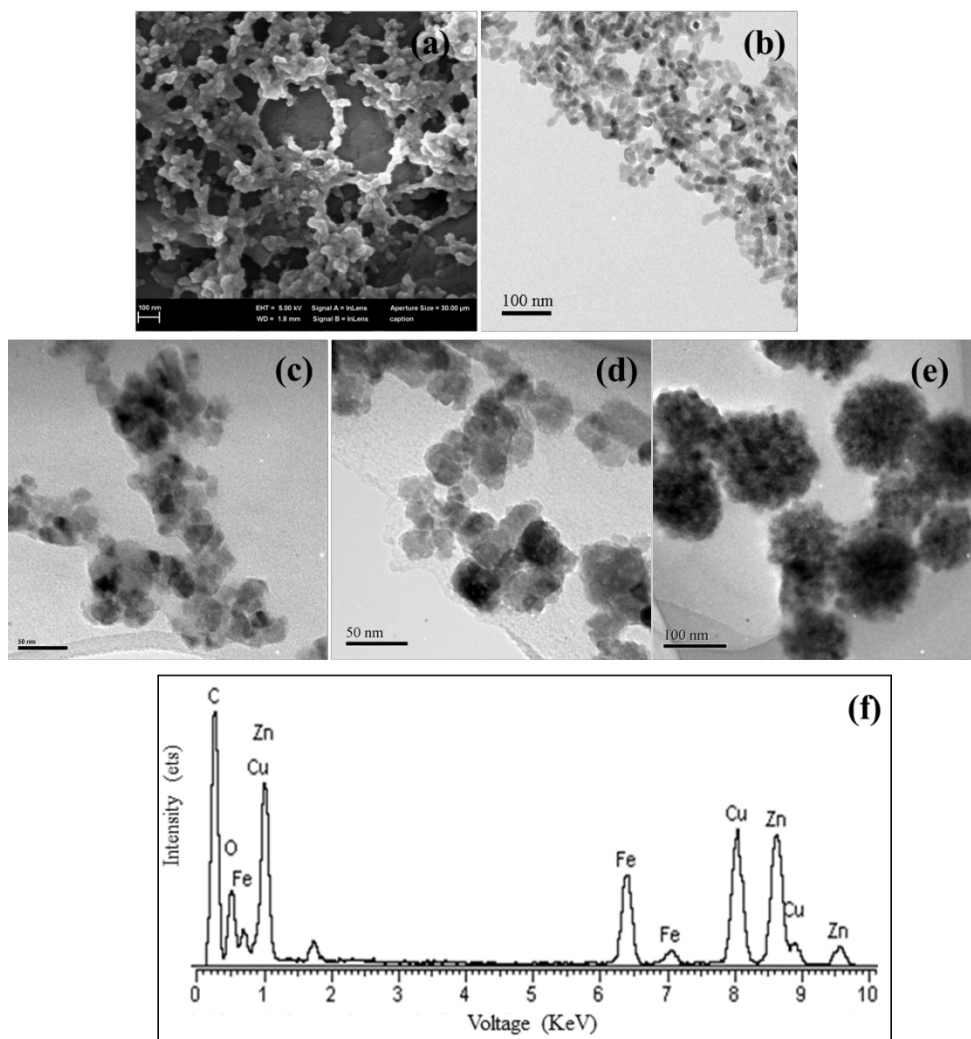


Fig.4.3 FESEM image of (a) Fe_3O_4 ; TEM images of (b) ZnO , (c) $\text{Fe}_3\text{O}_4\text{-ZnO}(2)$, (d) $\text{Fe}_3\text{O}_4\text{-ZnO}(4)$ and (e) $\text{Fe}_3\text{O}_4\text{-ZnO}(8)$; and EDS spectrum of (f) $\text{Fe}_3\text{O}_4\text{-ZnO}(8)$, showing the morphology, the size and the presence of elemental Fe, Zn and O in the relevant nanoparticles. In (f), Cu is from the copper grid and C is from the carbon film on the copper grid.

The XRD patterns of the produced nanoparticles are presented in Fig. 4.4. For pure Fe_3O_4 , the diffraction peaks at $2\theta = 30.1^\circ, 35.5^\circ, 43.2^\circ, 53.3^\circ, 57.0^\circ$ and 62.7° match well with the (220), (311), (400), (422), (511) and (440) planes, respectively, of the face-centred cubic structure (Feng et al. 2011). Four new peaks were identified in each of the $\text{Fe}_3\text{O}_4\text{-ZnO}$ hybrid nanoparticles. These were $2\theta = 31.9^\circ, 34.5^\circ, 36.1^\circ$ and 47.3° (Fig. 4-4(b-d)), and they are seen also in ZnO (Fig. 4.4e). They are indexed for the crystal faces of (100), (002), (101) and (102) of hexagonal wurtzite-structured ZnO (Hong et al. 2006). The relative intensities of ZnO components increased with the increase of the ratio, $\text{ZnO}:\text{Fe}_3\text{O}_4$.

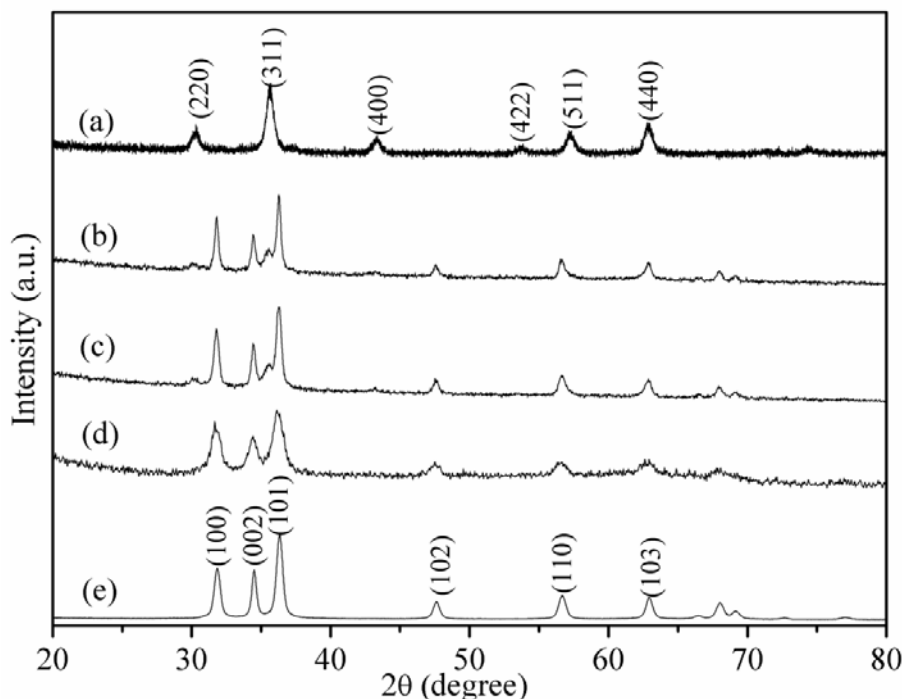


Fig. 4.4 XRD patterns of (a) Fe_3O_4 , (b) $\text{Fe}_3\text{O}_4\text{-ZnO}(2)$, (c) $\text{Fe}_3\text{O}_4\text{-ZnO}(4)$, (d) $\text{Fe}_3\text{O}_4\text{-ZnO}(8)$ and (e) ZnO .

FTIR spectra of all nanoparticles are shown in Fig. 4.5. For Fe_3O_4 , the peak at 540 cm^{-1} is attributed to the stretching vibration of the Fe-O bond. There is a weak peak at 1640 cm^{-1} which corresponds to the bending vibration of -OH groups that is commonly seen in Fe_3O_4 , produced by the chemical co-precipitation reaction (Liu et al. 2004). For ZnO , the absorption peak at 375 cm^{-1} is due to the stretching vibration of Zn-O, which agrees well with the results reported in the literature (Xiong et al. 2006, Ramani et al. 2013). The stretching vibrations of both the Fe-O bond, at 540 cm^{-1} , and the Zn-O bond, at 375 cm^{-1} , were observed in $\text{Fe}_3\text{O}_4\text{-ZnO}$ hybrid nanoparticles (Fig. 4.5(b-d)). In addition, there are two absorption peaks at 1419 cm^{-1} and 1560 cm^{-1} , which appeared in the FTIR spectra of the $\text{Fe}_3\text{O}_4\text{-ZnO}$ hybrid nanoparticles. These are caused by the stretching vibrations in the acetate groups of the C-O and C=O, respectively, indicating the presence of the metal complexes $\text{Zn}(\text{OH}^{-1})_x(\text{Ac})_{2-x}$ during the dehydration of $\text{Zn}(\text{Ac})_2 \cdot 2\text{H}_2\text{O}$ in DEG. The metal complex has been considered as an intermediate in the formation of ZnO , produced according to Eqs. (4.2-4.3) (Cheng et al. 2005b). The two weak peaks at 2920 cm^{-1} and 2853 cm^{-1} are due to the symmetric and asymmetric stretching

vibrations of the -CH₃ groups in the acetate groups (Xiong et al. 2006). It also is noticed that the relative strengths of the two signals at 540 cm⁻¹ and 375 cm⁻¹ change with varying ZnO content in the hybrid nanoparticles. The higher is the ZnO content, the stronger is the 375 cm⁻¹ peak.

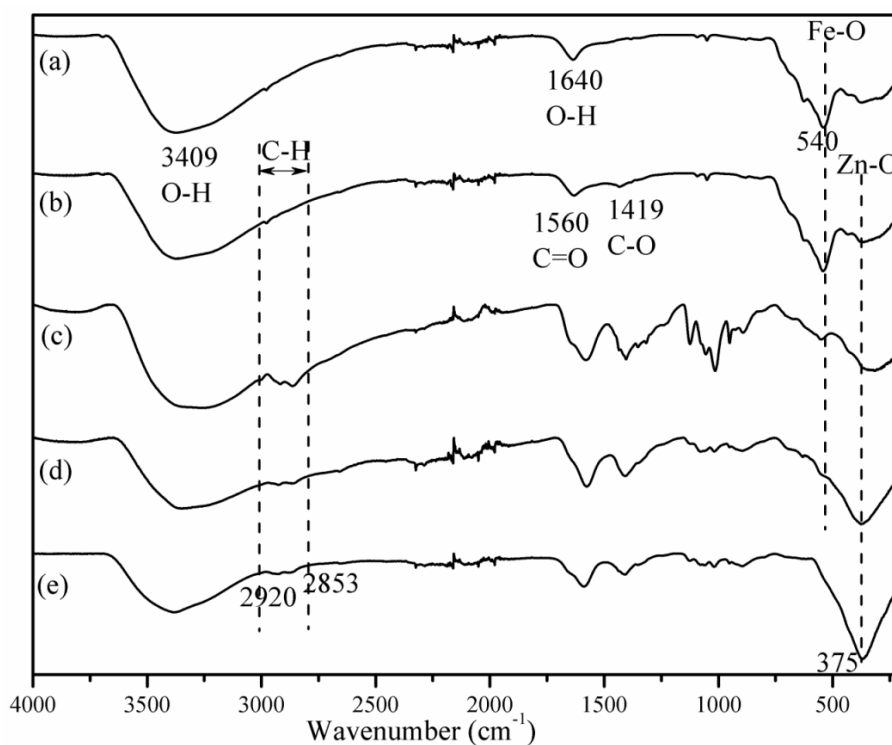
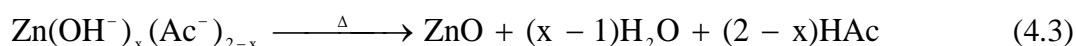


Fig. 4.5 FTIR spectra of (a) Fe₃O₄, (b) Fe₃O₄-ZnO(2), (c) Fe₃O₄-ZnO(4), (d) Fe₃O₄-ZnO(8) and (e) ZnO.

The metal content values for Fe and Zn were determined by AAS and are shown in Table 4.1. The measured mass ratios of Fe₃O₄ to ZnO based on these data are 1:7.4, 1:5.1 and 1:3.0 for Fe₃O₄-ZnO (8), Fe₃O₄-ZnO(4) and Fe₃O₄-ZnO(2), respectively.

The optical properties of various nanoparticles were probed by UV-Vis DRS. As presented in Fig. 4.6e, the absorption threshold of pure ZnO was 390 nm. The

corresponding band gap energy was 3.2 eV, which is consistent with the reported value (Xu et al. 2011). In the case of Fe_3O_4 (Fig. 4.6a), there was a broad band at 300-750 nm that can be attributed to the octahedral Fe^{3+} (Xing et al. 2011). The UV-Vis spectra of the resultant Fe_3O_4 -ZnO hybrid nanoparticles demonstrate absorptions in both sections, and the change in the mass ratio of Fe_3O_4 to ZnO is reflected well.

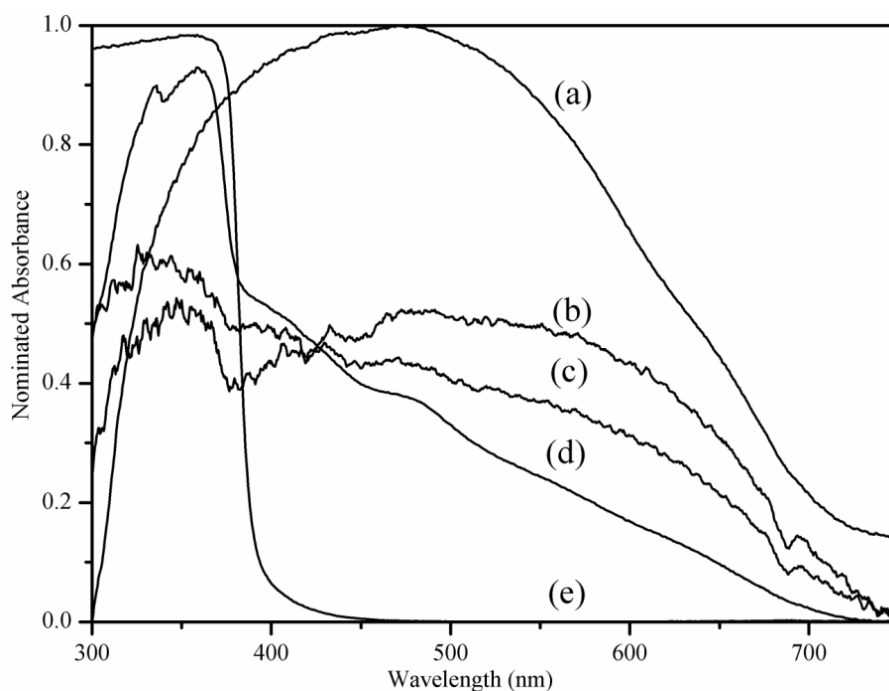


Fig. 4.6 UV-Vis spectra of (a) Fe_3O_4 , (b) Fe_3O_4 -ZnO(2), (c) Fe_3O_4 -ZnO(4), (d) Fe_3O_4 -ZnO(8) and (e) ZnO.

4.3.2 Photocatalytic properties of Fe_3O_4 -ZnO hybrid nanoparticles

The photocatalytic properties of the obtained nanoparticles were evaluated based on the photodegradation of phenol under light radiation. Phenol is considered to be one of the important organic pollutants discharged into the environment, causing significant damage and threat to the ecosystem in water bodies and human health. They can be degraded into carbon dioxide and water in the presence of photocatalysts under UV light. The degradation process involves reactions of the ROS with the phenyl ring, yielding catechol, resorcinol and hydroquinone. These

organic compounds then break up to produce maleic, oxalic, acetic, formic acids, and finally carbon dioxide. Various photodegradation pathways have been proposed (Guo et al. 2006, Grabowska et al. 2012). The models vary from one to another in the number and species of the intermediate compounds and by-products. The ultimate degradation products are carbon dioxide and water. In this study, phenol was used as a model compound to compare the photocatalytic properties of the produced nanoparticles.

Prior to the photocatalytic degradation experiments, adsorption of phenol on the nanoparticles was investigated. The results showed no phenol adsorption capacity, for both the Fe₃O₄ and Fe₃O₄-ZnO hybrid nanoparticles, in the first 150 min. For photodegradation, the percentage degradation of phenol at various time intervals is displayed in Fig. 4.7. No phenol degradation was observed during the first 150 min when Fe₃O₄ nanoparticles were used. In the presence of Fe₃O₄-ZnO(2), Fe₃O₄-ZnO(4) and Fe₃O₄-ZnO(8), the percentage degradation of phenol was 65.5%, 82.8% and 38.0%, respectively. The phenol degradation was only 52% when pure ZnO was used, which is lower than that in the presence of either Fe₃O₄-ZnO(4) or Fe₃O₄-ZnO(2). The apparent rate constants of these catalysts were estimated using the Langmuir–Hinshelwood equation (Wu et al. 2006):

$$\ln\left(\frac{C_0}{C}\right) = kt \tag{4.4}$$

where k is the apparent reaction rate constant in the unit of min^{-1} , C_0 is the initial concentration and C is the concentration at time t . The k values for Fe₃O₄-ZnO(2), Fe₃O₄-ZnO(4), Fe₃O₄-ZnO(8) and ZnO were 0.0057, 0.0108, 0.0029 and 0.0039 min^{-1} , respectively. The least squared R values for each fitting were 0.996, 0.972, 0.995 and 0.997, respectively.

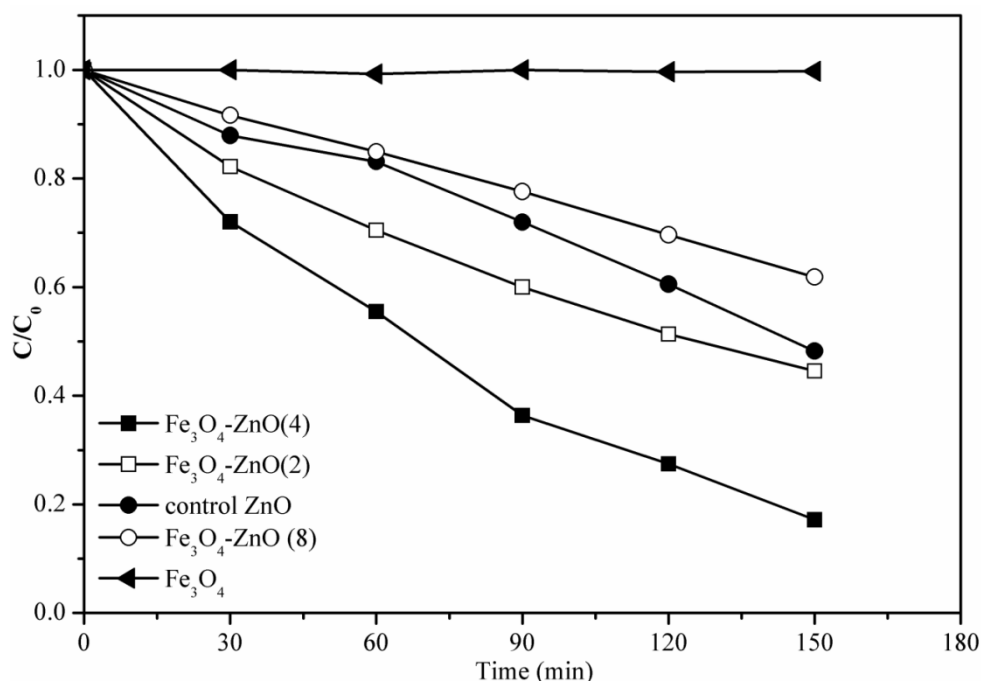


Fig. 4.7 Phenol concentration changes with time.

In comparison with pure ZnO, significantly enhanced photocatalytic activity was demonstrated well in both Fe₃O₄-ZnO(2) and Fe₃O₄-ZnO(4) hybrid nanoparticles. An increase in photocatalytic activity, as ZnO content in the hybrid nanoparticles increases, is indicated by the higher phenol degradation efficiency and the greater reaction rate constant value in the presence of Fe₃O₄-ZnO(4) than those in the presence of Fe₃O₄-ZnO(2).

A similar finding was reported by (Hong et al. 2008). The authors claimed that the lower photoactivity of ZnO was due to the larger particle size and size distribution. In this study, the particle sizes of ZnO, Fe₃O₄-ZnO(2) and Fe₃O₄-ZnO(4) were similar (Fig. 4.3 and Table 4.1). The enhanced photocatalytic activity of Fe₃O₄-ZnO(4) and Fe₃O₄-ZnO(2) possibly can be attributed to the retardation of the recombination of electron-hole pairs. In order to confirm this, the optical properties of ZnO and Fe₃O₄-ZnO(4) were further investigated using a PerkinElmer L55 Fluorescence Spectrometer with an excitation source set at 390 nm and a scanning rate of 10 nm min⁻¹. The obtained spectra are shown in Fig. 4.8. Both samples are centred well at 386 nm, however the photoemission intensity of the hybrid nanoparticles is lower than that of ZnO, indicating a slower electron-hole recombination in the hybrid nanoparticles. This is probably due to the presence of

Fe^{3+} ions in the hybrid nanoparticles. It has been reported that Fe^{3+} ions in Fe_3O_4 can act as photoexcited electron-trapping sites to prevent the fast recombination of photoinduced charge carriers and, thus, prolong their lifetime (Ambrus et al. 2008, Ahmed et al. 2013). In this study, the photo-generated electron in the conduction band of ZnO might be captured by the Fe^{3+} ions. This would lead to the formation of reduced iron ions, Fe^{2+} , which are relatively unstable in comparison with Fe^{3+} . The Fe^{2+} ions further react with the oxygen dissolved in the reaction mixture to generate Fe^{3+} ions and $\bullet\text{O}_2^-$ radicals. The photocatalysis continues (Fig. 4.9). A similar phenomenon has been observed in Fe-doped TiO_2 and ZnO by various researchers (Yu et al. 2009, Ba-Abbad et al. 2013). The presence of Fe^{3+} also has been suggested as a trigger for the enhanced photocatalytic activity observed in $\text{Fe}_3\text{O}_4\text{-TiO}_2$ (Tung and Daoud 2009, Jing et al. 2013).

The hybrid nanoparticles containing highest ZnO, i.e., $\text{Fe}_3\text{O}_4\text{-ZnO}(8)$, showed a lower photocatalytic activity than the other two types of hybrid nanoparticle, as well as the pure ZnO. This is most likely due to their much greater size, which reduces the reactive surface area of the nanocatalyst. In addition, the much lower Fe_3O_4 content is probably insufficient to suppress the recombination of the photo-induced electron-hole pairs.

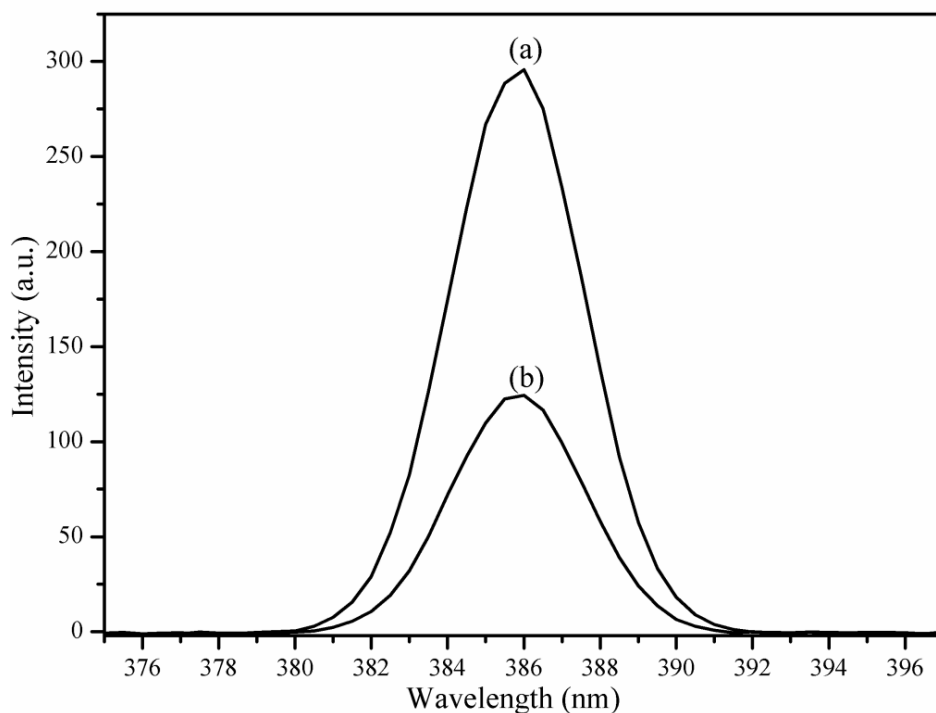


Fig. 4.8 Photoluminescence spectra of (a) ZnO and (b) Fe₃O₄-ZnO(4) hybrid nanoparticles.

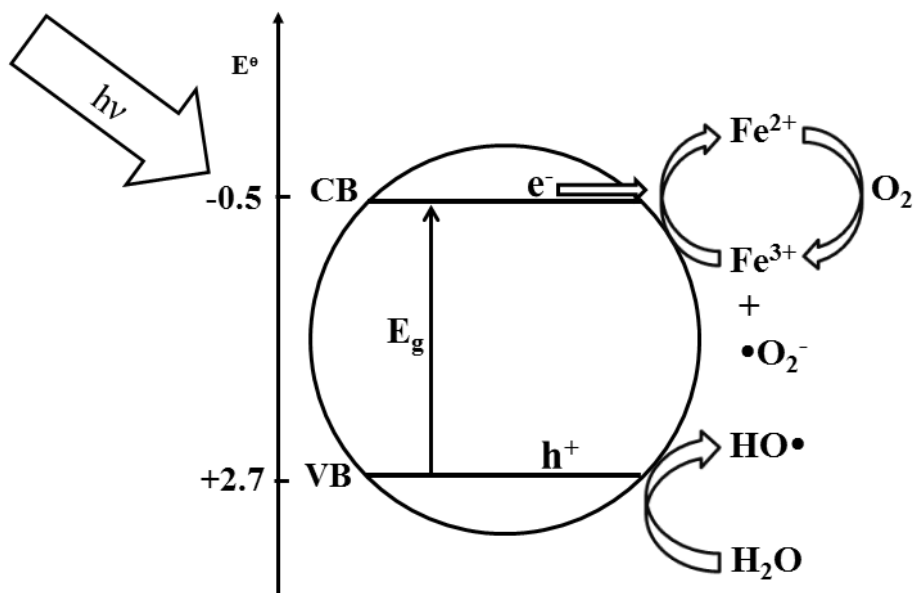


Fig.4.9 A hypothesised photocatalytic reaction mechanism of the Fe₃O₄-ZnO hybrid nanoparticles.

4.3.3 Reusability and stability of the catalyst

$\text{Fe}_3\text{O}_4\text{-ZnO}(4)$ hybrid nanoparticles exhibited superior photocatalytic activity as compared to ZnO nanoparticles in phenol degradation under UV light. Due to the difficulties in re-collection of such ultrafine nanoparticles and the potential secondary pollution caused by the lost catalyst, the recyclability and stability of the hybrid nanoparticles after the photocatalytic reaction deserve attention and have been investigated. Also, leaching of iron and zinc from the hybrid nanoparticles during the photocatalytic reaction is another factor that influences the stability of the hybrid nanoparticles.

As the reusability of the catalyst is an important parameter of the photodegradation process, the repetitive use of $\text{Fe}_3\text{O}_4\text{-ZnO}(4)$ was investigated in this study. A suspension of the hybrid nanoparticles in the phenol solution is shown in Fig. 4.10a. When a magnet was applied to the suspension, the hybrid nanoparticles immediately accumulated to the side of the glass vial near the magnet, leaving the phenol solution colourless (Fig. 4.10b), and demonstrating great ease of magnetic separation.

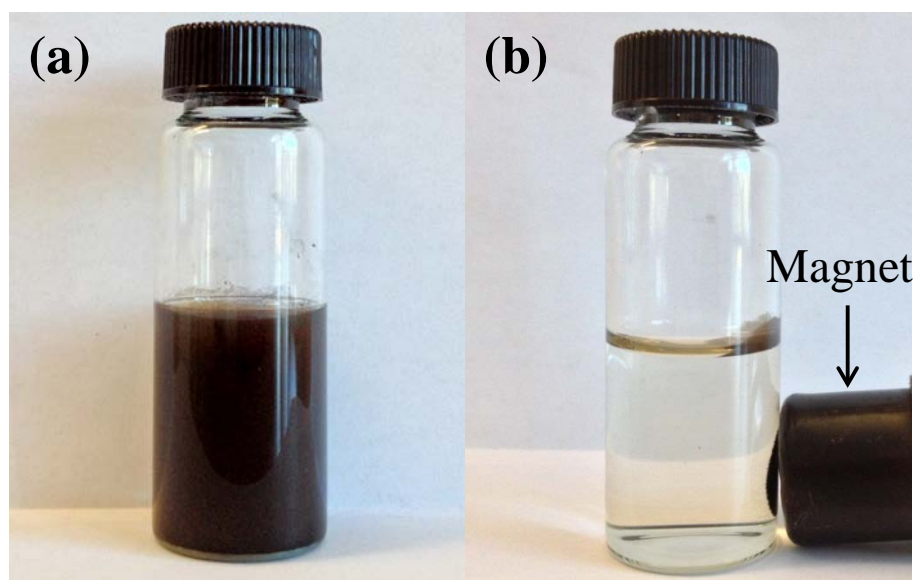


Fig. 4.10 Photographs of a $\text{Fe}_3\text{O}_4\text{-ZnO}(4)$ suspension (a) before, and (b) after, an external magnetic field was applied.

Phenol degradation in the presence of recycled Fe₃O₄-ZnO(4) nanoparticles was investigated under the same conditions used for freshly-made nanoparticles. Three cycles were examined. An average of 89% hybrid nanoparticles was recovered when using a magnet. This is much higher than that of ZnO (77%). The phenol removal was 82.8% in cycle one, which was reduced to 72.4% in cycle two and 65.1% in cycle three. All these values are much greater than that of the freshly-made ZnO (52%), indicating a high performance of the produced hybrid nanoparticles. The Zn content in the hybrid nanoparticles was determined using AAS. The values were 67.2 ± 0.8 wt%, 64.1 ± 0.4 wt% and 60.6 ± 0.2 wt%, respectively in these cycles, indicating that the mass ratios of Fe₃O₄ to ZnO in these particles were 1:5.1, 1:4.0 and 1:2.7. An AAS examination also was performed on the liquid samples collected after the completion of the third cycle of the photocatalysis reaction. The results showed that $7.18 \mu\text{g ml}^{-1}$ zinc ions and $0.35 \mu\text{g ml}^{-1}$ iron ions were present in the final phenol solution, representing a loss of 3.7% of zinc and 0.59% of iron after photocatalytic reaction (150 min). The loss of the zinc and iron ions is most likely due to the photocorrosion of the hybrid nanoparticles, in which the photo-induced holes react with Fe₃O₄ and ZnO, yielding Zn²⁺ and Fe³⁺/Fe²⁺ ions which are soluble in water (Beydoun et al. 2000, Li et al. 2009b). The presence of Fe³⁺/Fe²⁺ ions further demonstrated that the enhanced photocatalytic activity of Fe₃O₄-ZnO(2) and Fe₃O₄-ZnO(4) is likely to be a result of the retardation of the recombination of electron-hole pairs by the iron ions. This is in agreement with the hypothesis described in the photocatalytic properties section. The results also indicate that the reduced zinc ions in each cycle, due to the photocorrosion of ZnO, has led to the reduced photocatalytic activity of the recycled Fe₃O₄-ZnO(4) hybrid nanoparticles.

4.5 Conclusions

In summary, Fe₃O₄-ZnO hybrid nanoparticles were synthesised, using a seed-mediated process, through the dehydration of Zn(Ac)₂·2H₂O in the presence of DEG and Fe₃O₄ nanoparticles. By varying the amounts of Fe₃O₄ nanoparticles added into the reaction mixture, three hybrid nanoparticles, Fe₃O₄-ZnO (2), Fe₃O₄-ZnO (4) and Fe₃O₄-ZnO (8) were produced. TEM images indicated that the sizes of the hybrid nanoparticles increased with a decrease in the amounts of Fe₃O₄ added into the

reaction mixture. The presence of elemental Zn, Fe and O in the hybrid nanoparticles was proved using EDS. XRD and FTIR demonstrated the presence of Fe_3O_4 and ZnO in the hybrid nanoparticles. They also revealed that the relative intensities of ZnO components increased with the increasing mass ratio of ZnO: Fe_3O_4 . The quantitative analysis of elemental Fe and Zn was performed using AAS. The measured mass ratios of Fe_3O_4 to ZnO were 1:7.4, 1:5.1 and 1: 3.0 for Fe_3O_4 -ZnO (8), Fe_3O_4 -ZnO (4) and Fe_3O_4 -ZnO (2), respectively.

Upon exposure to UV light, the hybrid nanoparticles showed greatly enhanced photocatalytic activities compared with those of the pure ZnO nanoparticles, when the particle sizes were similar to each other. Also, there was an increase in photocatalytic activity, as ZnO content in the hybrid nanoparticles was evident. However, increased particle size had a negative impact on the photoreactivity. The enhancement of the photocatalytic properties was due to the suppressing effect of the hybrid nanoparticles on the recombination of the photoinduced charge carriers, confirmed by the Fluorescence Spectrometer. It is speculated that the presence of ferric ions in hybrid nanoparticles can act as electron-trapping sites to capture the photogenerated electrons, leading to deceleration of the electron-hole recombination and improving the catalytic efficiency of ZnO. The high photocatalytic performance also was demonstrated in the recycled Fe_3O_4 -ZnO hybrid nanoparticles. This can be of great importance in the application of nano-photocatalysis in water treatment.

Photocorrosion of ZnO and Fe_3O_4 was apparent. Whilst the loss of ZnO by photocorrosion might have led to the reduced photoreactivity of the recycled hybrid nanoparticles, the dissolution of iron ions could be critical for the enhanced overall photocatalytic properties of Fe_3O_4 -ZnO. It is concluded that the incorporation of Fe_3O_4 into ZnO nanoparticles not only has improved the recoverability, but also has enhanced the photocatalytic properties of ZnO nanocatalysts. The formed Fe_3O_4 -ZnO hybrid nanoparticles, as a potential photosensitizer, could target the cancerous lesions by alternating the external magnetic field. Additionally, Fe_3O_4 in the hybrid nanoparticles could serve as photothermal therapeutic agent in cancer treatment (Chu et al. 2013). More detailed study of the effects of catalyst dosage, phenol concentration and pH value on the photocatalytic properties and the photodissolution of hybrid nanoparticles is necessary for better understanding and adequate application of the developed photocatalytic nanoparticle enhancement

mechanisms. This will be presented in the next chapter. In addition, the viability of both L929 and KB cells in the presence of the hybrid nanoparticles, both in dark and under light irradiation, is under investigation.

CHAPTER 5 INVESTIGATION OF THE PHOTOCATALYSIS MECHANISM OF Fe₃O₄-ZnO HYBRID NANOPARTICLES

5.1 Introduction

This chapter focuses on the investigation of various reaction conditions and on the photocatalytic properties of the magnetic zinc oxide (ZnO) hybrid nanoparticles. Iron oxide (Fe₃O₄) nanoparticles were first synthesised according to the procedures described in Chapter 4. They were then suspended within two different surfactant solutions. Two types of hybrid Fe₃O₄-ZnO nanoparticles then were synthesised using these two types of seed. The resultant nanoparticles were characterised using various instruments as described in the previous chapters. The photocatalytic properties of the produced nanoparticles were investigated using plain ZnO and commercial TiO₂ as comparisons. The effects of the various reaction parameters, such as catalyst dosage, initial phenol concentration and pH value, on the photoreactivity of the Fe₃O₄-ZnO hybrid nanoparticles were further investigated. The iron and zinc contents dissolved, before and after photocatalytic reactions, were measured using inductively coupled plasma-atomic emission spectroscopy (ICP-AES). The results demonstrated that, under irradiation by light, the hybrid nanoparticles exhibited enhanced photocatalytic activity, reaching a phenol degradation efficiency of 73.9% for Fe₃O₄(TMAH)-ZnO and 54.7% for Fe₃O₄(CA)-ZnO, as compared to only 51.9% for pure ZnO. The possible mechanism of the enhanced photoreactivity was further explored. Iron ions were found to be associated with the improvement. They acted as electron-trappers and decelerated the recombination of the photo-induced charge carriers of ZnO. The pH value also plays an important role in the photocatalysis reaction. At pH=4, the degradation rate of phenol was optimal, which is comparable to the optimal result of the commercial P25 (at pH=5.6) that is generally accepted as the best semiconductor photocatalyst available.

5.1.1 Background

Nano-sized zinc oxide (ZnO), which is characterised by its unique properties of high photocatalytic activity and photo-oxidizing ability against chemical and biological species, has found applications in pharmaceuticals, cosmetics, paints and so on (Dutta et al. 2010). ZnO, similar to TiO₂, has received increasing attention for its application in cancer treatment methods (Zhang et al. 2008b). One of the major advantages of utilising ZnO in the biomedical field is that it can induce selective toxicity towards some cancer cell lines without damage to normal cell lines, in the dark (Muhammad et al. 2011a). For example, Ostrovsky et al (2009) noticed that ZnO nanoparticles were capable of killing brain, breast and prostate cancer cells without damaging normal cells, in the dark. Similarly Premanathan et al. (2011) revealed that ZnO nanoparticles significantly inhibited the proliferation of human myeloblastic leukemia (HL60) cancerous cells without any damage to normal blood cells. The selective toxicity of ZnO nanoparticles to cancerous cells is mostly attributable to reactive oxygen species (ROS), resulting in cancer cell death via oxidative damage (Guo et al. 2008). It has been reported that the selective toxicity exhibited by ZnO nanoparticles is size-dependent. Generally, ZnO with smaller particle size shows greater toxicity on cancer cells (Brunner et al. 2006). Another important feature is that ZnO nanoparticles could overcome the multidrug resistance (MDR) problem which is a major drawback related to conventional cancer therapy. MDR is characterised as the over-expression of P-gly-coprotein as a drug-efflux pump that causes a decrease in the concentration of anticancer agents at cancerous sites. It has been reported that ZnO nanoparticles have shown significantly greater cytotoxicity to cancer cells that overexpress P-gly-coprotein than to normal cells (Hamada and Tsuruo 1988, Gottesman et al. 2012).

In addition, ZnO nanoparticles, as potential photosensitisers, can induce apoptosis or necrosis in cancerous cells in the presence of light. This is because ZnO, which is similar to TiO₂, can be photoexcited to form charge carriers. The produced charge carriers react with surrounding oxygen and water to generate ROS such as hydroxyl radical, hydrogen peroxide and superoxide. The reaction between the ROS and cell membranes result in the destruction of the cell membranes and then the efflux of the intercellular components (Dougherty et al. 1998). It has been reported that, under light irradiation, folic acid-conjugated graphene-ZnO nanohybrid nanoparticles can

induce apoptotic death to HeLa cancer cells (Hu et al. 2013). Additionally, the application of light irradiation could enhance the ability of ZnO nanoparticles to overcome the MDR problem (Guo et al. 2008). Furthermore, ZnO nanoparticles easily can be functionalised by drug molecules and targeting ligands due to the presence of neutral hydroxyl groups, and the combination of ZnO with chemotherapeutic agents can induce the synergistic effects upon the cancer cells. Zhang et al. (2011) noticed that the combination of ZnO with the anticancer drug daunorubicin (DNR) could obviously increase the intracellular accumulation of DNR and enhance its anticancer efficiency. Upon exposure to UV light, the antitumor activity had been significantly improved due to the action of photo-generated ROS. Although promising results have been achieved in killing cancer cells, there are still some limitations that hamper the clinical application of ZnO in PDT. One concern is that ZnO nanoparticles lack the important property of specific targeting to cancer cells. Another concern is that the photodynamic activity of ZnO can be compromised due to fast recombination of photoinduced charge carriers. It has been reported that around 90% of these charge carriers quickly recombine, leading to a decrease in amount of ROS formed (Rothenberger et al. 1985). A solution to improve the photocatalytic performance of ZnO and enhance the cell-specific targeting is to combine Fe_3O_4 with ZnO to form Fe_3O_4 -ZnO hybrid nanoparticles.

Based on the consideration above, Fe_3O_4 -ZnO hybrid nanoparticles were successfully synthesised by dehydration of $\text{Zn}(\text{Ac})_2 \cdot 2\text{H}_2\text{O}$ in DEG using two different types of Fe_3O_4 seeding templates. The physicochemical properties and photocatalytic properties of the produced hybrid nanoparticles were investigated. The effects of catalyst dosage, initial phenol concentration and pH value on the photocatalytic activity of the hybrid nanoparticles were systematically studied. Photodissolution of the Fe_3O_4 -ZnO hybrid nanoparticles also was evaluated.

5.2 Experimental

5.2.1 Materials

Ferrous chloride tetrahydrate ($\text{FeCl}_2 \cdot 4\text{H}_2\text{O}$, 99.99%), ferric chloride hexahydrate ($\text{FeCl}_3 \cdot 6\text{H}_2\text{O}$, 99.99%), sodium hydroxide (NaOH , $\geq 97.0\%$), zinc acetate dehydrate ($\text{Zn}(\text{Ac})_2 \cdot 2\text{H}_2\text{O}$, $\text{Ac}=\text{CH}_3\text{COO}$, $\geq 98\%$), diethylene glycol (DEG, 99%), phenol ($\text{C}_6\text{H}_5\text{OH}$, $\geq 96.0\%$), citric acid ($\text{C}_6\text{H}_8\text{O}_7$, $\geq 98\%$), trisodium citrate dehydrate ($\text{C}_6\text{H}_5\text{O}_7\text{Na}_3 \cdot 2\text{H}_2\text{O}$, $\geq 99.0\%$), sodium carbonate (Na_2CO_3 , $\geq 99.5\%$) and sodium bicarbonate (NaHCO_3 , 99%) were purchased from Sigma-Aldrich. Tetramethylammonium hydroxide (TMAH, 25%) was supplied by Fluka. Degussa P25 (TiO_2 nanoparticulate material consisting of 75% anatase and 25% rutile) was purchased from Degussa. Deionised water was used in all experiments.

5.2.2 Synthesis of $\text{Fe}_3\text{O}_4(\text{TMAH})$ and $\text{Fe}_3\text{O}_4(\text{CA})$ nanoparticles

Magnetite nanoparticles (Fe_3O_4) were prepared using a chemical co-precipitation method. Firstly, $\text{FeCl}_3 \cdot 6\text{H}_2\text{O}$ (3.24 g, 0.012 mol) and $\text{FeCl}_2 \cdot 4\text{H}_2\text{O}$ (1.19 g, 0.006 mol) were dissolved into deionised water (20 ml) and constantly stirred under nitrogen protection. The obtained iron salt solution was then gradually added to NaOH solution (100 ml, 0.5 M) under mechanical stirring. After stirring for 1 h, the black precipitate was collected by applying an external magnetic field and washed five times with deionised water (5×10 ml).

In this study, two types of surfactant were used. One was tetramethylammonium hydroxide (TMAH) and the other was citric acid (CA). For TMAH-suspended iron oxide ($\text{Fe}_3\text{O}_4(\text{TMAH})$), the obtained Fe_3O_4 nanoparticles (0.4 g, 1.73 mmol) were suspended in TMAH solution (0.5 ml) and then further diluted using deionised water to a total volume of 4.0 ml. For CA-suspended nanoparticles ($\text{Fe}_3\text{O}_4(\text{CA})$), the same amount of magnetite nanoparticles were dispersed into an aqueous citric acid solution (5 ml, 0.1 M) followed by ultrasonic vibration for 30 min. Both suspensions were maintained at 4 °C for further investigation.

5.2.3 Preparation of Fe₃O₄-ZnO hybrid nanoparticles

Fe₃O₄-ZnO(4) hybrid nanoparticles were fabricated using the seed-mediated method presented in Chapter 4. In brief, Fe₃O₄(TMAH) nanoparticles (0.2 g, 0.043 mmol) were suspended in 30 ml DEG using ultrasonic vibration for 30 min to form a homogeneous suspension. Zn(Ac)₂•2H₂O (2.19 g, 0.01 mol) was added into DEG (100 ml) and the reaction mixture was heated to 150 °C with constant stirring under nitrogen protection. Then, the Fe₃O₄(TMAH) suspension was added, dropwise, to the above reaction mixture, followed by heating to 160 °C. After 2 h of reaction time, the reaction mixture was air cooled to room temperature. The resultant hybrid nanoparticles were collected by applying an external magnetic field. The obtained sample was washed five times with deionised water (5×15 ml) then three times with ethanol (3×15 ml) and dried under vacuum. A similar experiment was carried out using Fe₃O₄(CA) nanoparticles as seeds. The obtained hybrid nanoparticles were denoted as Fe₃O₄(TMAH)-ZnO and Fe₃O₄(CA)-ZnO, respectively. The reaction yields for Fe₃O₄(TMAH)-ZnO and Fe₃O₄(CA)-ZnO were 59.4% and 40.6%, respectively. It was noted that the former powder was black in colour and the latter was brown.

5.2.4 Physicochemical characterisations

A TEM (JEOL JSM 2011) equipped with a Gatan Digital Camera was used to examine the morphology of Fe₃O₄ and Fe₃O₄-ZnO hybrid nanoparticles. Prior to the TEM examination, the sample was suspended in DEG by ultrasonication for 10 min, resulting in a final concentration of around 0.02 mg L⁻¹. Then one drop of the suspension was placed onto a copper grid (with a carbon film substrate) and the grid was dried in an oven at 100 °C overnight. The TEM images were recorded at an accelerating voltage of 200 kV. The sizes of the nanoparticles were measured using the in-built JEOL operational software, DigitalMicrograph, which is correlated with the magnification bar of the TEM images.

A FESEM (Zeiss Neon 40EsB FIB-SEM) was used to analysis the morphology of ZnO nanoparticles. The sample, suspended in DEG, was deposited onto an

aluminium stub and heated to 160 °C in an oven overnight. Then the stub was coated with platinum that was applied as a conducting material.

The particle size and size distribution in both aqueous solution and DEG suspension were estimated by dynamic light scattering (DLS) using a Malvern Zetasizer Nano-ZS. Prior to DLS analysis, samples were suspended in deionised water and DEG, respectively, using ultrasonic vibration. The suspensions were equilibrated to 20 °C. Each sample was measured in triplicate and the results were presented as mean \pm standard deviation.

The zeta potential also was measured using the Malvern Zetasizer Nano-ZS. For zeta potential measurement, NaCl aqueous solution (10 ml, 0.01 mol L⁻¹) was used as a conductive regulator. The pH of the NaCl solution was adjusted to 4, 7, 8 and 10 by using an aqueous solution of NaOH (0.01 mol L⁻¹) and HCl (0.01 mol L⁻¹). Afterward, the sample (1 mg) was suspended into each of the resulting solutions (10 ml) using ultrasonic vibration (20 min), yielding the final particle concentration of 0.1 mg ml⁻¹. Each solution was measured three times.

FTIR analysis was carried out on all samples using a Thermo Scientific Nicolet iS50 equipped with an Automated Beamsplitter Exchanger (ABX) having a resolution of 4 cm⁻¹. All the spectra were recorded ranging from 200 to 4000 cm⁻¹.

UV-visible diffuse reflectance spectra (UV-vis DRS) of all samples were collected on a Jasco V670 spectrophotometer with a Φ 60 mm integrating sphere, using BaSO₄ as the reference material. UV-Vis DRS was monitored over a wavelength range between 300 and 700 nm with a band width of 2 nm.

The photoluminescence (PL) spectra of the samples were obtained using a Cary Eclipse (MY13060002) Fluorescence Spectrometer with an excitation wavelength of 390 nm. The emission spectra were recorded in the region of 370-410 nm and both exciting and emission slit widths were 5 nm. For sample preparation, the samples (around 10 mg) were suspended in deionised water and further diluted to 2 μ g ml⁻¹.

An inductively coupled plasma-atomic emission spectroscopy (ICP-AES) analysis was carried out to determine the ratio of iron and zinc elements in the hybrid nanoparticles using a Vista Axial CCD Simultaneous ICP-AES instrument.

Brunauer-Emmett-Teller (BET) analysis was conducted to evaluate the surface area, pore volume and pore size distribution of the hybrid nanoparticles using nitrogen sorption at -196 °C on a Micromeritics Tristar 3000 apparatus. Prior to BET examination, all samples were preheated to 200 °C under vacuum overnight.

The chemical and physical properties of the produced nanoparticles are listed in Table 5.1.

Table 5.1 Chemical and physical properties of the synthesised nanoparticles.

Sample ID	Fe ₃ O ₄ :Zn O	Particle size (nm)	Hydrodynamic diameter (nm)		Iron Content by ICP-AES (mg L ⁻¹)	BET analysis		
			Deionised Water	Diethylene Glycol		Pore size (nm)	Pore Volume (cm ³ g ⁻¹)	Surface Area (m ² g ⁻¹)
Fe ₃ O ₄	1:0	10.6±1.4	233.2±1.2	57.3±1.7	<0.002	-	-	-
Fe ₃ O ₄ (CA)	1:0	7.1±2.3	138.8±1.2	17.5±0.2	28.4	-	-	-
Fe ₃ O ₄ (TMAH)	1:0	10.5±2	82.3±5.7	8.3±0.4	<0.002	-	-	-
Fe ₃ O ₄ (TMAH)- ZnO	1:4.2	34.5±6.2	-	-	-	5.8	0.19	95.6
Fe ₃ O ₄ (CA)-ZnO	1:1.6	293±32	-	-	-	2	0.16	73.8
TiO ₂	-	24±1	-	-	-	2.1	0.21	68.9

5.2.5 Photoreactivity study

The photocatalytic performance of the magnetic ZnO hybrid nanoparticles was evaluated based on the phenol degradation rate under UV radiation. The light irradiation was induced by an MSR 575/2 metal halide lamp (575 W, Philips) with a wavelength ranging from 315 nm to 1050 nm. The experiments were carried out in a 1L double-jacketed reactor, fitted with a cooling water system to maintain the temperature at 25 ± 1 °C. In brief, a certain amount of each of the hybrid nanoparticles was suspended in aqueous phenol solution (200 ml). Prior to the photocatalytic reaction, each reaction suspension was constantly stirred at 600 rpm in the dark for 30 min to achieve the absorption/desorption equilibrium between the hybrid nanoparticles and phenol solution. The hybrid nanoparticles suspension was subsequently illuminated by the light. During the irradiation period, 10 ml of the suspension was withdrawn at the prescribed time intervals and filtered using a 0.45 μm Millipore filter to remove the residual hybrid nanoparticles. The liquid was maintained and sent to be analysed using a HPLC (Varian) in which the UV detector was adjusted to 270 nm. To determine the iron and zinc elemental content during the photocatalytic reaction, the phenol solution also was analysed by ICP-AES.

Varying concentrations of the nanocatalysts and the initial phenol, as well as various pH values were investigated using the above experimental procedure. Details are summarised in Table 5.2. Buffer solutions of citric acid-sodium citrate, phosphate buffer saline (PBS) and sodium carbonate-sodium bicarbonate were added to phenol solution, prior to the photocatalysis experiment, so as to adjust the pH value to 2.5, 4, 8 and 10, respectively. The aforementioned photoreactivity experiments were performed once. It is worthy to mention that the method employed in the work is well established and proven reproducible in our previous work (Sun et al. 2011).

Table 5.2 Kinetic parameters, phenol degradation efficiency, and the dissolved content of iron and zinc obtained using various reaction parameters.

Sample ID	Catalyst Con. (g L ⁻¹)	Phenol Con. (mg L ⁻¹)	pH	Phenol Removal (%)	Rate constant (k, min ⁻¹)	R ²	Metal Content by ICP-AES (mg L ⁻¹)	
							Fe	Zn
ZnO	0.325	20		51.8	0.0039	0.997	-	10
Fe ₃ O ₄ (TMAH)-ZnO	0.1	20		62.7	0.0062	0.9888	<0.01	7.8
	0.325		71.3	0.0082	0.9985	0.13	5.9	
	0.5		63.6	0.0067	0.9911	<0.01	6.7	
	1.0		57.5	0.0061	0.9798	0.04	8.0	
	0.325	10		78.0	0.0099	0.9938	<0.01	8.2
		80		25.9	0.0022	0.9377	<0.01	8.0
	0.325	20	2.5	51.9	0.0050	0.9506	24	240
			4	100.0	0.0170	0.9129	22	220
			8	30.8	0.0030	0.8478	<0.01	0.43
			10	14.5	0.0013	0.9723	<0.01	0.67
Fe ₃ O ₄ (CA)-ZnO	0.1	20		23.0	0.0017	0.9788	<0.01	7.4
	0.325		54.7	0.0045	0.9706	0.06	8	
	0.5		34.6	0.0028	0.9912	<0.01	9.5	
	1.0		23.9	0.0019	0.9546	<0.01	14	
	0.325	80		16.6	0.0013	0.952	<0.01	7.4
	0.325	20	2.5	34.7	0.0041	0.9881	34	200
			4	64.3	0.0085	0.9874	26	270
			8	23.2	0.0023	0.9993	0.05	0.23
			10	13.9	0.0013	0.9807	0.03	0.86

5.3 Results and Discussion

Fe_3O_4 nanoparticles were synthesised by the co-precipitation of the iron chloride precursor (molar ratio of $\text{Fe}^{3+}/\text{Fe}^{2+} = 2:1$) (Massart 1981). Using TMAH and CA, three Fe_3O_4 suspensions, Fe_3O_4 , $\text{Fe}_3\text{O}_4(\text{TMAH})$ and $\text{Fe}_3\text{O}_4(\text{CA})$, were prepared. Dehydration of $\text{Zn}(\text{Ac})_2 \cdot 2\text{H}_2\text{O}$, in the presence of these nanoparticles in DEG, led to the formation of two hybrid nanoparticles: $\text{Fe}_3\text{O}_4(\text{TMAH})\text{-ZnO}$ and $\text{Fe}_3\text{O}_4(\text{CA})\text{-ZnO}$.

5.3.1 Characterisation of Fe_3O_4 , $\text{Fe}_3\text{O}_4(\text{TMAH})$ and $\text{Fe}_3\text{O}_4(\text{CA})$

As presented in Fig. 5.1a, Fe_3O_4 were spherical-like with an average size of 10.6 ± 1.4 nm and tended to aggregate. The morphology of the produced $\text{Fe}_3\text{O}_4(\text{CA})$ and $\text{Fe}_3\text{O}_4(\text{TMAH})$ nanoparticles (Fig. 5.1b-c) were generally the same as that of the pure Fe_3O_4 . However, they were more uniform and spread further apart from each other. The analysis of 30 nanoparticles from each of the TEM images indicated that the average sizes of the resultant nanoparticles were 7.1 ± 2.3 nm and 10.5 ± 2 nm for $\text{Fe}_3\text{O}_4(\text{CA})$ and $\text{Fe}_3\text{O}_4(\text{TMAH})$, respectively. The decreased particle size of $\text{Fe}_3\text{O}_4(\text{CA})$ nanoparticles is because the Fe_3O_4 nanoparticles may react with citric acid to form iron complexes that are leachable from the surface of solid particles to the aqueous acid solution (Panias et al. 1996). The ICP-AES results demonstrated that there was 28.4 mg L^{-1} of elemental iron in the liquid obtained from the $\text{Fe}_3\text{O}_4(\text{CA})$ suspension, indicating 0.48% of loss of the Fe_3O_4 into citric acid solution. However, the Fe_3O_4 nanoparticles stored in deionised water and aqueous TMAH solution were stable, showing a loss of Fe_3O_4 that was below 0.002 mg L^{-1} (Table 5.1) (Note that 0.002 mg L^{-1} is the detection limit of the ICP-AES used).

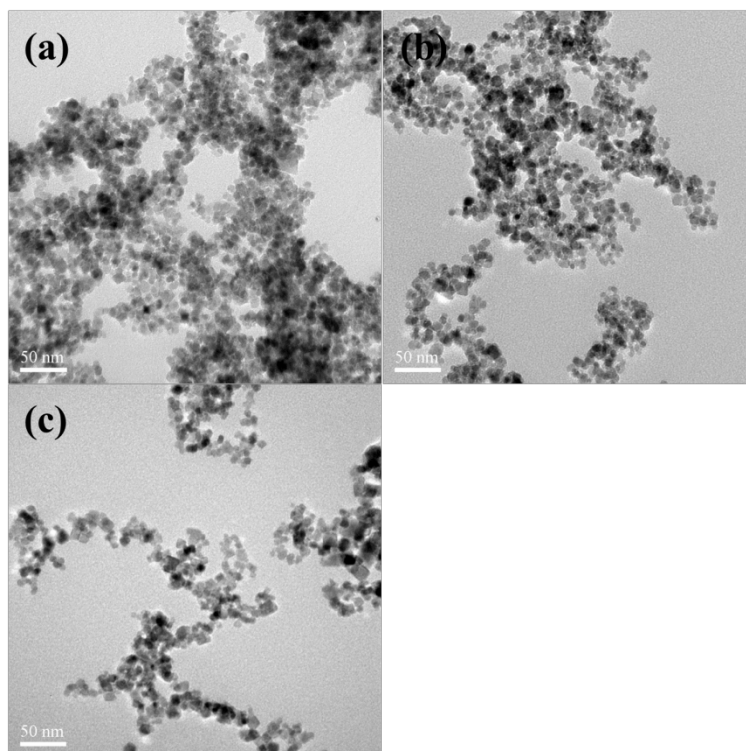


Fig. 5.1 TEM images of (a) pure Fe₃O₄, (b) Fe₃O₄(CA) and (c) Fe₃O₄(TMAH).

DLS was used to further analyse the particle size and size distribution of the resultant nanoparticles (Fig. 5.2). Pure Fe₃O₄ nanoparticles suspended in deionised water showed an average hydrodynamic diameter of 233.2 ± 1.2 nm, with a polydispersity index (PDI) of 0.262. This was reduced to 138.8 ± 1.2 nm for Fe₃O₄(CA) and 82.3 ± 5.7 nm for Fe₃O₄(TMAH). An apparent decrease in the hydrodynamic diameter of Fe₃O₄(CA) and Fe₃O₄(TMAH) in aqueous solution was observed. This is because, in the presence of a surfactant (CA or TMAH), the attraction force among surfactant-coated magnetite nanoparticles is compensated by the electrostatic interparticle repulsion force (Racuciu 2009). It should be noted that these results were much larger than those obtained from TEM images. Particle aggregation and hydrodynamic influence are the main causes for such a difference. DLS measures the hydrodynamic radius of clusters of magnetite nanoparticles in aqueous solution while TEM measurement is based on single particles. Prior to the dehydration of Zn(Ac)₂·2H₂O, magnetite nanoparticles (as seeds) were suspended in DEG at room temperature. The hydrodynamic diameters of the pure Fe₃O₄, Fe₃O₄(CA) and Fe₃O₄(TMAH) in DEG were further reduced to 57.3 ± 1.7 nm, 17.5 ± 0.2 nm and

8.3±0.4 nm, respectively, indicating that DEG is a good surfactant for these nanoparticles. There was a fraction of Fe₃O₄(TMAH) showing a diameter of 1480±12 nm. This is possibly due to aggregates of the small particles that could be separated by centrifugation.

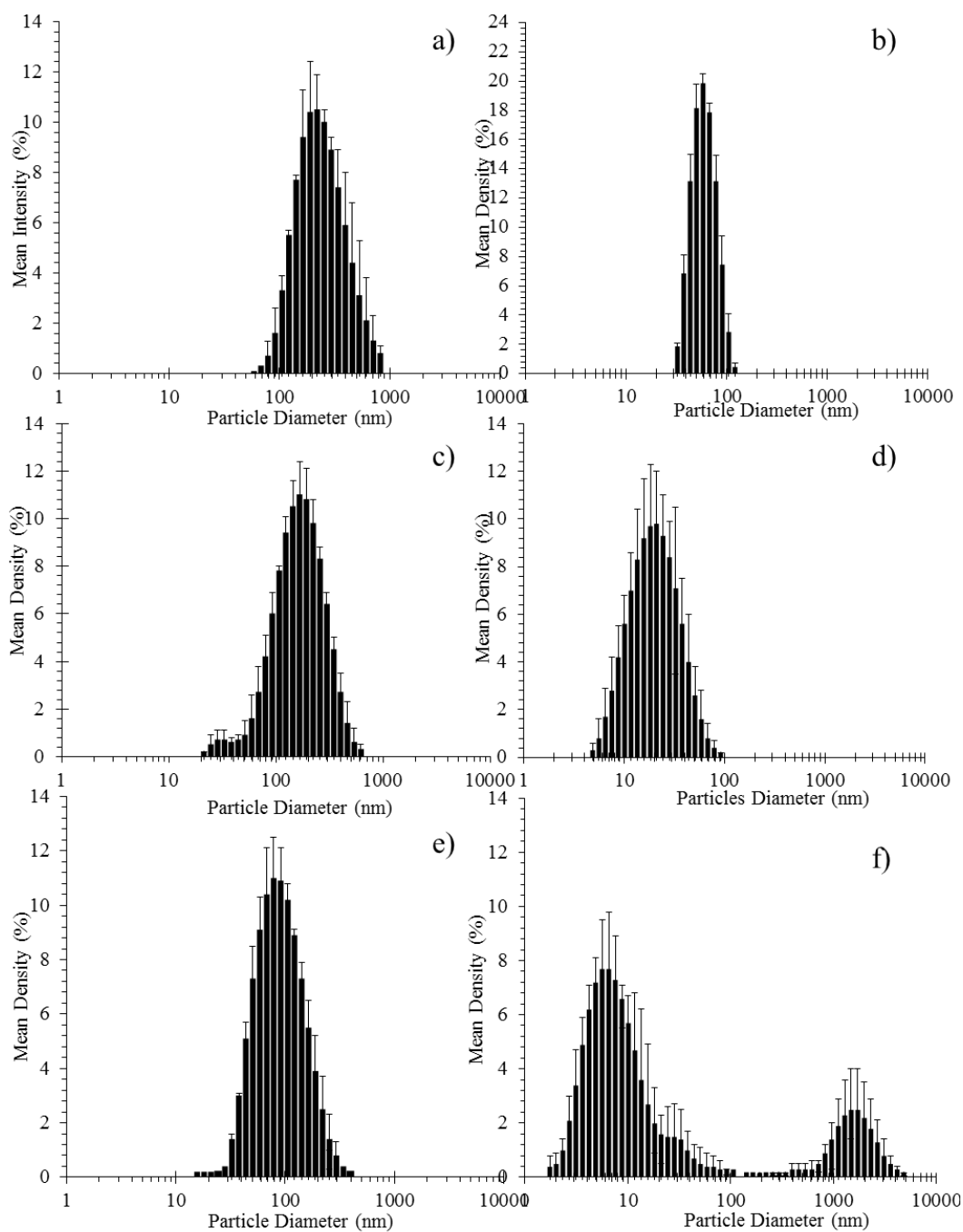


Fig. 5.2 The DLS spectra of (a, b) Fe_3O_4 , (c, d) Fe_3O_4 (CA) and (e, f) Fe_3O_4 (TMAH). The left panel is nanoparticles suspended in deionised water and the right panel is nanoparticles suspended in DEG.

The zeta potentials of Fe_3O_4 , Fe_3O_4 (CA) and Fe_3O_4 (TMAH) at various pH values are shown in Fig. 5.3. It can be observed that as pH value increases from 4 to 10, a decrease in the magnitude of zeta potential was demonstrated for all nanoparticles. For Fe_3O_4 (TMAH), a drastic decrease from +52.5 mV To -55.4 mV was observed,

showing an isoelectric point of $pI=7.8$. Hence, when the pH value is below 7.8, $Fe_3O_4(TMAH)$ is positively charged, suggesting that the $N(CH_3)_4^+$ ions from TMAH were accumulated on the surface of $Fe_3O_4(TMAH)$ to form a positively charged shell. For pure Fe_3O_4 , the zeta potential of Fe_3O_4 was negative over the investigated pH range, due to the accumulation of $-OH$ groups on the surface of the nanoparticles. For $Fe_3O_4(CA)$, the zeta potential was similar to that of Fe_3O_4 , being negative over the investigated pH range. The negative charge of the shell is probably a due to the presence of citrate ions ($C_6H_5O_7^{3-}$). At acidic conditions ($pH < 7$), the zeta potential value increases with decreasing pH for $Fe_3O_4(TMAH)$. However it decreases with reduced pH value for both pure Fe_3O_4 and $Fe_3O_4(CA)$. These result in greater tendency of aggregation of Fe_3O_4 and $Fe_3O_4(CA)$ in acidic conditions. Indeed, in both deionised water and DEG suspensions, the size of these particles show a similar pattern of $Fe_3O_4 > Fe_3O_4(CA) > Fe_3O_4(TMAH)$ (Fig. 5.2).

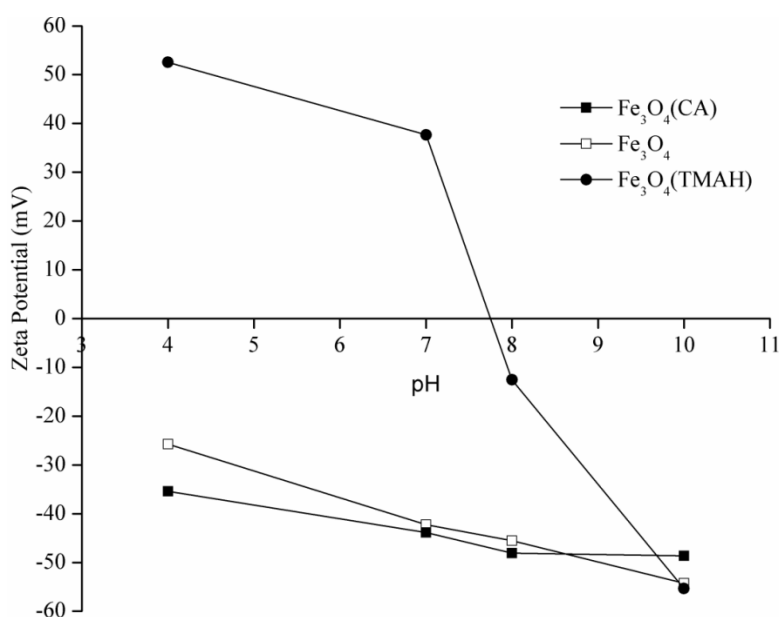


Fig. 5.3 Zeta potential of Fe_3O_4 , $Fe_3O_4(TMAH)$ and $Fe_3O_4(CA)$ nanoparticles versus pH values.

FTIR spectra of all samples are shown in Fig. 5.4. For pure Fe_3O_4 nanoparticles, the characteristic peak of the Fe-O bond in Fe_3O_4 nanoparticles appears at 530 cm^{-1} . There is a weak peak at 1640 cm^{-1} assignable to the bending vibration of $-OH$ groups (Liu et al. 2004). After surface modification using citric acid, a new absorption peak

at 1560 cm^{-1} appeared, which can be attributed to the symmetric stretching vibration of C=O from carboxylate (citrate ions). For pure citric acid, the absorption peak for C=O stretching vibration is at 1710 cm^{-1} (Sahoo et al. 2005a). The shift of the absorption peak to a lower wavenumber was because the citrate ions from the citric acid would have combined with Fe-OH molecules on the surface of the magnetite nanoparticles to form iron complex (Sousa et al. 2013). Furthermore, the absorption peak at 1380 cm^{-1} is due to the bond formed between iron and carboxyl groups, and the weak band at 830 cm^{-1} was caused by the hydrogen bond between the carboxyl groups (Kalska-Szostko et al. 2014). All these results indicate that citric acid was successfully bound to the surface of Fe_3O_4 nanoparticles by chemisorption of the carboxylate groups, leaving a negatively charged surface of magnetite nanoparticles (Todorovsky et al. 2002). This is consistent with the measure zeta potential value in the previous section. For Fe_3O_4 (TMAH), the presence of tetramethylammonium cations on the surface of magnetite nanoparticles was confirmed through the strong absorption peaks at 1490 cm^{-1} and 950 cm^{-1} , which are attributable to the asymmetric bending vibration of $-\text{CH}_3$ groups and the asymmetric stretching vibration of C-N groups, respectively. It is indicated that the tetramethylammonium cations dissociated from TMAH molecules combined with negatively charged Fe-OH molecules, leading to a positively charged shell around the magnetite nanoparticles (Cheng et al. 2005a). The relative chemical reactions for the Fe_3O_4 (TMAH) and Fe_3O_4 (CA) preparations are schematically displayed in Fig.5.5.

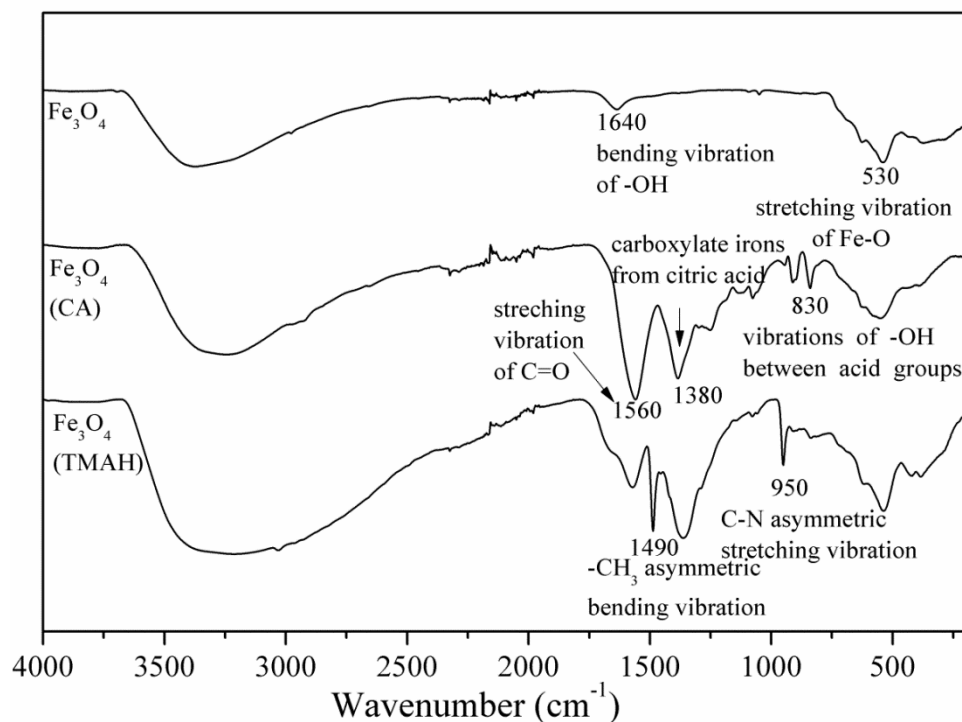


Fig. 5.4. FTIR spectra of Fe_3O_4 , $\text{Fe}_3\text{O}_4(\text{CA})$ and $\text{Fe}_3\text{O}_4(\text{TMAH})$.

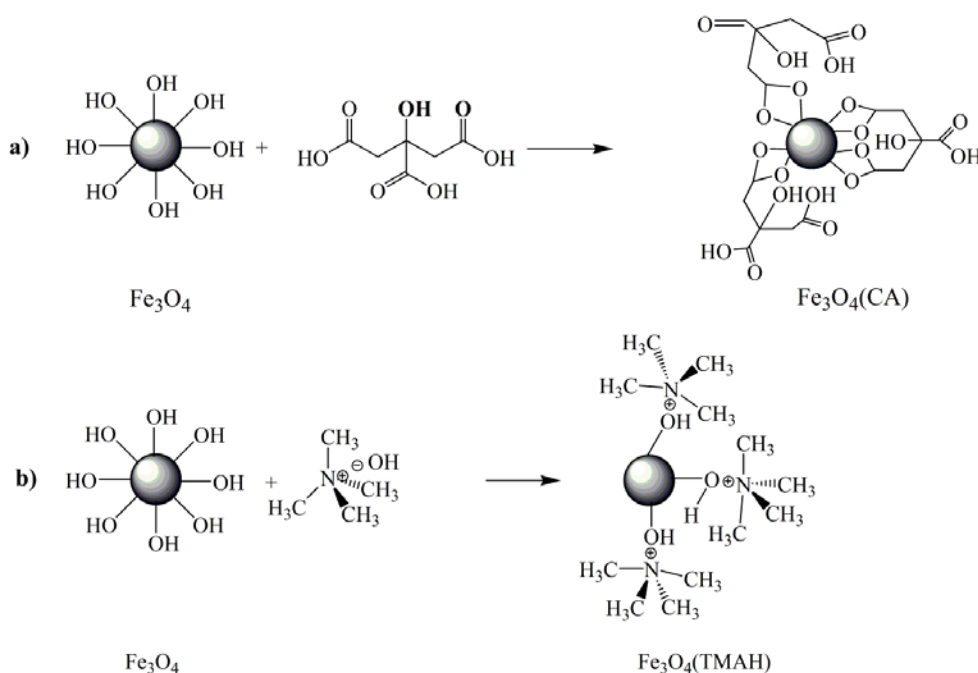


Fig. 5.5. Schematic presentation of (a) Fe_3O_4 (CA) and Fe_3O_4 (TMAH) nanoparticles (Cheng et al. 2005a, Sahoo et al. 2005a).

5.3.2 Characterisation of Fe₃O₄(TMAH)-ZnO and Fe₃O₄(CA)-ZnO hybrid nanoparticles

Whilst the effect of the surfactants on the Fe₃O₄ dispersion in aqueous solution was well demonstrated by their hydrodynamic sizes, this effect also is reflected in the Fe₃O₄-ZnO hybrid nanoparticles produced using various Fe₃O₄ dispersions as a seeding template. TEM images, displayed in Fig. 5.6(a-b), indicate that the morphologies of Fe₃O₄(TMAH)-ZnO and Fe₃O₄(CA)-ZnO were generally the same. The sizes of the Fe₃O₄(TMAH)-ZnO and Fe₃O₄(CA)-ZnO were 34.5±6.2 nm and 293±32 nm, respectively. For control purposes, ZnO nanoparticles, prepared using a similar seed-mediated method, also were examined, showing a mean diameter of 267±26 nm.

The size difference of the produced Fe₃O₄(TMAH)-ZnO and Fe₃O₄(CA)-ZnO is a result of the presence of different surfactants on the surfaces of the Fe₃O₄ nanoparticles. It should be noted that the condensation of Zn(Ac)₂ releases acetic acid (HAc) which is acidic. In this condition, Fe₃O₄(TMAH) nanoparticles are positively charged, as indicated by their zeta potential values in the previous section. These positively charged Fe₃O₄(TMAH) nanoparticles are attractive to the negatively charged [Zn(OH)₄]²⁻ species, leading to the deposition of ZnO on the surface of Fe₃O₄ nanoparticles, therefore forming a relatively dense morphology, as shown in Fig. 5.6a. For Fe₃O₄(CA) nanoparticles, the condensation of Zn(Ac)₂ occurs randomly on the negatively charged surfaces of Fe₃O₄, leading to a formation of a loosely structured ZnO layer, as demonstrated in Fig. 5.6b. This hypothesised reaction mechanism was further confirmed by the reaction yield. It was noticed that, by applying the external magnet, the reaction yield of Fe₃O₄(CA)-ZnO (40.6%) was lower than that of Fe₃O₄(TMAH)-ZnO (59.6%). White coloured powders were evident in the reaction mixture, indicating the formation of pure ZnO nanoparticles in the mixture. A similar observation was reported by Wang et al. in the synthesis of titania-coated polystyrene (PS) particles using ammonia catalysis (Wang et al. 2006). They concluded that, due to the presence of NH₄⁺ species on the surface of the PS spheres, the negatively charged ≡ TiO⁻ were adsorbed by the NH₄⁺ species onto the surfaces of the PS nanoparticles and, subsequently, the deposition of TiO₂ with the aid of NH₄⁺ species arises easily on the surface of the PS nanoparticles.

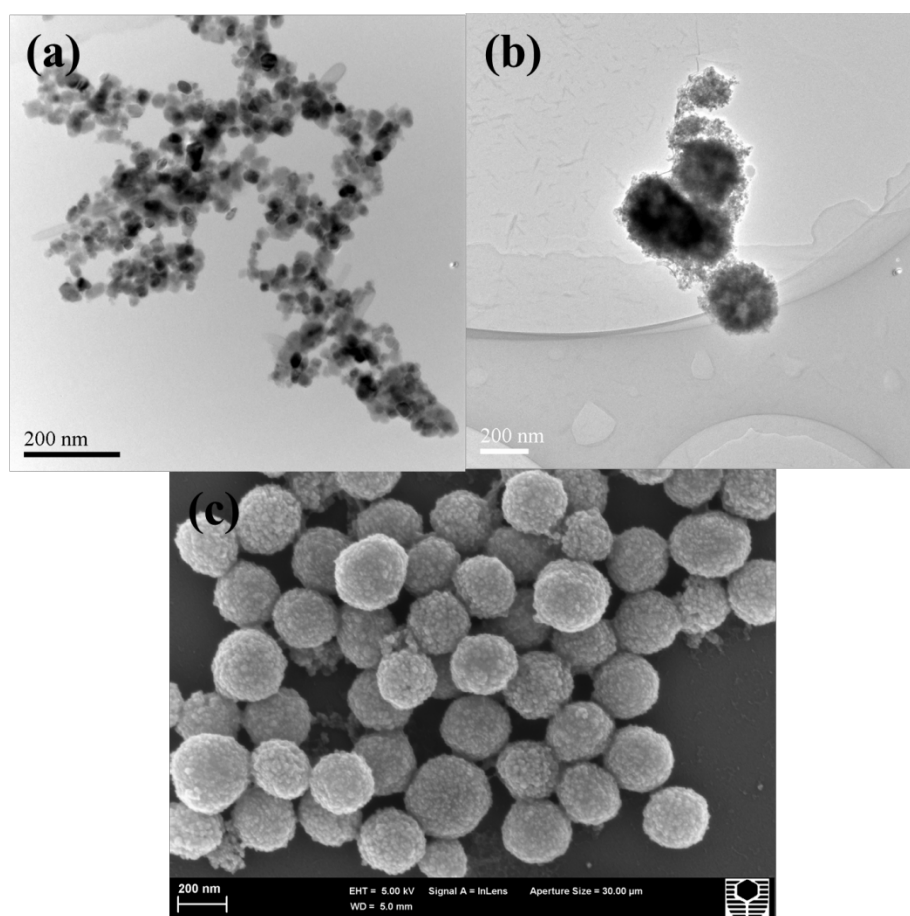


Fig. 5.6 TEM images of (a) $\text{Fe}_3\text{O}_4(\text{TMAH})\text{-ZnO}$ and (b) $\text{Fe}_3\text{O}_4(\text{CA})\text{-ZnO}$; FESEM image of (c) ZnO nanoparticles.

FTIR spectra of the produced hybrid nanoparticles are presented in Fig. 5.7. For pure Fe_3O_4 , the characteristic peak for the Fe-O stretching vibration appears at 530 cm^{-1} . For ZnO, there is an absorption peak at 375 cm^{-1} ascribed to the stretching vibration of Zn-O (Feng et al. 2014). The absorption peaks for both Fe-O and Zn-O stretching vibrations are presented simultaneously in the FTIR spectra of the $\text{Fe}_3\text{O}_4\text{-ZnO}(4)$ hybrid nanoparticles, displayed in Fig. 5.7 (b-c), confirming the successful fabrication of the $\text{Fe}_3\text{O}_4\text{-ZnO}$ hybrid nanoparticles. Moreover, there are two absorption peaks at 1406 cm^{-1} and 1586 cm^{-1} , corresponding to the stretching vibration of C-O and C=O from acetate groups. It suggests the presence of the metal complexes $\text{Zn}(\text{OH}^{-1})_x(\text{Ac})_{2-x}$ as an intermediate during the seed-mediated process and has been observed in a previous study (Feng et al. 2014). It was noticed that the

relative intensities of the two absorption peaks at 540 cm^{-1} and 375 cm^{-1} vary in the FTIR spectra of the $\text{Fe}_3\text{O}_4(\text{TMAH})\text{-ZnO}$ and $\text{Fe}_3\text{O}_4(\text{CA})\text{-ZnO}$ hybrid nanoparticles.

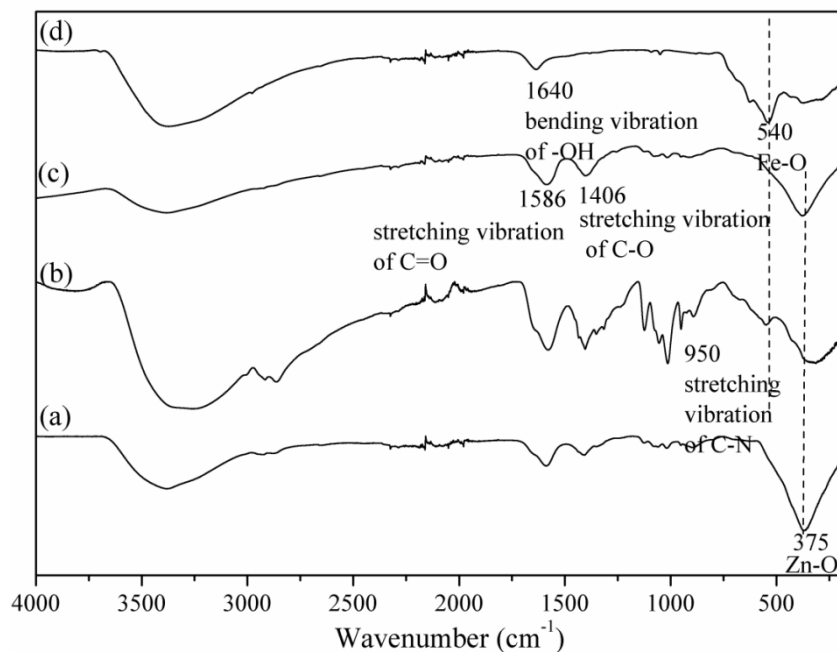


Fig. 5.7 FTIR spectra of (a) ZnO, (b) $\text{Fe}_3\text{O}_4(\text{TMAH})\text{-ZnO}$, (c) $\text{Fe}_3\text{O}_4(\text{CA})\text{-ZnO}$ and (d) Fe_3O_4 .

$\text{Fe}_3\text{O}_4(\text{TMAH})\text{-ZnO}$ and $\text{Fe}_3\text{O}_4(\text{CA})\text{-ZnO}$ hybrid nanoparticles were subjected to further analysis of pore size and surface area, as presented in Fig. 5.8a. According to the International Union of Pure Applied Chemistry (IUPAC) classification, both $\text{Fe}_3\text{O}_4(\text{TMAH})\text{-ZnO}$ and $\text{Fe}_3\text{O}_4(\text{TMAH})\text{-ZnO}$ hybrid nanoparticles exhibited type IV isotherms with a type H3 hysteresis loop, indicating mesoporous structure of the hybrid nanoparticles. The pore volumes of $\text{Fe}_3\text{O}_4(\text{TMAH})\text{-ZnO}$ and $\text{Fe}_3\text{O}_4(\text{CA})\text{-ZnO}$ were 0.19 and $0.16\text{ cm}^3\text{ g}^{-1}$, respectively. Using the Barrett-Joyner-Halenda (BJH) model, the estimated pore size of $\text{Fe}_3\text{O}_4(\text{TMAH})\text{-ZnO}$ was centred at 5.8 nm while that of $\text{Fe}_3\text{O}_4(\text{CA})\text{-ZnO}$ was centred at 2 nm . The corresponding surface areas measured by BET were calculated to be $95.6\text{ m}^2\text{ g}^{-1}$ for $\text{Fe}_3\text{O}_4(\text{TMAH})\text{-ZnO}$ and $73.8\text{ m}^2\text{ g}^{-1}$ for $\text{Fe}_3\text{O}_4(\text{CA})\text{-ZnO}$. The 29.5% increase in surface area in the $\text{Fe}_3\text{O}_4(\text{TMAH})\text{-ZnO}$, in comparison with $\text{Fe}_3\text{O}_4(\text{CA})\text{-ZnO}$, is likely to be due to the smaller size of the former. For TiO_2 nanoparticles with a mean diameter of $24\pm 1\text{ nm}$, the measured surface area was $68.9\text{ m}^2\text{ g}^{-1}$ and the calculated pore size was centred at

2.1 nm. The relative pore volume was $0.21 \text{ cm}^3 \text{ g}^{-1}$, which is slightly greater than that of $\text{Fe}_3\text{O}_4(\text{TMAH})\text{-ZnO}$ ($0.19 \text{ cm}^3 \text{ g}^{-1}$) and much greater than that of $\text{Fe}_3\text{O}_4(\text{CA})\text{-ZnO}$ ($0.16 \text{ cm}^3 \text{ g}^{-1}$).

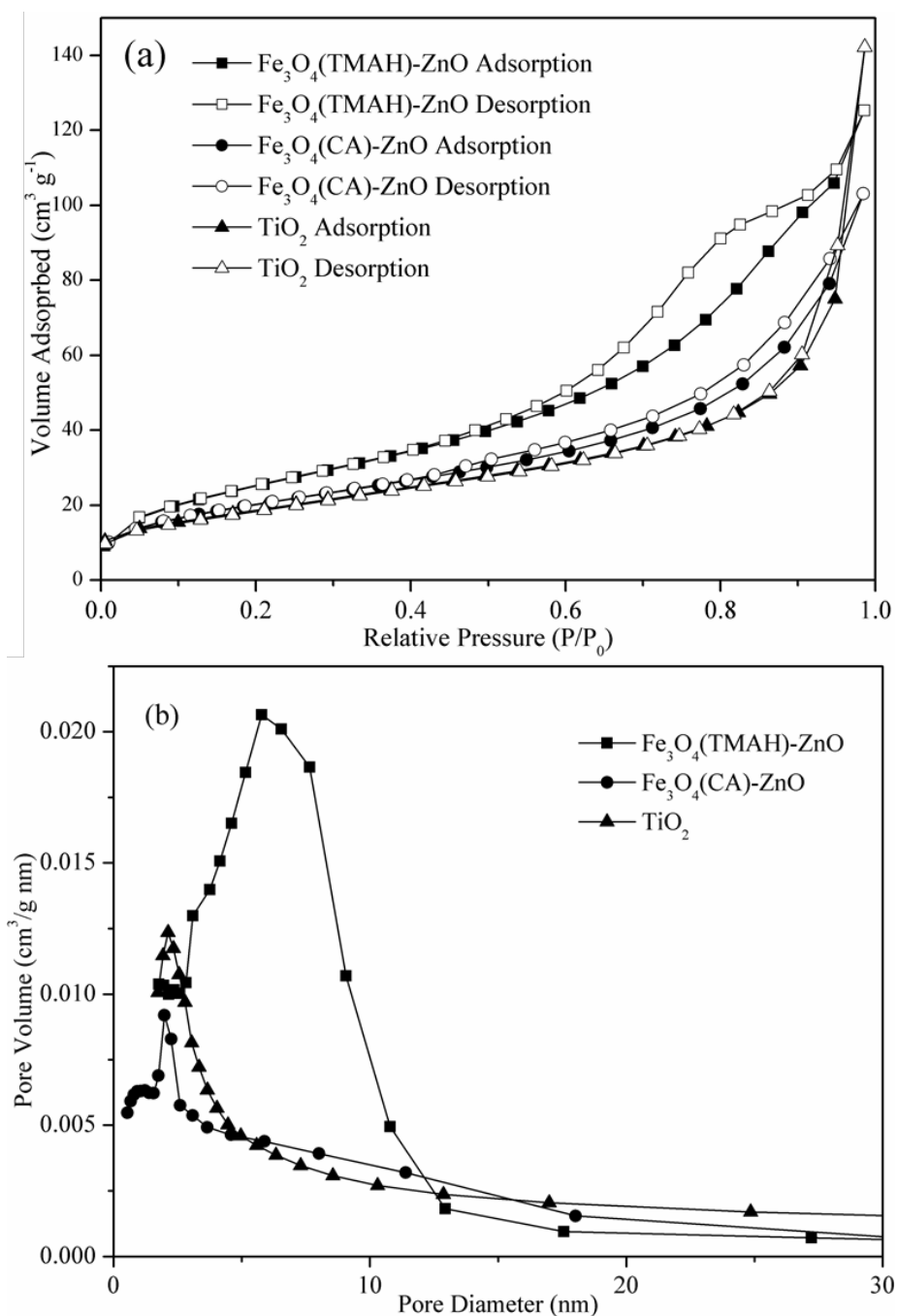


Fig. 5.8 (a) Nitrogen adsorption-desorption isotherms and (b) BJH pore-size distribution curves for TiO_2 , $\text{Fe}_3\text{O}_4(\text{TMAH})\text{-ZnO}$ and $\text{Fe}_3\text{O}_4(\text{CA})\text{-ZnO}$ hybrid nanoparticles.

The UV-Vis spectrum of Fe_3O_4 shows the broad absorption peak ranging from 300 nm to 750 nm due to the octahedral ferric ions (Xing et al. 2011). The UV-vis spectrum of ZnO showed an absorption threshold at 391 nm. The estimated band gap energy was 3.2 eV, which agrees well with the reported value (Xu et al. 2011). The absorption threshold of TiO_2 (Fig. 5.9b) was estimated to be 410 nm. The corresponding band gap energy was calculated to be 3.0 eV. After forming hybrid nanoparticles, a strong absorption was observed at 330 nm, particularly in $\text{Fe}_3\text{O}_4(\text{TMAH})\text{-ZnO}$, indicating the dominant contribution of ZnO. Visible light absorption was more dominant in $\text{Fe}_3\text{O}_4(\text{CA})\text{-ZnO}$, which could be due to the higher content of Fe_3O_4 that was confirmed by ICP-AES results. ICP-AES demonstrated that the measured mass ratios of Fe_3O_4 and ZnO in the $\text{Fe}_3\text{O}_4(\text{TMAH})\text{-ZnO}$ and $\text{Fe}_3\text{O}_4(\text{CA})\text{-ZnO}$ were 1:4.2 and 1:1.6, respectively.

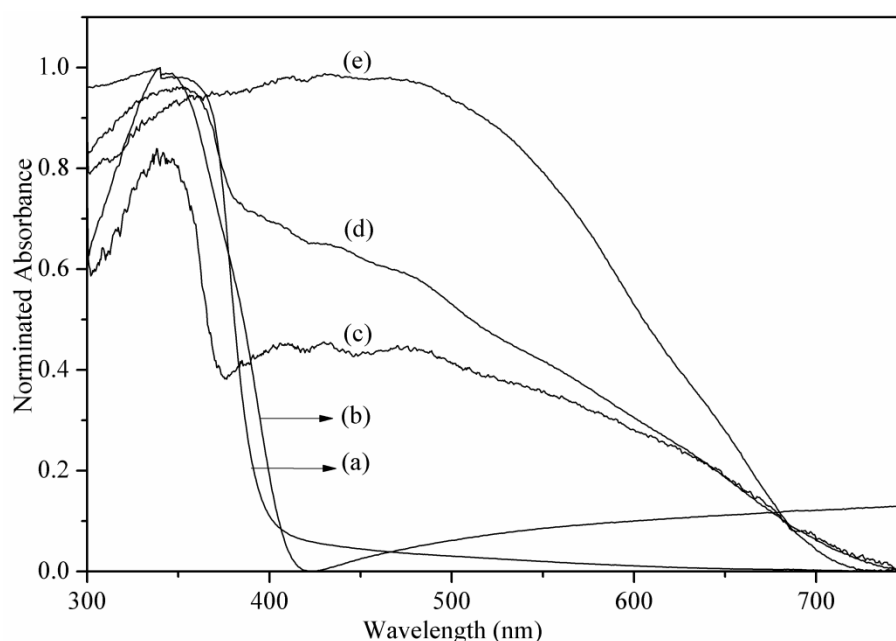


Fig. 5.9 UV-Vis spectra of (a) ZnO, (b) TiO_2 , (c) $\text{Fe}_3\text{O}_4(\text{TMAH})\text{-ZnO}$, (d) $\text{Fe}_3\text{O}_4(\text{CA})\text{-ZnO}$ and (e) Fe_3O_4 .

5.3.3 Photocatalytic properties of $\text{Fe}_3\text{O}_4\text{-ZnO}$ hybrid nanoparticles

The degradation of phenol under light irradiation was conducted in the presence of various materials. The initial concentration of phenol was 20 mg L^{-1} and the sample concentration was 0.325 g L^{-1} . The variation of phenol concentration against

the illumination time is shown in Fig. 5.10. No phenol degradation was observed after 150 min of irradiation when Fe₃O₄ was used. In the presence of the hybrid nanoparticles, the percentages of phenol degradation were 71.3% and 54.7% for Fe₃O₄(TMAH)-ZnO and Fe₃O₄(CA)-ZnO, respectively. When ZnO and TiO₂ were used, there were 51.8% and 100% of phenol degradation after 150 min of irradiation, respectively.

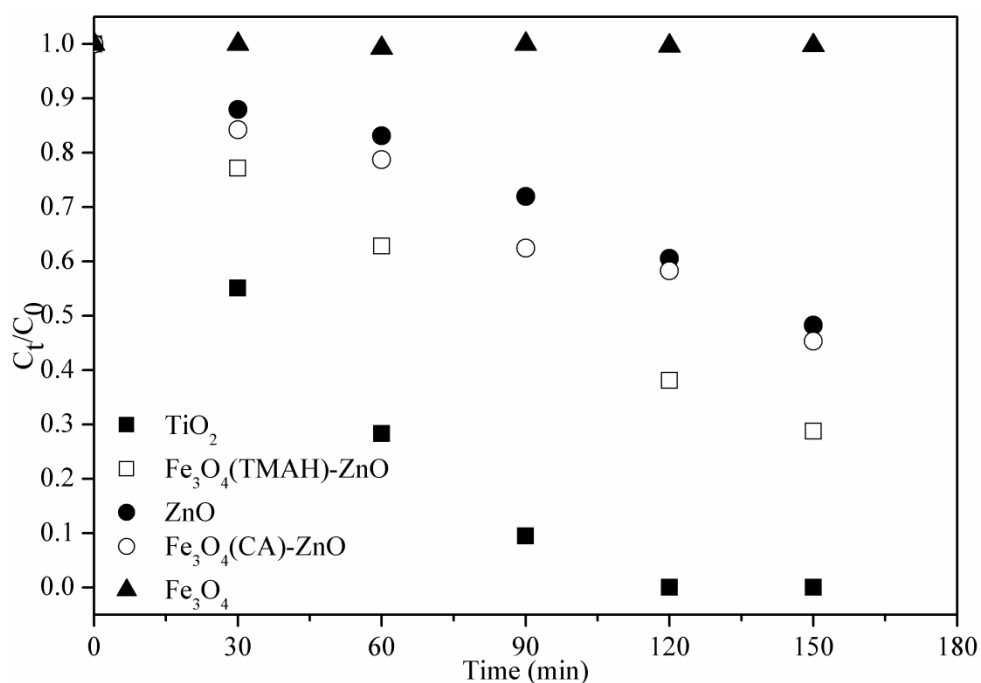


Fig. 5.10 Phenol concentration changes with time

The apparent rate constants of these samples were calculated using the following equation:

$$\ln \frac{C}{C_0} = -kt \quad (5.1)$$

where k is apparent reaction rate constant (min^{-1}), C_0 is initial concentration and C is the concentration at t . The calculated k values for TiO₂, Fe₃O₄(TMAH)-ZnO, Fe₃O₄(CA)-ZnO and ZnO were 0.0242, 0.0082, 0.0045 and 0.0039 min^{-1} , respectively. It should be noted that the calculation was performed using the

experimental data up to 120 min. The corresponding least squared R value for each fitting was 0.972, 0.981, 0.971 and 0.997, respectively.

In comparison with pure ZnO, the hybrid nanoparticles exhibited enhanced photocatalytic efficiency for phenol degradation. The enhanced photocatalytic activities of both the Fe₃O₄(TMAH)-ZnO and Fe₃O₄(CA)-ZnO hybrid nanoparticles are likely to be due to the deceleration of the rate of recombination of photo-induced charge carriers. To illustrate this, the photoluminescence (PL) spectra of all samples are presented in Fig. 5.11. The excitation source was set at 390 nm. The PL spectra of the produced nanoparticles exhibit the near-band-emission (NBE) centred well at 391 nm. The NBE arises from the recombination of electrons in singly occupied oxygen vacancies with photoinduced holes in the valence band, hence, the corresponding photoemission density reveals the separation and recombination of photoinduced charge carriers (Vanheusden et al. 1996). The photoemission intensity of the hybrid nanoparticles is lower than that of pure ZnO, suggesting the retardation of the fast recombination of the photogenerated carriers in hybrid nanoparticles. Studies on TiO₂ and Fe₃O₄(TMAH)-ZnO have shown similar photoemission density results which were considered to be due to the presence of iron ions in the Fe₃O₄(TMAH)-ZnO. In this study, the ICP-AES examination was carried out on the liquid samples collected from the photocatalytic reactions. It was found that there were 0.13 mg L⁻¹ and 0.06 mg L⁻¹ of iron ions present in phenol solution when Fe₃O₄(TMAH)-ZnO and Fe₃O₄(CA)-ZnO, respectively, were used after degradation (Table 5.2). In the previous chapter, it was speculated that the photoinduced electrons in the hybrid nanoparticles of Fe₃O₄-ZnO were transferred from the conduction band of ZnO to Fe³⁺ ions, resulting in the formation of Fe²⁺ ions. The reduced Fe²⁺ ions can be oxidized by oxygen dissolved in the reaction solution to produce Fe³⁺ ions, releasing the superoxide radicals (Feng et al. 2014). The presence of elemental iron further confirmed the hypothesis.

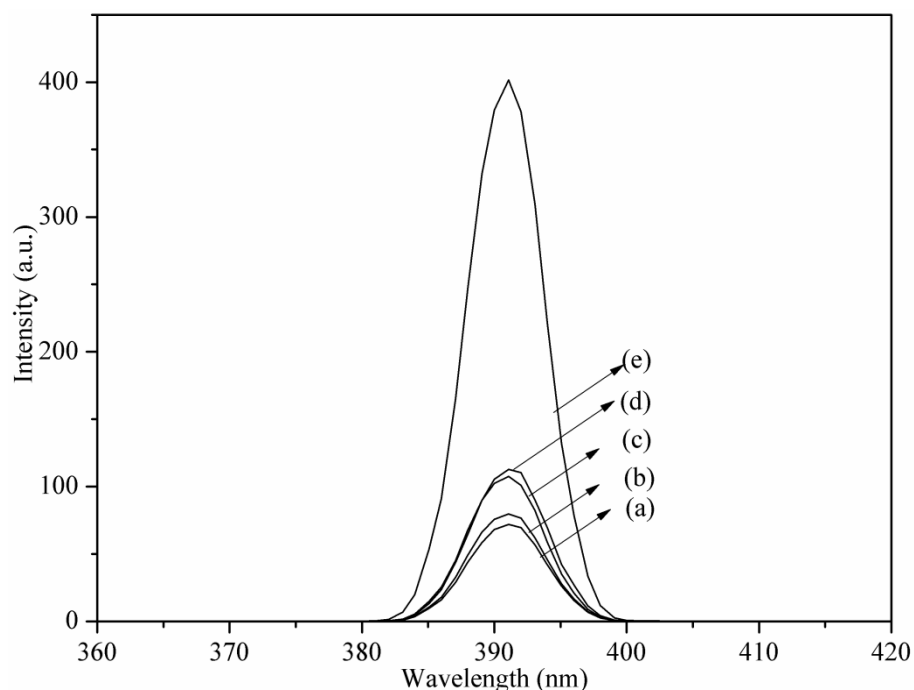


Fig. 5.11 PL emission spectra of (a) TiO_2 , (b) $\text{Fe}_3\text{O}_4(\text{TMAH})\text{-ZnO}$, (c) $\text{Fe}_3\text{O}_4(\text{CA})\text{-ZnO}$ (d) ZnO and (e) Fe_3O_4

In addition, the $\text{Fe}_3\text{O}_4(\text{TMAH})\text{-ZnO}$ hybrid nanoparticles exhibited better photocatalytic activity than the $\text{Fe}_3\text{O}_4(\text{CA})\text{-ZnO}$ hybrid nanoparticles. The major differences between these two types of hybrid particle include the particle size, the ZnO content, the structure/morphology and the iron ion concentration in the phenol degradation concentration. Firstly, the size of $\text{Fe}_3\text{O}_4(\text{CA})\text{-ZnO}$ nanoparticles are nine times bigger than that of $\text{Fe}_3\text{O}_4(\text{TMAH})\text{-ZnO}$ nanoparticles, as displayed in Fig. 5.6, resulting in the decrease in reactive surface area confirmed by the specific surface area measured using BET analysis. Secondly, ZnO contents in $\text{Fe}_3\text{O}_4(\text{TMAH})\text{-ZnO}$ and $\text{Fe}_3\text{O}_4(\text{CA})\text{-ZnO}$ obtained by ICP-AES results were 80.6% and 61.4%, respectively, indicating a 31.2% increase in ZnO content in the $\text{Fe}_3\text{O}_4(\text{TMAH})\text{-ZnO}$. Thirdly, the morphologies of the two types of hybrid nanoparticle are quite different. As shown in Figure 5.6, the $\text{Fe}_3\text{O}_4(\text{CA})\text{-ZnO}$ is more loosely structured due to the presence of $\text{Fe}_3\text{O}_4(\text{CA})$, which might make the electron transfer from ZnO to Fe_3O_4 less effective, even when there are iron ions present in the reaction solution. This can be seen in the PL spectra of the $\text{Fe}_3\text{O}_4(\text{CA})\text{-ZnO}$ that shows photoemission intensity which is similar to that of ZnO and greater than that of $\text{Fe}_3\text{O}_4(\text{TMAH})\text{-ZnO}$. Also,

the elemental iron concentration in $\text{Fe}_3\text{O}_4(\text{TMAH})\text{-ZnO}$ containing the reaction mixture was higher than that in the $\text{Fe}_3\text{O}_4(\text{CA})\text{-ZnO}$ containing reaction mixture.

Commercial TiO_2 (P25) also was used in this study for comparison purposes. A much higher phenol degradation rate was observed for P25 (0.0242 min^{-1}) than that of $\text{Fe}_3\text{O}_4(\text{TMAH})\text{-ZnO}$ (0.0082 min^{-1}), although the photoemission intensities of the two were similar. It is worth mentioning that the concentration of TiO_2 used in the degradation reaction was 0.325 g L^{-1} , however the ZnO content in $\text{Fe}_3\text{O}_4(\text{TMAH})\text{-ZnO}$ was only 81%, representing a weight concentration of 0.26 g L^{-1} . At a similar concentration, the rate constant of TiO_2 was 0.0152 min^{-1} (Chapter 2), which is two times of the rate constant of $\text{Fe}_3\text{O}_4(\text{TMAH})\text{-ZnO}$. In addition, most of the $\text{Fe}_3\text{O}_4(\text{TMAH})\text{-ZnO}$ nanoparticles (86%) could be readily recovered from the phenol solution using a magnet, indicating that the hybrid nanoparticles are a more economical product.

5.3.3.1 Effect of reaction parameters on the photocatalytic activity of $\text{Fe}_3\text{O}_4(\text{TMAH})\text{-ZnO}$

Reaction parameters such as catalyst dosage, initial phenol concentration and pH values exert great influences on the photocatalytic reaction. Hence, a series of experiments were conducted using $\text{Fe}_3\text{O}_4(\text{TMAH})\text{-ZnO}$ as the catalyst, and the loss of iron and zinc ions during the photochemical reaction was monitored.

Effect of catalyst dosage

The comparison of percentage phenol degradation using 0.1, 0.325, 0.5 and 1.0 g L^{-1} of $\text{Fe}_3\text{O}_4(\text{TMAH})\text{-ZnO}$ hybrid nanoparticles after 150 min of irradiation is presented in Fig. 5.12. When catalyst concentration was at 0.1, 0.325, 0.5 and 1.0 g L^{-1} , the percentage phenol degradation was 62.7%, 71.3%, 63.6% and 57.5%, respectively.

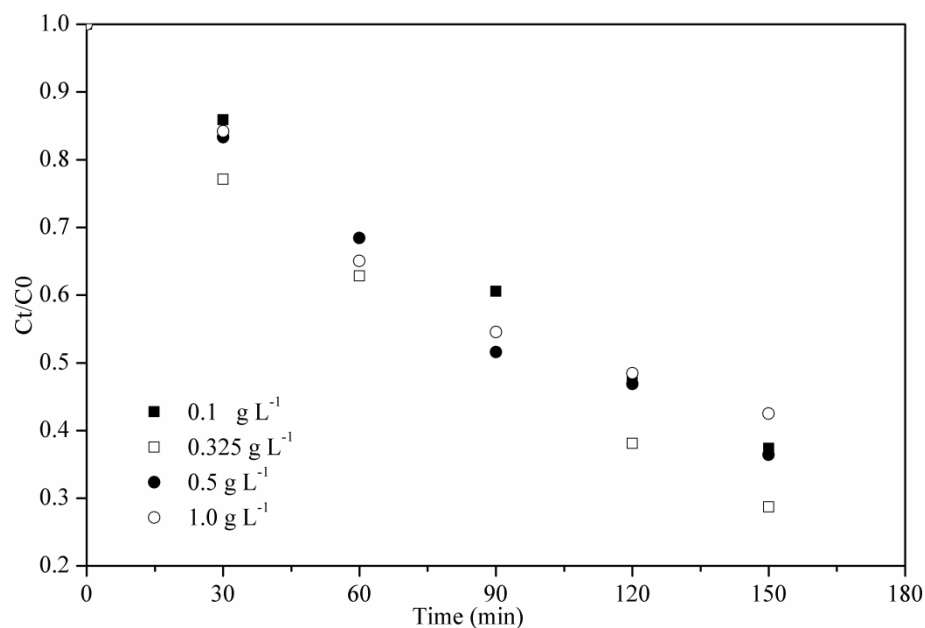


Fig. 5.12. Phenol concentration changes as a function of catalyst loading

The corresponding apparent rate constants were 0.0062, 0.0082, 0.0067 and 0.0061 min⁻¹, respectively. The corresponding least square R values were 0.9888, 0.9985, 0.9911 and 0.9791. It was found that degradation rate increased as the catalyst concentration was increased up to 0.325 g L⁻¹. This was due to the enhancement of the photoinduced charge carrier and therefore the increase in total number of catalyst sites on the catalyst surface. However, when the catalyst concentration was over 0.325 g L⁻¹, the degradation rate of phenol decreased with increasing catalyst concentration. Particle aggregation and the shielding effect of light at higher concentrations were two major reasons for the decrease in the phenol degradation rate. In this study, particle agglomeration at higher catalyst concentration led to the decrease in surface area and, subsequently, the total number of catalytic sites on the catalyst surface. Also, the pathway of light may have been blocked at the higher catalyst concentration (Chen and Ray 1998). Similar phenomena were observed when P25 was used as the catalyst, as presented in Chapter 2. In this study, the optimal catalyst concentration for Fe₃O₄(TMAH)-ZnO hybrid nanoparticles was 0.325 g L⁻¹.

The loss of zinc ions during the photochemical reaction was examined by ICP-AES using the liquid samples collected. The results are summarised in Table 5.2. It

was found that when the catalyst concentrations were 0.1, 0.325, 0.5 and 1.0 g L⁻¹, the concentrations of zinc ions in phenol solution were 7.8, 5.9, 6.7 and 8.0 mg L⁻¹, respectively. The relatively constant zinc ion concentration could have been the maximum solubility of zinc oxide.

Effect of initial phenol concentration

The effect of initial phenol concentration on phenol degradation was investigated using the fixed catalyst concentration of 0.325 g L⁻¹, displayed in Fig. 5.13. When phenol concentrations were at 10, 20 and 80 mg L⁻¹, the removal of phenol was 78.0%, 71.3% and 25.9%, respectively. The corresponding apparent rate constants were estimated to be 0.0099, 0.0082 and 0.0022 min⁻¹, respectively. The decrease in degradation rate with increasing phenol concentration is possibly due to the limited catalytic sites presented on the surface of hybrid nanoparticles when the catalyst concentration was fixed. Additionally, during the photochemical reaction, the excess reaction intermediates formed may also have occupied the active sites, leading to a decrease in degradation rate (Wei and Wan 1991). For the rest of the study, phenol aqueous solution (20 mg L⁻¹) was used. The iron and zinc contents in phenol solution are summarised in Table 5.2.

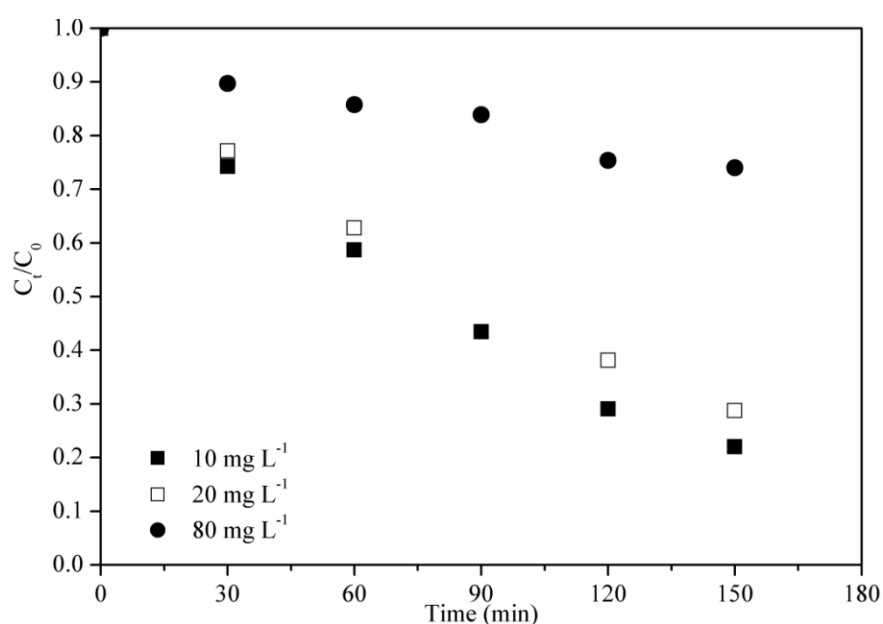


Fig. 5.13 Effect of initial phenol concentration on performance of Fe₃O₄(TMAH)-ZnO.

Effect of pH value on phenol degradation

The effect of pH value on nanoparticle performance was explored using four pH conditions (pH=2.5, 4, 8 and 10). The relative experiments were carried out at fixed concentrations of phenol (20 mg L^{-1}) and catalyst (0.325 g L^{-1}). The pH value of the previously discussed experimental solution was measured to be 5.6 (Deionised water was used without buffer.). Fig. 5.14 shows the phenol concentration changes at various pH values. An apparent change was seen in both phenol degradation efficiency and degradation rate. When pH was at 2.5, 4, 5.6, 8 and 10, the percentage phenol degradation was 51.9%, 100%, 71.3%, 30.8% and 14.5%, respectively. The degradation rate constants were 0.0050 , 0.0170 , 0.0082 , 0.0030 and 0.0013 min^{-1} , respectively. There was a thirteen-fold increase observed when pH value was reduced from 10 to 4. The ICP-AES analysis showed that, prior to the photocatalytic reaction, the iron content was 0 mg L^{-1} at pH 10 and 18 mg L^{-1} at pH 4. This further confirmed that the presence of iron ions could decelerate the fast recombination of photogenerated electron-hole pairs, therefore improving the photocatalytic activity (Feng et al. 2014). However, when pH value was 2.5, the degradation rate constant was drastically reduced to 0.0050 min^{-1} . The decrease in phenol degradation rate was, most likely, due to the complete dissolution of ZnO. The ICP-AES results demonstrated that, prior to the photocatalytic reaction, there were 22 mg L^{-1} iron ions and 220 mg L^{-1} zinc ions present in phenol solution, representing a loss of 42.1% of iron ions and 91.7% of zinc ions. After photocatalytic reactions (150 min), there were 24 mg L^{-1} iron ions and 240 mg L^{-1} zinc ions, indicating a loss of 46% of iron ions and 100% of zinc ions in the final phenol solution. The total loss of the ZnO could be a combined result of chemical- and photo-dissolution. The latter has been discussed in Chapter 4. In an alkaline solution (pH>7), the phenol degradation rate becomes slower. This can be attributed to the low iron ions present in the phenol solution, which also was confirmed by ICP-AES results. When the pH value was 10, the iron ions concentration was below the detection limit of 0.01 mg L^{-1} before the photocatalytic reaction. Also, the basic solution could lower the oxidation potential of hydroxyl radicals, leading to a decrease in oxidation efficiency of the phenol in solution (Chiou et al. 2008, Hayat et al. 2011).

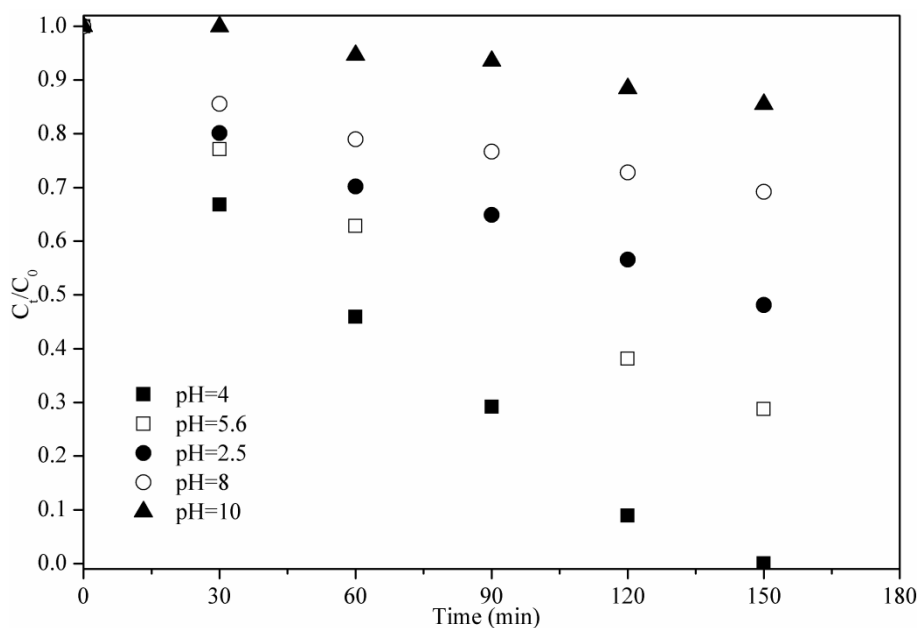


Fig. 5.14 Effect of pH value on performance of Fe₃O₄(TMAH)-ZnO regarding phenol degradation.

5.3.3.2 Effect of reaction parameters on photoreactivity of Fe₃O₄(CA)-ZnO

Similar investigations were carried out in the presence of Fe₃O₄(CA)-ZnO nanoparticles. Fig. 5.15 shows the phenol concentration changes against irradiation time. When the catalyst concentrations were 0.1, 0.325, 0.5 and 1.0 g L⁻¹, the percentage phenol removal was 23.0%, 54.7%, 34.6% and 23.9%, respectively. The corresponding rate constants were 0.0017, 0.0045, 0.0028 and 0.0019 min⁻¹. It is obvious that the system with 0.325 g L⁻¹ yielded the highest phenol degradation efficiency and degradation rate. With catalyst concentrations of 0.1, 0.325, 0.5 and 1.0 g L⁻¹, the zinc ion concentrations in the final phenol solution were 7.4, 8.0, 9.5 and 14 mg L⁻¹, respectively.

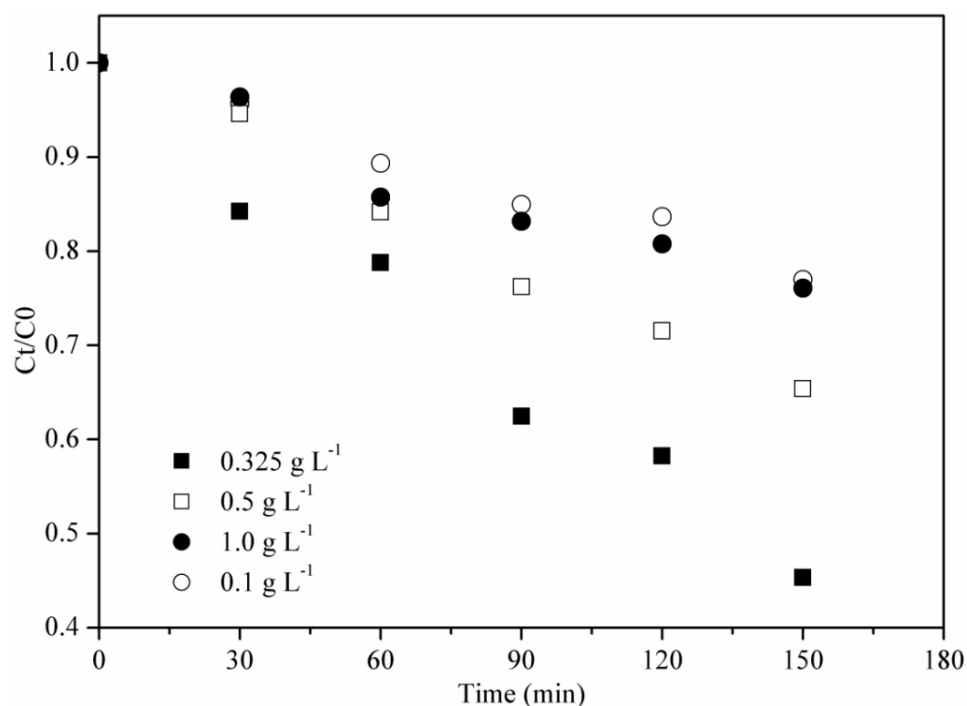


Fig. 5.15 Effect of catalyst dosage on the performance of $\text{Fe}_3\text{O}_4(\text{CA})\text{-ZnO}$ in regard to phenol degradation

When the catalyst concentration was at 0.325 g L^{-1} , the degradation rate was reduced from 0.0045 to 0.0013 min^{-1} as the phenol concentrations were increased from 20 to 80 mg L^{-1} . For the subsequent investigation, 20 mg L^{-1} of phenol aqueous solution was used. As pH value was decreased from 10 to 2.5 , an apparent change was observed in phenol degradation efficiency, as presented in Fig. 5.16. Similar to the results for $\text{Fe}_3\text{O}_4(\text{TMAH})\text{-ZnO}$, the degradation rate, in order, was $\text{pH } 4 > \text{pH } 5.6 > \text{pH } 2.5 > \text{pH } 8 > \text{pH } 10$ when $\text{Fe}_3\text{O}_4(\text{CA})\text{-ZnO}$ was used as the photocatalyst.

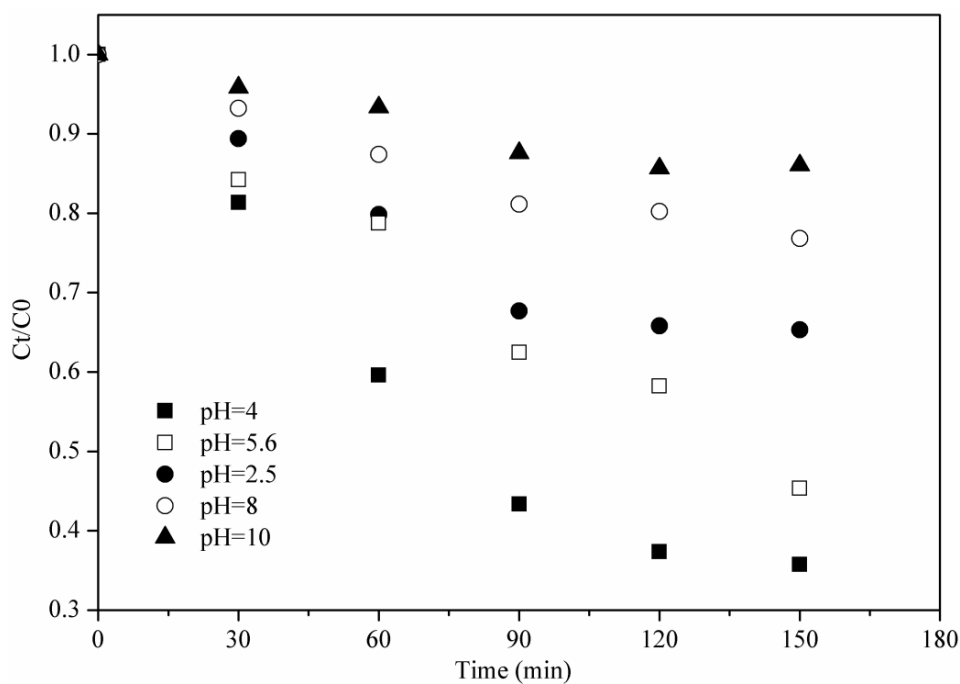


Fig. 5.16 Effect of pH on the performance of $\text{Fe}_3\text{O}_4(\text{CA})\text{-ZnO}$ regarding phenol degradation.

5.3.4 Comparison of photocatalytic properties of different nanoparticles

The photocatalytic properties of $\text{Fe}_3\text{O}_4(\text{TMAH})\text{-ZnO}$, $\text{Fe}_3\text{O}_4(\text{CA})\text{-ZnO}$ and TiO_2 are summarised and presented in Fig. 5.17. For $\text{Fe}_3\text{O}_4(\text{TMAH})\text{-ZnO}$ an optimal degradation rate constant of 0.0170 min^{-1} was achieved at $\text{pH}=4$, which is nine times that of commercial TiO_2 (0.0020 min^{-1}). An optimal degradation rate constant of 0.0085 min^{-1} was observed for $\text{Fe}_3\text{O}_4(\text{CA})\text{-ZnO}$ at the same condition which is four times that of TiO_2 . In contrast to these observations, commercial TiO_2 performed the best at $\text{pH}=5.6$, presenting a rate constant of 0.0154 min^{-1} , which is slightly lower than that of $\text{Fe}_3\text{O}_4(\text{CA})\text{-ZnO}$ at $\text{pH}=4$.

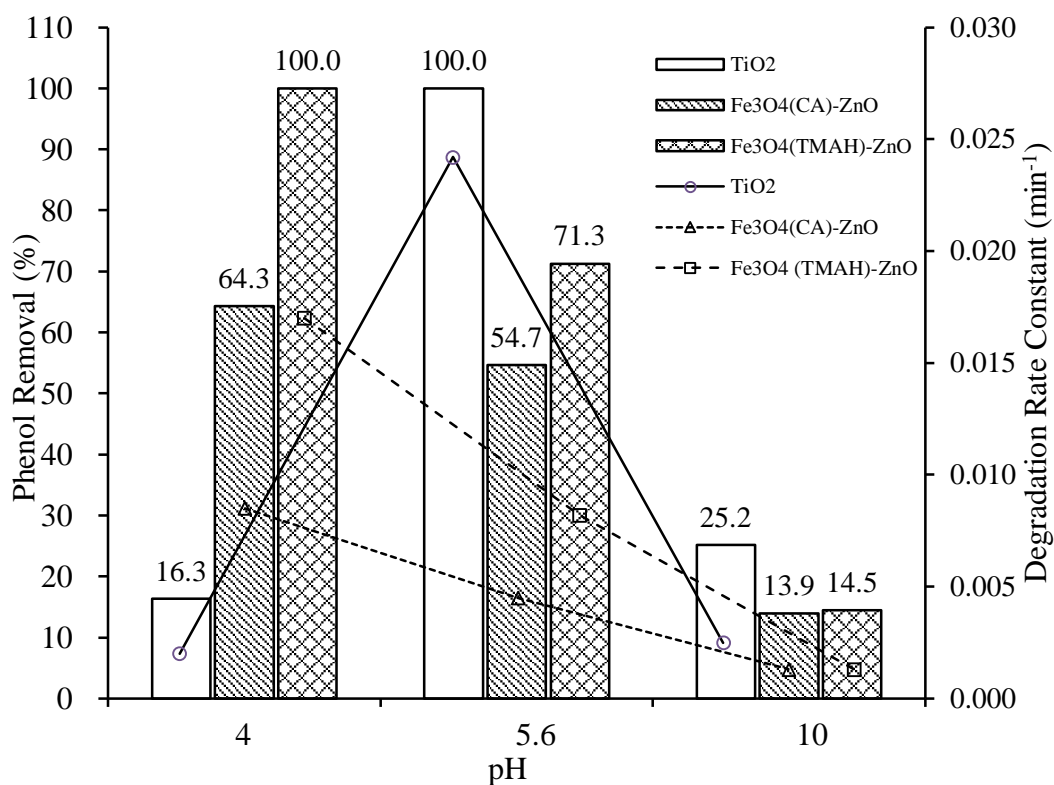


Fig.5.17 Phenol removal as a function of pH in the presence of various materials. The catalyst concentration was 0.325 g L^{-1} . The initial phenol concentration was 20 mg L^{-1} .

5.4 Conclusion

In summary, magnetite (Fe_3O_4) nanoparticles, prepared using a chemical co-precipitation method, were suspended in a cationic surfactant (tetramethylammonium hydroxide, TMAH) and an anionic surfactant (citric acid, CA). Both surfactants have shown ability to stabilise the Fe_3O_4 nanoparticles which is believed to be due to the presence of positively charged tetramethylammonium ions on $\text{Fe}_3\text{O}_4(\text{TMAH})$ and negatively charged carboxyl ions on $\text{Fe}_3\text{O}_4(\text{CA})$ respectively. $\text{Fe}_3\text{O}_4\text{-ZnO}$ hybrid nanoparticles produced TMAH-stabilised nanoparticles, $\text{Fe}_3\text{O}_4(\text{TMAH})\text{-ZnO}$, have an average size of $34.5 \pm 6.2 \text{ nm}$ which is much smaller than those produced from CA-stabilised nanoparticles ($\text{Fe}_3\text{O}_4(\text{CA})\text{-ZnO}$) nanoparticles ($293 \pm 32 \text{ nm}$). BET results demonstrated that $\text{Fe}_3\text{O}_4(\text{TMAH})\text{-ZnO}$ ($95.6 \text{ m}^2 \text{ g}^{-1}$) has a slightly larger (29.5%) surface area than $\text{Fe}_3\text{O}_4(\text{CA})\text{-ZnO}$ ($73.8 \text{ m}^2 \text{ g}^{-1}$). Upon exposure to illumination, the both types of hybrid nanoparticles showed enhanced photocatalytic activities in comparison with pure ZnO, resulting from a decreased recombination

rate of the photoinduced charge carriers. The enhanced photoreactivity of Fe₃O₄-ZnO is strongly associated with the presence of iron ions in the reaction mixture. It is speculated that the iron ions acted as photoexcited electron-trappers to prevent the fast recombination of the charge carriers. The pH value is another important factor that influenced the photocatalytic reactivity of the hybrid nanoparticles. For both types of hybrid nanoparticles, the optimal pH value is 4 at which the photodegradation of phenol by Fe₃O₄(TMAH)-ZnO is as efficient as that by P25, the most widely applied photocatalyst, at its optimal condition (pH=5.6). Hence, as potential photosensitiser, the produced Fe₃O₄-ZnO hybrid nanoparticles exhibited better photocatalytic activity at acid condition when the catalyst concentration was 325 µg ml⁻¹. It suggests that the hybrid nanoparticles are capable of effective killing cancer cells that often show an internal pH value below 7 (Jana et al. 2007, Muhammad et al. 2011b). Based on these results, future work involving the cytotoxicity, haemolysis and photo-toxicity study could be carried out at the particle concentration below 325 µg ml⁻¹.

CHAPTER 6 CONCLUSION AND RECOMMENDATIONS

6.1 Conclusion

In this thesis, folic acid-conjugated titanium dioxide-silica ($\text{TiO}_2\text{-SiO}_2$) composite nanoparticles and iron oxide-zinc oxide ($\text{Fe}_3\text{O}_4\text{-ZnO}$) hybrid nanoparticles were successfully synthesised, and systematically investigated as potential nano-photosensitisers for effective and targeted photokilling of cancerous cells.

For folic acid-conjugated $\text{TiO}_2\text{-SiO}_2$ nanoparticles (TS-FA), conclusive results are listed below:

- Silica coating improved the stability and dispersity of TiO_2 nanoparticles, however, it reduced their photocatalytic activity. When the silica shell thickness was minimised to 5.5 nm, the photocatalytic activity of coated TiO_2 was very close to non-coated TiO_2 nanoparticles;
- The presence of a silica shell improved the compatibility of the core TiO_2 nanoparticles with mouse connective tissue cells (L929), and the $\text{TiO}_2\text{-SiO}_2$ exhibited good haemocompatibility;
- The phototoxicity of $\text{TiO}_2\text{-SiO}_2$ with optimised shell thickness was well demonstrated when the nanoparticles were irradiated under UV-light. Its photokilling ability was comparable to that of the non-coated commercial TiO_2 ;
- When the $\text{TiO}_2\text{-SiO}_2$ was conjugated with folic acid, further improvement of cellular compatibility was well demonstrated, for both primary adherent mouse fibroblast connective tissue cells (L929 cells) and the human nasopharyngeal epidermoid cancer cells (KB cells), and this corresponded to a wide concentration range of nanoparticles (between 12.5 and 200 $\mu\text{g ml}^{-1}$);
- Whilst the contribution of the silica shell to such improvement is indicated, the nutritional factors of the folate element were more predominant;
- Upon exposure to UV light, the folic acid-conjugated $\text{TiO}_2\text{-SiO}_2$ nanoparticles were toxic to KB cells due to their high photocatalytic activities.

- It was demonstrated that photokilling effects were improved by stronger concentration and longer exposure time;
- TS-FA particles were bound to KB cells (folate receptor-positive cells), indicating a high ability to target cancerous cells;
- The dual targeting capabilities, through both the folic acid-conjugation and the photoinduced cancer killing of the TS-FA system, promises great potential in the treatment of cancer, and possibly other diseases.
- A further investigation, to optimise the photokilling ability of the TS-FA system is underway.

For iron oxide-zinc oxide ($\text{Fe}_3\text{O}_4\text{-ZnO}$) hybrid nanoparticles, the conclusions are summarised below:

- Highly enhanced photocatalytic activity of ZnO nanoparticles was achieved through the hybridisation with Fe_3O_4 , which is a first in this field;
- A decelerated recombination rate of photogenerated electron-hole pairs was demonstrated through the reduction in photoluminescence;
- It is speculated that the free iron ions acted as an electron-trapping site to prevent the fast recombination of photogenerated charge carriers, therefore improving the photocatalytic properties;
- Slight acidic conditions can further improve the photoreactivity of the hybrid nanoparticles, which is a useful finding for cancer-targeting as pH is relatively low in tumour cells.

Other observations on $\text{Fe}_3\text{O}_4\text{-ZnO}$ hybrid nanoparticles include:

- Surfactants stabilise the Fe_3O_4 nanoparticles and affect their surface charge, hydrodynamic size and size distribution. This in turn affects the properties of the hybrid nanoparticles produced from the surfactant-stabilised Fe_3O_4 .
- Positively charged Fe_3O_4 nanoparticles have led to the production of hybrid nanoparticles of a relatively smaller size that are higher in ZnO content and of denser morphology when compared to the hybrid nanoparticles prepared from negatively charged Fe_3O_4 nanoparticles, resulting in better photocatalytic properties;

- Leaching and photodissolution of Fe_3O_4 and ZnO was noticeable during the reaction process. Whilst the loss of ZnO resulted in reduced photocatalytic efficiency, the increased concentration of leached iron ions improved the efficiency of reactive oxygen species (ROS);
- The viability of both L929 and KB cells in the presence of these nanoparticles, both in the dark and under light irradiation, is under investigation.

6.2 Limitation of the Work and Future Direction

Although this thesis provides comprehensive studies on the potential application of titanium dioxide- and zinc oxide-based photosensitisers in PDT, there are still some limitations of the developed nanoparticles that require future investigations.

For folic acid-conjugated titanium dioxide-silica (TS-FA) composite nanoparticles, limitations and required future work are listed below:

- After the cells incubated with TS-FA, a strong increase in the viability of both L929 cells and KB cells were demonstrated. This is due to nutrimental function of the folate elements. Further investigations are required to optimise the photokilling ability of TS-FA.
- In comparison with near-infrared (NIR) light excitation, ultraviolet (UV) light excitation provides poorer tissue penetration ability. For example, when the UV excitation wavelength was at 365 nm, the penetration depth was approximately 20 μm (Masters et al. 1997). However, when NIR light excitation was in the region of 700-1000 nm, the penetration depth was around 1.0 mm (Chu et al. 2013). This should be considered in the development of the novel generation of nanphotosensitizers for PDT.

For iron oxide-zinc oxide (Fe_3O_4 - ZnO) hybrid nanoparticle:

- The recent study is focused on the investigation of major reaction parameters including the mass ratio of Fe_3O_4 and ZnO , catalyst dosage and pH value to achieve optimized photocatalytic efficiency. Further evaluation of the optimised nanoparticles both *in vitro* and *in vivo* is required.

REFERENCES

- The Australian National Health and Medical Research Council Nutrient reference values for Australia and New Zealand. http://www.nrv.gov.au/sites/default/files/page_pdf/n35-iron_0.pdf.
- American Cancer Society. 2011. Global Cancer Factors & Figures 2nd Edition. <http://www.cancer.org>.
- International Agency for Research on Cancer. 2012. Globocan 2012: Estimated cancer incidence mortality and prevalence worldwide in 2012. <http://globocan.iarc.fr>.
- Australia Institute of Health and Welfare. 2013. Cancer in Australia: Key facts. <http://www.aihw.gov.au/cancer/cancer-in-australia>.
- Ackroyd, R., C. Kelty, N. Brown and M. Reed. 2001. The history of photodetection and photodynamic therapy. *Photochemistry and Photobiology* 74(5): 656-669.
- Aguado, J., R. Grieken, M. J. López-Muñoz and J. Marugán. 2002. Removal of cyanides in wastewater by supported TiO₂-based photocatalysts. *Catalysis Today* 75(1-4): 95-102.
- Ahmed, M. A., E. E. El-Katori and Z. H. Gharni. 2013. Photocatalytic degradation of methylene blue dye using Fe₂O₃/TiO₂ nanoparticles prepared by sol-gel method. *Journal of Alloys and Compounds* 553: 19-29.
- Ahn, C. H., S. Y. Chae, Y. H. Bae and S. W. Kim. 2004. Synthesis of biodegradable multi-block copolymers of poly(L-lysine) and poly(ethylene glycol) as a non-viral gene carrier. *Journal of Controlled Release* 97(3): 567-574.
- Alexander, C. M., K. L. Hamner, M. M. Maye and J. C. Dabrowiak. 2014. Multifunctional DNA-gold nanoparticles for targeted doxorubicin delivery. *Bioconjugate Chemistry*.
- Allison, R. R., G. H. Downie, R. Cuenca, X. H. Hu, C. J. H. Childs and C. H. Sibata. 2004. Photosensitizers in clinical PDT. *Photodiagnosis and Photodynamic Therapy* 1(1): 27-42.
- Allison, R. R. and C. H. Sibata. 2010. Oncologic photodynamic therapy photosensitizer: A clinical review. *Photodiagnosis and Photodynamic Therapy* 7(2): 61-75.

- Ambrus, Z., N. Balázs, T. Alapi, G. Wittmann, P. Sipos, A. Dombi and K. Mogyorósi. 2008. Synthesis, structure and photocatalytic properties of Fe(III)-doped TiO₂ prepared from TiCl₃. *Applied Catalysis B: Environmental* 81(1–2): 27-37.
- Ansari, S. A., Q. Husain, S. Qayyum and A. Azam. 2011. Designing and surface modification of zinc oxide nanoparticles for biomedical applications. *Food and Chemical Toxicology* 49(9): 2107-2115.
- Arruebo, M., R. Fernandez-Pacheco, M. R. Ibarra and J. Santamaria. 2007. Magnic nanoparticles for drug delivery. *NanoToday* 2(3): 22-32.
- Awan, M. A. and S. A. Tarin. 2006. Review of photodynamic therapy. *Surgeon* 4(4): 231-236.
- Ba-Abbad, M. M., A. A. H. Kadhum, A. B. Mohamad, M. S. Takriff and K. Sopian. 2013. Visible light photocatalytic activity of Fe³⁺-doped ZnO nanoparticle prepared via sol–gel technique. *Chemosphere* 91(11): 1604-1611.
- Bae, B. C. and K. Na. 2010. Self-quenching polysaccharide-based nanogels of pullulan/folate-photosensitizer conjugates for photodynamic therapy. *Biomaterials* 31(24): 6325-6335.
- Bagwe, R. P., L. R. Hilliard and W. Tan. 2006. Surface modification of silica nanoparticles to reduce aggregation and nonspecific binding. *Langmuir* 22: 4357-4362.
- Banerjee, T., S. Mitra, A. K. Singh, R. K. Sharma and A. Maitra. 2002. Preparation, characterization and biodistribution of ultrafine chitosan nanoparticles. *International Journal of Pharmaceutics* 243(1-2): 93-105.
- Barolet, D. 2008. Light-emitting diodes (LED) in dermatology. *Seminars in cutaneous medicine and surgery* 27(4): 227-238.
- Barreto, J. A., W. O. Malley, M. Kubeil, B. Graham, H. Stephan and L. Spiccia. 2011. Nanomaterials: Applications in cancer imaging and therapy. *Advanced Materials* 23(12): H18-H40.
- Bekkouche, S., M. Bouhelassa, N. H. Salah and F. Z. Meghlaoui. 2004. Study of adsorption of phenol on titanium oxide (TiO₂). *Desalination* 166: 355-362.
- Berg, K., P. Selbo, A. Weyergang, A. Dietze, L. Prasmickaite, A. Bonsted, B. Engesaeter, E. Angell-Petersen, T. Warloe, N. Frandsen and A. Hogest. 2005. Porphyrin-related photosensitizers for cancer imaging and therapeutic application. *Journal of Microscopy* 218(2): 133-147.

- Berlin, N. I., A. Neuberger and J. J. Scott. 1956a. The metabolism of d-aminolaevulinic acid: 2. Normal pathways, studied with the aid of ^{14}C . *Biochemical Journal* 64(1): 90-100.
- Berlin, N. I., A. Neuberger and J. J. Scott. 1956b. The metabolism of d-paminolaevulinic acid: 1. Normal pathways, studied with the aid of ^{15}N . *Biochemical Journal* 64(1): 80-90.
- Bertrand, N., J. Wu, X. Xu, N. Kamaly and O. C. Farokhzad. 2014. Cancer nanotechnology: The impact of passive and active targeting in the era of modern cancer biology. *Advanced Drug Delivery Reviews* 66: 2-25.
- Beydoun, D., R. Amal, G. K. C. Low and S. McEvoy. 2000. Novel photocatalyst: Titania-coated magnetite. activity and photodissolution. *The Journal of Physical Chemistry B* 104(18): 4387-4396.
- Bhattacharya, R., C. R. Patra, A. Earl, S. Wang, A. Katarya, L. Lu, J. N. Kizhakkedathu, M. J. Yaszemski, P. R. Greipp, D. Mukhopadhyay and P. Mukherjee. 2007. Attaching folic acid on gold nanoparticles using noncovalent interaction via different polyethylene glycol backbones and targeting of cancer cells. *Nanomedicine: Nanotechnology, Biology and Medicine* 3(3): 224-238.
- Biju, V. 2014. Chemical modifications and bioconjugate reactions of nanomaterials for sensing imaging drug delivery and therapy. *Chemical Society Reviews* 43(3): 744-764.
- Bonechis, C., A. Donati, R. Lampariello, S. Martini, M. P. Picchi, M. Ricci and C. Rossi. 2004. Solution structure of folic acid molecular mechanics and NMR investigation. *Spectrochimica Acta Part A: Molecular and Biomolecular Spectroscopy* 60: 1411-1419.
- Brizel, D. M., M. E. Albers, S. R. Fisher, R. L. Scher, W. J. Richtsmeier, V. Hars, S. L. George, A. T. Huang and L. R. Prosnitz. 1998. Hyperfractionated irradiation with or without concurrent chemotherapy for locally advanced head and neck cancer. *The New England Journal of Medicine* 338(25): 1798-1804.
- Brunner, T. J., P. Wick, P. Manser, P. Spohn, R. N. Grass, L. K. Limbach, A. Bruinink and W. J. Stark. 2006. In vitro cytotoxicity of oxide nanoparticles: Comparison to asbestos, silica, and the effect of particle solubility. *Environmental Science & Technology* 40(14): 4374-4381.

- Buchko, G. W., J. R. Wagner, J. Cadet, S. Raoul and M. Weinfeld. 1995. Methylene blue-mediated photooxidation of 7,8-dihydro-8-oxo-2'-deoxyguanosine. *Biochimica et Biophysica Acta* 1263: 17-24.
- Buggiani, G., M. Troiano, R. Rossi and T. Lotti. 2008. Photodynamic therapy: Off-label and alternative use in dermatological practice. *Photodiagnosis and Photodynamic Therapy* 5(2): 134-138.
- Cai, R., Y. Kubota, T. Shuin, H. Sakai, K. Hashimoto and A. Fujishima. 1992. Induction of cytotoxicity by photoexcited TiO₂ particles. *Cancer Research* 52(8): 2346-2348.
- Caley, A. and R. Jones. 2012. The principles of cancer treatment by chemotherapy. *Surgery (Oxford)* 30(4): 186-190.
- Carter, P. 2001. Improving the efficacy of antibody-based cancer therapies. *Nature Reviews Cancer* 1(2): 118-129.
- Carturan, G., R. D. Toso, S. Boninsegni and R. D. Monte. 2004. Encapsulation of functional cells by sol-gel silica: Actual progress and perspectives for cell therapy. *Journal of Materials Chemistry* 14(14): 2087-2098.
- Castano, A. P., T. N. Demidova and M. R. Hamblin. 2004. Mechanisms in photodynamic therapy: Part one-photosensitizers, photochemistry and cellular localization. *Photodiagnosis and Photodynamic Therapy* 1(4): 279-293.
- Chae, S. Y., M. K. Park, S. K. Lee, T. Y. Kim, S. K. Kim and W. I. Lee. 2003. Preparation of size-controlled TiO₂ nanoparticles and derivation of optically transparent photocatalytic films. *Chemistry of Materials* 15(17): 3326-3331.
- Chaplin, D. J., S. A. Hill, K. M. Bell and G. M. Tozer. 1998. Modification of tumor blood flow: Current status and future directions. *Seminars in Radiation Oncology* 8(3): 151-163.
- Chatterjee, D. K., L. S. Fong and Y. Zhang. 2008. Nanoparticles in photodynamic therapy: An emerging paradigm. *Advanced Drug Delivery Reviews* 60(15): 1627-1637.
- Chaudhuri, R. G. and S. Paria. 2012. Core/shell nanoparticles: Classes, properties, synthesis mechanisms, characterization, and applications. *Chemical Reviews* 112(4): 2373-2433.
- Chen, D. and A. K. Ray. 1998. Photodegradation kinetics of 4-nitrophenol in TiO₂ suspension. *Water Research* 32(11): 3223-3234.

- Chen, H. J., L. Shao, T. Ming, Z. Sun, C. Zhao, B. Yang and J. Wang. 2010a. Understanding the photothermal conversion efficiency of gold nanocrystals. *Small* 6(20): 2272-2280.
- Chen, Q., X. Wang, F. Chen, Q. Zhang, B. Dong, H. Yang, C. Liu and Y. Zhu. 2011. Functionalization of upconverted luminescent NaYF₄ : Yb/Er nanocrystals by folic acid–chitosan conjugates for targeted lung cancer cell imaging. *Journal of Materials Chemistry* 21: 7661-7667.
- Chen, X., Y. He, Q. Zhang, L. Li, D. Hu and T. Yin. 2010b. Fabrication of sandwich-structured ZnO/reduced graphite oxide composite and its photocatalytic properties. *Journal of Materials Science* 45(4): 953-960.
- Chen, X. and S. S. Mao. 2007. Titanium dioxide nanomaterials: Synthesis, properties, modification, and applications. *Chemical Reviews* 107(7): 2891-2959.
- Cheng, F., C. Su, Y. yang, C. Yeh, C. Tsai, C. Wu, M. Wu and D. Shieh. 2005a. Characterization of aqueous dispersions of Fe₃O₄ nanoparticles and their biomedical applications. *Biomaterials* 26(7): 729-738.
- Cheng, H., H. Hsu, S. Chen, W. Wu, C. Kao, L. Lin and W. Hsieh. 2005b. Efficient UV photoluminescence from monodispersed secondary ZnO colloidal spheres synthesized by sol–gel method. *Journal of Crystal Growth* 277(1–4): 192-199.
- Chiou, C. H., C. Y. Wu and R. S. Juang. 2008. Influence of operating parameters on photocatalytic degradation of phenol in UV/TiO₂ process. *Chemical Engineering Journal* 139(2): 322-329.
- Chithrani, B. D., A. A. Ghazani and W. C. W. Chan. 2006. Determining the size and shape dependence of gold nanoparticles uptake into mammalian cells. *Nano Letters* 6(4): 662-668.
- Choi, H., W. Liu, P. Misra, E. Tanaka, J. P. Zimmer, B. Itty Ipe, M. G. Bawendi and J. V. Frangioni. 2007. Renal clearance of quantum dots. *Nature Biotechnology* 25(10): 1165-1170.
- Choi, W., A. Termin and M. R. Hoffmann. 1994. The role of metal ion dopants in quantum-sized TiO₂: Correlation between photoreactivity and charge carrier recombination dynamics. *The Journal of Physical Chemistry* 98(51): 13669-13679.
- Chu, M., Y. Shao, J. Peng, X. Dai, H. Li, Q. Wu and D. Shi. 2013. Near-infrared laser light mediated cancer therapy by photothermal effect of Fe₃O₄ magnetic nanoparticles. *Biomaterials* 34(16): 4078-4088.

- Chu, Z., Y. Huang, L. Li, Q. Tao and Q. Li. 2012. Physiological pathway of human cell damage induced by genotoxic crystalline silica nanoparticles. *Biomaterials* 33(30): 7540-7546.
- Chung, J., J. Chun, J. Lee, S. H. Lee, Y. J. Lee and S. W. Hong. 2012. Sorption of Pb(II) and Cu(II) onto multi-amine grafted mesoporous silica embedded with nano-magnetite: Effects of steric factors. *Journal of Hazardous Materials* 239–240: 183-191.
- Coley, W. B. 1991. The treatment of malignant tumor by repeated inoculations of erysipelas: With a report of ten original cases *Clinical Orthopaedics and Related Research* 262: 3-11.
- Colon, G., M. C. Hidalgo and J. A. Navio. 2001. Influence of carboxylic acid on the photocatalytic reduction of Cr(VI) using commercial TiO₂. *Langmuir* 17: 7174-7177.
- Cornelis, K. and C. S. Hurlburt. 1977. *Manual of Mineralogy*. New York, Wiley.
- Corrie, P. G. 2011. Cytotoxic chemotherapy: Clinical aspects. *Medicine* 39(12): 717-722.
- Crișan, M., A. Brăileanu, M. Răileanu, M. Zaharescu, D. Crișan, N. Drăgan, M. Anastasescu, A. Ianculescu, I. Nițoi, V. E. Marinescu and S. M. Hodoroagea. 2008. Sol-gel S-doped TiO₂ materials for environmental protection. *Journal of Non-Crystalline Solids* 354(2–9): 705-711.
- D'Angelo, I., C. Conte, A. Miro, F. Quaglia and F. Ungaro. 2014. Core-shell nanocarriers for cancer therapy. Part I: biologically oriented design rules. *Expert Opinion on Drug Delivery* 11(2): 283-297.
- Daniels, T., T. Delgado and G. Helguera. 2006 The transferrin receptor part II: Targeted delivery of therapeutic agents into cancer cells. *Clinical Immunology* 121(2): 159-176.
- Davids, L. M. and B. Kleemann. 2011. Combating melanoma: The use of photodynamic therapy as a novel, adjuvant therapeutic tool. *Cancer Treatment Reviews* 37(6): 465-475.
- Detty, M. R., S. L. Gibson and S. J. Wagner. 2004. Current clinical and preclinical photosensitizers for use in photodynamic therapy. *Journal of Medical Chemistry* 47(16): 3897-3915.

- Diamond, I., A. F. McDonagh, C. B. Wilson, S. G. Granelli, S. Nielsen and R. Jaenicke. 1972. Photodynamic therapy of malignant tumours. *The Lancet* 300(7788): 1175–1177.
- Dobson, J. 2006. Magnetic nanoparticles for drug delivery. *Drug Development Research* 67(1): 55-60.
- Dolans, D. E. J. G. J., D. Fukumura and R. K. Jain. 2003. Photodynamic therapy for cancer *Nature Reviews Cancer* 3: 380-389.
- Dolmans, D. E. J. G. J., D. Fukumura and R. K. Jain. 2003. Photodynamic therapy for cancer *Nature Reviews Cancer* 3: 380-387.
- Dordi, B., H. Schonherr and G. J. Vancso. 2003. Reactivity in the confinement of self-assembled monolayers: Chain length effects on the hydrolysis of N-Hydroxysuccinimide ester disulfides on gold. *Langmuir* 19: 5780-5786.
- Dougherty, T. J., C. J. Gomer, B. W. Henderson, G. Jori, D. Kessel, M. Korbelik, J. Moan and Q. Peng. 1998. Photodynamic Therapy. *Journal of the National Cancer Institute* 90(12): 889-905.
- Dougherty, T. J., G. B. Grindey, R. Fiel, K. R. Weishaupt and D. G. Boyle. 1975. Photoradiation therapy. II. Cure of animal tumors with hematoporphyrin and light. *Journal of the National Cancer Institute* 55(1): 115-121.
- Dowlati, A., M. Loo, T. Bury, G. Fillet and Y. Beguin. 1997. Soluble and cell-associated transferrin receptor in lung cancer. *British Journal of Cancer* 75(12): 1802-1806.
- Dutta, R. K., P. K. Sharma, R. Bhargava, N. Kumar and A. C. Pandey. 2010. Differential susceptibility of escherichia coli cells toward transition metal-doped and matrix-embedded ZnO nanoparticles. *The Journal of Physical Chemistry B* 114(16): 5594-5599.
- El-Toni, A. M., S. Yin, T. Sato, T. Ghannam, M. Al-Hoshan and M. Al-Salhi. 2010. Investigation of photocatalytic activity and UV-shielding properties for silica coated titania nanoparticles by solvothermal coating. *Journal of Alloys and Compounds* 508(1): L1-L4.
- El-Wahed, M. G. A., M. S. Refat and S. M. El-Megharbel. 2008. Synthesis, spectroscopic and thermal characterization of some transition metal complex of folic acid. *Spectrochimica Acta Part A* 70: 916-922.

- Elnakat, H. and M. Ratnam. 2004. Distribution, functionality and gene regulation of folate receptor isoforms: Implications in targeted therapy. *Advanced Drug Delivery Reviews* 56(8): 1067-1084.
- Epstein, J. H. 1990. Phototherapy and photochemotherapy. *The New England Journal of Medicine* 322(16): 1149-1151.
- Erogbogbo, F., C.-A. Tien, C.-W. Chang, K.-T. Yong, W.-C. Law, H. Ding, I. Roy, M. T. Swihart and P. N. Prasad. 2011. Bioconjugation of luminescent silicon quantum dots for selective uptake by cancer cells. *Bioconjugate Chemistry* 22(6): 1081-1088.
- Erogbogbo, F., K. T. Yong, I. Roy, G. Xu, P. N. Prasad and M. T. Swihart. 2008. Biocompatible luminescent silicon quantum dots for imaging of cancer cells. *ACS Nano* 2(5): 873-878.
- Etacheri, V., M. K. Seery, S. J. Hinder and S. C. Pillai. 2010. Highly visible light active $\text{TiO}_2\text{-xN}_x$ heterojunction photocatalysts. *Chemistry of Materials* 22(13): 3843-3853.
- Fang, J., H. Nakamura and H. Maeda. 2011. The EPR effect: Unique features of tumor blood vessels for drug delivery, factors involved, and limitations and augmentation of the effect. *Advanced Drug Delivery Reviews* 63(3): 136-151.
- Fang, J., T. Sawa and H. Maeda. 2003. Factors and mechanism of "EPR" effect and the enhanced antitumor effects of macromolecular drugs including SMANCS. *Advances in Experimental Medicine and Biology* 519: 29-49.
- Feng, J., J. Mao, X. Wen and M. Tu. 2011. Ultrasonic-assisted in situ synthesis and characterization of superparamagnetic Fe_3O_4 nanoparticles. *Journal of Alloys and Compounds* 509(37): 9093-9097.
- Feng, X., H. Guo, K. Patel, H. Zhou and X. Lou. 2014. High performance recoverable $\text{Fe}_3\text{O}_4\text{-ZnO}$ nanoparticles for enhanced photocatalytic degradation of phenol. *Chemical Engineering Journal* 244: 327-334.
- Feng, X., S. Zhang and X. Lou. 2013. Controlling silica coating thickness on TiO_2 nanoparticles for effective photodynamic therapy. *Colloids and Surface B: Biointerfaces* 107: 220-226.
- Fernández-Ibáñez, P., J. Blanco, S. Malato and F. J. Nieves. 2003. Application of the colloidal stability of TiO_2 particles for recovery and reuse in solar photocatalysis. *Water Research* 37(13): 3180-3188.
- Finsen, N. 1901. *Phototherapy*, Edward Arnold.

- Flensch, C., M. Joubert, E. Bourgeat-Lami, S. Mornet, E. Duguet, C. Delaite and P. Dumas. 2005. Organoliane-modified maghmite nanoparticles and their use as co-initiator in the ring-opening polymerization of ϵ -caprolactone. *Colloids and Surfaces A: Physicochemical and Engineering Aspects* 262(1-3): 150-157.
- Fu, H., T. Xu, S. Zhu and Y. Zhu. 2008. Photocorrosion inhibition and enhancement of photocatalytic activity for ZnO via hybridization with C₆₀. *Environmental Science & Technology* 42(21): 8064-8069.
- Fujishima, A. and K. Honda. 1972. Electrochemical photolysis of water at a semiconductor electrode. *Nature* 238(37-38): 37.
- Fujishima, A., T. N. Rao and D. A. Tryk. 2000. Titanium dioxide photocatalysis. *Journal of Photochemistry and Photobiology C: Photochemistry Reviews* 1(1): 1-21.
- Fujishima, A., J. Ohtsuki, T. Yamashita and H. S. 1986. Behavior of tumor cells on photoexcited semiconductor surface. *Photomedicine and Photobiology* 8: 45-46.
- Georgieva, J., E. Valova, S. Armyanov, N. Philippidis, I. Poullos and S. Sotiropoulos. 2012. Bi-component semiconductor oxide photoanodes for the photoelectrocatalytic oxidation of organic solutes and vapours: A short review with emphasis to TiO₂-WO₃ photoanodes. *Journal of Hazardous Materials* 211-212: 30-46.
- Gottesman, M. M., T. Fojo and S. E. Bates. 2012. Multidrug resistance in cancer: Role of ATP-dependent transporters. *Nature Reviews Cancer* 2(1): 48-58.
- Grabowska, E., J. Reszczyńska and A. Zaleska. 2012. Mechanism of phenol photodegradation in the presence of pure and modified-TiO₂: A review. *Water Research* 46(17): 5453-5471.
- Grief, A. D. and G. Richardson. 2005. Mathematical modelling of magnetically targeted drug delivery. *Journal of Magnetism and Magnetic Materials* 293(1): 455-463.
- Guanawa, C., W. Y. Teoh, C. P. Marquis, J. Lifla and R. Amal. 2009. Reversible antimicrobial photoswitching in nanosilver. *Small* 5(3): 341-344.
- Guo, D., C. Wu, H. Jiang, Q. Li, X. Wang and B. Chen. 2008. Synergistic cytotoxic effect of different sized ZnO nanoparticles and daunorubicin against leukemia cancer cells under UV irradiation. *Journal of Photochemistry and Photobiology B: Biology* 93(3): 119-126.

- Guo, J., B. Ma, A. Yin, K. Fan and W. Dai. 2011. Photodegradation of rhodamine B and 4-chlorophenol using plasmonic photocatalyst of Ag–AgI/Fe₃O₄@SiO₂ magnetic nanoparticle under visible light irradiation. *Applied Catalysis B: Environmental* 101(3–4): 580-586.
- Guo, W., G. H. Hinkle and R. J. Lee. 1999. ^{99m}Tc-HYNIC-Folate: A novel receptor-based targeted radiopharmaceutical for tumor imaging. *The Journal of Nuclear Medicine* 40(9): 1563-1569.
- Guo, Z., R. Ma and G. Li. 2006. Degradation of phenol by nanomaterial TiO₂ in wastewater. *Chemical Engineering Journal* 119(1): 55-69.
- Gupta, A. K. and M. Gupta. 2005. Synthesis and surface engineering of iron oxide nanoparticles for biomedical applications. *Biomaterials* 26(18): 3995-4021.
- Hajjaji, N. and P. Bognoux. 2013. Selective sensitization of tumors to chemotherapy by marine-derived lipids: A review. *Cancer Treatment Reviews* 39(5): 473-488.
- Hakami, O., Y. Zhang and C. J. Banks. 2012. Thiol-functionalised mesoporous silica-coated magnetite nanoparticles for high efficiency removal and recovery of Hg from water. *Water Research* 46(12): 3913-3922.
- Halliwell, B. and O. I. Aruoma. 1991. DNA damage by oxygen-derived species its mechanism and measurement in mammalian systems. *FEBS Letters* 281(1–2): 9-19.
- Hamada, H. and T. Tsuruo. 1988. Characterization of the ATPase activity of the Mr 170,000–180,000 membrane glycoprotein (P-glycoprotein) associated with multidrug resistance in K562/ADM cells. *Cancer Research* 48(17): 4962-4932.
- Hamley, I. W. 2003. Nanotechnology with soft materials. *Angewandte Chemie International Edition* 42(15): 1692-1712.
- Han, R., M. Yu, Q. Zheng, L. Wang, Y. Hong and Y. Sha. 2009. A facile synthesis of small-sized, highly photoluminescent, and monodisperse CdSeS QD/SiO₂ for live cell imaging. *Langmuir* 25(20): 12250-12255.
- Harada, Y., K. Ogawa, Y. Irie, H. Endo, L. B. Feril Jr, T. Uemura and K. Tachibana. 2011. Ultrasound activation of TiO₂ in melanoma tumors. *Journal of Controlled Release* 149(2): 190-195.
- Hatz, S., J. D. C. Lambert and P. R. Oqilby. 2007. Measuring the lifetime of singlet oxygen in a single cell: Addressing the issue of cell viability. *Photochemical & Photobiological Sciences* 6(10): 1106-1116.

- Hayat, K., M. A. Gondal, M. M. Khaled and S. Ahmed. 2011. Effect of operational key parameters on photocatalytic degradation of phenol using nano nickel oxide synthesized by sol-gel method. *Journal of Molecular Catalysis A: Chemical* 336(1-2): 64-71.
- He, C., Y. Hu, L. Yin, C. Tang and C. Yin. 2010. Effect of particle size and surface charge on cellular uptake and biodistribution of polymeric nanoparticles. *Biomaterials* 31: 3657-3666.
- He, X., X. Wu, X. Cai, S. Lin, M. Xie, X. Zhu and D. Yan. 2012. Functionalization of magnetic nanoparticles with dendritic-linear-brush-like triblock copolymers and their drug release properties. *Langmuir* 28(32): 11929-11938.
- He, Y., X. C. Wang, P. K. Jinn, B. Zhao and X. Fan. 2009. Complexation of anthracene with folic acid studied by FTIR and UV spectroscopies. *Spectrochimica Acta Part A: Molecular and Biomolecular Spectroscopy* 72(4): 876-879.
- Henderson, B. W. and T. J. Dougherty. 1992. How does photodynamic therapy work? *Photochemistry and Photobiology* 55(1): 145-157.
- Hoffman, A. J., E. R. Carraway and M. R. Hoffmann. 1994. Photocatalytic production of H₂O₂ and organic peroxides on quantum-sized semiconductor colloids. *Environmental Science & Technology* 28(5): 776-785.
- Hoffmann, M. R., S. T. Martin, W. Choi and D. W. Bahnemann. 1995. Environmental applications of semiconductor photocatalysis. *Chemical Reviews* 95(1): 69-96.
- Hogle, W. P. 2006. The State of the Art in Radiation Therapy. *Seminars in Oncology Nursing* 22(4): 212-220.
- Hong, R., T. Pan, J. Qian and H. Li. 2006. Synthesis and surface modification of ZnO nanoparticles. *Chemical Engineering Journal* 119(2-3): 71-81.
- Hong, R. Y., S. Z. Zhang, G. Q. Di, H. Z. Li, Y. Zheng, J. Ding and D. G. Wei. 2008. Preparation, characterization and application of Fe₃O₄/ZnO core/shell magnetic nanoparticles. *Materials Research Bulletin* 43(8-9): 2457-2468.
- Hu, Y., H. L. Tsai and C. L. Huang. 2003. Effect of brookite phase on the anatase-rutile transition in titania nanoparticles. *Journal of the European Ceramic Society* 23(5): 691-696.
- Hu, Z., J. Li, C. Li, S. Zhao, N. Li, Y. Wang, F. Wei, L. Chen and Y. Huang. 2013. Folic acid-conjugated graphene-ZnO nanohybrid for targeting photodynamic

- therapy under visible light irradiation. *Journal of Materials Chemistry B* 1(38): 5003-5013.
- Huang, C., K. G. Neoh, E.-T. Kang and B. Shuter. 2011a. Surface modified superparamagnetic iron oxide nanoparticles (SPIONs) for high efficiency folate-receptor targeting with low uptake by macrophages. *Journal of Materials Chemistry* 21(40): 16094-16102.
- Huang, N., H. Wang, J. Zhao, H. Lui, M. Korbelik and H. Zeng. 2010. Single-wall carbon nanotubes assisted photothermal cancer therapy: Animal study with a murine model of squamous cell carcinoma. *Lasers in Surgery and Medicine* 42(9): 798-808.
- Huang, P., L. Bao, C. Zhang, J. Lin, T. Luo, D. Yang, M. He, Z. Li, G. Gao, B. Gao, S. Fu and D. Cui. 2011b. Folic acid-conjugated silica-modified gold nanorods for X-ray/CT imaging-guided dual-mode radiation and photo-thermal therapy. *Biomaterials* 2011: 9796-9809.
- Huang, X., P. K. Jain, I. H. El-Sayed and M. A. El-Sayed. 2008. Plasmonic photothermal therapy (PPTT) using gold nanoparticles. *Lasers in Medical Science* 23(3): 217-228.
- Huang, X., L. Li, T. Liu, N. Hao, H. Liu, D. Chen and F. Tang. 2011c. The shape effect of mesoporous silica nanoparticles on biodistribution, clearance, and biocompatible *in vivo*. *ACS nano* 5(7): 5390-5399.
- Hughes, G. A. 2005. Nanostructure-mediated drug delivery. *Nanomedicine: Nanotechnology, Biology and Medicine* 1(1): 22-30.
- Irie, H., Y. Watanabe and K. Hashimoto. 2003. Nitrogen-concentration dependence on photocatalytic activity of $\text{TiO}_{2-x}\text{N}_x$ powders. *The Journal of Physical Chemistry B* 107(23): 5483-5486.
- Ishida, H., C. H. Chiang and J. L. Koenig. 1982. The structure of aminofunctional silane coupling agents: 1. γ -Aminopropyltriethoxysilane and its analogues. *Polymer* 23(2): 251-257.
- Ito, A., Y. Kuga, H. Honda, H. Kikkawa, A. Horiuchi, Y. Watanabe and T. Kobayashi. 2004. Magnetite nanoparticle-loaded anti-HER2 immunoliposomes for combination of antibody therapy with hyperthermia. *Cancer Letters* 212(2): 167-175.
- Jain, R. K. 1998. Delivery of molecular and cellular medicine to solid tumors. *Advanced Drug Delivery Reviews* 46(1-3): 149-168.

- Jana, N. R., H.-h. Yu, E. M. Ali, Y. Zheng and J. Y. Ying. 2007. Controlled photostability of luminescent nanocrystalline ZnO solution for selective detection of aldehydes. *Chemical Communications* 2007(14): 1406-1408.
- Jiang, T., T. Xie, Y. Zhang, L. Chen, L. Peng, H. Li and D. Wang. 2010. Photoinduced charge transfer in ZnO/Cu₂O heterostructure films studied by surface photovoltage technique. *Physical Chemistry Chemical Physics* 12(47): 15476-15481.
- Jing, J., J. Li, J. Feng, W. Li and W. W. Yu. 2013. Photodegradation of quinoline in water over magnetically separable Fe₃O₄/TiO₂ composite photocatalysts. *Chemical Engineering Journal* 219: 355-360.
- José Velasco, M., F. Rubio, J. Rubio and J. L. Oteo. 1999. DSC and FT-IR analysis of the drying process of titanium alkoxide derived precipitates. *Thermochimica Acta* 326(1-2): 91-97.
- Juarranz, Á., P. Jaén, F. Sanz-Rodríguez, J. Cuevas and S. González. 2008. Photodynamic therapy of cancer. Basic principles and application. *Clinical and Translation Oncology* 10(3): 148-154.
- Jung, H.-S., D.-S. Moon and J.-K. Lee. 2012. Quantitative analysis and efficient surface modification of silica nanoparticles *Journal of Nanomaterials* 2012: 1-8.
- Juzenas, P., W. Chen, Y.-P. Sun, M. A. N. Coelho, R. Generalov, N. Generalova and I. L. Christensen. 2008. Quantum dots nanoparticles for photodynamic and radiation therapies of cancer. *Advanced Drug Delivery Reviews* 60(15): 1600-1614.
- Juzeniene, A. and J. Moan. 2007. The history of PDT in Norway: Part one: identification of basic mechanisms of general PDT. *Photodiagnosis and Photodynamic Therapy* 4(1): 3-11.
- Juzeniene, A., Q. Peng and J. Moan. 2007. Milestones in the development of photodynamic therapy and fluorescence diagnosis. *Photochemical & Photobiological Sciences* 6(12): 1234-1245.
- Kalele, S., S. W. Gosavi, J. Urban and S. K. Kulkarni. 2006. Nanoshell particles: Synthesis, properties and applications. *Current Science* 91(8): 1038-1053.
- Kalska-Szostko, B., U. Wylowska, D. Satula and E. Zambizycka. 2014. Stability of core-shell magnetite nanoparticles. *Colloid and Surfaces B: Biointerfaces* 113: 295-301.

- Kelly, J. F. and M. E. Snell. 1976. Hematoporphyrin derivative: A possible aid in the diagnosis and treatment of carcinoma of the bladder. *The Journal of Urology* 115(2): 150-151.
- Kelly, J. F., M. E. Snell and C. B. M. 1975. Photodynamic destruction of human bladder carcinoma. *British Journal of Cancer* 31: 237-244.
- Kenneth, D., S. Charles, L. Kevin, L. Guoda, G. Donald and J. Matthew. 2005. Epithelial internalization of superparamagnetic nanoparticles and response to external magnetic field. *Biomaterials* 26(14): 2061-2072.
- Kessel, D., P. Thompson, B. Musselman and C. K. Chang. 1987a. Chemistry of hematoporphyrin-derived photosensitizers. *Photochemistry and Photobiology* 46(5): 563-568.
- Kessel, D., P. Thompson, B. Musselman and C. K. Chang. 1987b. Probing the structure and stability of the tumor-localizing derivative of hematoporphyrin by reductive cleavage with LiAlH_4 . *Cancer Research* 47(17): 4642-4645.
- Kievit, F. M. and M. Zhang. 2011. Surface engineering of iron oxide nanoparticles for targeted cancer therapy. *Accounts of Chemical Research* 44(10): 853-862.
- Kirpotin, D. B., D. C. Drummond, Y. Shao, M. R. Shalaby, K. Hong, U. B. Nielsen, J. D. Marks, C. C. Benz and J. W. Park. 2006. Antibody targeting of long-circulating lipidic nanoparticles does not increase tumor localization but does increase internalization in animal models. *Cancer Research* 66(13): 6732-6740.
- Kohane, D. S. and R. Langer. 2010. Biocompatibility and drug delivery systems. *Chemical Society Review* 1: 441-446.
- Konan, Y. N., R. Gurny and E. Allemann. 2002. State of the art in the delivery of photosensitizers for photodynamic therapy. *Journal of Photochemistry and Photobiology B: Biology* 66(2): 89-106.
- Kortesuo, P., M. Ahola, S. Karlsson, I. Kangasniemi, A. Yli-Urpo and J. Kiesvaara. 2000. Silica xerogel as an implantable carrier for controlled drug delivery--evaluation of drug distribution and tissue effects after implantation. *Biomaterials* 21(2): 193-198.
- Kreimeier-Birnbaum, M. 1989. Modified porphyrins, chlorins, phthalocyanines and purpurin: Second generation photosensitizers for photodynamic therapy. *Seminars in Hematology* 26: 157-173.
- Kristjansson, S. R., A. Nesbakken, M. S. Jordhoy, E. Skovlund, R. A. Audisio, H. O. Johannessen, A. Bakka and T. B. Wyller. 2010. *Comprehensive geriatric*

- assessment can predict complications in elderly patients after elective surgery for colorectal cancer: A prospective observational cohort study. *Critical Reviews in Oncology/Hematology* 76(3): 208-217.
- Kubacka, A., M. Fernández-García and G. Colón. 2011. Advanced nanoarchitectures for solar photocatalytic applications. *Chemical Reviews* 112(3): 1555-1614.
- Kukowska-Latallo, J. F., K. A. Candido, Z. Cao, S. S. Nigavekar, I. J. Majoros, T. P. Thomas, L. P. Balogh, M. K. Khan and J. R. Baker. 2005. Nanoparticle targeting of anticancer drug improves therapeutic response in animal model of human epithelial cancer. *Cancer Research* 65(12): 5317-5324.
- Lai, T.-Y. and W.-C. Lee. 2009. Killing of cancer cell line by photoexcitation of folic acid modified titanium dioxide nanoparticles. *Journal of Photochemistry and photobiology A: Chemistry* 204: 148-153.
- Laurent, S., D. Forge, M. Port, A. Roch, C. Robic, L. V. Elst and R. N. Muller. 2008. Magnetic iron oxide nanoparticles: Synthesis, stabilization, vectorization, physicochemical characterization, and biological application. *Chemical Reviews* 108(6): 2064-2110.
- Lee, J., Y. Lee, J. K. Youn, H. B. Na, T. Yu, H. Kim, S. M. Lee, Y. M. Koo, J. H. Kwak, P. H.G, H. N. Chang, M. Hwang, J. G. Park, J. Kim and T. Hyeon. 2008. Simple synthesis of functionalized superparamagnetic magnetite/silica core/shell nanoparticles and their application as magnetically separable high-performance biocatalysts. *Small* 4(1): 143-152.
- Lee, J., S. Mahendra and P. J. J. Alvarez. 2010. Nanomaterials in the construction industry: A review of their applications and environmental health and safety considerations. *ACS Nano* 4(7): 3580-3590.
- Lee, J. S., M. Ankone, E. Pieters, R. M. Schiffelers, W. E. Hennink and J. Feijen. 2011. Circulation kinetics and biodistribution of dual-labeled polymersomes with modulated surface charge in tumor-bearing mice: Comparison with stealth liposomes. *Journal of Controlled Release* 155: 282-288.
- Lee, R. J. and P. S. Low. 1994. Delivery of liposomes into cultured KB cells via folate receptor-mediated endocytosis. *Journal of Biological Chemistry* 269(5): 3198-3204.
- Lefemine, V. and H. Sweetland. 2012. The role of surgeons in cancer management *Surgery (Oxford)* 30(4): 181-185.

- Lesnikovich, A. I., T. M. Shunkevich, V. N. Naumenko, S. A. Vorobyova and M. V. Baykov. 1990. Dispersity of magnetite in magnetic liquids and the interaction with a surfactant. *Journal of Magnetism and Magnetic Materials* 85(1–3): 14-16.
- Li, J., D. Guo, X. Wang, H. Wang, H. Jiang and B. Chen. 2010. The photodynamic effect of different size ZnO nanoparticles on cancer cell proliferation in vitro. *Nanoscale Research Letters* 5(6): 1063-1071.
- Li, Q., X. Wang, X. Lu, H. Tian, H. Jiang, G. Lv, D. Guo, C. Wu and B. Chen. 2009a. The incorporation of daunorubicin in cancer cells through the use of titanium dioxide whiskers. *Biomaterials* 30(27): 4708-4715.
- Li, S. D. and L. Huang. 2008. Pharmacokinetics and biodistribution of nanoparticles. *Molecular Pharmacology* 5(4): 496-504.
- Li, T. S. C., T. Yawata and K. Honke. 2014. Efficient SiRNA delivery and tumor accumulation mediated by ionically cross-linked folic acid-poly(ethylene glycol)-chitan oligosaccharie Lactate nanoparticles: For the potential targeted ovarian gene therapy. *European Journal of Pharmaceutical Science* 52: 48-61.
- Li, X., Y. Hou, Q. Zhao and G. Chen. 2011a. Synthesis and photoinduced charge-transfer properties of a ZnFe₂O₄-Sensitized TiO₂ nanotube array electrode. *Langmuir* 27(6): 3113-3120.
- Li, Y., W. Xie, X. Hu, G. Shen, X. Zhou, Y. Xiang, X. Zhao and P. Fang. 2009b. Comparison of dye photodegradation and its coupling with light-to-electricity conversion over TiO₂ and ZnO. *Langmuir* 26(1): 591-597.
- Li, Z., L. Mi, P. Wang and J. Chen. 2011b. Study on the visible-light-induced photokilling effect of nitrogen-doped TiO₂ nanoparticles on cancer cells. *Nanoscale Research Letters* 6(1): 356-363.
- Lin, M. M., D. K. Kim, A. J. ElHaj and J. Dobson. 2008. Development of superparamagnetic iron oxide nanoparticles (SPIONS) for translation to clinical applications. *IEEE Transactions on Nanobioscience* 7(298-305): 298.
- Linsebigler, A. L., G. Lu and J. T. Yates. 1995. Photocatalysis on TiO₂ surfaces: Principles, mechanisms, and selected results. *Chemical Reviews* 95(3): 735-758.
- Liu, J., S. Qiao, Q. Hu and G. Lu. 2011. Magnetic nanocomposites with mesoporous structure: Synthesis and applications. *Small* 7(4): 425-443.
- Liu, L., X. Gu, C. Sun, H. Li, Y. Deng, F. Gao and L. Dong. 2012. In situ loading of ultra-small Cu₂O particles on TiO₂ nanosheets to enhance the visible-light photoactivity. *Nanoscale* 4(20): 6351-6359.

- Liu, X., Z. Ma, J. Xing and H. Liu. 2004. Preparation and characterization of amino-silane modified superparamagnetic silica nanospheres. *Journal of Magnetism and Magnetic Materials* 270(1-2): 1-6.
- Liz-Marzán, L. M., M. Giersig and P. Mulvaney. 1996. Synthesis of nanosized gold-silica core-shell particles. *Langmuir* 12(18): 4329-4335.
- Lopez, R. F. V., N. Lange, R. Guy and M. V. L. B. Bentley. 2004. Photodynamic therapy of skin cancer: Controlled drug delivery of 5-ALA and its esters. *Advanced Drug Delivery Reviews* 56(1): 77-94.
- Lopez, T., E. Ortiz, M. Alvarez, J. Navarrete, J. A. Odriozola, F. Martinez-Ortega, E. A. Páez-Mozo, P. Escobar, K. A. Espinoza and I. A. Rivero. 2010. Study of the stabilization of zinc phthalocyanine in sol-gel TiO₂ for photodynamic therapy applications. *Nanomedicine: Nanotechnology, Biology, and Medicine* 6(6): 777-785.
- Low, P. S. and A. C. Antony. 2004. Folate receptor-targeted drugs for cancer and inflammatory diseases. *Advanced Drug Delivery Reviews* 56(8): 1055-1058.
- Lu, A.-H., E. L. Salabas and F. Schuth. 2007. Magnetic nanoparticles: Synthesis, protection, functionalization and application. *Angewandte Chemie International Edition* 46(8): 1222-1244.
- Lu, T., J. Sun, X. Chen, P. Zhang and X. Jing. 2009. Folate-conjugated micelles and their folate-receptor-mediated endocytosis. *Bioscience* 9: 1059-1068.
- Lukyanets, E. A. 1999. Phthalocyanine as photosensitizers in the photodynamic therapy of cancer. *Journal of Porphyrins and Phthalocyanines* 3(6-7): 424-432.
- Ma, J. and L. Jiang. 2001. Photogeneration of singlet oxygen (¹O₂) and free radicals (Sen⁻, O₂⁻) by tetra-brominated hypocrellin B derivative. *Free Radical Research* 35(6): 767-777.
- Maeda, H. 2001. SMANCS and polymer-conjugated macromolecular drugs: Advantages in cancer chemotherapy. *Advanced Drug Delivery Reviews* 46(1-3): 169-185.
- Maeda, H. 2010. Tumor-selective delivery of macromolecular drug via the EPR effect: Background and future prospects. *Bioconjugate Chemistry* 21(5): 797-802.
- Maeda, H., H. Nakamura and J. Fang. 2013. The EPR effect for macromolecular drug delivery to solid tumors: Improvement of tumor uptake, lowering of

- systemic toxicity, and distinct tumor imaging in vivo. *Advanced Drug Delivery Reviews* 65(1): 71-79.
- Mahmoudi, M., S. Sant, B. Wang, S. Laurent and T. Sen. 2011. Superparamagnetic iron oxide nanoparticles (SPIONs): Development, surface modification and applications in chemotherapy. *Advanced Drug Delivery Reviews* 63(1-2): 24-46.
- Maity, A. R., A. Saha, A. Roy and J. Nikhil R. 2013. Folic acid functionalized nanoprobes for fluorescence-, dark-field-, and dual-imaging-based selective detection of cancer cells and tissue. *ChemPlusChem* 78(3): 259-267.
- Maki, S., T. Konno and H. Maeda. 1985. Image enhancement in computerized tomography for sensitive diagnosis of liver cancer and semiquantitation of tumor selective drug targeting with oily contrast medium. *Cancer* 56(4): 751-757.
- Maness, P. C., S. Smolinski, D. M. Blake, Z. Huang, E. J. Wolfrum and W. A. Jacoby. 1999. Bactericidal activity of photocatalytic TiO₂ reaction: Toward an understanding of its killing mechanism. *Applied and Environmental Microbiology* 65(9): 4094-4098.
- Manthe, R. L., S. P. Foy, N. Krishnamurthy, B. Sharma and V. Labhasetwar. 2010. Tumor ablation and nanotechnology. *Molecular Pharmaceutics* 7(6): 1880-1898.
- Martinez, S. R. and S. E. Young. 2008. A rational surgical approach to the treatment of distant melanoma metastases. *Cancer Treatment Reviews* 34(7): 614-620.
- Massart, R. 1981. Preparation of aqueous magnetic liquids in alkaline and acidic media. *Magnetics, IEEE Transactions on* 17(2): 1247-1248.
- Master, A., M. Livingston and A. S. Gupta. 2013. Photodynamic nanomedicine in the treatment of solid tumor: Perspectives and challenges. *Journal of Controlled Release* 168(1): 88-102.
- Masters, B. R., P. T. So and E. Gratton. 1997. Multiphoton excitation fluorescence microscopy and spectroscopy of in vivo human skin. *Biophysical Journal* 72(6): 2405-2412.
- Matsunaga, T., R. Tomoda, T. Nakajima and H. Wake. 1985. Photoelectrochemical sterilization of microbial cells by semiconductor powders. *FEMS Microbiology Letters* 29(1-2): 211-214.
- Mbeh, D. A., R. França, Y. Merhi, X. F. Zhang, T. Veres, E. Sacher and L. Yahia. 2012. In vitro biocompatibility assessment of functionalized magnetite

- nanoparticles: Biological and cytotoxicological effects. *Journal of Biomedical Materials Research Part A* 100(6): 1637-1646.
- Meyer-Betz, F. 1913. Untersuchungen über die biologische (photodynamische) Wirkung des Hamtoporphyrins und anderer Derivate des Blau- und Galenfarbstoffs. *Dtsch Arch Klin Med.* 112: 476-503.
- Miotti, S., P. Facheris, A. Tomassetti, F. Bottero, C. Bottini, F. Ottone, M. I. Colnaghi, M. A. Bunni, D. G. Priest and S. Canevari. 1995. Growth of ovarian carcinoma cell lines at physiological folate concentration: Effect on folate-binding protein expression *in vitro* and *in vivo*. *International Journal of Cancer* 63(3): 395-401.
- Misra, R., S. Acharya and S. K. Sahoo. 2010. Cancer nanotechnology: Application of nanotechnology in cancer therapy. *Drug Discovery Today* 15(19-20): 842-850.
- Moroz, P., S. K. Jones and B. N. Gray. 2002. Magnetically mediated hyperthermia: Current status and future directions. *International Journal of Hyperthermia* 18(4): 267-284.
- Muhammad, F., M. Guo, Y. Guo, W. Qi, F. Qu, F. Sun, H. Zhao and G. Zhu. 2011a. Acid degradable ZnO quantum dots as a platform for targeted delivery of anticancer drug. *Journal of Materials Chemistry* 21(35): 13406-13412.
- Muhammad, F., M. Guo, W. Qi, F. Sun, A. Wang, Y. Guo and G. Zhu. 2011b. pH-triggered controlled drug release from mesoporous silica nanoparticles via intracellular dissolution of ZnO nanolids. *Journal of American Chemical Society* 133(23): 8778-8781.
- Murray, C. B., D. J. Norris and M. G. Bawendi. 1993. Synthesis and characterization of nearly monodisperse CdE (E=ulfur, selenium, tellurium) semiconductor nanocrystallites. *Journal of the American Chemical Society* 115(21): 8706-8715.
- Nel, A., T. Xia, L. Madler and N. Li. 2006. Toxic potential of materials at the nanolevel. *Science* 311(5761): 622-627.
- Nohara, K., H. Hidaka, E. Pelizzetti and N. Serpone. 1997. Processes of formation of NH_4^+ and NO_3^- ions during the photocatalyzed oxidation of N-containing compounds at the titania/water interfaces. *Journal of Photochemistry and Photobiology A: Chemistry* 102: 265-272.
- Nolan, N. T., M. K. Serry and S. C. Pillai. 2009. Spectroscopic investigation of the anatase-to-rutile transformation of sol-gel-synthesized TiO_2 photocatalysts. *The Journal of Physical Chemistry C* 113(36): 16151-16157.

- Nyst, H. J., I. B. Tan, F. A. Stewart and A. J. M. Balm. 2009. Is photodynamic therapy a good alternative to surgery and radiotherapy in the treatment of head and neck cancer? *Photodiagnosis and Photodynamic Therapy* 6(1): 3-11.
- Ogura, K., K. Nakaoka, M. Nakayama, M. Kobayashi and A. Fujii. 1999. Thermogravimetry/mass spectrometry of urease-immobilized sol-gel silica and the application of such a urease-modified electrode to the potentiometric determination of urea. *Analytica Chimica Acta* 384(2): 219-225.
- Okabayashi, H., I. Shimizu, E. Nishio and C. J. O'Connor. 1997. Diffuse reflectance infrared fourier transform spectral study of the interaction of 3-aminopropyltriethoxysilane on silica gel. Behavior of amino groups on the surface. *Colloid and Polymer Science* 275(8): 744-753.
- Orive, G., R. M. Hernández, A. R. Gascón, A. Domínguez-Gil and J. L. Pedraz. 2003. Drug delivery in biotechnology: Present and future. *Current Opinion in Biotechnology* 14(6): 659-664.
- Ostrovsky, S., G. Kazimirsky, A. Gedanken and C. Brodie. 2009. Selective cytotoxic effect of ZnO nanoparticles on glioma cells. *Nano Research* 2(11): 882-890.
- Pan, L., J.-J. Zou, S. Wang, Z.-F. Huang, A. Yu, L. Wang and X. Zhang. 2013. Quantum dot self-decorated TiO₂ nanosheets. *Chemical Communications* 49(59): 6593-6595.
- Pandurangi, R. S., M. S. Seehra, B. L. Razzaboni and P. Bolsaitis. 1990. Surface and bulk infrared modes of crystalline and amorphous silica particles: A study of the relation of surface structure to cytotoxicity of respirable silica. *Environmental Health Perspectives* 86: 327-336.
- Panias, D., M. Taxiarchou, I. Paspaliaris and A. Kontopoulos. 1996. Mechanisms of dissolution of iron oxides in aqueous oxalic acid solutions *Hydrometallurgy* 42(2): 257-265.
- Pankhurst, Q. A., J. Connolly, S. K. Jones and J. Dobson. 2003. Application of magnetic nanoparticles in biomedicine. *Journal of Physics D: Applied Physics* 36(13): R167-R181.
- Pass, H. I. 1993. Photodynamic therapy in oncology: Mechanisms and clinical use. *Journal of the National Cancer Institute* 85(6): 443-456.
- Paszko, E., C. Ehrhardt, M. O. Senge, D. P. Kelleher and J. V. Reynolds. 2011. Nanodrug applications in photodynamic therapy. *Photodiagnosis and Photodynamic Therapy* 8(1): 14-29.

- Pazokifard, S., S. M. Mirabedini, M. Esfandeh, M. Mohseni and Z. Ranjbar. 2012. Silane grafting of TiO₂ nanoparticles: Dispersibility and photoactivity in aqueous solutions. *Surface and Interface Analysis* 44(1): 41-47.
- Peer, D., J. M. Karp, S. Hong, O. C. Farokhzad, R. Margalit and R. Langer. 2007. Nanocarriers as an emerging platform for cancer therapy. *Nature Nanotechnology* 2(12): 751-760.
- Pelaez, M., N. T. Nolan, S. C. Pillai, M. K. Serry, P. Falaras, A. G. Konoto, P. S. M. Dunlop, J. W. J. Hamilton, J. A. Byrne, K. O'Shea, M. H. Entezari and D. D. Dionysiou. 2012. A review on the visible light active titanium dioxide photocatalysts for environmental application. *Applied Catalysis B: Environmental* 125: 331-349.
- Peng, Q., T. Warloe, K. Berg, J. Moan, M. Kongshaug, K. E. Giercksky and J. M. Nesland. 1997. 5-Aminolevulinic acid-based photodynamic therapy. *Clinical research and future challenges. Cancer* 79: 2282-2308.
- Pirkanniemi, K. and M. Sillanpää. 2002. Heterogeneous water phase catalysis as an environmental application: A review. *Chemosphere* 48(10): 1047-1060.
- Pozzo, R. L., M. A. Baltanás and A. E. Cassano. 1997. Supported titanium oxide as photocatalyst in water decontamination: State of the art. *Catalysis Today* 39(3): 219-231.
- Premanathan, M., K. Karthikeyan, K. Jeyasubramanian and G. Manivannan. 2011. Selective toxicity of ZnO nanoparticles toward Gram-positive bacteria and cancer cells by apoptosis through lipid peroxidation. *Nanomedicine: Nanotechnology, Biology and Medicine* 7(2): 184-192.
- Pun, S. H., F. Tack and C. N. Bellocq. 2004. Targeted delivery of RNA-cleaving DNA enzyme (DNAzyme) to tumor tissue by transferrin-modified, cyclodextrin-based particles. *Cancer Biology & Therapy* 3: 641-650.
- Qiao, R. R., C. H. Yang and M. Y. Gao. 2009. Superparamagnetic iron oxide nanoparticles: From preparation to in vivo MRI applications. *Journal of Materials Chemistry* 19: 6274-6293.
- Qin, Z. and J. C. Bischof. 2012. Thermophysical and biological response of gold nanoparticle laser heating *Chemical Society Review* 41: 1191-1217.
- Quintanar-Guerrero, D., A. Ganem-Quintanar, M. G. Nava-Arzaluz and E. Piñón-Segundo. 2009. Silica xerogels as pharmaceutical drug carriers. *Expert Opinion on Drug Delivery* 6(5): 485-498.

- Raab, O. 1900. Ueber die wirkung fluoreszierenden stoffe auf Infusorien. *Zeitschrift fuer Biologie* 39: 524-526.
- Racuciu, M. 2009. Synthesis protocol influence on aqueous magnetic fluid properties. *Current Applied Physics* 9(5): 1062-1066.
- Rajeshwar, K., M. E. Osugi, W. Chanmanee, C. R. Chenthamarakshan, M. V. B. Zaroni, P. Kajitvichyanukul and R. Krishnan-Ayer. 2008. Heterogeneous photocatalytic treatment of organic dyes in air and aqueous media. *Journal of Photochemistry and Photobiology C: Photochemistry Reviews* 9(4): 171-192.
- Ramani, M., S. Ponnusamy, C. Muthamizhchelvan, J. Cullen, S. Krishnamurthy and E. Marsili. 2013. Morphology-directed synthesis of ZnO nanostructures and their antibacterial activity. *Colloids and Surface B: Biointerfaces* 105: 24-30.
- Reiter, Y. 2001. Recombination immunotoxins in targeted cancer cell therapy. *Advances in Cancer Research* 81: 93-124.
- Roberts, D. J. H. and F. Cairnduff. 1995. Photodynamic therapy of primary skin cancer: A review. *British Journal of Plastic Surgery* 48: 360-370.
- Rosenholm, J. B., P. Stenius and I. Danielsson. 1976. A study of the micelle formation of short-chain carboxylates by laser-Raman spectroscopy. *Journal of Colloid and Interface Science* 57(3): 551-563.
- Rosenholm, J. M., A. Meinander, E. Peuhu, R. Niemi, J. E. Eriksson, C. Sahlgren and M. Linden. 2009. Targeting of porous hybrid silica nanoparticles to cancer cells. *ACS Nano* 3(1): 197-206.
- Rothenberger, G., J. Moser, M. Graetzel, N. Serpone and D. K. Sharma. 1985. Charge carrier trapping and recombination dynamics in small semiconductor particles. *Journal of the American Chemical Society* 107(26): 8054-8059.
- Rother, D., T. Sen, D. East and I. J. Bruce. 2011. Silicon, silica and its surface patterning/activation with alkoxy- and amino-silane for nanomedical application. *Nanomedicine* 6(2): 281-300.
- Sabharanjak, S. and S. Mayor. 2004. Folate receptor endocytosis and trafficking. *Advanced Drug Delivery Reviews* 56(8): 1099-1109.
- Sahoo, Y., A. Goodarzi, M. T. Swihart, T. Y. Ohulchanskyy, N. Kaur, E. P. Furlani and P. N. Prasad. 2005a. Aqueous ferrofluid of magnetite nanoparticles: Fluorescence labeling and magnetophoretic control. *The journal of Physical Chemistry B* 109(9): 3879-3885.

- Sahoo, Y., A. Goodarzi, M. T. Swihart, T. Y. Ohulchanskyy, N. Kaur, E. P. Furlani and P. N. Prasad. 2005b. Aqueous ferrofluid of magnetite nanoparticles: Fluorescence labeling and magnetophoretic control. *The Journal of Physical Chemistry B* 109: 3879-3885.
- Sahu, S. K. and S. K. Mallick. 2010. In vitro evaluation of folic acid modified carboxymethyl chitosan nanoparticles loaded with doxorubicin for targeted delivery. *Journal of Materials Science: Materials in Medicine* 21(5): 1587-1597.
- Sanchez-del-Campo, L., M. F. Montenegro, J. Cabezas-Herrera and J. N. Rodriguez-Lopez. 2009. The critical role of alpha-folate receptor in the resistance of melanoma to methotrexate. *Pigment Cell & Melanoma Research* 22(5): 588-600.
- Sato, S., R. Nakamura and S. Abe. 2005. Visible-light sensitization of TiO₂ photocatalysts by wet-method N-doping. *Applied Catalysis A: General* 284(1-2): 131-137.
- Seeling, E. W., B. Tang, A. Yamilov, H. Cao and R. P. H. Chang. 2003. Self-assembled 3D photonic crystals from ZnO colloidal spheres. *Materials Chemistry and Physics* 80(1): 257-263.
- Semelka, R. C. and T. K. Helmberger. 2001. Contrast agents for MR imaging of the liver. *Radiology* 218(1): 27-38.
- Sen, T., S. Magdassi, G. Nizri and I. J. Bruce. 2006. Dispersion of magnetic nanoparticles in suspension. *Micro & Nano Letters* 1(1): 39-42.
- Serpone, N., D. Lawless, R. Khairutdinov and E. Pelizzetti. 1995. Subnanosecond relaxation dynamics in TiO₂ colloidal sols (particle sizes $R_p=1.0-3.4$ nm). Relevance to heterogeneous photocatalysis. *The Journal of Physical Chemistry* 99(45): 16655-16661.
- Shi, J., Y. Hedberg, M. Lundin, I. Odnevall Wallinder, H. L. Karlsson and L. Möller. 2012. Hemolytic properties of synthetic nano- and porous silica particles: The effect of surface properties and the protection by the plasma corona. *Acta Biomaterialia* 8(9): 3478-3490.
- Shibu, E. S., M. Hamada, N. Murase and V. Biju. 2013. Nanomaterials formulations for photothermal and photodynamic therapy of cancer. *Journal of Photochemistry and Photobiology C: Photochemistry Reviews* 15: 53-72.
- Shmeeda, H., L. Mak, D. Tzemach, P. Astrahan, M. Tarshish and A. Gabizon. 2006. Intracellular uptake and intracavitary targeting of folate-conjugated liposomes

- in a mouse lymphoma model with up-regulated folate receptors. *Molecular Cancer Therapeutics* 5(4): 818-824.
- Shylesh, S., V. Schünemann and W. R. Thiel. 2010. Magnetically separable nanocatalysts: Bridges between homogeneous and heterogeneous catalysis. *Angewandte Chemie International Edition* 49(20): 3428-3459.
- Siddiquey, I. A., T. Furusawa, M. Sato, N. M. Bahadur, M. Mahbul Alam and N. Suzuki. 2012. Sonochemical synthesis, photocatalytic activity and optical properties of silica coated ZnO nanoparticles. *Ultrasonic Sonochemistry* 19(4): 750-755.
- Siddiquey, I. A., T. Furusawa, M. Sato and N. Suzuki. 2008. Microwave-assisted silica coating and photocatalytic activities of ZnO nanoparticles. *Materials Research Bulletin* 43(12): 3416-3424.
- Siegel, R., D. Naishadham and A. Jemal. 2012. Cancer statistics, 2013. *CA: Cancer Journal for Clinicians* 63(1): 11-30.
- Simard, P. and J. C. Leroux. 2010. In vivo evaluation of pH-sensitive polymer-based immunoliposomes targeting the CD33 antigen. *Molecular Pharmaceutics* 7(4): 1098-1107.
- Singh, A. and S. K. Sahoo. 2014. Magnetic nanoparticles: A platform for cancer theranostics. *Drug Discovery Today* 19(4): 474-481.
- Sjogren, C. E., K. Briley-Saebo, M. Hanson and C. Johansson. 1994. Magnetic characterization of iron oxides for magnetic resonance imaging. *Magnetic Resonance in Medicine* 31(3): 268-272.
- Slivisatos, A. P. 1996. Semiconductor clusters, nanocrystals, and quantum dots. *Science* 271(5251): 933-937.
- Song, E.-Q., Z.-L. Zhang, Q.-Y. Luo, W. Lu, Y.-B. Shi and D.-W. Pang. 2009. Tumor cell targeting using folate-conjugated fluorescent quantum dots and receptor-mediated endocytosis. *Clinical Chemistry* 55(5): 955-963.
- Song, M., R. Zhang, Y. Sai, F. Gao, H. Chi, G. Lv, B. Chen and X. Wang. 2006. The in vitro inhibition of multidrug resistance by combined nanoparticulate titanium dioxide and UV irradiation. *Biomaterials* 27(23): 4230-4238.
- Sousa, M. E. d., M. B. F. v. Raap, P. C. Riva, P. M. Zelis, P. Girardin, G. A. Pasquevich, J. L. Alessandrini, D. Muraca and F. H. Sanchez. 2013. Stability and relaxation mechanisms of citric acid coated magnetite nanoparticles for

- magnetic hyperthermia. *The Journal of Physical Chemistry C* 117(10): 5436-5445.
- Sousa, M. H. and F. A. Tourinho. 2001. New electric double-layered magnetic fluids based on copper, nickel and zinc ferrite nanostructures. *The Journal of Physical Chemistry B* 105(6): 1168-1175.
- Stöber, W., A. Fink and E. Bohn. 1968. Controlled growth of monodisperse silica spheres in micron size range. *Journal of Colloid and Interface Science* 26(1): 62-69.
- Stefanou, E., A. Evangelou and P. Falaras. 2010. Effects of UV-irradiated titania nanoparticles on cell proliferation, cancer metastasis and promotion. *Catalysis Today* 151(1-2): 58-63.
- Sugimoto, T. and E. Matijevic. 1980. Formation of uniform spherical magnetite particles by crystallization from ferrous hydroxide gels. *Journal of Colloid and Interface Science* 74(1): 217-234.
- Sugimoto, T. and X. Zhou. 2002. Synthesis of uniform anatase TiO₂ nanoparticles by the gel-sol method: 2. Adsorption of OH⁻ ions to Ti(OH)₄ gel and TiO₂ particles. *Journal of Colloid and Interface Science* 252(2): 347-353.
- Sugimoto, T., X. Zhou and A. Muramatsu. 2002. Synthesis of uniform anatase TiO₂ nanoparticles by gel-sol method: 1. Solution chemistry of Ti(OH)_n⁽⁴⁻ⁿ⁾⁺ complexes. *Journal of Colloid and Interface Science* 252(2): 339-346.
- Sugimoto, T., X. Zhou and A. Muramatsu. 2003a. Synthesis of uniform anatase TiO₂ nanoparticles by gel-sol method: 3. Formation process and size control. *Journal of Colloid and Interface Science* 259(1): 43-52.
- Sugimoto, T., X. Zhou and A. Muramatsu. 2003b. Synthesis of uniform anatase TiO₂ nanoparticles by gel-sol method: 4. Shape control. *Journal of Colloid and Interface Science* 259(1): 53-61.
- Sultan, R. A. 1990. Tumour ablation by laser in general surgery. *Lasers in Medical Science* 5(2): 185-193.
- Sun, C., J. S. H. Lee and M. Zhang. 2008. Magnetic nanoparticles in MR imaging and drug delivery. *Advanced Drug Delivery Reviews* 60(11): 1252-1265.
- Sun, C., R. Sze and M. Zhang. 2006. Folic acid-PEG conjugated superparamagnetic nanoparticles for targeted cellular uptake and detection by MRI. *Journal of Biomedical Materials Research Part A* 78A(3): 550-557.

- Sun, H., Y. Bai, H. Liu, W. Jin and N. Xu. 2009. Photocatalytic decomposition of 4-chlorophenol over an efficient N-doped TiO₂ under sunlight irradiation. *Journal of Photochemistry and Photobiology A: Chemistry* 201(1): 15-22.
- Sun, H., X. Feng, S. Wang, H. M. Ang and M. O. Tadé. 2011. Combination of adsorption, photochemical and photocatalytic degradation of phenol solution over supported zinc oxide: Effects of support and sulphate oxidant. *Chemical Engineering Journal* 170(1): 270-277.
- Sun, Y., L. Duan, Z. Guo, Y. DuanMu, M. Ma, L. Xu, Y. Zhang and N. Gu. 2005. An improved way to prepare superparamagnetic magnetite-silica core-shell nanoparticles for possible biological application. *Journal of Magnetism and Magnetic Materials* 285(1-2): 65-70.
- Svaasand, L. O., C. J. Gomer and E. Morinelli. 1990. On the physical rationale of laser induced hyperthermia. *Lasers in Medical Science* 5(2): 121-128.
- Tang, F., L. Li and D. Chen. 2012. Mesoporous silica nanoparticles: Synthesis, biocompatibility and drug delivery. *Advanced Materials* 24: 1504-1534.
- Tang, S. C. N. and I. M. C. Lo. 2013. Magnetic nanoparticles: Essential factors for sustainable environmental applications. *Water Research* 47(8): 2613-2632.
- Teleki, A., M. Suter, P. R. Kidambi, O. Ergeneman, F. Krumeich, B. J. Nelson and S. E. Pratsinis. 2009. Hermetically coated superparamagnetic Fe₂O₃ particles with SiO₂ nanofilms. *Chemistry of Materials* 21(10): 2094-2100.
- Thevenot, P., J. Cho, D. Wavhal, R. B. Timmons and L. Tang. 2008. Surface chemistry influences cancer killing effect of TiO₂ nanoparticle. *Nanomedicine: Nanotechnology, Biology and Medicine* 4: 226-236.
- Todorovsky, D. S., D. G. Dumanova, R. V. Todorovska and M. M. Getsova. 2002. Preparation and characterization of yttrium-iron citric acid complexes. *Croatica Chemica Acta* 75(1): 155-164.
- Torchilin, V. P. 2005. Recent advances with liposomes as pharmaceutical carriers. *Nature Review Drug Discovery* 4(2): 145-160.
- Tsay, J. M. and X. Michalet. 2005. New light on quantum dot cytotoxicity. *Chemistry & Biology* 12(11): 1159-1161.
- Tung, W. S. and W. A. Daoud. 2009. New approach toward nanosized ferrous ferric oxide and Fe₃O₄-doped titanium dioxide photocatalysts. *ACS Applied Materials & Interfaces* 1(11): 2453-2461.

- Ullah, R. and J. Dutta. 2008. Photocatalytic degradation of organic dyes with manganese-doped ZnO nanoparticles. *Journal of Hazardous Materials* 156(1-3): 194-200.
- Valeur, E. and M. Bradley. 2009. Amide bond formation: Beyond the myth of coupling reagents. *Chemical Society Review* 38(2): 606-631.
- Vanheusden, K., W. L. Warren, C. J. Seager, D. R. Tallant and J. A. Voigt. 1996. Mechanisms behind green photoluminescence in ZnO phosphor powders. *Journal of Applied Physics* 79(10): 7983-7990.
- Vansant, E. F., P. v. d. Voort and K. C. Vrancken. 1995. Characterization and chemical modification of silica surface. Amsterdam, The Netherlands.
- Velasco, M. J., F. Rubio, J. Rubio and J. L. Oteo. 1999. DSC and FT-IR analysis of the drying process of titanium alkoxide precipitates. *Thermochimica Acta* 326(1-2): 91-97.
- Vohra, M. S. and K. Tanaka. 2003. Photocatalytic degradation of aqueous pollutants using silica-modified TiO₂. *Water Research* 37(16): 3992-3996.
- Von Tappeiner, H. and A. Jodlbauer. 1904. Über die Wirkung der photodynamischen (fluoreszierenden) Stoffe auf Protozoen und Enzyme. *Dtsch Arch Klin Med* 80: 427-487.
- Vora, A., A. Rega, D. Dollimore and K. S. Alexander. 2002. Thermal stability of folic acid. *Thermochimica Acta* 392: 209-220.
- Wagner, P., M. Hegner, P. Kern, F. Zaugg and G. Semenza. 1996. Covalent immobilization of native biomolecules onto Au (111) via N-hydroxysuccinimide ester functionalized self-assembled monolayers for scanning probe microscopy. *Biophysical Journal* 70: 2052-2066.
- Walling, M. A., J. A. Novak and J. R. E. Shepard. 2009. Quantum dots for live cell and in vivo imaging. *International Journal of Molecular Sciences* 10(2): 441-491.
- Walther, C., K. Meyer, R. Rennert and I. Neundorff. 2008. Quantum dot-carrier peptide conjugates suitable for imaging and delivery application. *Bioconjugate Chemistry* 19(12): 2346.
- Wang, P., D. Chen and Fang-Qiong Tang. 2006. Preparation of titania-coated polystyrene particles in mixed solvents. *Langmuir* 22(10): 4832-4835.
- Wang, X., Y. Wang, Z. G. Chen and D. M. Shin. 2009. Advance of cancer therapy by nanotechnology. *Cancer Research and Treatment* 41(1): 1-11.

- Wang, Y. and L. Chen. 2011. Quantum dots, lighting up the research and development of nanomedicine *Nanomedicine: Nanotechnology, Biology and Medicine* 7(4): 385-402.
- Wang, Y., R. Shi, J. Lin and Y. Zhu. 2011. Enhancement of photocurrent and photocatalytic activity of ZnO hybridized with graphnrite-like C₃N₄. *Energy & Environmental Science* 4: 2922-2929.
- Wei, T. Y. and C. C. Wan. 1991. Heterogeneous photocatalytic oxidation of phenol with titanium dioxide powders. *Industrial & Engineering Chemistry Research* 30(6): 1293-1300.
- Weishaupt, K. R., C. J. Gomer and T. J. Dougherty. 1976. Identification of singlet oxygen as cytotoxic agent in photo-inactivation of a murine tumor. *Cancer Research* 36: 2326-2329.
- Weitman, S. D., R. H. Lark, L. R. Coney, D. W. Fort, V. Frasca, V. R. Zurawski and B. A. Kamen. 1992. Distribution of the folate receptor GP38 in normal and malignant cell lines and tissues. *Cancer Research* 52(12): 3396-3401.
- Winkelman, W. and G. H. Collins. 1987. Neurotoxicity of tetraphenylporphinesulfonate TPPS₄ and its relation to photodynamic therapy. *Photochemical and Photobiological Sciences* 46(5): 801-807.
- Wu, C., H. Chang and J. Chern. 2006. Basic dye decomposition kinetics in a photocatalytic slurry reactor. *Journal of Hazardous Materials* 137(1): 336-343.
- Xin, X., Q. Wei, J. Yang, L. Yan, R. Feng, G. Chen, B. Du and H. Li. 2012. Highly efficient removal of heavy metal ions by amine-functionalized mesoporous Fe₃O₄ nanoparticles. *Chemical Engineering Journal* 184(0): 132-140.
- Xing, S., Z. Zhou, Z. Ma and Y. Wu. 2011. Characterization and reactivity of Fe₃O₄/FeMnO_x core/shell nanoparticles for methylene blue discoloration with H₂O₂. *Applied Catalysis B: Environmental* 107(3-4): 386-392.
- Xiong, G., U. Pal, J. G. Serrano, K. B. Ucer and R. T. Williams. 2006. Photoluminescence and FTIR study of ZnO nanoparticles: the impurity and defect perspective. *Physica Status Solidi (c)* 3(10): 3577-3581.
- Xu, H., Z. Zheng, L. Zhang, H. Zhang and F. Deng. 2008. Hierarchical chlorine-doped rutile TiO₂ spherical clusters of nanorods: Large-scale synthesis and high photocatalytic activity. *Journal of Solid State Chemistry* 181(9): 2516-2522.

- Xu, J., Y. Sun, J. Huang, C. Chen, G. Liu, Y. Jiang, Y. Zhao and Z. Jiang. 2007. Photokilling cancer cells using highly cell-specific antibody-TiO₂ bioconjugates and electroporation. *Bioelectrochemistry* 71(2): 217-222.
- Xu, T., L. Zhang, H. Cheng and Y. Zhu. 2011. Significantly enhanced photocatalytic performance of ZnO via graphene hybridization and the mechanism study. *Applied Catalysis B: Environmental* 101(3-4): 382-387.
- Yano, S., S. Hirohara, M. Obata, Y. Hagiya, S.-i. Ogura, A. Ikeda, H. Kataoka, M. Tanka and T. Joh. 2011. Current states and future views in photodynamic therapy. *Journal of Photochemistry and Photobiology C: Photochemistry Reviews* 12(1): 46-67.
- Ye, M., Q. Zhang, Y. Hu, J. Ge, Z. Lu, L. He, Z. Chen and Y. Yin. 2010. Magnetically recoverable core-shell nanocomposites with enhanced photocatalytic activity. *Chemistry-A European Journal* 16(21): 6243-6250.
- Yoon, T. J., K. N. Yu, E. Kim, J. S. Kim, B. G. Kim, S. H. Yun, B. H. Sohn, M. H. Cho, J. K. Lee and S. B. Park. 2006. Specific targeting, cell sorting, and bioimaging with smart magnetic silica core-shell nanomaterials. *Small* 2(2): 209-215.
- Yu, G., J. Gao, J. C. Hummelen, F. Wudl and A. J. Heeger. 1995. Polymer photovoltaic cells: Enhanced efficiencies via a network of internal donor-acceptor heterojunctions. *Science* 270(5243): 1789-1791.
- Yu, J., Q. Xiang and M. Zhou. 2009. Preparation, characterization and visible-light-driven photocatalytic activity of Fe-doped titania nanorods and first-principles study for electronic structures. *Applied Catalysis B: Environmental* 90(3-4): 595-602.
- Yu, J. and X. Yu. 2008. Hydrothermal synthesis and photocatalytic activity of zinc oxide hollow spheres. *Environmental Science & Technology* 42(13): 4902-4907.
- Zanella, R., S. Giorgio, C. R. Henry and C. Louis. 2002. Alternative methods for the preparation of gold nanoparticles supported on TiO₂. *The Journal of Physical Chemistry B* 106(31): 7634-7642.
- Zhang, C., J. Sui, J. Li, Y. Tang and W. Cai. 2012a. Efficient removal of heavy metal ions by thiol-functionalized superparamagnetic carbon nanotubes. *Chemical Engineering Journal* 210: 45-52.

- Zhang, H., B. Chen, H. Jiang, C. Wang, H. Wang and X. Wang. 2011. A strategy for ZnO nanorod mediated multi-mode cancer treatment. *Biomaterials* 32(7): 1906-1914.
- Zhang, H., R. Shi, A. Xie, J. Li, L. Chen, P. Chen, S. Li, F. Huang and Y. Shen. 2012b. Novel TiO₂/PEGDA hybrid hydrogel prepared in situ on tumor cells for effective photodynamic therapy. *ACS Applied Materials & Interfaces* 5(23): 12317-12322.
- Zhang, J., S. Rana, R. S. Srivastava and R. D. K. Misra. 2008a. On the chemical synthesis and drug delivery response of folate receptor-activated polyethylene glycol-functionized magnetite nanoparticles. *Acta Biomaterialia* 4: 40-48.
- Zhang, J., Y. Wu, M. Xing, S. A. K. Leghari and S. Sajjad. 2010. Development of modified N doped TiO₂ photocatalyst with metals, nonmetals and metal oxides. *Energy & Environmental Science* 3(6): 715-726.
- Zhang, Q., C. Wang, L. Qiao, H. Yan and K. Liu. 2009. Superparamagnetic iron oxide nanoparticles coated with a folate-conjugated polymer. *Journal of Materials Chemistry* 19(44): 8393-8402.
- Zhang, W., Y. Lu, T. Zhang, W. Xu, M. Zhang and S. Yu. 2008b. Controlled synthesis and biocompatibility of water-soluble ZnO nanorods/Au nanocomposites with tunable UV and visible emission intensity. *The Journal of Physical Chemistry C* 112(50): 19872-19877.
- Zhou, J., N. S. Xu and Z. L. Wang. 2006. Dissolving behavior and stability of ZnO wires in biofluids: A study on biodegradability and biocompatibility of ZnO nanostructures. *Advanced Materials* 18(18): 2432-2435.
- Zhu, J., W. Zheng, B. He, J. Zhang and M. Anpo. 2004. Characterization of Fe-TiO₂ photocatalysts synthesized by hydrothermal method and their photocatalytic reactivity for photodegradation of XRG dye diluted in water. *Journal of Molecular Catalysis A: Chemical* 216(1): 35-43.
- Zrazhevskiy, P., M. Sena and X. Gao. 2010. Designing multifunctional quantum dots for bioimaging, detection, and drug delivery *Chemical Society reviews* 39(11): 4326-4354.

Every reasonable effort has been made to acknowledge the owners of the copyright material. I would be pleased to hear from any copyright owner who has been omitted or incorrectly acknowledges.